University of Alberta

Geochemistry and Geochronology of the late Archean Prince Albert group (PAg), Nunavut, Canada

by

Trevor George MacHattie ©

A thesis submitted to the Faculty of Graduate Studies and Research
in partial fulfillment of the requirements for the degree of

Doctor of Philosophy

Department of Earth and Atmospheric Sciences

Edmonton, Alberta
Fall 2008

Library and
Archives Canada

Published Heritage
Branch

395 Wellington Street
Ottawa ON K1A 0N4
Canada

Bibliothèque et
Archives Canada

Direction du
Patrimoine de l'édition

395, rue Wellington
Ottawa ON K1A 0N4
Canada

Your file Votre référence
ISBN: 978-0-494-46373-4
Our file Notre référence
ISBN: 978-0-494-46373-4

NOTICE:
The author has granted a non-exclusive license allowing Library and Archives Canada to reproduce, publish, archive, preserve, conserve, communicate to the public by telecommunication or on the Internet, loan, distribute and sell theses worldwide, for commercial or non-commercial purposes, in microform, paper, electronic and/or any other formats.

The author retains copyright ownership and moral rights in this thesis. Neither the thesis nor substantial extracts from it may be printed or otherwise reproduced without the author's permission.

AVIS:
L'auteur a accordé une licence non exclusive permettant à la Bibliothèque et Archives Canada de reproduire, publier, archiver, sauvegarder, conserver, transmettre au public par télécommunication ou par l'Internet, prêter, distribuer et vendre des thèses partout dans le monde, à des fins commerciales ou autres, sur support microforme, papier, électronique et/ou autres formats.

L'auteur conserve la propriété du droit d'auteur et des droits moraux qui protège cette thèse. Ni la thèse ni des extraits substantiels de celle-ci ne doivent être imprimés ou autrement reproduits sans son autorisation.

In compliance with the Canadian Privacy Act some supporting forms may have been removed from this thesis.

While these forms may be included in the document page count, their removal does not represent any loss of content from the thesis.

Conformément à la loi canadienne sur la protection de la vie privée, quelques formulaires secondaires ont été enlevés de cette thèse.

Bien que ces formulaires aient inclus dans la pagination, il n'y aura aucun contenu manquant.

Canada

Abstract

New U-Pb age constraints indicate that all late Archean orthoquartzite-komatiite associated supracrustal belts within the central/northeastern Rae domain of Nunavut, including the Woodburn Lake group (WLg), Prince Albert group (PAg), and Mary River group (MRg) are components of a much larger, northeasterly-trending network (~1400 km long and up to ~400 km wide) of co-genetic, clastic-dominated supracrustal belts. The predominant mafic-ultramafic and associated felsic volcanism within these belts formed between 2735-2690 Ma and upon 2750-2870 Ma continental crust. Extensive detrital zircon age dating, however, indicates components of the Rae crust are much older, ranging between ~3.3-3.8 Ga. Nd isotopic data indicate that this crust is located to the west of the crustal corridor containing the supracrustal belts. The formation of these belts upon juvenile crust, adjacent to ancient components suggests a continental-margin setting. The focusing of magmatism/sedimentation along this crustal corridor for ~45 m.y. suggests that the pre-existing lithospheric architecture and structures controlled the large-scale distribution of magmatism. Moreover, the initial "pulses" of magmatism began abruptly between 2735-2730 Ma. With no evidence for uplift or age progressions, these data suggest active lithospheric extension preceded/facilitated the initiation of magmatism. Within the PAg segment, this phase of magmatism is unusually well-preserved and characterized by a voluminous (> 300 km^2 and ~3 km thick) komatiite-dominated mafic-ultramafic volcanic succession. Exceptional major/trace element geochemical fractionations and their correlation with stratigraphic height require decompression melting of a single "parcel" of hot peridotitic mantle separated into two

principal stages. Initial melting within the garnet-stability field generated a spectrum of HREE-depleted ultramafic magmas that pooled at shallow lithospheric depths and differentiated to form basalt. The continued rise of residues from the initial melting eventually began a renewed stage of melting. These low-density magmas traversed the crust rapidly without differentiation. The short time span separating the eruption of garnet-present and garnet-absent melt products requires pre-existing space to facilitate the upwelling. These data can be reconciled if mantle upwelling and melting were focused from beneath the thick, ancient Rae cratonic root toward its thin, juvenile margin. The origin of the thermally anomalous mantle is presumed to be a lower thermal boundary layer produced at the base of the upper mantle at ca. 2.7 Ga.

Table of Contents

Chapter 1. Introduction

Objective and scope of the thesis 1

The discovery and contributions on the origin of komatiite 3

Chapter 2. The Archean Prince Albert group (PAg), Central and Northeastern Rae domain, Nunavut, Canada: Age, Stratigraphy, and Regional Correlations

Introduction 23

Regional geology of the Committee Bay area 25

Chronostratigraphic subdivision of the PAg 27

Lower PAg mafic-ultramafic volcanic succession and associated sedimentary rocks within the Laughland Lake area 29

- Mafic-ultramafic and intermediate-felsic volcanic rocks 31
- Sedimentary rocks 33

Western Walker Lake and Kinngalugjuaq Mountain areas 35

U-Pb geochronology 35

- Methodology 35
- Analytical techniques 36
- U-Pb results 38
  - Dacite T-3319-B 38
  - Dacite H-1337 39
  - Rhyolite T-3151 40

Granodiorite HS0-334 42
Granodiorite dyke T-3459 42
Orthoquartzite TM0-106-A 43
Subarkose arenite HS0-329 45
Quartz arenite TM-11 46
Chronostratigraphy of orthoquartzite-komatiite associated supracrustal sequences of the PAg 47
Laughland Lake area 48
Western Walker Lake and Kinngalugjuaq Mountain areas 51
Regional correlation of orthoquartzite-komatiite associated supracrustal belts within the central and northeastern Rae domain 52
> 2735 Ma crust in the Rae domain imaged through detrital zircon age dating 55
Constraints for the setting of mafic-ultramafic magmatism 58
Significance of ≤ 2624 and 2612 Ma siliciclastic supracrustal rocks 60
Conclusions 61

Chapter 3. The Archean Prince Albert group (PAg), Central and Northeastern Rae domain, Nunavut, Canada: Evidence for an Extensional Continental Margin Setting

Introduction 100
Regional Archean geology of the central and northeastern Rae domain 102
General geology of the Committee Bay area and chronostratigraphy of the PAg 104

Stratigraphy, volcanology, and petrographic aspects of mafic, ultramafic, and intermediate-felsic volcanic rocks within the lower PAg 105

Basalt 106

Komatiite 107

Intermediate-felsic volcanic rocks 107

Geochemistry 108

Trace elements 109

Basalt 110

Komatiite 111

Intermediate-felsic volcanic rocks 111

Major elements 112

Basalt 112

Komatiite 113

Intermediate-felsic volcanic rocks 114

Nd isotopic data 114

U-Pb zircon isotopic results 115

Nature of the PAg basement and the origin of the intermediate-felsic volcanic rocks 117

Xenocrystic zircon constraints 117

Major and trace element constraints 118

Nd isotopic constraints 121

Trace element modeling of crust-mantle mixing 123

Group-1 basalt 124

Group-2 basalt 126

Group-1 komatiite 127

Group-2 komatiite 127

Insights into the magmatic development of the lower PAg 128

HREE-depleted komatiite, group-1 basalt, and primitive andesite association 129

Group-2 basalt and group-1 and -2 komatiite 130

New constraints for the regional setting of mafic ultramafic magmatism within the central and northeastern Rae domain 131

Conclusions 133

Appendix A. Sample preparation and analytical methods 135

Chapter 4. Generation of Archean Al-undepleted komatiite: Insights from ca. 2730 Ma mafic-ultramafic magmas within the lower Prince Albert group, Nunavut, Canada

Introduction 181

Regional Archean geology of supracrustal belts within the central and northeastern Rae domain and setting of mafic-ultramafic magmatism 183

General geology and chronostratigraphy of the PAg 184

Stratigraphy and petrology of the lower PAg mafic and ultramafic volcanic rocks 186

Komatiite 187

Basalt 188

Geochemistry 188

Preliminaries 188

Trace elements and subdivision – mafic magmatism 189

  Highly enriched group-1 basalt (EB-1) 189

  Moderately enriched group-2 basalt (EB-2) 190

  Minimally enriched group-3 basalt (EB-3) 191

  Depleted basalt (DB) 191

Trace elements and subdivision – ultramafic magmatism 192

  Group-A komatiite 192

  Group-B komatiite 193

  Group-C komatiite 193

  Group-D komatiite 194

Major elements 194

  Mafic magmatism 195

  Ultramafic magmatism 195

Nd isotopes 197

Hf isotopes 198

Isotopic composition of the mantle source 199

Defining basalt and komatiite compositional continua 201

Basalt compositional continuum 202

Komatiite compositional continuum 202

Approach to modeling basalt and komatiite petrogenesis 203

Depleted basalt generation 204

Highly enriched basalt generation 204

HREE-depleted group-A komatiite generation 208
HREE-enriched group-D komatiite generation 209
Origin of the compositional continua and two stage magmatic development of the lower PAg 212
Phase equilibria constraints 216
Regional setting of mafic-ultramafic magmatism and the importance of pre-existing lithospheric architecture and structures 220
Thermal, physical, and chemical structure of thermally anomalous mantle upwellings and their origin 223
Summary and conclusions 229
Appendix A. Sample preparation and analytical methods 230
Appendix B. Assessment of high-field-strength element anomalies 233
Appendix C. Assessment of crustal contamination and detection limit effects on highly incompatible trace element ratios 235
Appendix D. Quantification of the most HREE-enriched komatiite liquid 236
Appendix E. Plagioclase and low-CaO pyroxene (pigeonite) fractionation 238

Chapter 5. Summary of major conclusions and avenues for future research

Introduction 328
Extent, duration, and regional setting of supracrustal belts within the central and northeastern Rae domain 329
Detailed magmatic evolution of the lower PAg 331
The thermal and physical structure, temporal lifespan, and origin

of the mantle upwelling(s) within the PAg 334

Implications for the chemical and thermal structure of the Archean mantle 336

Avenues for future research: central and northeastern Rae domain 337

Avenues for future research: Al-undepleted komatiite and associated basalt petrogenesis 339

List of Tables

Table 2-1. U-Pb zircon isotopic data obtained by isotope dilution-TIMS 66

Table 2-2. U-Pb zircon isotopic data obtained by laser ablation-MC-ICP-MS 67

Table 3-1. Major and trace element compositions of Prince Albert group felsic, mafic and ultramafic volcanic rocks 141

Table 3-2. Sm-Nd isotopic compositions of Prince Albert group felsic, mafic and ultramafic volcanic rocks 144

Table 3-3. U-Pb zircon isotopic data obtained by laser ablation-MC-ICP-MS 145

Table 3-4. Major and trace element compositions of low $(Th/Nb)_N$ komatiite and basalt employed in geochemical modeling 146

Table 4-1. Major and trace element compositions of Prince Albert group mafic and ultramafic rocks 243

Table 4-2. Sm-Nd and Lu-Hf isotopic compositions of Prince Albert group mafic and ultramafic volcanic rocks 250

Table 4-3. Distribution coefficients used in trace element modeling 252

Table 4-4. Major element compositions of garnet peridotite (KR-4003) melts and komatiite 254

Table 4-5. Major element compositions of garnet peridotite (KR-4003) residues at ~4.5 GPa and various peridotitic mantle compositions 255

Table 4-A-1. Duplicate trace element analyses of basalt and komatiite 256

List of Figures

Fig. 2-1. The distribution of ca. 2.7 Ga supracrustal belts within the central and northeastern Rae domain of Nunavut 77

Fig. 2-2. General geological map of the Committee Bay region delineating the supracrustal rocks of the PAg from granitoid rocks 78

Fig. 2-3. Detailed geological map of the Laughland Lake mafic-ultramafic volcanic succession within the northeast volcanic zone 79

Fig. 2-4. Detailed geological map of the Laughland Lake mafic-ultramafic volcanic succession within the southwest volcanic zone 80

Fig. 2-5. (a-l) Selected images of PAg volcanic and sedimentary rocks 81

Fig. 2-6. (a-e) Concordia diagrams for PAg volcanic and intrusive rocks 83

Fig. 2-7. (a-c) Concordia diagrams and probability density histograms of $^{207}Pb/^{206}Pb$ age for detrital zircon separated from siliciclastic sedimentary rocks 84

Fig. 2-8. Chronostratigraphy of the Laughland Lake area 85

Fig. 2-9. U-Pb zircon ages for orthoquartzite-komatiite associated supracrustal belts of the central and northeastern Rae domain and their basement 86

Fig. 2-10. Plot of > 2735 Ma U-Pb zircon ages for the Rae domain and detrital zircon analysed in this study 87

Fig. 2-11. U-Pb zircon ages for > 2500 Ma and < 2700 Ma plutonic rocks of the Rae domain and the maximum depositional ages for subarkose arenite HS0-329 and quartz arenite TM-11 88

Fig. 3-1. The distribution of ca. 2.7 Ga supracrustal belts within the central and northeastern Rae domain of Nunavut 153

Fig. 3-2. General geological map of the Committee Bay region delineating the supracrustal rocks of the PAg from granitoid rocks 154

Fig. 3-3. Schematic composite PAg stratigraphy and subdivision into chronostratigraphic sequences 155

Fig. 3-4. (a-b) Selected images of PAg volcanic rocks 156

Fig. 3-5. MgO versus $(Th/Nb)_N$ for volcanic rocks of the PAg collected within the lower mafic-ultramafic volcanic succession 157

Fig. 3-6. Primitive mantle normalized extended element diagram for high $(Th/Nb)_N$ ($\geq$ to $>>$ 1) volcanic rocks 158

Fig. 3-7. (a) Plot of MgO versus $(Ce/Sm)_N$ and (b) $(Gd/Yb)_N$ for high $(Th/Nb)_N$ (≥ 1 to $>> 1$) volcanic rocks 159

Fig. 3-8. $(Th/Nb)_N$ versus $(Ce/Sm)_N$ for high $(Th/Nb)_N$ (≥ 1 to $>> 1$) volcanic rocks 160

Fig. 3-9. Plots of MgO versus selected major elements (SiO_2, Al_2O_3, Fe_2O_3T, TiO_2 and CaO) for volcanic rocks within the lower mafic-ultramafic volcanic succession 161

Fig. 3-10. (a) Plot of $^{147}Sm/^{144}Nd$ versus $\varepsilon Nd(2730\ Ma)$ and (b) Sm-Nd isochron diagram 162

Fig. 3-11. Concordia diagram and probability density histogram of $^{207}Pb/^{206}Pb$ age for xenocrystic zircon 163

Fig. 3-12. Primitive mantle normalized extended element diagram for intermediate-felsic volcanic rocks and various crustal compositions 164

Fig. 3-13. Nd isotopic evolution diagram for a hypothetical depleted mantle and ca. 2775, 2870 and 2950 Ma crust extracted from this mantle 165

Fig. 3-14. Plots of $(Th/Nb)_N$ versus $(Ce/Sm)_N$ and $(Gd/Yb)_N$ for high $(Th/Nb)_N$ basaltic volcanic rocks and various crust-mantle mixing curves 166

Fig. 3-15. (a-f) Primitive mantle normalized extended element diagrams summarizing the results of the mixing models 167

Fig. 3-16. MgO versus CaO, Al_2O_3, and TiO_2 plots for high $(Th/Nb)_N$ basaltic volcanic rocks and postulated olivine-dominated crystal fractionation pathway from parental komatiitic magma(s) 168

Fig. 4-1. The distribution of ca. 2.7 Ga supracrustal belts within the central and northeastern Rae domain of Nunavut 275

Fig. 4-2. General geological map of the Committee Bay region delineating the supracrustal rocks of the PAg from granitoid rocks 276

Fig. 4-3. Schematic composite PAg stratigraphy and subdivision into chronostratigraphic sequences 277

Fig. 4-4. Detailed geological map of the Laughland Lake mafic-ultramafic volcanic succession within the northeast volcanic zone (NVZ) 278

Fig. 4-5. Detailed geological map of the Laughland Lake mafic-ultramafic volcanic succession within the southwest volcanic zone (SVZ) 279

Fig. 4-6. (a-c and e) Transmitted light images of PAg mafic and ultramafic volcanic rocks. (d) Air photograph of komatiite flow sequence within the NVZ 280

Fig. 4-7. MgO versus $(Th/Nb)_N$ for volcanic rocks of the PAg collected within the lower mafic-ultramafic volcanic succession 281

Fig. 4-8. Primitive mantle normalized extended element diagram for the major basalt and komatiite groups 282

Fig. 4-9. Plots of MgO versus selected trace/minor elements for mafic and ultramafic volcanic rocks 283

Fig. 4-10. Plots of MgO versus HFSE/HFSE* ratios for mafic and ultramafic volcanic rocks 284

Fig. 4-11. Plots of MgO versus selected major elements and Al_2O_3/TiO_2 for mafic and ultramafic volcanic rocks 285

Fig. 4-12. Plots of $(Gd/Yb)_N$ versus major element oxides for group-A, -B and -C spinifex- and selected low-MgO olivine-phyric komatiite 286

Fig. 4-13. (a) Sm-Nd and (b) Lu-Hf isochron diagrams for low $(Th/Nb)_N$ basalt and komatiite 287

Fig. 4-14. (a) Plot of $^{147}Sm/^{144}Nd$ and (b) $(Gd/Yb)_N$ versus εNd(2730 Ma) for ca. 2690-2730 Ma mafic, ultramafic, and felsic volcanic rocks of the PAg 288

Fig. 4-15. (a) $(Ce)_N$ and (b) $(Yb)_N$ versus $(Ce/Yb)_N$ plots for members of the basalt compositional continuum. (c) MgO versus $(Yb)_N$ plot for members of the basalt compositional continuum 289

Fig. 4-16. (a) MgO versus $(Gd/Yb)_N$ for the group-A and group-C komatiite liquids and group-D komatiite. (b) Primitive mantle normalized extended element plot for the group-A and -C komatiite liquids and the result of un-mixing of these liquids to generate the group-D komatiite liquid 290

Fig. 4-17. (a) MgO versus Al_2O_3 plot for the DB, group-A komatiite liquid and a crystal fractionation pathway relating them. (b) Primitive mantle REE plot for the group-A komatiite sample TM0-239-12, the average low-MgO depleted basalt, and the result of 50 wt.% crystal fractionation of a mineral assemblage consisting of 70 wt.% olivine and 30 wt.% clinopyroxene from the komatiite 291

Fig. 4-18. MgO versus Al_2O_3 plot for members within the basalt compositional continuum and the group-A komatiite liquid 292

Fig. 4-19. (a) Melt (wt.%) versus Al_2O_3 plot for garnet-saturated experimental melts of the KR-4003 peridotite between ~4-7 GPa. (b) MgO versus Al_2O_3 plot for individual samples within the basalt compositional continuum, the group-A komatiite liquid, low-degree garnet-saturated experimental melts of the KR-4003 peridotite between ~4-7 GPa, various peridotite compositions, and postulated olivine and clinopyroxene crystal fractionation pathways relating parental komatiites and derivative basalt end-members. (c) Melt (wt.%) versus CaO plot for garnet-saturated experimental melts of the KR-4003 peridotite between ~4-7 GPa. (d) MgO versus CaO plot, samples and parameters as in Fig. 4-19(b) 293

Fig. 4-20. Solidus mineralogy of KR-4003 peridotite between 4-7 GPa 294

Fig. 4-21. (a and b) Various partition coefficients employed in modeling partial melting 295

Fig. 4-22. (a) $(Yb)_N$, (b) $(Ce)_N$, and (c) Hf/Hf* versus $(Ce/Yb)_N$ plots summarizing the results of modeling garnet peridotite melting attempting

to reproduce the group-E and -A komatiite liquid end-members.
(d) Primitive mantle normalized extended element plot displaying the group-A and -E komatiite liquid end-members, the depleted MORB mantle source, and selected results of modeling garnet peridotite melting 296

Fig. 4-23. MgO versus CaO plot for the group-A, -D, and -E komatiite liquids, the KR-4003 peridotite, the residue of ~25 wt.% melting of the KR-4003 peridotite at ~4.5 GPa, the refractory mantle peridotite DMM-1, and olivine and orthopyroxene compositions from residues of high-degree melting of the KR-4403 peridotite between ~3-4 GPa 297

Fig. 4-24. (a) Primitive mantle normalized extended element plot for the depleted MORB mantle and model residues generated from this mantle by the extraction of 2 and 25 wt.% melt between ~4-5 GPa. (b) Primitive mantle normalized extended element plot for the group-D komatiite liquid, residue of 25 wt.% melting between ~4-5 GPa, and the result of ~30 wt.% melting of this residue with a starting mode of 70 wt.% olivine and 30 wt.% orthopyroxene 298

Fig. 4-25. Extended element plot displaying the relative difference between the group-D komatiite liquid and the 30 wt.% model melt of refractory harzburgite, the partition coefficients employed in modeling this melting, the inverse of the bulk and orthopyroxene partition coefficients used to model harzburgite melting, and the relative difference between a 1 wt.% model melt and the harzburgite source 299

Fig. 4-26. (a) $(Ce)_N$ versus $(Ce/Yb)_N$ for the group-A and group-E komatiite liquid end-members, the minimally, moderately, and highly enriched members in the basalt compositional continuum, and their respective reconstituted parental ultramafic magmas. (b) Primitive mantle normalized REE plot for the group-A and –E komatiite liquid end-members, the parental ultramafic magmas to the minimally and moderately enriched members in the basalt compositional continuum, and mixtures involving the group-A and -E komatiite end-members 300

Fig. 4-27. Temperature versus pressure diagram illustrating the presumed melting pathways taken by the three primary end-member ultramafic magmas, the group-A, -D, and -E komatiite liquids 301

Fig. 4-28. Schematic cross-section of the lithospheric architecture (age and structure) present within the central and northeastern Rae domain during the formation of the lower PAg volcanic succession 302

Fig. 4-29. (a) MgO versus $(Gd/Yb)_N$ and (b) Hf/Hf* for basalt and komatiite collected within the lower PAg and those from map sheets east of the Laughland Lake area and from volcanic sequences in part constrained to be ca. 2710 and 2690 Ma 303

Fig. 4-B-1. (a) Lu (ppm) as determined by quadrupole-ICP-MS and versus Lu (ppm) as determined by ID-MC-ICP-MS and (b) Hf (ppm) as determined by quadrupole-ICP-MS and versus Hf (ppm) as determined by ID-MC-ICP-MS 304

Fig. 4-B-2. Plot of Hf/Hf* (quadrupol-ICP-MS) versus Hf/Hf* (ID-MC-ICP-MS) 305

Fig. 4-B-3. (a) P/P* versus Ti/Ti* and (b) P/P* versus Hf/Hf* (quadrupole-ICP-MS) for basalt and komatiite analysed in this study 306

Fig. 4-C-1. (a and b) $(Th/Nb)_N$ versus Nb/Nb* plot for low and high $(Th/Nb)_N$ basalt, komatiite, and intermediate felsic volcanic rocks collected within the lower PAg. (c) Primitive mantle normalized extended element plot for various basalt and komatiite samples and group averages and mixing and un-mixing models involving a TTG-type contaminant. (d) Un-mixing models involving dacite T-3319-B and basalt samples T-3318-A and T-3319-A 307

Fig. 4-D-1. (a) MgO versus TiO_2 and (b) Al_2O_3 for group-C and group-D komatiite. (c) Primitive mantle normalized MREE and HREE abundances for the group-C komatiite liquid and calculated cumulates 308

Fig. 4-D-2. (a) Primitive mantle normalized extended element plot for the group-D komatiite liquid, and the average the group-D komatiite from flows #4 and 6. (b) Primitive mantle normalized extended element plot for the group-D komatiite liquid and results of mixing with various crustal contaminants 309

Fig. 4-E-1. (a) Al_2O_3 versus CaO plot illustrating the presumed plagioclase, and low- and high-CaO clinopyroxene crystal differentiation control upon the composition of the group-3 enriched basalt. (b) Primitive mantle normalized REE plot for the group-3 enriched basalt end-members and the results of modeling 50 wt.% clinopyroxene and plagioclase fractionation from basalt sample HS0-091-I 310

List of Abbreviations

DB	Depleted basalt
EB-1	Highly enriched group-1 basalt
EB-2	Moderately enriched group-2 basalt
EB-3	Minimally enriched group-3 basalt
MORB	Mid-ocean-ridge basalt
MRg	Mary River group
NVZ	Northeast volcanic zone
PAg	Prince Albert group
SVZ	Southwest volcanic zone
WLg	Woodburn Lake group

Chapter 1. Introduction

OBJECTIVE AND SCOPE OF THE THESIS

This thesis, as initially conceived, was to involve the integration of field mapping with U-Pb zircon geochronology and geochemistry to determine the geodynamic setting and petrogenesis of Archean komatiite occurrences within the Prince Albert group (PAg). The PAg is a ~600 km long clastic-dominated supracrustal belt located within the Rae domain of the northeastern Canadian Shield, long recognized for its unique orthoquartzite-komatiite lithological association (Heywood, 1967; Schau, 1977). However, prior to the initiation of a new regional mapping initiative focused along a significant, ~300 km long segment of the PAg by the Geological Survey of Canada, Canada-Nunavut Geoscience Office, and university partners (this study), the age and stratigraphy of the group were unresolved, the major, trace element and isotope geochemistry of its volcanic deposits had not been investigated, and the relationship between the PAg and contiguous supracrustal belts, underlying ~0.5 million km^2 of the central and northeastern Rae domain, had not been satisfactorily established. Nearing the completion of the field mapping and with significant portions of the data collected toward resolving these issues, it was decided that this thesis would focus largely, but not exclusively, upon a spectacularly well-preserved and extensive (> 300 km^2 and ~3 km thick) mafic-ultramafic volcanic succession discovered within the Laughland Lake area (southwest PAg) and now recognized to comprise the basal sequence to the PAg.

With the regional and detailed field mapping, U-Pb zircon age dating, and major and trace element and isotope (Hf and Nd) geochemistry completed, it is clear that the lower PAg volcanic succession and supracrustal rocks within the Laughland Lake area in general, have retained important information specific to not only the setting and petrogenesis of mafic-ultramafic magmatism within the PAg and adjacent supracrustal belts, but insights applicable to broader issues surrounding the petrogenesis and setting of Archean mafic-ultramafic magmatism. In many respects, the lower PAg mafic-ultramafic volcanic succession mirrors the lava piles described by Wood (1979) in which incompatible element enriched, low-MgO volcanic rocks are overlain by those with higher MgO and displaying complimentary depletions in incompatible trace elements. However, in this Archean example, Al-undepleted komatiite is the dominant volcanic rock. Importantly, the preservation of this unique correlation between geochemistry and stratigraphic height can be used to model its formation, and unravel detailed information concerning the sources, processes and conditions of PAg komatiite magma generation.

In Chapter 2 the results of U-Pb zircon age dating of volcanic, plutonic and sedimentary rocks is presented, the PAg chronostratigraphy is defined, and the correlation of supracrustal belts within the northeastern Rae domain is examined. In Chapter 3 the geochemistry of crustally-derived/contaminated intermediate-felsic volcanic rocks and high $(Th/Nb)_N$ basalt and komatiite is presented along with whole rock Nd isotopic data and U-Pb age dating of xenocrystic zircons. This Chapter establishes the age of the lower PAg basement and provides more detailed insights into the setting of the supracrustal belts within the northeastern Rae domain. In Chapter 4 the geochemistry of uncontaminated, low $(Th/Nb)_N$ basalt and komatiite is presented. In this Chapter the nature and origin of the magmas is discussed, the tectonic setting further refined, and the implications of this work with respect to the petrogenesis of Archean mafic-ultramafic magmas and the chemical and thermal structure of the Archean mantle are highlighted. A summary of the main conclusions of Chapters 2 through 4 is detailed in Chapter 5, and below a review of the literature concerning komatiite petrogenesis is presented.

THE DISCOVERY AND CONTRIBUTIONS ON THE ORIGIN OF KOMATIITE

The detailed field descriptions and supporting major element analyses of ca. 3.5 Ga mafic and ultramafic rocks from South Africa by the Viljoen brothers (Viljoen & Viljoen, 1969*a* and *b*) is widely cited as the first definitive evidence for the existence of ultramafic lavas. These authors coined the name "peridotitic komatiite" to emphasize the very high MgO contents of these rocks (~33 wt.% on average; Table 2 of Viljoen & Viljoen, 1969*b*) and the location of their discovery, within the Komati formation of the Barberton belt. The prefix peridotitic also distinguished these very high MgO rocks from associated and possibly genetically related basaltic rocks, which they suggested be called basaltic komatiite. The distinctive, mega- to microscopic skeletal and bladed olivine textures that often develop within the upper portions of peridotitic komatiite flows was later called spinifex-texture by Nesbitt (1971), and has now become synonymous with them. Although the Viljoen brothers intended the name komatiite to represent a new ultramafic rock class, it was later suggested that komatiite be more simply defined as an ultramafic volcanic rock with > 18 wt.% MgO (Arndt & Brooks, 1980). The current IUGS classification defines komatiite as a volcanic rock with > 18 wt.% MgO, SiO_2 between 30-52 wt.%, $Na_2O+K_2O < 2$ wt.% and $TiO_2 < 1$ wt.% (Le Bas, 2000). Although the presence of spinifex-texture is not a necessary requirement for the IUGS definition, its importance to the identification of komatiite has been debated (e.g. Kerr & Arndt, 2001; Le Bas, 2001).

Although rare, a handful of exceptionally well-preserved ca. 2.7 Ga komatiite lava flows do retain a significant portion of their primary texture, mineralogy and geochemistry so that liquid compositions can, with some degree of confidence, be reliably ascertained. Importantly, these well-characterized examples indicate that some Archean komatiite magmas erupted with MgO contents as high as ~25-29 wt.% (Nisbet *et al.*, 1993). Since the MgO content of a liquid is a direct function of its temperature, these lavas would have erupted at the surface with temperatures between ~1520-1580 °C (Nisbet *et al.*, 1993) and, as such, are the hottest magmas known to have erupted on Earth. A peak in the preservation of komatiite in the Archean geological record, a noticeable decline in their abundance in the Proterozoic, and near absence from the Phanerozoic record (only low MgO varieties with ~18-20 wt.%) has been interpreted to track the overall decrease in mantle temperature since the Archean (e.g. de Wit & Ashwal, 1997), assuming that the processes of melt generation within the mantle and its bulk composition have not changed significantly through time.

Partial melting experiments of nominally anhydrous, natural lherzolites (e.g. KLB-1 and KR-4003), compositionally similar to estimates of the primitive depleted mantle (McDonough & Sun, 1995), as well as more recent estimates of the depleted upper mantle MORB source (Salters & Stracke, 2004; Workman & Hart, 2005) attempting to replicate the conditions of komatiite magma generation within the mantle (Takahashi & Scarfe, 1985; Takahashi, 1986; Herzberg & Zhang, 1996; Walter, 1998) have provided invaluable constraints for their formation. Importantly, these experiments have universally demonstrated that as the pressure of melting increases, near solidus melts (currently this is limited to the ~10 wt.% range because of physical, chemical, and technological limitations to high pressure experimentation) become increasingly more olivine-normative and are komatiitic at pressures ≥ 3-4 GPa. The most recent experiments of Walter (1998) using the KR-4003 lherzolite are particularly informative because melt fractions as low as ~10 wt.% and up to ~90 wt.% were investigated over a wide pressure interval between ~3-7 GPa. This study allows for a more quantitative examination of the affects of pressure, temperature and melt % on the composition of ultramafic melts. For example, although a ~55 wt.% partial melt of lherzolite KR-4003 at 3 GPa and a ~15 wt.% partial melt at 7 GPa are both komatiitic and possess ~24 wt.% MgO, other major and minor element contents (e.g. FeO, Al_2O_3, CaO and TiO_2) do allow for a distinction between these particular experimentally generated melts and, possibly then, inferences about the melting conditions of erupted komatiitic lavas. The low degree/high pressure melt generated at 7 GPa has higher FeO, CaO and TiO_2 and significantly lower Al_2O_3 than the high degree/low pressure melt; the latter resulting from a significant proportion of garnet within the residual mineral assemblage.

Although relatively "low" degree partial melting of nominally anhydrous lherzolite at high pressure (garnet-peridotite) may explain the origin of some Archean komatiite (e.g. variants of the aluminum-depleted variety; see Nesbitt *et al.*, 1979), the majority of Archean komatiite, and particularly the relatively large volumes produced at ca. 2.7 Ga are not depleted in Al_2O_3 (e.g. Sproule *et al.*, 2002). These are the so called aluminum-undepleted (see Nesbitt *et al.*, 1979) or "Munro-type" (e.g. Arndt, 1994) komatiite; the latter making reference to the exceptionally well-preserved komatiite flows of Munro Township in Ontario, Canada (see Arndt *et al.*, 1977). In general, this "type" of komatiite is characterized by Al_2O_3/TiO_2 ratios similar to estimates of the primitive mantle, moderate to strong depletion in the most incompatible trace elements, minimal fractionation of middle and heavy rare earth elements, and overall, quite low incompatible element abundances (Arndt *et al.*, 1997). These features are inconsistent with typical Al-undepleted komatiite magma generation by relatively low degrees of partial melting and are more consistent with high to very high degrees of mantle melting. For instance, the high MgO contents of some komatiite (up to ~29 wt.%) requires $\geq$ 50 wt.% equilibrium melting of lherzolites KR-4003 or KLB-1 (they possess ~37-39 wt.% MgO). However, as discussed by Arndt (1977), it is highly unlikely that komatiite magmas were produced in a single-stage high degree melting event because melt migration is expected to occur well below where these extremely high extents of melting are reached. Arndt (1977) suggested that komatiite magma was probably better produced in some form of sequential melting process in which earlier melt extraction, leaving depleted residua and minor trapped melt, was subsequently re-melted to produce komatiite.

The suggestion that Archean komatiite magma generation occurs by some form of multi-stage melting process as outlined by Arndt (1977) may be similar to what is now commonly referred to as continuous or dynamic melting theory; the middle ground between pure equilibrium and pure fractional melting (see detailed review of theory by Shaw (2000)). At the heart of dynamic melting theory is the idea that some specified amount of melt is always retained with the residual minerals and that melt extraction occurs continuously above a certain specified permeability threshold. The retention of some equilibrium melt essentially buffers the bulk residue (i.e. minerals and trapped melt) from approaching the extreme depletion that would occur by pure fractional melting alone and often melting models will describe this process as "near fractional" melting. By comparison with equilibrium melting, dynamic or multi-stage melting also allows a single source to generate a wider compositional spectrum of magmas than possible by simply varying the degree of equilibrium melting and, importantly, magmas more depleted in incompatible trace elements than their original source can be generated during the more advanced stages of melting, a feature not possible for single-stage equilibrium melting models.

Dynamic melting theory was initially developed by Langmuir *et al.* (1977) to explain some peculiar rare earth element variations (crossing patterns) in basalts from the FAMOUS area along the Mid-Atlantic Ridge. At approximately the same time, this theory was applied by Wood (1979) to try and explain why certain lava piles, erupted in different settings around the globe, including those found in Iceland, on the Faeroe Islands, the Isle of Skye (Scotland) and within the Troodos Massif in Cyprus, were all vertically compositionally zoned with the most Mg-rich and "hygromagmatophile" (incompatible) element depleted basalts concentrated toward the top of each lava pile. Wood (1979) suggested that a common melting process was involved in all these settings and that discrete portions of the mantle undergoing nearly continuous decompression melting must be capable of sequentially producing a compositional spectrum of lavas. As the most depleted magmas were expected to be the last to form in this process, they were the last to erupt. In this model, the highly depleted magmas are the end product of the previous extraction of enriched magmas. Following the pioneering work of Wood (1979), dynamic melting theory has been more recently applied to modeling plume-related decompression melting in Iceland (Elliott, 1991; Gurenko & Chaussidon, 1995), plume magmatism on the Hawaiian islands (Eggins, 1992), and the production of the famous Cretaceous komatiites (~18-20 wt.% MgO) located on Gorgona Island, forming part of the Caribbean oceanic plateau (Arndt *et al.*, 1997). Dynamic melting theory, coupled with complex melt transport models (e.g. channelized melt migration) have also been used to explain some of the major and trace element variability and U-series isotopic systematics of mid-ocean-ridge basalts (Kelemen *et al.*, 1995, 2000; Spiegelman & Kelemen, 2003; Elliott & Spiegelman, 2003) and rare, ultra-depleted trace element signatures (e.g. $(Ce/Yb)_N = 0.04$) observed for some olivine-hosted melt inclusions (Sobolev & Shimizu, 1993).

Although in detail dynamic or multi-stage melting models are invariably complex, particularly if the affects of melt transport are considered (see Spiegelman & Kelemen, 2003), the concept may help to explain how incompatible element depleted and MgO-rich ultramafic magmas can be generated at more realistic melt fractions than suggested from equilibrium partial melting experiments. Importantly though, if Archean komatiite, particularly those with the highest MgO contents (~29 wt.%) are indeed produced during the advanced stages of a dynamic and/or multi-stage melting regime, their bulk compositions cannot then be directly compared with the results of isobaric peridotite melting experiments conducted under equilibrium conditions. In this case, the melting conditions of more depleted compositions expected to be generated during the more advanced stages of melting (i.e. harzburgite) would need to be investigated. Alternatively, if the melts extracted during the earliest deeper stages of melting could be identified (e.g. high MgO magmas enriched in incompatible elements), they might provide important constraints concerning the original source composition and pressure of initial melting.

The common theme to the overview presented above is that Archean komatiite magma generation requires peridotitic sources, and that "typical" Al-undepleted komatiite requires high degrees of melting, either for simple equilibrium models or more complex multi-stage melting models. This indicates high temperatures must be present within the mantle source regions. However, equating the high eruption temperatures of some komatiite (up to ~1580 °C for magmas with ~29 wt.% MgO) to mantle source temperatures and depths of initial melting is problematical (Nisbet *et al.*, 1993). Some of the uncertainty in evaluating source temperature estimates include, assumptions about the pressure of melt segregation and lithospheric thickness at the time of melt generation, the complex and poorly understood processes of melt migration within the mantle (see Elliott & Spiegelman, 2003), and the appropriate peridotitic source composition and its corresponding solidus. With respect to the latter, solidus temperatures for the nearly identical natural lherzolites routinely used in melting experiments (e.g. KR-4003 and KLB-1), and both equally valid starting compositions, currently vary by close to 100 °C at 5 GPa (Herzberg *et al.*, 2000; Lesher *et al.*, 2002), apparently a result of subtle compositional differences (e.g. Hirschmann, 2000) and not to inter-laboratory biases (Lesher *et al.*, 2002). Clearly then, if back extrapolation of komatiite eruption temperatures without incorporation of significant error is even possible, uncertainty in the mantle solidus chosen will have a major influence on the inferred mantle potential temperature.

Largely because of the high eruption temperatures and inferred mantle source temperature estimates, models of komatiite magma generation have almost universally been linked with mantle plumes (Campbell *et al.*, 1989; Campbell & Griffiths, 1993; Herzberg, 1995; Arndt *et al.*, 1997; Tomlinson *et al.*, 1999). In plume-based models, komatiite-bearing volcanic successions are either interpreted as remnants of accreted oceanic plateau (Storey *et al.*, 1991; Arndt *et al.*, 1997; Puchtel *et al.*, 1998; Kerr *et al.*, 2000), or alternatively, if evidence of a continental influence is present, comparisons are drawn with continental flood basalt provinces and continental rifting (Compston *et al.*, 1986; Nelson, 1992; Blake, 1993; Blenkinsop *et al.*, 1993; Hunter *et al.*, 1998; Arndt, 1999; Cousens, 2000; Bolhar *et al.*, 2003; Shimizu *et al.*, 2004; 2005). However, in many instances the presence of komatiite is the only evidence suggestive of the possible involvement of mantle plumes and, due to the many uncertainties concerning their detailed petrogenesis highlighted above, the physical, chemical and thermal structure of inferred Archean mantle plumes is correspondingly poorly constrained. It is also unclear in many of these studies to what extent, if any, processes within the overriding lithosphere have in influencing potential mantle plumes, apart from simply acting as a barrier to continued decompression melting and as a contaminant to high-temperature magmas.

It has been statistically recognized that modern hotspot (plume) formation is suppressed at convergent plate boundaries and enhanced in divergent settings (Weinstein & Olson, 1989), an observation suggesting that mantle plumes are affected by convective motion within the mantle and can become entrained into, or are genetically related to large-scale upwellings. Moreover, it has been suggested that pre-existing lithospheric discontinuities, specifically thick cratonic roots adjacent to thin margins may not only focus mantle flow and potentially entrain plumes, but their existence may induce flow and concomitant decompression melting as hotter mantle from beneath thickened lithosphere flows toward thinner margins (King & Anderson, 1995; 1998). These observations and models are a significant departure from those suggesting that mantle plumes are created by thermally-induced buoyancy instabilities localized at the core mantle-boundary and interpreted to be largely independent of larger-scale convective motion within the mantle (e.g. Griffiths & Campbell, 1990; Campbell & Griffiths, 1993).

Another currently popular alternative to traditional plume-based models suggests that some komatiite-bearing mafic-ultramafic successions may have an origin within an Archean supra-subduction zone setting (Grove *et al.*, 1999; Parman *et al.*, 2001; Parman *et al.*, 2003). These authors have challenged the high MgO contents proposed for some komatiite, specifically the ~33 wt. % MgO contents suggested for some ca. 3.5 Ga Barberton komatiite; the latter yielded experimentally determined 1 atm liquidus temperatures of ~1650 °C (Green *et al.*, 1975). Instead, they highlight chemical similarities between Barberton basaltic komatiite (~10-18 wt. % MgO; see Fig. 1 of Parman *et al.*, 2001) and modern high-MgO subduction related magmas known as boninites (> 8 wt.% MgO, SiO_2 > 53 wt.% and TiO_2 < 1 wt.%; see Le Bas, 2000), or the results of water saturated (~6 wt.%) crystallization experiments on a Barberton komatiite analogue composition with significantly lower MgO (~24 wt.%). The latter displayed multiple saturation with olivine and orthopyroxene at relatively low pressure and temperature (~2.2 GPa and 1430 °C) suggesting a depleted harzburgite mantle fluxed with H_2O would melt to produce komatiite; an ideal setting for which would be an Archean subduction zone (Grove *et al.*, 1999).

REFERENCES

Arndt, N. T. (1977). Ultrabasic Magmas and High-Degree Melting of the Mantle. *Contributions to Mineralogy and Petrology* **64**, 205-221.

Arndt, N. T. (1994). Archean Komatiites. In: Condie, K.C. (ed.) *Archean Crustal Evolution*. Amsterdam: Elsevier, pp. 11-44.

Arndt, N. T. (1999). Why was flood volcanism on submerged continental platforms so common in the Precambrian? *Precambrian Research* **97**, 155-164.

Arndt, N. T., Albarède, F. & Nisbet, E. G. (1997). Mafic and Ultramafic Magmatism. In: de Wit, M.J. & Ashwal, L.D. (eds) *Greenstone Belts*. Oxford: Oxford University Press, pp. 233-254.

Arndt, N. T. & Brooks, C. (1980). Komatiites. *Geology* **8**, 155-156.

Arndt, N. T., Kerr, A. C. & Tarney, J. (1997). Dynamic melting in plume heads: the formation of Gorgona komatiites and basalts. *Earth and Planetary Science Letters* **146**, 289-301.

Arndt, N. T., Naldrett, A. J. & Pyke, D. R. (1977). Komatiitic and Iron-rich Tholeiitic Lavas of Munro Township, Northeast Ontario. *Journal of Petrology* **18**, 319-369.

Blake, T. S. (1993). Late Archaean crustal extension, sedimentary basin formation, flood basalt volcanism and continental rifting: the Nullagine and Mount Jope Supersequences Western Australia. *Precambrian Research* **60**, 185-241.

Blenkinsop, T. G., Fedo, C. M., Bickle, M. J., Eriksson, K. A., Martin, A., Nisbet, E. G. & Wilson, J. F. (1993). Ensialic origin for the Ngezi Group, Belingwe greenstone belt, Zimbabwe. *Geology* **21**, 1135-1138.

Bolhar, R., Woodhead, J. D. & Hergt, J. M. (2003). Continental setting inferred for emplacement of the 2.9-2.7 Ga Belingwe Greenstone Belt, Zimbabwe. *Geology* **31**, 295-298.

Campbell, I. H. & Griffiths, R. W. (1993). The evolution of the mantle's chemical structure. *Lithos* **30**, 389-399.

Campbell, I. H., Griffiths, R. W. & Hill, R. I. (1989). Melting in an Archaean mantle plume: heads it's basalts, tails it's komatiites. *Nature* **339**, 697-699.

Compston, W., Williams, I. S., Campbell, I. H. & Gresham, J. J. (1986). Zircon xenocrysts from the Kambalda volcanics, age constraints and direct evidence for older continental crust below the Kambalda-Norseman greenstones. *Earth and Planetary Science Letters* **76**, 299-311.

Cousens, B. L. (2000). Geochemistry of the Archean Kam Group, Yellowknife Greenstone Belt, Slave Province, Canada. *Journal of Geology* **108**, 181-197.

de Wit, M. J. & Ashwal, L. D. (1997). Convergence Towards Divergent Models of Greenstone Belts. In: de Wit, M. J. & Ashwal, L. D. (eds) *Greenstone Belts*. Oxford: Oxford University Press, pp. ix-xix.

Eggins, S. M. (1992). Petrogenesis of Hawaiian tholeiites: 2, aspects of dynamic melt segregation. *Contributions to Mineralogy and Petrology* **110**, 398-410.

Elliott, T. R., Hawkesworth, C. J. & Grönvold, K. (1991). Dynamic melting of the Iceland plume. *Nature* **351**, 201-206.

Elliott, T. & Spiegelman, M. (2003). Melt Migration in Oceanic Crustal Production: A U-series Perspective. In: Holland, H. D. & Turekien, K. K. (eds) *Treatise on Geochemistry* Amsterdam: Elsevier, **3**, 465-510.

Green, D. H., Nicholls, I. A., Viljoen, M. & Viljoen, R. (1975). Experimental Determination of the Existence of Peridotitic Liquids in Earliest Archean Magmatism. *Geology* **3**, 11-14.

Griffiths, R. W. & Campbell, I. H. (1990). Stirring and Structure in mantle starting plumes. *Earth and Planetary Science Letters* **99**, 66-78.

Grove, T. L., Parman, S. W. & Dann, J. C. (1999). Conditions of magma generation for Archean komatiites from the Barberton Mountainland, South Africa. In: Fei, Y., Bertka, C. M. & Mysen, B. O. (eds) *Mantle Petrology: Field Observations and High Pressure Experimentation: A Tribute to Francis R. (Joe) Boyd*. The Geochemical Society, Special Publication No. 6, pp. 155-167.

Grove, T. L. & Parman, S. W. (2004). Thermal evolution of the Earth as recorded by komatiites. *Earth and Planetary Science Letters* **219**, 173-187.

Gurenko, A. A. & Chaussidon, M. (1995). Enriched and depleted primitive melts included in olivine from Icelandic tholeiites: Origin by continuous melting of a single melt column. *Geochimica et Cosmochimica Acta* **59**, 2905-2917.

Herzberg, C. (1995). Generation of plume magmas through time: an experimental perspective. *Chemical Geology* **126**, 1-16.

Herzberg, C., Raterron, P. & Zhang, J. (2000). New experimental observations on the anhydrous solidus for peridotite KLB-1. *Geochemistry Geophysics Geosystems* **1**, 2000GC000089.

Herzberg, C. & Zhang, J. (1996). Melting experiments on anhydrous peridotite KLB-1: Compositions of magmas in the upper mantle and transition zone. *Journal of Geophysical Research* **101**, 8271-8295.

Heywood, W. W. (1967). Geological notes, northeastern District of Keewatin and southern Melville Peninsula, District of Franklin, Northwest Territories (part 46, 47, 56, 57). Geological Survey of Canada, Special Paper 66-40.

Hirschmann, M. M. (2000). Mantle solidus: Experimental constraints and the effects of peridotite composition. *Geochemistry Geophysics Geosystems* **1**, 2000GC000070.

Hunter, M. A., Bickle, M. J., Nisbet, E. G., Martin, A. & Chapman, H. J. (1998). Continental extensional setting for the Archean Belingwe Greenstone Belt, Zimbabwe. *Geology* **26**, 883-886.

Kelemen, P. B., Shimizu, N. & Salters, V. J. M. (1995). Extraction of mid-ocean-ridge basalt from the upwelling mantle by focused flow of melt in dunite channels. *Nature* **375**, 747-753.

Kelemen, P. B., Braun, M. & Hirth, G. (2000). Spatial distribution of melt conduits in the mantle beneath oceanic spreading ridges: Observations from the Ingalls and Oman ophiolites. *Geochemistry Geophysics Geosystems* **1**, 1999GC000012.

Kerr, A. C. & Arndt, N. T. (2001). A Note on the Reclassification of the High-Mg and Picritic Volcanic Rocks. *Journal of Petrology* **42**, 2169-2171.

Kerr, A. C., White, R. V. & Saunders, A. D. (2000). LIP Reading: Recognizing Oceanic Plateaux in the Geological Record. *Journal of Petrology* **41**, 1041-1056.

King, S. D. & Anderson, D. L. (1995). An alternative mechanism of flood basalt formation. *Earth and Planetary Science Letters* **136**, 269-279.

King, S. D. & Anderson, D. L. (1998). Edge-driven convection. *Earth and Planetary Science Letters* **160**, 289-296.

Langmuir, C. H., Bender, J. F., Bence, A. E., Hanson, G. N. & Taylor, S. R. (1977). Petrogenesis of basalts from the FAMOUS area: Mid-Atlantic Ridge. *Earth and Planetary Science Letters* **36**, 133-156.

Le Bas, M. J. (2000). IUGS Reclassification of the High-Mg and Picritic Volcanic Rocks. *Journal of Petrology* **41**, 1467-1470.

Le Bas, M. J. (2001). Reply to Comment by Kerr and Arndt. *Journal of Petrology* **42**, 2173-2174.

Lesher, C. E., Pickering-Witter, J., Baxter, G. & Walter, M. J. (2003). Melting of garnet peridotite: Effects of capsules and thermocouples, and implications for the high-pressure mantle solidus. *American Mineralogist* **88**, 1181-1189.

McDonough, W. F. & Sun, S.-s. (1995). The Composition of the Earth. *Chemical Geology* **120**, 223-253.

Nelson, D. R., Trendall, A. F., de Laeter, J. R., Grobler, N. J. & Fletcher, I. R. (1992). A comparative study of the geochemical and isotopic systematics of late Archaean flood basalts from the Pilbara and Kaapvaal Cratons. *Precambrian Research* **54**, 231-256.

Nisbet, E. G., Cheadle, M. J., Arndt, N. T. & Bickle, M. J. (1993). Constraining the potentential temperature of the Archean mantle: A review of the evidence from komatiites. *Lithos* **30**, 291-307.

Nesbitt, R. W. (1971). Skeletal crystal forms in the ultramafic rocks of the Yilgarn Block, Western Australia: evidence for an Archaean ultramafic liquid. *Geol. Soc. Aust. Spec. Publ.* **3**, 331-348.

Nesbitt, R. W., Sun, S-s. & Purvis, A. C. (1979). Komatiites: Geochemistry and genesis. *Canadian Mineralogist* **17**, 165-186.

Parman, S. W., Grove, T. L. & Dann, J. C. (2001). The production of Barberton komatiites in an Archean subduction zone. *Geophysical Research Letters* **28**, 2513-2516.

Parman, S. W., Shimizu, N., Grove, T. L. & Dann, J. C. (2003). Constraints on the pre-metamorphic trace element composition of Barberton komatiites from ion probe analyses of preserved clinopyroxene. *Contributions to Mineralogy and Petrology* **144**, 383-396.

Puchtel, I. S., Hofmann, A. W., Mezger, K., Jochum, K. P., Shchipansky, A. A. & Samsonov, A. V. (1998). Oceanic plateau model for continental crustal growth in the Archaean: A case study from the Komstomuksha greenstone belt, NW Baltic Shield. *Earth and Planetary Science Letters* **155**, 57-74.

Salters, V. J. M. & Stracke, A. (2004). Composition of the depleted mantle. *Geochemistry Geophysics Geosystems* **5**, 2003GC000597.

Schau, M. (1977). Komatiites and quartzites in the Archean Prince Albert Group. In: Baragar, W. R. A., Coleman, L. S. & Hall, J. M. (eds) *Volcanic Regimes in Canada.* Geological Association of Canada Special Publication 16, pp. 341-354.

Shaw, D. M. (2000). Continuous (dynamic) melting theory revisited. *The Canadian Mineralogist* **38**, 1041-1063.

Shimizu, K., Nakamura, E., Kobayashi, K. & Maruyama, S. (2004). Discovery of Archean continental and mantle fragments inferred from xenocrysts in komatiites, the Belingwe greenstone belt, Zimbabwe. *Geology* **32**, 285-288.

Shimizu, K., Nakamura, E. & Maruyama, S. (2005). The Geochemistry of Ultramafic and Mafic Volcanics from the Belingwe Greenstone Belt, Zimbabwe: Magmatism in an Archean Continental Large Igneous Province. *Journal of Petrology* **46**, 2367-2394.

Skulski, T., Sandeman, H., Sanborn-Barrie, M., MacHattie, T., Young, M., Carson, C., Berman, R., Brown, J., Rayner, N., Panagapko, D., Byrne, D. & Deyell, C. (2003). Bedrock geology of the Ellice Hills map area and new constraints on the regional geology of the Committee Bay area, Nunavut. In: Current Research. Geological Survey of Canada, Paper 2003-C22.

Sobolev, A. V. & Shimizu, N. (1993). Ultra-depleted primary melt included in an olivine from the Mid-Atlantic Ridge. *Nature* **363**, 151-154.

Spiegelman, M. & Kelemen, P. B. (2003). Extreme chemical variability as a consequence of channelized melt transport. *Geochemistry Geophysics Geosystems* **4**, 2002GC000336.

Sproule, R. A., Lesher, C. M., Ayer, J. A., Thurston, P. C., Herzberg, C. T. (2002). Spatial and temporal variations in the geochemistry of komatiites and komatiitic basalts in the Abitibi greenstone belt. *Precambrian Research* **115**, 153-186.

Storey, M., Mahoney, J. J., Kroenke, L. W. & Saunders, A. D. (1991). Are oceanic plateaus sites of komatiite formation? *Geology* **19**, 376-379.

Takahashi, E. (1986). Melting of a Dry Peridotite KLB-1 up to 14 GPa: Implications on the Origin of Peridotitic Upper Mantle. *Journal of Geophysical Research* **91**, 9367-9382.

Takahashi, E. & Scarfe, C. M. (1985). Melting of Peridotite to 14 GPa and the genesis of komatiite. *Nature* **315**, 566-568.

Tomlinson, K. Y., Hughes, D. J., Thurston, P. C. & Hall, R. P. (1999). Plume magmatism and crustal growth at 2.9 to 3.0 Ga in the Steep Rock and Lumby Lake area, Western Superior Province. *Lithos* **46**, 103-136.

Viljoen, M. J. & Viljoen, R. P. (1969). The geology and geochemistry of the lower ultramafic unit of the Onverwacht Group and a proposed new class of igneous rock. *Upper Mantle Project, Spec. Publ. Geol. Soc. S. Afr.* **2**, 55-85.

Viljoen, M. J. & Viljoen, R. P. (1969). Evidence for the existence of a mobile extrusive peridotitic magma from the Komati formation of the Onverwatcht Group. *Upper Mantle Project, Spec. Publ. Geol. Soc. S. Afr.* **2**, 87-112.

Walter, M. J. (1998). Melting of Garnet Peridotite and the Origin of Komatiite and Depleted Lithosphere. *Journal of Petrology* **39**, 29-60.

Weinstein, S. A. & Olson, P. L. (1989). The proximity of hotspots to convergent and divergent plate boundaries. *Geophysical Research Letters* **16**, 433-436.

Wilson, J. F., Nesbitt, R. W. & Fanning, M. (1995). Zircon geochronology of Archaean felsic sequences in the Zimbabwe Craton: A revision of greenstone stratigraphy and a model for crustal growth. In: Coward, M. P. & Ries, A. C. (eds) *Early Precambrian processes*. London: Geological Society of London Special Publication, pp. 109-126.

Wood, D. A. (1979). Dynamic partial melting: its application to the petrogenesis of basalts erupted in Iceland, the Faeroe Islands, the Isle of Skye (Scotland) and the Troodos Massif (Cyprus). *Geochimica et Cosmochimica Acta* **43**, 1031-1046.

Workman, R. K. & Hart, S. R. (2005). Major and trace element composition of the depleted MORB mantle (DMM). *Earth and Planetary Science Letters* **231**, 53-72.

Chapter 2. The Archean Prince Albert group (PAg), Central and Northeastern Rae domain, Nunavut, Canada: Age, Stratigraphy, and Regional Correlations

INTRODUCTION

The central and northeastern Rae domain of Nunavut is underlain by an extensive, northeasterly-trending network of clastic-dominated, ca. 2.7 Ga supracrustal belts characterized, in part, by distinctive orthoquartzite-komatiite lithological associations (Fig. 2-1). These lithological associations have been well-recognized within the supracrustal belts known as the Woodburn Lake group-WLg (Ashton, 1988; Zaleski *et al.*, 1999) and Prince Albert group-PAg (Schau, 1977; 1982), and have been reported from more highly deformed and metamorphosed supracrustal rocks located on north-central Baffin Island, forming components of the Mary River group-MRg (Jackson, 1966; Young *et al.*, 2004). The co-linear distribution of these supracrustal belts (Fig. 2-1) and similar lithological associations have provided the principal basis for proposed regional correlations between the WLg, PAg and MRg, respectively (e.g. Jackson & Taylor, 1972; Zaleski *et al.*, 2001*a*). A composite supracrustal belt involving the WLg, PAg and MRg would be truly enormous; extending northeastward from the central mainland of Nunavut (Baker Lake area), across Committee Bay to Melville Peninsula and onto the northeastern tip of Baffin Island (Pond Inlet area), it would encompass a region at least 1400 km long and up to 400 km wide covering ~0.5 million km^2 (Fig. 2-1).

Despite the long recognized potential for correlation of these supracrustal belts, fundamental aspects of their geology, including their age, stratigraphy, and the nature of underlying basement components has only been relatively recently revealed for portions of the WLg (Davis & Zaleski, 1998; Zaleski *et al.*, 2001*a*; 2001*b*) and MRg (Wodicka *et al.*, 2002; Bethune & Scammell, 2003; Scott *et al.*, 2003; Young *et al.*, 2004). Within the context of a composite supracrustal belt, the PAg is centrally located and forms the largest and most laterally continuous segment at ~ 600 km (Fig. 2-1). However, despite its size and important position, the age and stratigraphy of the PAg have yet to be established, in part because earlier geological work in the area was, by necessity, reconnaissance in nature (≥ 1:250 000 scale; Heywood, 1961; 1967; Frisch, 1982; Schau, 1982) and also lacked supporting high-precision U-Pb zircon age dating. The remote location of the PAg (largely above the Arctic Circle) and correspondingly high cost of fieldwork has been an obstacle to further study since this early pioneering work.

New regional bedrock mapping southwest of Committee Bay (Fig. 2-1) was recently conducted between 2000 and 2002 as part of a collaborative effort between the Geological Survey of Canada, Canada-Nunavut Geoscience Office, and university partners (Fig. 2-2). A major component of this mapping initiative was focused toward establishing the age and stratigraphy of the PAg and its relationship to adjacent supracrustal belts within the Rae domain (e.g. MacHattie *et al.*, 2002a; 2002*b*; 2003*a*; 2003*b*; Skulski *et al.*, 2002; 2003*a*; 2003*b*; 2003*c*). Specifically, this study reports the results of detailed mapping and high-resolution sampling of volcanic, sedimentary, and plutonic rocks for U-Pb zircon age dating to resolve the age and stratigraphy of selected, well-preserved portions of the PAg. The detailed mapping (presented here at ~1:50 000 and 1:100 000 scales) and most of the sampling for U-Pb zircon whole work (6/8 samples) was focused within the southwestern portion of the Committee Bay belt (Laughland Lake area) where an extensive and spectacularly well-preserved komatiite-dominated mafic-ultramafic volcanic succession has been discovered. The age, volcanology, and stratigraphy of this volcanic succession and its temporal relationship with spatially associated siliciclastic sedimentary rocks comprise a significant component of this contribution and provide the framework for detailed geochemical and isotopic studies to follow (e.g. Chapters 3 and 4).

REGIONAL GEOLOGY OF THE COMMITTEE BAY AREA

The reconnaissance geological investigations of Heywood (1961) southwest of Committee Bay (1:500 000 scale) roughly delineated supracrustal from surrounding granitoid rocks. Heywood (1967) coined the term Prince Albert group (PAg) to include measedimentary and metavolcanic rocks extending from the Laughland Lake area northeastwards across Committee Bay and onto Melville Peninsula (Fig. 2-1). More detailed geological investigations conducted at 1:250 000 scale followed in parts of the Laughland Lake and Walker Lake areas (Schau, 1982) and on Melville Peninsula (Frisch, 1982) further subdividing the supracrustal and granitoid rocks. The new regional mapping conducted southwest of Committee Bay between 2000 and 2002 is outlined in Fig. 2-1 and displayed in Fig. 2-2 (simplified from Skulski *et al.*, 2003*c*). The general geology and regional 1:100 000 scale open file maps specific to this area are reported in Sandeman *et al.* (2001*a*; 2001*b*; 2004) and Skulski *et al.* (2002, 2003*a*; 2003*c*), while details specific to the structural and metamorphic history are reported in Sandeman *et al.* (2001*c*), Johnstone *et al.* (2002), Sanborn-Barrie *et al.* (2002; 2003), Carson *et al.* (2004), and Berman *et al.* (2005), respectively.

The Committee Bay map area depicted in Fig. 2-2 has been subdivided into three, northeast-trending crustal sub-domains based on lithological associations and/or metamorphic grade (see Skulski *et al.*, 2003*c*). The central PAg sub-domain (this study) is underlain by greenschist- to middle amphibolite-facies sedimentary and volcanic rocks of the PAg and cross-cutting, ca. 2610-2580 Ma felsic plutonic rocks (Skulski *et al.*, 2003*c*). The southern sub-domain is entirely plutonic and is dominated by ca. 2610 Ma K-feldspar megacrystic granodiorite and lesser, post-tectonic, ca. 1820 Ma biotite-magnetite±fluorite granite (Skulski *et al.*, 2003*c*). The northern sub-domain consists of upper amphibolite-facies migmatitic paragneiss, metatexite and diatexite intruded by ca. 2610-2580 Ma plutonic rocks (Carson *et al.*, 2004).

The major northeast-striking, southeast-dipping structural fabric of rocks exposed within the Committee Bay area was produced during D_2-M_2 tectonometamorphism; a response to northwesterly-vergent folding and crustal thickening initiated at ca. 1870 Ma, and culminating in penetrative tectonometamorphism at ca. 1850 Ma (Carson *et al.*, 2004; Berman *et al.*, 2005). Earlier, pre-D_2 fabrics are predominantly north-striking, easterly-dipping, and associated with upright to westerly-vergent F_1 folds. The timing of D_1-M_1 is well-constrained within the southwestern Laughland Lake area, where fabric-aligned monazite inclusions in late- to post-D_1 garnet and staurolite yield ages of ca. 2350 Ma (Berman *et al.*, 2005). The ca. 2350 Ma and ca. 1850 Ma tectonometamorphic reworking of the Committee Bay area has been linked with collisional orogenesis on the western Rae margin (D_1-M_1), and within the Trans-Hudson Orogen (D_2-M_2) to the south (Sanborn-Barrie *et al.*, 2003; Carson *et al.*, 2004; Berman *et al.*, 2005), respectively.

CHRONOSTRATIGRAPHIC SUBDIVISION OF THE PAG

The regional mapping and preliminary U-Pb zircon age dating conducted within the PAg southwest of Committee Bay has revealed that volcanism within the group is dominated by komatiite, that a definite spatial and temporal association exists between orthoquartzite and other siliciclastic sedimentary rocks with iron formation and komatiite, that komatiite-dominated volcanism within the PAg spans a minimum duration of ~40 m.y., and that this volcanism is distributed within at least three distinctive chronostratigraphic sequences. These sequences are informally referred to as the lower (ca. 2730 Ma), middle (ca. 2710) and upper (≤ 2690 Ma) PAg, respectively (see Skulski *et al.*, 2003*c*).

The lower PAg is located within the central Laughland Lake area and well-exposed along the northeast and southwest margins of a cross-cutting, 2718 ± 2 Ma tonalite/granodiorite pluton (central tonalite in Fig. 2-2; Skulski *et al.*, 2002). The lower PAg, as currently exposed, is almost entirely comprised of mafic and ultramafic volcanic rocks. Although dominated by komatiite and lesser basalt, minor occurrences of intermediate-felsic volcanic rocks and rare iron formation have been recognized (MacHattie, 2002*b*). Skulski *et al.* (2002) obtained a preliminary U-Pb zircon age of 2732 +8/-2 Ma for a rhyolite intercalated with basalt along the northeastern margin of the central tonalite (see Fig. 2-2 and 2-3); this currently represents the oldest age obtained for the PAg.

The middle PAg has been documented northeast of the Laughland Lake area, within the central Walker Lake area (Fig. 2-2), and is predominantly comprised of siliciclastic sedimentary rocks, although mafic, ultramafic, and felsic volcanic rocks and iron formation also occur. A cross-bedded, ridge-forming orthoquartzite at the core of a major supracrustal strand within the central Walker Lake area yielded a maximum depositional age (detrital zircon) of 2722 ± 11 Ma (Fig. 2-2; Table 1 in Skulski *et al.*, 2003*c*), and ~15 km to the northeast, a 2711 ± 3 Ma dacite (Table 1 in Skulski *et al.*, 2003*c*) overlies orthoquartzite (Fig. 2-2). Overall, a prominent association of orthoquartzite with komatiite is well-recognized within the middle PAg (e.g. Fig. 2-5(a and l) and later discussion). A preliminary U-Pb zircon age of 2706 +5/-4 Ma for a dacite intercalated with ultramafic rocks and iron formation south-southwest of the Walker Lake strand is tentatively included within the middle PAg, although potentially may represent a marginally younger sequence.

The upper PAg has been documented within both the northern and central PAg sub-domains and is at least partially dominated by siliciclastic sedimentary rocks (e.g. northern sub-domain paragneiss). Within the northern sub-domain (Arrowsmith River area), a graywacke yielded a maximum depositional age (detrital zircon) of 2691 ± 16 Ma (Fig. 2-2; Table 1 in Skulski *et al.*, 2003*c*). Within the north-central Ellice Hills area, graywacke and iron formation occur interbedded with spinifex-textured komatiite flows. A sample of this graywacke yielded a maximum deposition age (detrital zircon) of 2687 ± 10 Ma. A minimum age for the upper PAg is provided by the cross-cutting relationship with ca. 2580 Ma granitic plutonic rocks (Table 1 in Skulski *et al.*, 2003*c*; Table 1 in Sandeman *et al.*, 2004).

LOWER PAG MAFIC-ULTRAMAFIC VOLCANIC SUCCESSION AND ASSOCIATED SEDIMENTARY ROCKS WITHIN THE LAUGHLAND LAKE AREA

Within the Laughland Lake area and positioned along the southwestern and northeastern margins of the central tonalite (Fig. 2-2), the predominant mafic and ultramafic volcanic rocks of the lower PAg are exceptionally well-preserved and exposed. These areas, covering > 300 km^2, are hereafter informally referred to as the northeast (NVZ) and southwest volcanic zone (SVZ), respectively. Detailed geological maps of the NVZ (Fig. 2-3) and SVZ (Fig. 2-4) display the relationships between mafic-ultramafic volcanic rocks, intercalated intermediate-felsic volcanic rocks and iron formation, and spatially associated argillaceous to quartz-rich siliciclastic sedimentary rocks. The regional outcrop patterns of supracrustal and granitoid rocks within the NVZ and SVZ are strongly controlled by the large-scale interference patterns developed between upright- to westerly-vergent F_1, and northwest-vergent F_2 folds. This relationship has produced a broad dome and basin-type structural pattern in which plutonic domes are surrounded by supracrustal synformal keels, a relationship which is particularly well-developed within the NVZ (Fig. 2-3). Unraveling the locally complex folding and reconstructing the original stratigraphic sequence of the volcanic succession has only been possible due to the abundance of well-preserved spinifex-textured komatiite flows that provide the only unequivocal younging directions and form the basis of the relative stratigraphic sequence discussed below.

From detailed field mapping and preliminary geochemical analyses of volcanic rocks within the NVZ and SVZ, the lower PAg can be accurately described as a mafic-ultramafic volcanic succession characterized by an abundance of peridotitic komatiite and which possesses a distinctively bi-modal stratigraphy. Within both the NVZ and SVZ, an unequal distribution of basalt and komatiite with stratigraphic height, provides the basis for a subdivision of the volcanic succession into two volcanic horizons; a lower horizon dominated by basalt, hereafter referred to as the basalt horizon, and an upper horizon dominated by peridotitic komatiite with comparatively minor amounts of intercalated basalt, hereafter referred to as the komatiite horizon. The prefix "peridotitic" is used here to emphasize the high-MgO contents of lower PAg komatiite (≥ 25 wt.%; see Chapter 3 and 4) as compared to the 18 wt.% minimum requirement (see Le Bas, 2000). Geochemical sampling of basalt and komatiite within the NVZ and SVZ has confirmed that the lower PAg magmatism is indeed distinctly bi-modal (~4-13 wt.% and ≥ 25 wt.% MgO) and no volcanic rocks possessing > 13 wt.% MgO have been documented within the basalt horizon (Chapter 3 and 4).

Although it is difficult to assess true thicknesses of the basalt and komatiite horizons, due primarily to the locally complex folding, conservative minimum thickness can be estimated. Within the SVZ, ~1.5 km of basalt is bound to the west by the komatiite horizon and to the east by the central tonalite (Fig. 2-4). Considering the uniform ~60° dip of basalt in this area, a minimum thickness of ~1 km for the basalt horizon is suggested. Within the north-central NVZ and located on the western limb of an F_1 syncline, ~2.5 km of easterly dipping komatiite (~60° on average) is underlain by basalt to the west and overlain by siliciclastic sedimentary rocks coring the syncline to the east (Fig. 2-3). This suggests a minimum thickness of ~2 km for the komatiite horizon.

Mafic-ultramafic and intermediate-felsic volcanic rocks

Rocks within the PAg sub-domain of the Laughland Lake area, including the areas comprising the NVZ and SVZ, are at greenschist- to amphibolite-facies (e.g. see Berman *et al.*, 2005), as such, most of the primary mineralogy of the mafic and ultramafic volcanic rocks has been replaced by secondary mineral assemblages consisting of tremolite-actinolite, chlorite, serpentine, magnetite, albite, calcite and quartz. However, in general, the excellent outcrop- to thin section-scale textual preservation of most mafic and ultramafic volcanic rocks allows the original mineralogy and rock types to be readily identified. For these reasons, the prefix meta- is omitted and reference is made to the original mineralogy and texture below.

Mafic magmatism within the basalt and komatiite horizon is largely in the form of aphyric massive flows, however, medium- to coarse-grained gabbroic pods and sills are locally abundant within the basalt horizon. Basaltic rocks are predominantly comprised of stubby to acicular (~100 to ≥ 500 μm) pyroxene crystals, interstitial plagioclase, and minor Fe-Ti oxides (e.g. see Fig. 3-4(a) in Chapter 3). Although only recognized within the komatiite horizon, some basaltic flows do possess upper zones consisting of what is commonly referred to as pyroxene spinifex-texture. This distinctive texture is comprised of numerous highly acicular crystals (up to several cm long) arranged into divergent cone-shaped booklets up to ~20-30 cm long. Also recognized within the komatiite horizon, some basaltic rocks consist almost entirely of cm-sized polyhedra surrounded by a complexly intertwined fracture network (Fig. 2-5(c)), a texture which resembles (on a larger scale) the quenched flow tops recognized in komatiite flows (see below).

Komatiites are generally well-exposed upon high (up to ~75 m) glacially sculpted ridges that commonly contain numerous lava flows (e.g. flow sequence depicted in Fig. 2-5(d)). Olivine spinifex-textured flows (e.g. Fig. 2-5(e and f)) are the most recognizable manifestation of ultramafic volcanism within the komatiite horizon and identical to those described and illustrated in Arndt *et al.* (1977) from Munro Township (e.g. see flow type A in their Fig. 7). These flows display considerable variability in thickness, ranging from as thin as ~0.3 m to ~100 m in total thickness (e.g. see flow sequence depicted in Fig. 2-5(g)). The flow tops are defined by the presence of a complex network of polyhedral fractures (a few to 10's of cm thick) which encase sub-cm to cm-sized spheroids of quenched komatiite and angular shards of glass developed above the spinifex zones. The basal sections contain variable amounts of loosely to closely packed, elongated to stubby olivine and minor chromite encased in a glassy matrix. Komatiite flows which lack spinifex-texture, yet possess identifiable quenched flow tops are also common and, similar to the basal sections of spinifex-textured flow units, consist of variable amounts of olivine and chromite encased in a glassy matrix (e.g. see flow type C in Fig. 7 of Arndt *et al.* (1977)). Some komatiites, however, lack recognizable spinifex or quench textures so there is potential for the presence of ultramafic sills within the package. Other important manifestations of ultramafic volcanism include pillowed komatiite flow units (e.g. Fig. 2-5(h)) and a potential remnant lava channel. The latter consists of alternating layers of fine- to coarse-grained (< 100 μm up to ~1-2 cm), polyhedral olivine dominated komatiite in which the textural layering is at a high angle to and truncates the adjacent underlying spinifex-textured flows (e.g. top right of flow sequence depicted in Fig. 2-5(g)).

Intermediate-felsic volcanic rocks (andesite-dacite; ~60-70 wt.% SiO_2 and ≤ to << 5 wt.% Na_2O + K_2O; see Chapter 3) are rare within the lower PAg, however they have been documented within both the basalt and komatiite horizons. Within the southern portion of the NVZ komatiite horizon, dacitic lavas (Fig. 2-5(i); U-Pb sample of dacite H-1337) and volcanic breccias are intercalated with spinifex-textured komatiite. Within the SVZ basalt horizon, basaltic rocks are intercalated with andesitic-dacitic flows (Fig. 2-4; U-Pb sample of dacite T-3319-B) and intermediate volcanic breccias containing cm-sized fragments of plagioclase-phyric basalt (Fig. 2-5(b)). The 2732 +8/-2 Ma rhyolite intercalated with basalt within the NVZ (Skulski *et al.* (2002)) is the only other occurrence of intermediate-felsic volcanic rocks currently recognized within the lower PAg.

Sedimentary rocks

Similar to the strategy used to describe the mafic and ultramafic volcanic rocks above, metamorphic terminology for sedimentary rocks is not used (when possible) as most samples examined in detail in this study are generally well-preserved such that relict sedimentary structures and/or identifiable clastic material can be readily identified.

With the exception of an extensive iron formation intercalated with komatiite within the NVZ (e.g. see Fig. 2-3), sedimentary rocks have not been observed "interbedded" with basalt or komatiite within the lower PAg. It is possible that this may simply be a reflection of the degree of exposure as the erosive action of the glaciers have clearly sculpted resistant and massive rocks and removed/covered less competent ones.

Within portions of the NVZ, large sculpted komatiite ridges are conspicuously separated from one another by significant expanses (up to ~1-2 km) where no outcrop is present.

Where exposed in the SVZ, a distinctive sedimentary rock association consisting of interbedded orthoquartzite, oxide-facies banded iron formation and argillite (Fig. 2-5(j); U-Pb sample of orthoquartzite TM0-106-A) is closely associated with komatiite and stratigraphically overlies a thin strand forming the western limb of an F_2 fold (Fig. 2-4). The position of orthoquartzite along the northwestern and southeastern margins of this strand (Fig. 2-4) appears to be due to F_2 fold repetition. A granodiorite pluton at the centre of the SVZ (Fig. 2-4; U-Pb sample of granodiorite HS0-334) intrudes both komatiite and orthoquartzite along this contact and provides a minimum age (stratigraphic or structural) for the juxtaposition of these units. Along the southwestern margin of this pluton, and lying westward of aforementioned komatiite strand, is a north-northeasterly trending supracrustal sequence consisting of subarkose arenite (Fig. 2-4; U-Pb sample of subarkose arenite HS0-329), graywacke, orthoquartzite and rare quartz-pebble conglomerate. Contacts between this siliciclastic sedimentary rock-dominated sequence and both the komatiite strand and granodiorite are not exposed and a presumed faulted contact with the orthoquartzite-iron formation-argillite rock association described above appears to occur along its northwestern margin (Fig. 2-4).

Within the north-central portion of the NVZ, rocks immediately overlying the komatiite horizon are situated within the core of an F_1 syncline (Fig. 2-3). These consist of sparse, poorly exposed, low lying outcrops of intercalated cross-laminated quartz arenite, schistose mafic rocks, and chert. The quartz arenite contains several cm-sized, angular clasts of banded iron formation (Fig. 2-5(k); U-Pb sample of quartz arenite TM-

11). This rock sequence is situated structurally and stratigraphically above komatiite and the position of this sequence within the core of an F_1 syncline indicates its deposition is synchronous with, or predates D_1 (ca. 2350 Ma; Berman *et al.*, 2005).

WESTERN WALKER LAKE AND KINNGALUGJUAQ MOUNTAIN AREAS

The western Walker Lake and Kinngalugjuaq Mountain areas are located along the same supracrustal strand that exposes portions of the middle PAg (Fig. 2-2). The western Walker Lake section contains intercalated basalt, iron formation and south-younging (~2-5 m thick) spinifex-textured komatiite flows along its northern flank, a central portion dominated by intermediate-felsic volcanic rocks (Fig. 2-2; U-Pb sample of rhyolite T-3151) and associated fine grained felsic intrusive rocks, and a southern section consisting of intercalated basalt and komatiite.

The Kinngalugjuaq Mountain area is characterized by (and named for) a massive ridge-forming orthoquartzite that forms the resistant horizon of a ca. 30 km long upright F_2 antiformal culmination (Fig. 2-2; Sanborn-Barrie *et al.*, 2003). The orthoquartzite stratigraphically overlies semipelite, pelite, and iron formation, and is intercalated with komatiite flows and injected by ultramafic sills along most of its length. A spectacular contact between komatiite and orthoquartzite is well exposed along the southwestern end of the ridge (Fig. 2-5(l)). A granodiorite dyke cutting the orthoquartzite was collected to constrain its minimum depositional age (Fig. 2-2; U-Pb sample granodiorite T-3459).

U-PB GEOCHRONOLOGY

Methodology

A total of 8 samples for U-Pb zircon age dating were collected for this study and include: three dacitic to rhyolitic volcanic rocks, three siliciclastic sedimentary rocks, and two felsic intrusive rocks. Two methods of U-Pb zircon isotopic dating have been employed in this study: (1) isotope dilution-thermal ionization mass spectrometry (ID-TIMS); and (2) laser ablation-multicollector-inductively coupled plasma-mass spectrometry (LA-MC-ICP-MS). The ID-TIMS method was used to determine precise crystallization ages for the volcanic and plutonic rocks, whereas detrital zircon provenance ages of siliciclastic rocks were investigated with LA-MC-ICP-MS. Additional zircons from selected volcanic and plutonic rocks were also analysed by LA-MC-ICP-MS (see below).

Analytical techniques

All samples were processed at the University of Alberta Radiogenic Isotope Facility, Edmonton, Alberta. Clean fist-sized rock fragments were pulverized to a fine powder using a jaw crusher and Bico disk mill. The fine powder (< 100 mesh) was passed over a Wilfley Table to obtain a heavy mineral concentrate. Zircons were separated from the dried concentrate by magnetic (Frantz isodynamic separator) and density (methylene iodide) based techniques. For the five igneous samples, grains were selected from the least magnetic zircon fractions using a binocular microscope. The zircons separated from the samples selected for provenance studies received only cursory magnetic separation so as to avoid inducing an age bias. All ID-TIMS single- and multi-grain zircon fractions were air abraded (Krogh, 1982) and uranium and lead were isolated and purified from zircon fractions using the anion exchange chromatographic methods first developed by Krogh (1973). Smaller samples (< 0.005 mg) were not processed through anion exchange chromatography. U and Pb aliquots were loaded together onto outgassed Re filaments and their isotopic compositions were determined on a VG354 mass spectrometer operated in single analogue Daly collector peak hopping mode. Details of the U-Pb zircon ID-TIMS technique at the University of Alberta are outlined in Heaman *et al.* (2002).

U-Pb age determinations by LA-MC-ICP-MS were obtained using a NuPlasma MC-ICP-MS coupled to a New Wave Research Nd:YAG ($\lambda = 213$ nm) laser ablation system. The details of the U-Pb zircon dating technique by LA-MC-ICP-MS at the University of Alberta are outlined in Simonetti *et al.* (2005) and briefly summarized below. Selected zircons from the sample and an in-house zircon standard were mounted and polished together in an epoxy puck. Ablation was conducted using a laser energy output of ~2 J/cm^2 and laser spot size of ~40 μm diameter. An individual ablation run consisted of a ~30 second blank measurement prior to aspiration of a 1 ppb Tl solution into the plasma source using a desolvating nebulizer (DSN-100) during ablation. The simultaneous measurement of U (faraday collectors), Pb (ion counters) and Tl (faraday collectors) isotopes is conducted during a ~30 second ablation run. A common Pb correction was necessary for only a very small number of analyses and its application is discussed in Simonetti *et al.* (2005). A typical external reproducibility (2σ) of ~0.6-0.7 % for ^{207}Pb/^{206}Pb and ~3 % for ^{206}Pb/^{238}U (and ^{207}Pb/^{235}U) was obtained for international zircon standards (Simonetti *et al.*, 2005) and is applied to the measured isotopic data reported in this study. Very few analyses had in-run errors that exceeded this external reproducibility.

The ^{238}U (1.55125 x 10^{-10} a^{-1}) and ^{235}U (9.8485 x 10^{-10} a^{-1}) decay constants used in age calculations are those determined by Jaffey *et al.* (1971). Age calculations (ID-TIMS and LA-MC-ICP-MS) were preformed using the Isoplot version 3.00 software (e.g. Ludwig, 1992; 2003). Error ellipses and quoted ages on concordia diagrams are at the 2σ level of uncertainty. Error due to uncertainty in U decay constants has not been included.

U-Pb results

The ID-TIMS U-Pb results for dacite T-3319, dacite H-1337, rhyolite T-3151, granodiorite HS0-334, and granodiorite dyke T-3459 are listed in Table 2-1 and plotted on concordia diagrams in Fig. 2-6(a-e). Selected zircons from rhyolite T-3151 and granodiorites HS0-334 and T-3459 were also analysed by LA-MC-ICP-MS. These results are listed in Table 2-2 and plotted with the ID-TIMS data on concordia diagrams where the latter are represented by the filled ellipses. The U-Pb results obtained by LA-MC-ICP-MS for orthoquartzite TM0-106-A, subarkose arenite HS0-329, and quartz arenite TM-11 are listed in Table 2-2 and plotted on concordia diagrams and cumulative probability histograms of $^{207}Pb/^{206}Pb$ age in Fig. 2-7(a-c). In the following discussion, the U-Pb results for volcanic and plutonic rocks are discussed first and followed by detrital zircon geochronology of siliciclastic supracrustal rocks.

Dacite T-3319-B

A quartz-phyric dacite was sampled from a ~1-2 metre thick volcanic layer intercalated with basaltic rocks near the top of the basalt horizon within the SVZ (Fig. 2-4). The sample yielded abundant colourless, euhedral to subhedral prismatic zircon ranging between 50 and 150 μm in the longest dimension. A small number of zircon grains displayed anhedral, and embayed external forms with smooth surface textures, features that are interpreted to reflect a moderate to high degree of zircon resorption.

Seven small multi-grain zircon fractions were analysed from the euhedral to subhedral population (Table 2-1; Fig. 2-6(a)). All fractions have low U (109-150 ppm), moderate Th/U ratios (0.572–0.616) and all but one concordant analysis plot slightly above the concordia curve (~0.2-1.4 %). The $^{207}Pb/^{206}Pb$ ages for all fractions are similar and range between 2729 to 2734 Ma. The five most concordant fractions yield a very precise, weighted mean $^{207}Pb/^{206}Pb$ age of 2729.5 ± 0.8 Ma (MSWD = 0.69) and this is considered a robust estimate of the crystallization age of the dacite. The slightly older $^{207}Pb/^{206}Pb$ ages of 2731 (#7) and 2734 Ma (#2) is interpreted to reflect the presence of a slightly older inherited Pb component. The cause of the reverse discordance exhibited by almost all zircon fractions is not yet resolved. Incomplete dissolution of zircon (which generally tends to force analyses to higher Pb/U ages while preserving consistent Pb/Pb ages) seems unlikely as the fractions are generally small (≤ 23 μg). However, incomplete dissolution cannot be ruled out as a possible cause of the reverse discordance.

Dacite H-1337

A plagioclase-phyric dacite (Fig. 2-5(i)) was collected from the southern portion of the NVZ (Fig. 2-3) where it is intercalated with spinifex-textured peridotitic komatiite flows. The dacite yielded abundant zircon that possibly consists of more than one population. The main zircon population consists of colourless, 100-300 μm long prismatic grains with well-developed crystal faces and terminations. These zircon grains are interpreted to have crystallized from the dacite magma. In addition to the main population, several large (> 200 and up to 600 μm long), subhedral, dark brown to pink grains, as well as clear, colourless, anhedral and embayed, zircon were documented. These grains are interpreted to represent xenocrystic zircon and have not been analysed as part of this study.

Six zircon fractions from the main zircon population were analysed (Table 2-1; Fig. 2-6(b)) including a single grain (#5), and both small (2-6 grains) and large multi-grain fractions (#4; 16 grains). All fractions are characterized by low to extremely low U contents (22-92 ppm). The six fractions show both normal (up to 2.9 %) and reverse discordance (up to 1.8 %). The analysed zircon fractions have similar $^{207}Pb/^{206}Pb$ ages between 2728 and 2730 Ma, with the exception of multi-grain fraction (#4), which has a slightly lower age of 2726 Ma. The lower $^{207}Pb/^{206}Pb$ age of fraction #4 is interpreted to be due to a component of ancient Pb loss possibly related to the large surface area to mass ratio of these small zircons. Excluding fraction #4, a weighted mean $^{207}Pb/^{206}Pb$ age of 2729.5 ± 0.9 Ma (MSWD = 0.92) is obtained and is interpreted as the crystallization age of the dacite. Interestingly, this age is identical to the crystallization age of dacite T-3319-B (2729.5 ± 0.8 Ma) intercalated with basalt in the SVZ, over 30 km to the southwest (Fig. 2-2).

Rhyolite T-3151

A quartz-phyric rhyolite was collected from the western Walker Lake area and centrally located in the main supracrustal strand (Fig. 2-2). The zircon appeared to be largely from one population, although several grains have clearly visible cores and rims.

The main population consists predominantly of colourless prismatic grains that range in size from 50-250 μm in their longest dimension.

Three multi-grain fractions and two single grain zircon fractions (#4 and #5) from the main zircon population were analysed (Table 2-1; Fig. 2-6(c)). The three multi-grain fractions are concordant to moderately discordant (up to 3.8 %) with $^{207}Pb/^{206}Pb$ ages between 2701 and 2708 Ma. The two single grain analyses are slightly reversely discordant (~1 %) and are both older than the multi-grain fractions with $^{207}Pb/^{206}Pb$ ages of 2713 and 2717 Ma, respectively. A similar Th/U ratio for all zircon fractions (0.462-0.548) suggests a common source such that the ~20 m.y range in $^{207}Pb/^{206}Pb$ age is not obviously due to zircon inheritance. With the exception of the concordant fraction #3 (Fig. 2-6(c)), decreasing $^{207}Pb/^{206}Pb$ age is associated with increasing discordance. A linear regression of the data (excluding fraction #3) yields an upper intercept age of 2712.5 ± 1.9 Ma (MSWD = 1.1). A lower intercept age of 583 Ma is interpreted to be geologically meaningless due to the large uncertainty related to a rather long projection. As fraction #3 lies to the left of this regression it would suggests this fraction has experienced some non-zero age Pb-loss (e.g. possibly at ca. 1850 or 2350 Ma, corresponding to the timing of metamorphism in the region) and the concordance of this analysis could be fortuitous. Three zircons (identical to those analysed by ID-TIMS) were analysed by LA-MC-ICP-MS and are plotted along with the ID-TIMS data (Fig. 2-6(c) and Table 2-2). Although these analyses have large errors compared with the ID-TIMS data, a regression of the three analyses yields a similar upper intercept age of 2715 ± 25 Ma, in agreement with an interpreted crystallization age of 2712.5 ± 1.9 Ma for the rhyolite.

Granodiorite HS0-334

Plagioclase porphyritic biotite granodiorite from the core of a centrally located pluton within the SVZ (Fig. 2-4) was collected to provide a minimum age for the supracrustal rocks it intrudes (orthoquartzite and spinifex-textured komatiite), and a maximum age for deformation in this area. Zircon in the sample consists of uniform pink grains with well-formed facets and mainly euhedral external forms. Most of the grains were between 100 and 200 μm in the longest dimension and rarely up to 350 μm long.

Two small multi-grain fractions (2 and 3 grains) were analysed (Table 2-1; Fig. 2-6(d)). Both fractions have moderate U contents (174-105 ppm) and similar Th/U ratios (0.368-0.380). Both fractions are concordant (filled ellipses in Fig. 2-6(d)) with similar ^{207}Pb/^{206}Pb ages of 2601 and 2603 Ma. Together, a weighted mean ^{207}Pb/^{206}Pb age of 2601.7 ± 1.3 Ma (2σ internal; MSWD = 2.3) is obtained. Seven euhedral pale pink grains (indistinguishable from those analysed by ID-TIMS) were analysed by LA-MC-ICP-MS. All grains were < 3 % discordant and yielded ^{207}Pb/^{206}Pb ages between 2584 and 2610 Ma (Table 2-2). A weighted mean ^{207}Pb/^{206}Pb age of 2601.3 ± 6.4 Ma (MSWD = 1.0) is obtained using all seven analyses, a result identical to that obtained by ID-TIMS. The preferred crystallization age for the granodiorite is 2601.7 ± 1.3 Ma

Granodiorite dyke T-3459

A biotite granodiorite dyke was sampled from the Kinngalugjuaq Mountain area along the southwest portion of a massive ridge forming orthoquartzite (Fig. 2-2). The ~3-5 metre wide dyke cuts orthoquartzite near the centre of the ridge and thereby provides a minimum age for the Kinngalugjuaq sequence. The granodiorite yielded abundant 50-200 μm long, pale brown, oscillatory zoned zircon.

Two multi-grain fractions (#1 and #2; 3 and 2 grains, respectively) and five single-grain zircon fractions were analysed (Table 2-1; Fig. 2-6(e)). All the zircons analysed were slightly to moderately discordant (2.2-9.5 %) and $^{207}Pb/^{206}Pb$ ages decrease steadily with increasing discordance from 2549 Ma (2.2 %; #5) to 2397 Ma (9.5 %; #1). A poorly fitted regression through all seven data points (not shown) yielded a model-2 upper intercept age of 2586 ± 33 Ma (MSWD = 16) and a lower intercept of 1521 ± 130 Ma. A more selective regression, including two single-grain and one 3-grain fraction (#1, #5, and #6; Fig. 2-6(e)) yields an upper intercept age of 2583 ± 6 Ma (MSWD = 0.025) and lower intercept of 1470 Ma. Seven zircons from the sample were analysed by LA-MC-ICP-MS and the results of these analyses are plotted along with the ID-TIMS data (Fig. 2-6(e) and Table 2-2). Five of the grains analysed display a similar discordia pattern to the ID-TIMS data with $^{207}Pb/^{206}Pb$ ages ranging between 2462 Ma (#6) and 2590 Ma (#3). Two analyses overlap with the concordia curve (#3 and #4; Fig. 2-6e) and yield a concordia age of 2583 ± 10 Ma, identical to that obtained by ID-TIMS. One grain analysed by LA-MC-ICP-MS has a significantly older $^{207}Pb/^{206}Pb$ age of 2707 Ma and is believed to be inherited. The interpreted crystallization age of the granodiorite dyke is 2583 ± 6 Ma.

Orthoquartzite TM0-106-A

An orthoquartzite was collected from the SVZ (Fig. 2-4) for detrital zircon age dating to constrain its depositional age and to monitor the age distribution of the zircon detritus. The sample was collected from a massive, ~15 metre wide layer of bleached white orthoquartzite in contact with a grey argillite (Fig. 2-5(j)) and is located ~500 metres northwest of a belt of stratigraphically underlying spinifex-textured komatiite (Fig. 2-4).

The sample yielded abundant, moderately rounded zircon and 77 grains were analysed (Table 2-2). Of the 77 grains analysed, 15 displayed a significant amount of discordance (15-46 %). These have been included in the $^{207}Pb/^{206}Pb$ age histogram but excluded from the concordia diagram for display purposes. The majority of zircon analysed (n=55) have tightly clustered $^{207}Pb/^{206}Pb$ ages ranging between 2650 and 2760 Ma. Older zircon form a continuous "tail" in ages (~1 or 2 grains) extending up to 3130 Ma, and the oldest grain analysed is 3352 Ma (Fig. 2-7(a)). Two major age populations have been documented within this sample and occur at 2680 (the largest) and 2734 Ma, respectively. A maximum depositional age for the orthoquartzite is estimated from the youngest, statistically significant age population (2680 Ma). Of the 21 youngest zircon grains analysed (grey filled age bins in Fig. 2-7(a)) two are highly discordant (40 and 46 %) compared with the other 19 (< 25 %). Compared to the 2680 Ma peak, one of the discordant zircons does appear to be associated with an anomalously young $^{207}Pb/^{206}Pb$ age of 2650 Ma (grain #46; Table 2-2), the other (#32; 2677 Ma; Table 2-2), however, is not. For consistency, both discordant analyses have not been used to estimate the maximum depositional age of the orthoquartzite. We chose to base the maximum depositional age upon the < 25 % discordant analyses (n=19 grains and n=22 analyses) that possess very tightly clustered $^{207}Pb/^{206}Pb$ ages between 2668 and 2688 Ma. A linear regression of these 22 analyses yields a precise upper intercept age of 2688.3 ± 5.5 Ma (MSWD = 0.35) and lower intercept of 137 ± 110 Ma (Fig. 2-7(a)).

Subarkose arenite HS0-329

A subarkose arenite was collected from the western portion of the SVZ map area for detrital zircon age dating (Fig. 2-4). The sample contains sand-sized colourless to blue-grey quartz and subhedral microcline set in a finer matrix of biotite and quartz. Some small lithic fragments (generally < 1-2 cm) include microcrystalline (10-30 μm sized grains) quartz-rich rock fragments (chert ?) and coarser orthoquartzite, as well as one ~2-3 cm felsic granitoid clast. The latter appears be associated with the abundant microcline crystals.

The sample yielded a moderate amount of zircon with considerable variability in size, morphology and colour. Several grains are well rounded, pale to dark brown and pink in colour, although a significant and distinctive population consists of pale pink to colourless, euhedral zircon (e.g. grains #70 and #71; Fig. 2-7(b)). The 72 grains analysed (Table 2-2) are plotted on a concordia diagram and probability density histogram of $^{207}Pb/^{206}Pb$ age in Fig. 2-7(b). Most analyses conform closely to the concordia curve and display moderate positive (almost all < 11 %) and negative discordance (up to 6.4 %). No systematic decrease in $^{207}Pb/^{206}Pb$ age is observed with increasing discordance in any of the grains analyzed in multiple spots (e.g. grain #20(a and b); Table 2-2). The most striking feature of the age distribution is the extremely wide range in $^{207}Pb/^{206}Pb$ age (> 1100 Ma), ranging between 2613 and 3741 Ma (mean $^{207}Pb/^{206}Pb$ age of 2 analyses of grain #39). Broadly speaking, the spectrum of detrital zircon ages can be divided into 4 main age groupings: 2613-2629 Ma; 2698-2968 Ma; 2996-3101 Ma; and ≥ 3421 Ma within which significant age populations occur at 2623, 2714, 2750, 2799, 2828, 2870 (the largest peak), 2916, 3000, 3033 and 3533 Ma, respectively. The youngest zircon population in the sample consists of 5 grains (grey filled bins in Fig. 2-7(b)) with $^{207}Pb/^{206}Pb$ ages between 2613 and 2628 Ma. The zircon that comprise this age population are all euhedral and possess well-developed facets and terminations (e.g. grains #70 and #71; Fig. 2-7(b)) suggesting very little mechanical abrasion. A weighted mean $^{207}Pb/^{206}Pb$ age of 2623.5 ± 6.3 Ma (MSWD = 0.60) for the 5 youngest zircons provides a good estimate of the maximum depositional age of the subarkose arenite.

Quartz arenite TM-11

A quartz arenite was collected from a thin, less than 3 metre thick bed located within the core of a refolded F_1 syncline in the northern portion of the NVZ (Fig. 2-3). In outcrop this sample is distinguished from orthoquartzite TM0-106-A by its rusty brown to beige colour. This sample also preserves relict cross-bedding and contains cm-sized angular clasts of banded iron formation (Fig. 2-5(k)).

The quartz arenite yielded abundant zircon displaying a considerable range in size, colour, and morphology. A total of 49 grains were analysed encompassing the full spectrum of zircon types observed (Table 2-2 and Fig. 2-7(c)). Generally, most analyses plot near to the concordia curve (except grain #2, which is ~41 % discordant and not shown on Fig. 2-7(c)). As with subarkose arenite HS0-329, the detrital zircon ages can be broadly subdivided into four main groupings: 2605-2628 Ma (largest age peak); 2692-2958 Ma; ~3022 Ma; and ≥ 3271 up to 3522 Ma). With the exception of three grains between 3271 and 3375 Ma, the detrital zircon age profile is nearly identical to subarkose arenite HS0-329. The most significant and well-defined age populations occur at 2616, 2703, 2797, 2850, 2915, and 3022 Ma, respectively. The youngest zircon population in the sample consists of 10 grains with $^{207}Pb/^{206}Pb$ ages between 2605 and 2628 Ma (grey filled bins in Fig. 2-7(c)). A finer scale $^{207}Pb/^{206}Pb$ age histogram for these 10 zircon (inset to Fig. 2-7(c)) reveals the 2616 Ma age peak is predominantly comprised of 2610 Ma zircon (n=5) and that slightly older and younger ages straddle this age population. A good estimate for the maximum depositional age of this quartz arenite is interpreted to be the weighted mean $^{207}Pb/^{206}Pb$ age of 2612.1 ± 6.8 Ma (MSWD = 0.07) calculated for these 5 zircon analyses.

CHRONOSTRATIGRAPHY OF ORTHOQUARTZITE-KOMATIITE ASSOCIATED SUPRACRUSTAL SEQUENCES OF THE PAG

The mapping and U-Pb geochronology presented in this study has placed constraints on the relative and absolute timing of volcanism and sedimentation within the PAg, approximately doubled the U-Pb zircon age dataset for PAg supracrustal rocks, and thus significantly strengthens our understanding of the regional chronostratigraphy (Skulski *et al.*, 2003*c*). A schematic illustration of the chronostratigraphy developed for the Laughland Lake area is presented in Fig. 2-8. The newly recognized and significantly younger siliciclastic supracrustal rock sequences are shown, however, their significance and relationship to older orthoquartzite-komatiite associated sequences of the PAg will be discussed in a later section.

Laughland Lake area

Detailed mapping in this study has revealed that the lower PAg volcanic stratigraphy is divisible into a lower basalt- and upper komatiite-dominated volcanic horizon, respectively (Fig. 2-8). Although the compositional transition from mafic- to ultramafic-dominated volcanism is sharply defined in the field, coincident U-Pb ages of 2729.5 ± 0.8 Ma for dacite T-3319-B (Fig. 2-6(a)) intercalated with basalt in the SVZ, and 2729.5 ± 0.9 Ma for dacite H-1337 (Fig. 2-6(b)) with komatiite in the NVZ, indicate that the transition took place rapidly, perhaps < 1 m.y. Indeed, the physical volcanology of komatiite within the NVZ, particularly the thickness of many of the flow units, is also indicative of a rapid generation and eruption of large volumes of ultramafic lava. The 2732 +8/-2 Ma age obtained for a rhyolite intercalated with basalt in the NVZ (Skulski *et al.*, 2002) is within error of the more precise age determinations obtained in this study and, taken together, suggest that the formation of the mafic-ultramafic volcanic succession occurred abruptly at ca. 2730 Ma. A minimum age of 2718 ± 2 Ma, established by crosscutting relationships with the central tonalite (Skulski *et al.*, 2002) indicates a maximum of ~10 m.y. for its formation. Although the basement to the volcanic succession has yet to be directly sampled, xenocrystic zircon identified within dacite T-3319-B and H-1337 combined with the major, trace element, and Nd isotopic signatures for the volcanics indicates they are partial melts of ca. 2750-2800 Ma crust (see Chapter 3). The identification of rare pillowed flows (Fig. 2-5(h)), the glassy quench textures of komatiite flow tops, and the rare intercalation of iron formation with komatiite suggest the lower volcanic succession was emplaced subaqueously.

Immediately overlying the komatiite horizon in the SVZ, an orthoquartzite unit with the orthoquartzite-iron formation-argillite rock association (Fig. 2-5(j)) has a maximum depositional age of 2688 ± 6 Ma based on the youngest and most abundant detrital zircon population it contains (Fig. 2-7(a)). This result indicates that ~40 m.y. of time is either encapsulated within the strata of the SVZ or missing from the geological section. A minimum age for orthoquartzite within the SVZ is provided by the intrusive contact between the 2602 Ma granodiorite (Fig. 2-6(d)) along its northwest margin (Fig. 2-4). The close spatial association between orthoquartzite and komatiite within the SVZ and potential for a ~40 m.y. time gap is interpreted to likely reflect the presence of an unrecognized unconformity or fault contact rather than ~40 m.y. of continuous sediment deposition. Importantly though, the cross-cutting 2602 Ma granodiorite predates D_1-D_2 folding, indicating that the juxtaposition of these units occurred prior to the first tectonometamorphic event recognized within the area at ca. 2350 Ma (Berman *et al.*, 2005). Although more equivocal, the significant amount of ca. 2730 Ma detrital zircon contained within the orthoquartzite (Fig. 2-7(a)) could indicate the lower PAg was exposed and a source of detritus for the orthoquartzite. If so, the ~40 m.y. age discrepancy between the two sequences could suggest the presence of an unconformity or intra-sequence disconformity separating the lower and upper PAg in this area (Fig. 2-8).

The 2688 ± 6 Ma maximum depositional age for the orthoquartzite is coincident with two other ca. 2690 Ma maximum depositional age determinations for siliciclastic sedimentation within the upper PAg (see Fig. 2-2; Table 1 in Skulski *et al.* 2003*c*; Table 1 in Sandeman *et al.* 2004). Based on these maximum depositional age constraints, the orthoquartzite-iron formation-argillite rock association recognized in the SVZ is considered a component of the upper PAg. Unfortunately, the deposition of the upper PAg is poorly constrained to the ~60-70 m.y. time interval between ca. 2690 Ma and the initiation of regional ca. 2.6 Ga plutonism between ca. 2630-2620 Ma (e.g. see Fig. 2-11 and later discussion). Importantly though, the large ca. 2690 Ma detrital zircon population within the SVZ orthoquartzite and documentation of a similar maximum age in two other siliciclastic rocks separated by 100's of km (Fig. 2-2) is considered to be geologically significant. These findings indicate that zircon-bearing, ca. 2690 Ma volcanic and/or syn-volcanic plutonic rocks must be important source components for the uppermost PAg and could represent a currently undated ca. 2690 Ma felsic volcanic/syn-volcanic plutonic component of the PAg. As komatiitic volcanism is known to have persisted until at least 2687 ± 10 Ma based on the maximum depositional age for an interbedded pasammite (Fig. 2-2; Table 1 in Sandeman *et al.* 2004) and older komatiite-bearing volcanic sequences have associated felsic volcanic rocks, it seems plausible that PAg felsic volcanism may also have persisted to at least ca. 2690 Ma.

The detrital zircon age profiles of the newly recognized ≤ 2624 and ≤ 2612 Ma siliciclastic rocks within the Laughland Lake area suggest that ca. 2690 Ma may in fact record the termination of PAg magmatic activity. Both quartz arenite TM-11 and subarkose arenite HS0-329 lack zircon between their maximum depositional ages and ca. 2690 Ma (e.g. quartz arenite grain #41 is 2692 Ma and 1.7 % discordant and subarkose arenite grain #24 and #47 are both 2698 Ma and -1.3 and -2.5 % discordant, respectively). As these siliciclastic rocks do not appear to have been selective in their imaging of the known pre-2.6 Ga Rae crust (see later discussion) this observation suggests that the time interval between ca. 2690-2630 Ma represents a period of magmatic inactivity, consistent with termination of PAg associated magmatism at 2690 Ma.

Western Walker Lake and Kinngalugjuaq Mountain areas

The relative and absolute stratigraphy in the western Walker Lake area is less well constrained than that of the Laughland Lake area owing to the poor exposure of the major lithological units. The 2712.5 ± 1.9 Ma age for rhyolite determined in this study is very similar to the 2711 ± 3 Ma age obtained for a dacite located ~25 km to the northeast (Fig. 2-2; Table 1 in Skulski *et al.*, 2003*a*). The latter stratigraphically overlies orthoquartzite interpreted to be correlative with the ≤ 2722 Ma orthoquartzite situated midway along this supracrustal strand (Fig. 2-2; Table 1 in Skulski *et al.*, 2003*a*). The 2712 Ma rhyolite age confirms that the Walker Lake supracrustal strand, over a significant strike length, is comprised of a mixed volcanic/sedimentary rock sequence containing ultramafic-felsic volcanic rocks, iron formation and orthoquartzite that are broadly ca. 2710 Ma in age and constitute the middle sequence of the PAg (e.g. Skulski *et al.*, 2003*c*).

In the Kinngalugjuaq Mountain area, the 2583 ± 6 Ma granodiorite dyke cross cutting orthoquartzite demonstrates that this massive, ~25 km long, ridge system (Fig. 2-2) is Archean in age. This is an important finding because a similarly large orthoquartzite ridge located along the south-southwest margin of the central tonalite (Fig. 2-2) was found to be Proterozoic in age (Skulski *et al.*, 2002). As the Kinngalugjuaq Mountain orthoquartzite is closely associated with ultramafic sills along most of its length, correlation along strike with the middle PAg recognized to the southwest is most likely. The emplacement of sills requires that the siliciclastic rocks along this ridge system were largely consolidated prior to their emplacement. The sills may be correlative with the komatiitic volcanism recognized within the north-central Ellice Hills area at ca. 2687 Ma (Table 1 in Sandeman *et al.* 2004).

REGIONAL CORRELATION OF ORTHOQUARTZITE-KOMATIITE ASSOCIATED SUPRACRUSTAL BELTS WITHIN THE CENTRAL AND NORTHEASTERN RAE DOMAIN

The new mapping and U-Pb age dating within the PAg can now be used to quantitatively test the validity of proposed regional correlations of orthoquartzite-komatiite associated supracrustal belts within the central and northeastern Rae domain (e.g. Jackson & Taylor, 1972). The U-Pb zircon ages for volcanism, syn-volcanic plutonism, basement, and maximum depositional ages for siliciclastic sedimentary rocks are displayed in Fig. 2-9 for the WLg (Davis & Zaleski, 1998; Zaleski *et al.*, 2001*a*), PAg (this study; Skulski *et al.*, 2002; Table 1 in Skulski *et al.*, 2003*b*; Table 1 in Sandeman *et al.*, 2004), and MRg (Jackson *et al.*, 1990; Wodicka *et al.*, 2002; Bethune & Scammell, 2003), respectively.

In the Baker Lake area of the central Rae domain, the orthoquartzite-komatiite associated sequences of the WLg overlie a basement complex consisting of ca. 2870 Ma granodiorite that intrudes mafic-felsic banded gneisses (Fig. 2-1; Zaleski *et al.*, 2001*a*). Overlying the basement, three cycles of bimodal, mafic-ultramafic and felsic volcanism are recognized at ca. 2735, 2720, and 2710 Ma, respectively (Fig. 2-9). The oldest volcanic cycle contains pillowed tholeiitic basalt, whereas younger, ca. 2720-2710 Ma sequences contain abundant felsic pyroclastic flows and komatiite interbedded with iron formation. The minimum depositional ages for orthoquartzite and clastic sedimentary rock-dominated sequences deposited largely upon these older volcanic cycles are constrained by crosscutting granitic intrusions to be > 2620 Ma in age. In the Pipedream Lake area however, Kjarsgaard *et al.* (1997) report orthoquartzite underlying spinifex-textured komatiite flows and rare orthoquartzite xenoliths within komatiite indicating the presence of some orthoquartzite older than komatiite. Although more detailed chronostratigraphic data are currently unavailable from the WLg, overall, the strikingly similar lithological associations and ages for volcanism within the WLg and PAg (Fig. 2-9), and their close spatial relationship (Fig. 2-1) suggests that they are the same supracrustal belt.

In the northeastern Rae domain on Baffin Island, the MRg overlies a basement complex with multiple age components (Fig. 2-1). Older, ca. 2850 and 2830 Ma tonalite and granodiorite gneiss have been documented on north-central and central Baffin Island (Jackson *et al.* 1990; Wodicka *et al.*, 2002), whereas younger, ca. 2775 and 2778 Ma granulite-facies tonalitic gneisses occur within the Eqe Bay area (Fig. 2-1; Bethune & Scammell, 2003). Importantly, the younger basement ages are identical to the xenocrystic zircon age peak identified within the lower PAg felsic volcanic rocks (Fig. 2-9; Chapter 3). At Eqe Bay, a ca. 2732 Ma age was reported for a felsic volcanic flow interbedded with mafic-intermediate volcanic rocks and overlain by graywacke (Bethune & Scammell, 2003). Minor iron formation and orthoquartzite are interbedded with the volcanic and siliciclastic units. A ca. 2718 Ma dacite from north-central Baffin was collected ~10 km northeast of the ca. 2850 Ma basement and is associated with iron formation, orthoquartzite, schist, meta-basalt and meta-ultramafic rocks (Jackson *et al.*, 1990). Komatiite lavas have been confirmed within the north-central Baffin region and are well-preserved near the ca. 2718 Ma dacite locality (see Fig. 9(f) in Young *et al.*, 2004). Several crystallization ages have been reported for dioritic-monzogranitic, syn-volcanic intrusions on north-central Baffin Island and range between 2738 and 2702 Ma. More precise ages, however, suggest a maximum age of ca. 2726 Ma for syn-volcanic plutonism (Fig. 2-9). The presence of well-documented orthoquartzite-komatiite sequences within the north-central Baffin Island portion of the MRg, the initiation of volcanism within the group at ca. 2732 Ma and a similar age range for volcanism and syn-volcanic plutonism to that found in the WLg and PAg (Fig. 2-9) suggests that the MRg should be considered a northeastern extension of these belts.

Currently, more detailed chronostratigraphic correlations between the WLg, PAg and MRg are not possible due to the variable preservation states of lithological units, a lack of continuity between map areas, and the current resolution of mapping and sampling for U-Pb zircon age dating. Nevertheless, the data support the interpretation that the WLg, PAg, and MRg should, as originally proposed (e.g. Jackson & Taylor, 1972), be considered components of a composite, northeasterly-trending network of co-genetic, clastic-dominated supracrustal belts. This network is at least ~1400 km long and up to ~400 km wide, and delineates an extensive, ~0.5 million km^2 crustal corridor extending from the Baker Lake area in mainland Nunavut northeastward across Committee Bay and stretching as far as Pond Inlet on the northeastern tip of Baffin Island. Current U-Pb zircon age dating indicates that the predominant mafic-ultramafic and associated felsic volcanism within these belts formed over a protracted, ~45 m.y. time period between ca. 2735-2690 Ma and upon relatively young, ca. 2775-2870 Ma continental crust.

> 2735 MA CRUST IN THE RAE DOMAIN IMAGED THROUGH DETRITAL ZIRCON AGE DATING

The U-Pb age dating of detrital zircon recovered from the three siliciclastic rocks within the Laughland Lake area (Fig. 2-7(a-c)) has revealed a ~1 b.y. record of pre-greenstone crustal formation within the Rae domain. This record, when compared with the current U-Pb zircon age database for > 2735 Ma crust within the domain, including crystallization, xenocrystic, and detrital ages, as well as some uniquely ancient depleted mantle Nd model ages, provide insight into the age structure and major crustal formation events within the region (Fig. 2-10).

The most prominent features of the > 2735 Ma detrital zircon age distribution displayed in Fig. 2-10 include: (1) a significant, ca. 2750-3750 Ma age range for pre-greenstone detrital zircon; (2) a decrease in zircon abundance with increasing age; (3) distinct, well-resolved age populations that produce an overall "spiky" pattern; and (4) clustering of these distinctive age populations into at least two and possibly three broad age groupings. The most significant, unequivocal large-scale age grouping includes detrital zircon that are ca. 2750-3130 Ma in age with important populations occurring at ca. 2750 (the largest), 2800 (second largest), 2870 (third largest), 2915, 2965, 3000, and 3030 Ma, respectively. Within this age grouping the youngest, ca. 2750-2800 Ma detrital zircon clearly predominate (~40 % of those ≤ 3130 Ma). Within the Eqe Bay area on the northwestern coast of Baffin Island, the plutonic basement to the MRg includes the directly dated 2775 and 2778 Ma crust (Fig. 2-1), as well as a significant number (n=10/22) of precisely dated (± 1-2 Ma (2σ)), near-concordant, ca. 2750-2800 Ma xenocrystic zircon contained within immediately overlying ca. 2730-2700 Ma felsic volcanic rocks of the MRg (Fig. 2-10; Bethune & Scammell, 2003). Although the ca. 2750-2800 Ma detritus may indeed be far traveled (~800 km), the prominent ca. 2750-2800 Ma xenocrystic zircon population identified within the ca. 2730 Ma felsic volcanic rocks within the lower PAg (see Chapter 3) suggests a more proximal source, i.e. the lower PAg basement within the Laughland Lake area. The very well-defined and significant ca. 2870 Ma detrital zircon population is identical to the 2870 Ma basement of the WLg (Fig. 2-10; Zaleski *et al.*, 2001*a*) located only ~200 km southwest of the lower PAg. Thus, the major source of > 2735 Ma detritus (~50 % of all detrital zircon) can be directly or indirectly attributed to the currently recognized, ca. 2750-2870 Ma basement components to the supracrustal belts within the central and northeastern Rae domain.

The prominent ca. 2915 Ma detrital zircon age population does not, as yet, correspond to any directly dated rock within the Rae domain (Fig. 2-10). A near-concordant, precisely dated 2911 ± 2 Ma zircon xenocryst identified within a 2720 Ma MRg felsic volcanic rock on Baffin Island (Bethune & Scammell, 2003) is the only other evidence for ca. 2915 Ma Rae crust. Although equivocal, the similar magnitude of the ca. 2915 Ma age peak with those recognized at ca. 2750, 2800 and 2870 Ma (Fig. 2-10) does suggests that, perhaps with more sampling, ca. 2915 Ma rocks will be discovered within the central and northeastern Rae domain, and presumably within the supracrustal corridor. A less prominent but well-defined ca. 2965 Ma age population has similarly not, as yet, been directly dated within the Rae domain. However, a significant number of precisely dated detrital zircons liberated from an orthoquartzite within the WLg (n=5/11; ID-TIMS) possess tightly clustered $^{207}Pb/^{206}Pb$ ages between 2955-2965 Ma (Davis &

Zaleski, 1998) that yield a weighted mean $^{207}Pb/^{206}Pb$ age of 2961 ± 5 Ma. These data suggest that ca. 2965 Ma crust may also be present within the supracrustal corridor. The marginally older ca. 3000 and 3030 Ma (shoulder up to 3065 Ma) age populations are similar to ca. 2999-3072 Ma crust recognized within the extreme southwestern portion of the Rae domain, ~1000 km to the southwest of the lower PAg, within the Lake Athabasca area of northern Saskatchewan (Fig. 2-10; Persons, 1988; Hartlaub *et al.*, 2004). Although ca. 3.0 Ga crust has yet to be directly dated from the central or northeastern Rae, a small number of zircons of this age have been recognized, including two ca. 3021-3025 Ma xenocrysts identified within a granitoid from the WLg area (Ashton, 1988), a single, precisely dated 2997 ± 2 Ma xenocryst within a MRg volcanic rock on Baffin Island (Bethune & Scammell, 2003), and a single precisely dated 2996 ± 2 Ma detrital zircon within a WLg orthoquartzite (Davis & Zaleski, 1998).

The small number of detrital zircons that comprise the tail of the more prominent ca. 3000 and 3030 Ma populations are ca. 3130 Ma in age and define the separation between a younger, ca. 2750-3130 Ma and older, ca. 3250-3750 Ma age grouping (Fig. 2-10). The upper, ca. 3130 Ma age of the younger age grouping is similar to a ca. 3126 Ma granitoid age from the southwestern Rae (Hanmer *et al.*, 2004) and a more proximal, ca. 3129 Ma granitoid age from the central Rae located only ~200 km west of the WLg and southern PAg segments (Fig. 2-1; Henderson & Thériault, 1994). These granitoids currently represent the oldest crust directly dated from the Rae domain. The source of the ancient ca. 3250-3750 Ma detrital zircon is uncertain, however, a single, ca. 3300 Ma zircon xenocryst was reported from a Proterozoic granite (Henderson & Loveridge, 1990) within the vicinity of the ca. 3129 Ma granitoid, as are several ca. 2.95-3.15 and ca. 3.25-

3.9 Ga depleted mantle Nd model ages for undated granitoids (Fig. 2-1; Thériault *et al.*, 1994). These data suggest that both the ca. 3130 Ma and older ca. 3250-3750 Ma detrital zircon were derived from this area. Hartlaub *et al.* (2004) also report ancient detritus of similar age to that recognized in this study from quartzite and psammitic metasedimentary rocks from the Murmac Bay group within southwestern Rae in Saskatchewan (~1000 km to the southwest). These ancient zircons have ages between 3456 and 3767 Ma (Fig. 2-10; < 10% discordant grains) and are remarkably similar to the well-established 3425-3745 Ma detrital zircon ages documented in this study.

Overall, the > 2735 Ma detrital zircon record preserved within the siliciclastic supracrustal rocks from the Laughland Lake area significantly compliments the current U-Pb zircon and Nd isotopic model age database for Archean crust within the Rae domain. Apart from the current lack of directly dated ca. 3.0 Ga crust within the central and northeastern Rae domain, all the detritus within these siliciclastic rocks can, with some degree of confidence, be attributed to sources located within the central and northeastern Rae domain, either from crust which directly underlies the supracrustal belts, or that which occupies a marginal position to the west.

CONSTRAINTS FOR THE SETTING OF MAFIC-ULTRAMAFIC MAGMATISM

Establishing that the WLg, PAg and MRg are components of the same, ~1400 km long and up to ~400 km wide, northeasterly-trending network of ca. 2735-2690 Ma supracrustal belts has important implications for the tectonic setting of mafic-ultramafic magmatism within these belts. Clearly, a continental setting is well-supported by the direct U-Pb age dating of ca. 2775-2870 Ma basement components (Jackson *et al.*, 1990; Wodicka *et al.*, 2002; Zaleski *et al.*, 2001*a*; Bethune & Scammell, 2003), similarly aged zircon xenocrysts contained within ca. 2730-2700 Ma felsic volcanic rocks (Bethune & Scammell, 2003; see Chapter 3) intercalated with basalt and komatiite, and the occurrence of continental detritus (> 2735 Ma) within siliciclastic supracrustal rocks located within the middle and upper PAg (e.g. orthoquartzite TM0-106-A (Fig. 2-7(a)); Skulski, pers. comm.).

Regional lithospheric extension coincident with the initiation of mafic-ultramafic magmatism would be consistent with the abrupt onset and short-duration of the initial outburst of volcanism along this supracrustal corridor. The available U-Pb zircon age constraints indicate that the initial pulses of mafic-ultramafic and associated felsic volcanism along the full extent of the supracrustal network occurred within a relatively narrow, ~5 m.y. time window between ca. 2735-2730 Ma (Fig. 2-9). A lack of evidence for uplift prior to the initiation of regional magmatism or any indication for an age progression along the ~1400 km strike of the supracrustal corridor suggests that extensional processes within the continental lithosphere preceded and facilitated the initiation of magmatism. As highlighted in the previous section, the central and northeastern Rae domain contains pre-greenstone crustal components spanning ~1 b.y, ranging between ca. 2750-3750 Ma (Fig. 2-10). The preferential occurrence of the oldest crustal components to the west of the supracrustal belts and within a parallel-trending corridor (Fig. 2-1) suggests that lithospheric extension along pre-existing regional structures potentially genetically related to this age structure exerted an important control upon the regional distribution of ca. 2735-2690 Ma mafic-ultramafic magmatism and sedimentation.

A more detailed evaluation/refinement of the setting and lithospheric controls upon the distribution of mafic-ultramafic magmatism are discussed later (see Chapter 3 and 4). Clearly though, an extensional continental setting is strongly supported by all the available field and U-Pb zircon age constraints.

SIGNIFICANCE OF ≤ 2624 AND 2612 MA SILICICLASTIC SUPRACRUSTAL ROCKS

The detrital zircon age dating of siliciclastic sedimentary rocks within the Laughland Lake area has revealed that ≤ 2610-2620 Ma supracrustal sequences unconformably overlie, and are infolded with, older ca. 2730-2690 Ma orthoquartzite-komatiite sequences of the PAg (Fig. 2-8). The similar detrital zircon age profiles and maximum depositional ages of quartz arenite TM-11 and subarkose arenite HS0-329 (Fig. 2-7(b and c)) suggests that they may be similar in age. Their maximum depositional ages coincide precisely with the initial phases of a regionally recognized, ca. 2620-2580 Ma intermediate-felsic granitoid magmatic event (e.g. LeCheminant & Roddick, 1991). The location of quartz arenite TM-11 within the core of an F_1 syncline mapped in the NVZ (Fig. 2-3) provides a minimum depositional age constraint of ca. 2350 Ma, i.e. deposition prior to or synchronous with the first recognized tectonometamorphic reworking of the region (Berman *et al.*, 2005).

In Fig. 2-11 the maximum depositional ages for subarkose arenite HS0-329 and quartz arenite TM-11 are displayed along with all published U-Pb zircon crystallization ages for 2.7-2.5 Ga Rae domain granitoids with < 10 m.y. (2σ) age uncertainties. This plot shows that both samples, particularly subarkose arenite HS0-329, have preferentially sampled only the earliest phases of this plutonism (ca. 2620-2610 Ma) and conspicuously lack detritus from the ca. 2610-2595 Ma and ca. 2585-2580 Ma components. With no evidence to suggest emplacement depth is related to age and that older ca. 2620-2610 Ma plutons are more prevalent than those < 2610 Ma, the preferential contribution of older plutons may be significant. One interpretation is that the deposition of these supracrustals may have occurred during the Neoarchean, contemporaneous with crustal extension that accompanied initiation of the 2.6 Ga granite bloom. This may explain the apparent preferential contribution of only the oldest phases of the granitoid bloom. Importantly, crustal extension would not only provide favorable sites for sedimentation, it is an efficient way in which to expose middle and upper crustal rocks. The fact that only the earliest formed granitoids (≥ 2610 Ma) appear to have been sampled could be explained if crustal extension, granitoid exposure, and siliciclastic sedimentation were ongoing prior to the terminal emplacement and exposure of the granitoids. Importantly, overlying the WLg only ~200 km to the southwest, a recently discovered ca. 2629 Ma rhyolite-orthoquartzite-iron formation-bearing supracrustal sequence confirms the existence of Archean supracrustal sequences temporally related to the initial phases of the ~2.6 Ga granitoid bloom (Fig. 2-11; Zaleski *et al*., 2001*a*).

CONCLUSIONS

(1) Mafic-ultramafic and associated felsic volcanism within the PAg formed over a protracted, ~40 m.y. time period between ca. 2730-2690 Ma and can be subdivided into

at least three distinctive, komatiite-bearing chronostratigraphic sequences. The lower ca. 2730 Ma sequence is dominated by mafic-ultramafic volcanic rocks, the middle ca. 2710 Ma sequence consists of a mixed ultramafic-felsic volcanic and sedimentary rock sequence, and the upper ≤ 2690 Ma sequence is dominated by siliciclastic sedimentary rocks but does contain at least one substantial komatiite flow sequence. Within the Laughland Lake area, the lower PAg consists predominantly of basalt and komatiite, rare intermediate-felsic volcanic rocks, and minor iron formation. The mafic-ultramafic volcanic succession is characterized by an exceptional komatiite occurrence and is compositionally stratified into lower basalt- and upper komatiite-dominated volcanic horizons, respectively. Interlayered 2729.5 ± 0.8 Ma dacite with basalt and 2729.5 ± 0.9 Ma dacite with komatiite confirms the age of this succession and indicate that the compositional transition from basalt- to komatiite-dominated volcanism, although sharply defined in the field, occurred abruptly and perhaps within < 1 m.y.

(2) The new U-Pb zircon age constraints for magmatism within the PAg have now confirmed that all of the late Archean supracrustal belts characterized by orthoquartzite-komatiite lithological associations within the central and northeastern Rae domain, including the WLg, PAg, and MRg should, as originally proposed (e.g. Jackson & Taylor, 1972), be considered components of a much larger, northeasterly-trending network of co-genetic, clastic-dominated supracrustal belts. This composite supracrustal network is at least 1400 km long and up to ~400 km wide, delineating an extensive, ~0.5 million km^2 crustal corridor extending from the Baker Lake area in mainland Nunavut northeastward across Committee Bay and stretching as far as Pond Inlet on the

northeastern tip of Baffin Island. Currently, direct (U-Pb zircon crystallization) and indirect (U-Pb detrital and xenocrystic zircon) age dating indicates that the predominant mafic-ultramafic and associated felsic volcanism within these belts formed over a protracted, ~45 m.y. time period between ca. 2735-2690 Ma.

(3) Pre-greenstone (> 2735 Ma) detrital zircons (n=121) recovered from a PAg orthoquartzite and two younger siliciclastic rocks collected within the Laughland Lake area have recorded an impressive ~ 1 b.y. of pre-greenstone magmatic activity within the Rae domain. The major age groups and well-defined detrital zircon age populations faithfully image the known ages of Rae crust and predict the presence of currently unrecognized and/or indirectly imaged ancient crustal components. The source of this ca. 2750-3750 Ma detritus appears to be from crust located within the central and northeast Rae domain. A compilation of available U-Pb age constraints indicates that the basement within the supracrustal corridor may not exceed ca. 3.0 Ga, and that the supracrustal belts are predominantly underlain by ca. 2750-2800 and ca. 2870 Ma crust, with potential for unknown quantities of ca. 2915 and 2965 Ma crust. In contrast, ~200 km to the west of the WLg and southern PAg supracrustal segments, the crust appears to be predominantly ≥ 2.95 Ga, contains documented ca. 3.1 Ga crust, and likely contains significantly older, ca. 3.25-3.8 Ga components.

(4) The supracrustal belts within the central and northeastern Rae domain formed within an extensional continental setting in which lithospheric extension along pre-existing NE-SW trending structures preceded and facilitated the initiation of volcanism between ca.

2735-2730 Ma. These regional structures appear to parallel and may be genetically related to a pre-greenstone crustal age structure in which older crust (≥ 2.95 and up to 3.25-3.8 Ga) occupies a westerly position relative to the inferred younger crust (≤ 2.95 and/or ≤ 2.87 Ga) underlying the PAg.

(5) A newly recognized ≤ 2630-2610 Ma subarkose arenite/quartz arenite supracrustal sequence has been documented in two locations within the Laughland Lake area. This sequence was deposited a minimum of ~60 m.y. after volcanism associated with older ca. 2730-2690 Ma orthoquartzite-komatiite associated sequences of the PAg. A minimum age of ≥ 2350 Ma (D_1-M_1; Berman *et al.*, 2005) indicates deposition preceded, or was potentially synchronous with the first recognized tectonometamorphic reworking of the region. Archean deposition temporally associated with the emplacement and exposure of a regionally-recognized ca. 2620-2580 Ma intermediate-felsic granitoid plutonic suite is a possibility. A recently recognized ca. 2629 Ma supracrustal sequence consisting of rhyolite, orthoquartzite and iron formation within the central Rae (Zaleski *et al.*, 2001*a*) may be correlative.

Table 2-1. All zircon (Zr.) have been air abraded with the number in parenthesis corresponding to the number of grains analysed. Th concentration calculated from ^{208}Pb/^{206}Pb and ^{207}Pb/^{206}Pb age. All errors quoted are at 1 sigma. Atomic ratios are corrected for fractionation, spike, 2 pg Pb and 0.5 pg U laboratory blanks, and initial common Pb (Stacey & Kramers, 1975). The percent discordance (% disc.) is calculated using the ^{206}Pb/^{238}U and ^{207}Pb/^{206}Pb ages.

Table 2-2. Counts per second (cps); counts per second radiogenic (cps rad.). The percent discordance (% disc.) is calculated using the ^{206}Pb/^{238}U and ^{207}Pb/^{206}Pb ages.

Table 2-1. U-Pb zircon isotopic data obtained by isotope dilution-TIMS.

Sample description	Weight (mg)	U (ppm)	Pb (ppm)	Th (ppm)	Th/U	TC Pb (pg)	Isotopic ratios			Apparent ages (Ma)			% disc.
							^{206}Pb/^{238}U	^{207}Pb/^{235}U	^{207}Pb/^{206}Pb	^{206}Pb/^{238}U	^{207}Pb/^{235}U	^{207}Pb/^{206}Pb	
Dacite T-3319													
1 Zr., (17)	0.016	109	67	64	0.589	37	0.5313(6)	13.809(16)	0.18852(8)	2746.7±2.5	2736.7±1.1	2729.3±0.7	-0.8
2 Zr., (8)	0.010	121	75	71	0.586	21	0.5356(6)	13.961(16)	0.18905(11)	2765.0±2.7	2747.1±1.1	2733.9±1.0	-1.4
3 Zr., (15)	0.012	129	81	80	0.616	26	0.5324(6)	13.849(19)	0.18866(11)	2751.5±2.8	2739.4±1.4	2730.5±1.0	-1.0
4 Zr., (16)	0.023	111	68	64	0.572	36	0.5303(8)	13.797(23)	0.18868(15)	2742.8±3.5	2735.9±1.6	2730.7±1.3	-0.5
5 Zr., (16)	0.018	118	72	68	0.574	45	0.5271(7)	13.696(19)	0.18846(10)	2729.2±3.0	2728.9±1.3	2728.8±0.9	0.0
6 Zr., (13)	0.017	129	80	77	0.592	69	0.5284(7)	13.733(18)	0.18851(11)	2734.6±2.8	2731.5±1.4	2729.2±0.9	-0.2
7 Zr., (13)	0.015	150	93	89	0.595	61	0.5329(6)	13.871(17)	0.18877(9)	2753.8±2.5	2740.9±1.2	2731.5±0.8	-1.0
Dacite H-1337													
1 Zr., (2)	0.008	64	38	38	0.589	5	0.5117(8)	13.290(24)	0.18837(11)	2663.9±3.6	2700.5±1.7	2728.0±1.0	2.9
2 Zr., (4)	0.009	36	23	24	0.649	23	0.5303(11)	13.796(38)	0.18868(32)	2742.8±4.7	2735.8±2.6	2730.7±2.8	-0.5
3 Zr., (6)	0.021	65	40	38	0.576	10	0.5282(7)	13.737(20)	0.18861(6)	2734.0±3.1	2731.7±1.4	2730.0±0.6	-0.2
4 Zr., (19)	0.011	92	58	66	0.712	9	0.5221(7)	13.546(18)	0.18816(6)	2708.3±2.9	2718.5±1.3	2726.2±0.5	0.8
5 Zr., (1)	0.008	22	14	13	0.594	11	0.5364(12)	13.945(37)	0.18854(24)	2768.5±5.3	2746.0±2.5	2729.5±2.1	-1.8
6 Zr., (6)	0.018	75	46	43	0.569	57	0.5308(7)	13.796(20)	0.18852(16)	2744.7±2.8	2735.8±1.4	2729.3±1.4	-0.7
Rhyolite T-3151													
1 Zr., (11)	0.009	184	106	97	0.529	57	0.5004(6)	12.788(17)	0.18535(11)	2615.5±2.5	2664.2±1.3	2701.3±1.0	3.8
2 Zr., (12)	0.009	118	70	63	0.533	35	0.5133(7)	13.169(20)	0.18605(13)	2670.9±3.0	2691.8±1.4	2707.6±1.2	1.6
3 Zr., (12)	0.016	180	109	98	0.543	111	0.5218(6)	13.334(18)	0.18531(13)	2707.1±2.7	2703.6±1.3	2700.9±1.1	-0.3
4 Zr., (1)	0.002	65	40	36	0.548	4	0.5287(12)	13.611(34)	0.18672(19)	2736.1±5.1	2723.1±2.4	2713.4±1.6	-1.0
5 Zr., (1)	0.002	67	40	31	0.462	2	0.5286(15)	13.638(41)	0.18710(17)	2735.8±6.3	2724.9±2.9	2716.9±1.5	-0.9
Granodiorite HS0-334													
1 Zr. (2)	0.002	205	113	76	0.368	2	0.5000(7)	12.029(17)	0.17447(8)	2613.9±3.0	2606.6±1.3	2601.0±0.8	-0.6
2 Zr. (3)	0.006	174	97	66	0.380	10	0.4993(8)	12.025(21)	0.17469(12)	2610.6±3.4	2606.4±1.7	2603.1±1.1	-0.4
Granodiorite dyke T-3459													
1 Zr., (3)	0.004	394	187	274	0.696	6	0.4075(8)	8.684(15)	0.15456(6)	2203.6±3.4	2305.5±1.7	2397.0±0.7	9.5
2 Zr., (2)	0.003	436	216	357	0.818	5	0.4127(5)	8.799(11)	0.15462(5)	2227.4±2.3	2317.4±1.1	2397.7±0.6	8.4
3 Zr., (1)	0.005	289	144	229	0.794	6	0.4188(5)	8.995(11)	0.15576(5)	2255.1±2.4	2337.4±1.2	2410.1±0.5	7.6
4 Zr., (1)	0.002	216	117	171	0.794	6	0.4512(6)	10.166(14)	0.16343(9)	2400.4±2.8	2450.0±1.4	2491.4±0.9	4.4
5 Zr., (1)	0.002	214	122	172	0.806	6	0.4741(6)	11.056(15)	0.16912(7)	2501.7±2.7	2527.8±1.3	2548.9±0.7	2.2
6 Zr., (1)	0.003	317	166	266	0.837	12	0.4344(9)	9.630(19)	0.16080(12)	2325.3±4.0	2400.1±1.9	2464.1±1.2	6.7
7 Zr., (1)	0.004	288	158	268	0.932	19	0.4458(10)	10.085(24)	0.16407(10)	2376.5±4.6	2442.6±2.3	2498.1±1.0	5.8

Table 2-2. U-Pb zircon isotopic data obtained by laser ablation-MC-ICP-MS.

Zr. #	^{204}Pb cps	^{206}Pb cps rad.	^{207}Pb/^{206}Pb	error (1σ)	^{207}Pb/^{235}U	error (1σ)	^{206}Pb/^{238}U	error (1σ)	^{207}Pb/^{206}Pb age	error (1σ)	% disc.
Rhyolite T-315											
1	0	160746	0.1866	0.0010	13.3244	0.1999	0.5180	0.0089	2712	8	1.0
2	0	64107	0.1847	0.0010	12.4903	0.1874	0.4900	0.0087	2695	9	5.6
3	2	64077	0.1856	0.0010	12.5737	0.1887	0.4912	0.0089	2704	9	5.7
Granodiorite HS0-334											
1	0	173057	0.1746	0.0009	11.6514	0.1748	0.4841	0.0083	2602	9	2.6
2	0	174590	0.1751	0.0009	11.9352	0.1791	0.4944	0.0088	2607	9	0.8
3	0	239822	0.1741	0.0009	11.6585	0.1749	0.4857	0.0081	2597	8	2.1
4	0	174053	0.1755	0.0009	11.7985	0.1770	0.4877	0.0083	2610	9	2.3
5	0	230327	0.1727	0.0009	11.5608	0.1735	0.4853	0.0081	2584	8	1.6
6	0	189851	0.1748	0.0009	11.7717	0.1766	0.4885	0.0084	2604	9	1.8
7	0	167989	0.1749	0.0009	11.6590	0.1750	0.4834	0.0086	2605	9	2.9
Granodioite dyke T-3459											
1	0	475439	0.1710	0.0009	10.9703	0.1646	0.4652	0.0077	2568	9	4.9
2	0	199121	0.1860	0.0009	12.7164	0.1908	0.4956	0.0085	2707	8	5.0
3	0	458953	0.1733	0.0009	11.8529	0.1778	0.4960	0.0078	2590	8	-0.3
4	0	401749	0.1718	0.0009	11.6040	0.1741	0.4896	0.0079	2575	9	0.3
5	0	388637	0.1674	0.0008	10.6033	0.1591	0.4593	0.0078	2532	9	4.5
6	0	470436	0.1606	0.0008	9.5962	0.1440	0.4333	0.0067	2462	9	6.8
Orthoquartzite TM0-106-A											
1	17	50321	0.1977	0.0011	14.5485	0.2183	0.5302	0.0088	2807	9	2.8
2	0	407427	0.2117	0.0011	16.8767	0.2532	0.5748	0.0098	2918	8	-0.4
3	0	347312	0.1881	0.0009	13.7766	0.2067	0.5280	0.0091	2726	8	-0.3
4	0	247167	0.1850	0.0010	13.4338	0.2016	0.5236	0.0093	2698	8	-0.7
5	0	156982	0.2113	0.0011	15.9969	0.2400	0.5456	0.0094	2916	8	4.6
6-a	0	125327	0.1819	0.0009	12.6013	0.1891	0.4993	0.0091	2670	8	2.7
6-b	2	131680	0.1824	0.0010	12.9461	0.1942	0.5115	0.0089	2675	9	0.5
7	0	234778	0.1820	0.0009	11.9375	0.1791	0.4727	0.0076	2671	9	7.9
8	0	269234	0.1834	0.0009	13.1481	0.1973	0.5169	0.0088	2683	8	-0.1
9	0	87332	0.1922	0.0010	13.6085	0.2042	0.5104	0.0088	2761	9	4.5
10	2	63594	0.2227	0.0012	17.1489	0.2573	0.5550	0.0097	3000	9	6.4
11	0	490563	0.1886	0.0010	13.7786	0.2067	0.5266	0.0093	2730	8	0.1
12	0	366124	0.1824	0.0009	12.7405	0.1912	0.5035	0.0085	2675	9	2.1
13	0	335790	0.1867	0.0010	13.5047	0.2026	0.5214	0.0086	2714	8	0.4
14	0	66314	0.1866	0.0010	12.9002	0.1935	0.4984	0.0085	2712	9	4.7
15	28	241673	0.1886	0.0010	12.8592	0.1929	0.4913	0.0086	2730	8	6.8
16	0	391514	0.1830	0.0009	12.3653	0.1855	0.4870	0.0080	2680	8	5.5
17	1	292209	0.1833	0.0009	12.9532	0.1943	0.5094	0.0080	2683	8	1.3
18	1	165004	0.1943	0.0010	14.0701	0.2111	0.5219	0.0090	2779	8	3.2
19	7	297157	0.1892	0.0010	13.7510	0.2063	0.5238	0.0089	2736	8	0.9
20	1	127669	0.1989	0.0010	14.3916	0.2159	0.5217	0.0087	2817	8	4.8
21	0	367127	0.1911	0.0010	11.5150	0.1727	0.4343	0.0071	2752	8	18.4
22	2	265742	0.1954	0.0010	14.4590	0.2169	0.5335	0.0089	2788	8	1.4
23	0	315467	0.1833	0.0009	12.2963	0.1845	0.4836	0.0084	2683	8	6.3
24	4	271630	0.1825	0.0009	10.7369	0.1612	0.4240	0.0084	2676	8	17.6
25	0	225145	0.1827	0.0009	10.0927	0.1515	0.3983	0.0081	2677	9	22.6
26	0	446424	0.1886	0.0010	13.5867	0.2038	0.5191	0.0085	2730	8	1.6
27	0	113151	0.1884	0.0010	11.9754	0.1797	0.4604	0.0089	2728	9	12.6
28	0	160629	0.2003	0.0010	13.6909	0.2054	0.4949	0.0081	2829	8	10.2
29	4	373380	0.1857	0.0010	13.1556	0.1974	0.5130	0.0085	2705	8	1.6
30	0	141367	0.2297	0.0012	18.8925	0.2834	0.5955	0.0095	3050	8	1.6
31	0	300955	0.2781	0.0014	26.3259	0.3950	0.6854	0.0125	3352	8	-0.5
32	13	318983	0.1824	0.0009	6.9948	0.1050	0.2777	0.0053	2675	8	46.0
33	0	221422	0.1836	0.0009	13.0279	0.1954	0.5139	0.0081	2686	8	0.6
34-a	0	136576	0.1830	0.0010	12.8219	0.1924	0.5076	0.0084	2680	9	1.5
34-b	0	167204	0.1833	0.0009	12.7636	0.1915	0.5042	0.0082	2683	8	2.3

Table 2-2. continued

Zr. #	^{204}Pb cps	^{206}Pb cps rad.	^{207}Pb/^{206}Pb	error (1σ)	^{207}Pb/^{235}U	error (1σ)	^{206}Pb/^{238}U	error (1σ)	^{207}Pb/^{206}Pb age	error (1σ)	% disc.
34-c	2	262404	0.1839	0.0009	13.1614	0.1975	0.5183	0.0084	2688	8	-0.2
35	0	509411	0.1827	0.0009	10.8662	0.1630	0.4308	0.0073	2677	8	16.3
36	0	150917	0.1848	0.0009	13.2239	0.1984	0.5183	0.0082	2696	8	0.2
37	0	143460	0.1844	0.0010	13.0666	0.1960	0.5133	0.0081	2693	9	1.0
38	1	132197	0.1892	0.0010	13.2819	0.1993	0.5084	0.0082	2735	9	3.8
39	3	288333	0.2038	0.0011	14.0031	0.2101	0.4976	0.0079	2857	8	10.8
40	0	509986	0.2067	0.0010	15.9423	0.2392	0.5586	0.0093	2880	8	0.8
41	4	193697	0.1900	0.0010	8.5923	0.1290	0.3275	0.0073	2742	8	38.2
42	1	345489	0.1967	0.0010	13.5354	0.2031	0.4982	0.0080	2799	8	8.4
43	10	257028	0.2321	0.0012	16.6727	0.2501	0.5204	0.0085	3066	8	14.6
44	0	81447	0.2072	0.0011	15.2482	0.2288	0.5332	0.0087	2884	9	5.5
45	0	161056	0.1901	0.0010	13.5611	0.2034	0.5168	0.0081	2743	8	2.5
46	0	292326	0.1797	0.0009	7.5516	0.1133	0.3044	0.0057	2650	8	40.1
47	0	442837	0.1901	0.0010	12.8738	0.1931	0.4905	0.0075	2743	8	7.5
48	0	432518	0.1821	0.0009	10.1312	0.1520	0.4029	0.0066	2672	8	21.6
49	0	290595	0.1898	0.0010	12.8894	0.1934	0.4920	0.0086	2740	8	7.1
50	3	317041	0.1848	0.0009	8.2943	0.1244	0.3250	0.0055	2696	8	37.4
51	0	180203	0.1873	0.0010	13.2565	0.1989	0.5126	0.0082	2719	9	2.3
52	0	125517	0.2179	0.0011	17.5517	0.2633	0.5832	0.0094	2966	8	0.2
53	0	224380	0.1871	0.0010	13.3775	0.2007	0.5176	0.0080	2717	8	1.3
54	10	121990	0.1904	0.0010	12.8299	0.1925	0.4879	0.0080	2746	8	8.1
55	0	370428	0.1821	0.0009	10.8500	0.1628	0.4315	0.0066	2673	8	16.0
56	1	506795	0.2197	0.0011	12.3246	0.1849	0.4062	0.0081	2979	8	30.8
57	0	141466	0.1893	0.0010	13.2046	0.1981	0.5051	0.0079	2736	9	4.5
58	0	289623	0.1908	0.0010	13.3817	0.2008	0.5080	0.0084	2749	8	4.5
59	6	383206	0.2136	0.0011	16.0708	0.2411	0.5449	0.0089	2933	8	5.4
60	0	409163	0.1880	0.0010	11.4973	0.1725	0.4430	0.0082	2725	8	15.8
61	5	381849	0.1879	0.0010	10.6415	0.1596	0.4101	0.0067	2724	8	22.0
62	1	148271	0.1908	0.0010	13.3149	0.1997	0.5054	0.0078	2749	8	4.9
63	0	400819	0.1816	0.0009	10.8828	0.1633	0.4338	0.0068	2668	8	15.4
64	2	238353	0.1855	0.0009	13.0624	0.1960	0.5101	0.0089	2702	8	2.1
65	0	162798	0.1854	0.0010	12.3971	0.1860	0.4841	0.0081	2702	9	7.0
66	9	270432	0.1830	0.0009	12.4549	0.1869	0.4929	0.0088	2680	8	4.4
67	0	171854	0.1822	0.0009	11.9757	0.1797	0.4761	0.0089	2673	9	7.3
68	0	592420	0.1882	0.0010	13.6444	0.2047	0.5251	0.0086	2726	8	0.3
69	0	489863	0.1835	0.0009	12.2730	0.1841	0.4844	0.0079	2685	8	6.2
70	1	308847	0.2326	0.0012	18.2230	0.2734	0.5673	0.0092	3070	8	7.0
71	0	282661	0.1918	0.0010	13.4150	0.2013	0.5064	0.0084	2758	8	5.1
72	2	281178	0.1897	0.0010	13.7882	0.2069	0.5263	0.0087	2740	8	0.6
73	0	218918	0.1827	0.0009	12.5621	0.1884	0.4981	0.0078	2677	9	3.2
74	0	212562	0.2270	0.0012	17.0703	0.2561	0.5446	0.0090	3031	8	9.3
75	0	252021	0.1920	0.0010	13.5428	0.2032	0.5108	0.0083	2760	8	4.4
76	0	348603	0.2414	0.0012	20.6888	0.3104	0.6207	0.0101	3129	8	0.7
77	0	374812	0.1886	0.0010	7.4949	0.1128	0.2878	0.0101	2730	8	45.4
Subarkose arenite HS0-329											
1	0	432542	0.2093	0.0011	16.1872	0.2429	0.5606	0.0098	2901	8	1.3
2	0	250009	0.2906	0.0015	27.4361	0.4116	0.6845	0.0115	3421	8	2.2
3	0	337935	0.2311	0.0012	18.8756	0.2832	0.5923	0.0102	3060	8	2.5
4	0	140397	0.2968	0.0015	28.7065	0.4306	0.7012	0.0122	3454	8	1.1
5	0	366350	0.2117	0.0011	16.4976	0.2475	0.5651	0.0093	2918	8	1.3
6	0	410810	0.2006	0.0010	15.3573	0.2304	0.5550	0.0102	2831	8	-0.6
7	0	261529	0.2095	0.0011	16.7536	0.2514	0.5800	0.0114	2901	8	-2.0
8	0	365281	0.2229	0.0011	16.5906	0.2489	0.5397	0.0083	3002	8	9.0
9	0	151300	0.2222	0.0011	17.8679	0.2681	0.5834	0.0100	2996	8	1.4
10-a	0	159494	0.3131	0.0016	30.6241	0.4594	0.7092	0.0113	3536	8	2.9
10-b	0	106183	0.3124	0.0016	29.4250	0.4414	0.6828	0.0111	3533	8	6.4
11	0	60549	0.2118	0.0011	15.3347	0.2301	0.5247	0.0098	2920	9	8.4
12	0	56645	0.1869	0.0010	12.6058	0.1892	0.4891	0.0090	2715	9	6.6
13	0	42309	0.1891	0.0011	12.4795	0.1873	0.4785	0.0093	2735	10	9.4
14	0	85733	0.3158	0.0017	29.8661	0.4481	0.6855	0.0139	3550	8	6.7

Table 2-2. continued

Zr. #	^{204}Pb cps	^{206}Pb cps rad.	^{207}Pb/^{206}Pb	error (1σ)	^{207}Pb/^{235}U	error (1σ)	^{206}Pb/^{238}U	error (1σ)	^{207}Pb/^{206}Pb age	error (1σ)	% disc.
15	0	76333	0.2056	0.0011	14.5416	0.2182	0.5128	0.0086	2871	8	8.6
16	0	12771	0.1956	0.0013	14.0087	0.2103	0.5195	0.0112	2790	11	4.1
17	2	24014	0.1964	0.0011	13.4406	0.2017	0.4960	0.0099	2797	9	8.7
18	0	87153	0.2055	0.0011	16.3445	0.2452	0.5769	0.0098	2870	8	-2.9
19	0	99956	0.1872	0.0010	14.1413	0.2122	0.5479	0.0098	2717	8	-4.5
20-a	0	196252	0.3372	0.0017	36.1251	0.5419	0.7768	0.0137	3650	8	-2.0
20-b	0	129618	0.3367	0.0017	31.9683	0.4796	0.6882	0.0116	3648	8	9.6
21	0	33227	0.2023	0.0011	14.0006	0.2101	0.5019	0.0090	2845	9	9.5
22	0	95371	0.2050	0.0011	13.8494	0.2078	0.4899	0.0083	2866	9	12.5
23	0	50902	0.1874	0.0010	12.2724	0.1841	0.4751	0.0083	2719	9	9.5
24	0	90860	0.1850	0.0010	13.4264	0.2014	0.5263	0.0091	2698	9	-1.3
25-a	0	56978	0.1864	0.0010	12.1640	0.1825	0.4733	0.0082	2710	9	9.5
25-b	0	58217	0.1861	0.0010	11.9828	0.1798	0.4669	0.0080	2708	9	10.6
26	0	68651	0.1856	0.0010	12.3058	0.1846	0.4809	0.0077	2703	9	7.7
27	0	108756	0.2280	0.0012	16.2189	0.2433	0.5150	0.0083	3038	9	14.5
28	0	448117	0.2047	0.0010	15.5538	0.2334	0.5505	0.0097	2864	8	1.6
29	0	55936	0.1997	0.0011	13.6315	0.2045	0.4951	0.0090	2823	9	9.9
30	0	179526	0.1907	0.0010	12.5162	0.1878	0.4758	0.0082	2748	8	10.5
31	0	72998	0.2052	0.0011	14.6581	0.2199	0.5182	0.0096	2868	9	7.5
32	0	188223	0.2111	0.0011	17.2017	0.2580	0.5908	0.0095	2914	8	-3.4
33-a	0	271582	0.2256	0.0011	19.7862	0.2968	0.6359	0.0106	3021	8	-6.4
33-b	0	401253	0.2267	0.0012	19.3411	0.2901	0.6186	0.0100	3029	8	-3.1
34	0	117649	0.2116	0.0012	17.4277	0.2614	0.5974	0.0097	2918	9	-4.4
35	0	138239	0.1947	0.0010	12.9842	0.1948	0.4834	0.0083	2782	8	10.4
36	0	81410	0.1961	0.0011	13.6202	0.2043	0.5042	0.0083	2794	9	7.1
37	0	67979	0.2056	0.0011	12.1279	0.1820	0.4275	0.0076	2871	9	23.8
38	0	60875	0.2108	0.0011	16.2118	0.2433	0.5577	0.0102	2912	8	2.3
39-a	0	353049	0.3574	0.0018	38.0784	0.5712	0.7727	0.0147	3739	8	1.7
39-b	0	392111	0.3586	0.0019	41.4017	0.6211	0.8376	0.0153	3744	8	-6.4
40	0	87996	0.1916	0.0010	13.1782	0.1978	0.4992	0.0094	2756	9	6.4
41	0	309309	0.1978	0.0010	13.7840	0.2068	0.5054	0.0088	2808	8	7.4
42	0	646267	0.2915	0.0015	28.1241	0.4219	0.6994	0.0108	3426	8	0.3
43	0	66594	0.1977	0.0011	13.6913	0.2054	0.5021	0.0083	2807	9	8.0
44	0	1140544	0.1886	0.0009	14.1863	0.2128	0.5454	0.0090	2730	8	-3.4
45	0	259172	0.2005	0.0010	15.0550	0.2259	0.5442	0.0104	2831	8	1.3
46	0	98443	0.1914	0.0010	13.4252	0.2014	0.5088	0.0087	2754	9	4.5
47	0	814299	0.1849	0.0009	13.5822	0.2038	0.5326	0.0086	2698	8	-2.5
48	0	203830	0.1967	0.0010	14.0825	0.2113	0.5194	0.0087	2799	8	4.5
49	0	301602	0.2288	0.0012	17.3383	0.2601	0.5495	0.0093	3044	8	8.9
50	16	282514	0.2372	0.0012	19.7363	0.2961	0.6034	0.0102	3101	8	2.3
51	0	235430	0.1867	0.0010	12.9773	0.1947	0.5041	0.0086	2714	8	3.7
52	0	144415	0.2154	0.0011	16.2909	0.2444	0.5485	0.0087	2947	8	5.4
53	0	280769	0.1758	0.0009	11.4943	0.1724	0.4742	0.0077	2613	8	5.1
54	0	612631	0.2273	0.0011	18.0588	0.2709	0.5761	0.0097	3033	8	4.1
55	0	250341	0.2231	0.0011	16.5523	0.2483	0.5379	0.0090	3003	8	9.4
56	0	229461	0.2091	0.0011	15.5784	0.2337	0.5403	0.0085	2898	8	4.8
57	0	176103	0.1909	0.0010	12.4931	0.1874	0.4745	0.0078	2750	9	10.8
58	0	256943	0.2000	0.0010	14.3896	0.2159	0.5218	0.0085	2826	8	5.2
59-a	0	348739	0.3118	0.0016	28.4830	0.4273	0.6629	0.0117	3530	8	9.1
59-b	0	313278	0.3124	0.0016	29.0660	0.4360	0.6746	0.0108	3533	8	7.6
60	0	464824	0.2276	0.0011	18.6404	0.2796	0.5939	0.0090	3035	8	1.2
61	0	75640	0.1962	0.0010	13.3847	0.2008	0.4946	0.0082	2795	9	8.9
62-a	0	222769	0.1940	0.0010	13.1621	0.1975	0.4920	0.0082	2776	8	8.6
62-b	0	262503	0.1934	0.0010	13.1983	0.1980	0.4949	0.0082	2771	8	7.8
63-a	0	302008	0.3125	0.0016	29.1919	0.4379	0.6774	0.0113	3533	8	7.2
63-b	0	318419	0.3120	0.0016	28.8063	0.4321	0.6696	0.0110	3531	8	8.2
64	0	318403	0.2071	0.0011	13.5281	0.2029	0.4737	0.0074	2883	8	16.0
65	0	403485	0.2268	0.0011	17.4643	0.2620	0.5583	0.0095	3030	8	6.9
66	0	128529	0.2053	0.0011	13.3924	0.2010	0.4731	0.0092	2869	8	15.6

Table 2-2. continued

Zr. #	^{204}Pb cps	^{206}Pb cps rad.	^{207}Pb/^{206}Pb	error (1σ)	^{207}Pb/^{235}U	error (1σ)	^{206}Pb/^{238}U	error (1σ)	^{207}Pb/^{206}Pb age	error (1σ)	% disc.
67-a	0	149253	0.2167	0.0011	16.3285	0.2450	0.5463	0.0092	2957	8	6.1
67-b	0	143536	0.2183	0.0011	16.6202	0.2493	0.5520	0.0095	2968	8	5.6
68-a	0	118220	0.2124	0.0011	15.0615	0.2260	0.5142	0.0087	2924	8	10.4
68-b	0	174103	0.2119	0.0011	15.1801	0.2277	0.5196	0.0086	2920	8	9.3
69	2	112078	0.1774	0.0010	11.7827	0.1768	0.4818	0.0074	2628	9	4.3
70-a	0	69070	0.1771	0.0010	11.1588	0.1674	0.4571	0.0072	2626	9	9.1
70-b	1	103043	0.1775	0.0009	11.3847	0.1708	0.4652	0.0075	2629	8	7.6
71-a	0	94126	0.1769	0.0009	11.2901	0.1694	0.4628	0.0074	2624	9	7.9
71-b	0	106147	0.1766	0.0009	10.8745	0.1631	0.4466	0.0071	2621	9	11.0
72	0	305646	0.1766	0.0009	11.5715	0.1736	0.4752	0.0073	2621	8	5.3
Quartz arenite TM-11											
1	0	115118	0.2821	0.0014	24.6721	0.3701	0.6343	0.0106	3375	8	7.8
2	0	57470	0.1826	0.0011	7.6978	0.1155	0.3047	0.0056	2677	10	40.8
3-a	0	267126	0.1763	0.0009	12.0173	0.1803	0.4943	0.0081	2618	8	1.3
3-b	0	346741	0.1755	0.0009	11.5717	0.1736	0.4782	0.0082	2611	8	4.2
4	0	306137	0.1967	0.0010	14.6371	0.2196	0.5394	0.0090	2799	8	0.8
5	0	242544	0.2019	0.0011	15.0240	0.2254	0.5398	0.0093	2842	8	2.5
6	1	567258	0.1860	0.0009	12.8579	0.1929	0.5014	0.0092	2707	8	3.9
7-a	0	799207	0.1773	0.0009	12.2613	0.1840	0.5013	0.0084	2628	8	0.4
7-b	13	864628	0.1765	0.0009	11.4439	0.1717	0.4702	0.0076	2620	8	6.2
8	0	728629	0.1755	0.0009	11.9280	0.1790	0.4925	0.0096	2610	9	1.3
9	6	866296	0.2276	0.0011	18.7469	0.2813	0.5975	0.0119	3035	8	0.6
10	0	158582	0.2110	0.0011	15.7355	0.2361	0.5409	0.0089	2913	8	5.3
11	5	189159	0.1913	0.0010	13.1748	0.1977	0.4996	0.0082	2753	8	6.2
12	0	764081	0.1962	0.0010	14.5429	0.2182	0.5376	0.0089	2795	8	0.9
13	4	536379	0.1964	0.0010	14.4288	0.2165	0.5329	0.0089	2796	8	1.9
14	0	291131	0.2060	0.0011	15.2654	0.2290	0.5375	0.0086	2874	8	4.3
15	5	352194	0.1973	0.0010	14.4712	0.2171	0.5321	0.0083	2804	8	2.4
16	0	311509	0.1951	0.0010	14.2556	0.2139	0.5302	0.0094	2785	8	1.9
17	16	948624	0.2048	0.0010	15.9211	0.2388	0.5639	0.0089	2865	8	-0.8
18	0	246550	0.2640	0.0013	22.9405	0.3441	0.6302	0.0104	3271	8	4.7
19	0	225763	0.1983	0.0010	14.8910	0.2234	0.5449	0.0089	2813	9	0.4
20	0	308029	0.1928	0.0010	14.2819	0.2143	0.5373	0.0092	2766	8	-0.2
21	0	506861	0.2260	0.0012	18.7825	0.2818	0.6027	0.0099	3024	8	-0.7
22	0	1161799	0.3102	0.0016	31.2019	0.4681	0.7297	0.0119	3522	8	-0.4
23	0	370028	0.2170	0.0011	17.6278	0.2645	0.5894	0.0102	2958	8	-1.2
24	0	584787	0.1850	0.0009	13.6536	0.2048	0.5352	0.0086	2699	8	-3.0
25	0	322829	0.1761	0.0009	12.1160	0.1818	0.4991	0.0094	2616	9	0.3
26	0	1201080	0.1768	0.0009	12.1624	0.1825	0.4990	0.0093	2623	8	0.6
27	0	654914	0.1858	0.0009	12.8309	0.1926	0.5010	0.0097	2705	8	3.9
28	5	370702	0.2115	0.0011	16.0554	0.2409	0.5507	0.0098	2917	8	3.8
29	5	719257	0.1755	0.0009	11.1412	0.1671	0.4605	0.0074	2611	8	7.8
30	0	346265	0.1756	0.0010	11.3415	0.1702	0.4675	0.0087	2612	9	6.4
31	0	614758	0.2119	0.0011	16.5123	0.2477	0.5653	0.0093	2920	8	1.4
32	0	1326727	0.2087	0.0011	16.1497	0.2424	0.5615	0.0112	2895	8	1.0
33	0	351871	0.1879	0.0010	12.8715	0.1931	0.4969	0.0087	2724	8	5.5
34	0	559638	0.2041	0.0010	15.1207	0.2268	0.5373	0.0089	2860	8	3.8
35	0	374793	0.1770	0.0010	11.6240	0.1745	0.4762	0.0094	2625	9	5.3
36	0	320582	0.2028	0.0010	14.8236	0.2224	0.5303	0.0092	2849	8	4.6
37	0	1278467	0.1749	0.0009	11.5945	0.1740	0.4810	0.0084	2605	8	3.4
38	0	647612	0.1955	0.0010	14.2697	0.2141	0.5293	0.0085	2789	8	2.2
39	5	732992	0.1897	0.0010	13.6461	0.2047	0.5217	0.0082	2740	8	1.5
40	0	1320553	0.1905	0.0010	13.8666	0.2080	0.5279	0.0089	2747	8	0.6
41	3	981328	0.1843	0.0009	12.9485	0.1943	0.5097	0.0083	2692	8	1.7
42	0	672077	0.1855	0.0009	12.9910	0.1949	0.5079	0.0083	2703	8	2.5
43	12	382511	0.1874	0.0010	12.7951	0.1920	0.4953	0.0087	2719	8	5.6
44	1	136347	0.2111	0.0011	15.5242	0.2329	0.5334	0.0090	2914	8	6.7
45	0	1005491	0.2087	0.0011	15.7905	0.2369	0.5488	0.0095	2896	8	3.2
46	1	661226	0.2112	0.0011	15.6447	0.2347	0.5373	0.0096	2915	8	6.0

Table 2-2. continued

Zr. #	^{204}Pb cps	^{206}Pb cps rad.	^{207}Pb/^{206}Pb	error (1σ)	^{207}Pb/^{235}U	error (1σ)	^{206}Pb/^{238}U	error (1σ)	^{207}Pb/^{206}Pb age	error (1σ)	% disc.
47	0	399911	0.1754	0.0009	11.3021	0.1696	0.4674	0.0089	2610	8	6.4
48	0	1402900	0.2690	0.0014	23.7230	0.3559	0.6397	0.0117	3300	8	4.3
49	0	419203	0.2021	0.0010	15.1123	0.2268	0.5424	0.0108	2844	8	2.2

Fig. 2-1. The distribution of ca. 2.7 Ga supracrustal belts characterized by orthoquartzite-komatiite lithological associations within the central and northeastern Rae domain of Nunavut including, (from southwest to northeast) the Woodburn Lake group (WLg), Prince Albert group (PAg), and Mary River group (MRg), respectively. Also shown are: (1) the locations of Neo- to Mesoarchean aged, ca. 2775-2870 Ma plutonic basement components of the WLg and MRg (Jackson *et al.*, 1990; Wodicka *et al.*, 2002; Zaleski *et al.*, 2001*a*; Bethune & Scammell, 2003); (2) the oldest, well-established U-Pb zircon crystallization age (3129 ± 10 Ma) currently recognized within the Rae domain (Henderson & Thériault, 1994); and (3) the locations of 15 undated granitoids within the central Rae that possess ca. 2.95-3.15 (n=4/15) and more "ancient" 3.25-3.9 Ga (n=11/15) depleted mantle Nd model ages (Thériault *et al.*, 1994). The extent of the regional bedrock mapping conducted southwest of Committee Bay between 2000 and 2002 is outlined (labeled Fig. 2-2; see Skulski *et al.*, 2003*c*) as is the location of this study, within the southwestern portion of the PAg, within the Laughland Lake area (LL area). Committee Bay (CB); Melville Peninsula (MP); Northwest Territories (NWT); Queen Maud Gulf (QMG).

Fig. 2-2. General geological map of the Committee Bay area delineating the supracrustal rocks of the PAg from granitoid rocks. Substantial occurrences of basalt, komatiite and orthoquartzite have been separated from undifferentiated PAg when possible. The U-Pb (zircon) geochronology sample locations and current ages for volcanism, syn-volcanic plutonism, and sedimentation (max. age) are shown. Inset shows the location of detailed mapping of the mafic-ultramafic volcanic succession within the northeast (NVZ; Fig. 2-

3) and southwest volcanic zones (SVZ; Fig. 2-4) within the Laughland Lake area. Map simplified after Skulski *et al.* (2003*c*).

Fig. 2-3. Detailed geological map of the Laughland Lake mafic-ultramafic volcanic succession within the northeast volcanic zone (NVZ). The locations of U-Pb (zircon) samples and field photographs (Fig. 2-5) are indicated.

Fig. 2-4. Detailed geological map of the Laughland Lake mafic-ultramafic volcanic succession within the southwest volcanic zone (SVZ). The locations of U-Pb (zircon) samples and field photographs (Fig. 2-5) are indicated.

Fig. 2-5. (a) Conformable contact between orthoquartzite and komatiite within the central Walker Lake supracrustal strand (see Fig. 2-2). (b) Intermediate volcanic breccia containing cm-sized basalt fragments (pen magnet is ~15 cm long; see Fig. 2-4). (c) Polyhedral fracture network developed in the upper portion of a basaltic flow (hammer is ~50 cm long; see Fig. 2-3). (d) Air photograph of a NVZ komatiite flow sequence consisting entirely of ~0.3 to 10 metre thick spinifex-textured flows (see Fig. 2-2). (e) Overturned spinifex-textured komatiite flows (hammer is ~50 cm long; see Fig. 2-4). (f) Coarse plate-spinifex within the upper portion of a spinifex-textured komatiite flow (hammer is ~50 cm long; Fig. 2-4). (g) Air photograph of komatiite flow sequence containing spinifex-textured flows of variable thickness (~2 to 100 m) underlying and flanking a thick fine- to coarse-grained, spinifex-free flow unit, interpreted as a remnant lava channel (see Fig. 2-3). (h) Ultramafic pillows (hammer is ~50 cm long; see Fig. 2-3).

(i) Plagioclase-phyric dacite (pen magnet is ~15 cm long; U-Pb sample H-1337; see Fig. 2-3). (j) Outcrop containing argillite (dark) and orthoquartzite (hammer is ~50 cm long; U-Pb sample TM0-106-A; see Fig. 2-4). (k) Cross-laminated quartz arenite containing cm-sized angular clasts of banded iron formation (U-Pb sample TM-11; see Fig. 2-3). (l) Conformable contact between orthoquartzite and komatiite flows along the southwestern portion of the Kinngalugjuaq Mountain ridge system (hammer is ~50 cm long; see Fig. 2-2).

Fig. 2-6. (a-e) Concordia diagrams for PAg volcanic and intrusive rocks. In Fig. 2-6(c-e) filled ellipses are ID-TIMS analyses and larger ellipses are LA-MC-ICP-MS analyses. The preferred ages are those outlined in boxes.

Fig. 2-7. Concordia diagrams and probability density histograms of $^{207}Pb/^{206}Pb$ age (bin width is 18 m.y.) for detrital zircon separated from (a) orthoquartzite TM0-106-A; (b) subarkose arenite HS0-329; and (c) quartz arenite TM-11. Inset concordia diagrams and/or smaller scale $^{207}Pb/^{206}Pb$ age histograms depict the analyses used to estimate the maximum depositional ages. Note that for sample TM0-106-A (> 15% discordant analyses including those used to estimate the maximum age are not shown on the concordia diagrams for display purposes. For zircon analysed in multiple spots (e.g. grains HS0-329-70 and -71) a weighted mean $^{207}Pb/^{206}Pb$ age is used for the histogram and the most concordant analysis plotted on the concordia diagram. Zircon images (sample HS0-329) were taken post-ablation and laser pits are ~40 μm in diametre.

Fig. 2-8. Chronostratigraphy of the Laughland Lake area including ca. 2730-2690 Ma orthoquartzite-komatiite sequences of the PAg and newly recognized, ≤ ca. 2624-2612 Ma siliciclastic supracrustal rocks. A prominent population of ca. 2750-2800 Ma zircon xenocrysts identified with ca. 2730 Ma felsic volcanic rocks within the lower PAg in interpreted to image the underlying basement (see Fig. 3-11 in Chapter 3).

Fig. 2-9. Plot of U-Pb zircon ages for: volcanism (triangles); syn-volcanic plutonism (squares); sedimentation (circles); and basement (diamonds) for orthoquartzite-komatiite associated supracrustal belts of the central and northeastern Rae domain. The ca. 2775 Ma basement age for the PAg is the age peak for a prominent population of ca. 2750-2800 Ma zircon xenocrysts identified within the ca. 2730 Ma felsic volcanic rocks within the lower PAg (see Fig. 3-11 in Chapter 3). References: WLg (Davis & Zaleski, 1998; Zaleski *et al.*, 2001*a*); PAg (this study; Chapter 3; Skulski *et al.*, 2002; Table 1 in Skulski *et al.*, 2003*b*; Table 1 in Sandeman *et al.*, 2004); MRg (Jackson *et al.*, 1990; Wodicka *et al.*, 2002; Bethune & Scammell, 2003).

Fig. 2-10. Composite plot of all > 2735 Ma detrital zircon separated from the three siliciclastic supracrustal rocks collected within the Laughland Lake area (n= 121; Fig. 2-7(a-c) and Table 2-2) and well-established, > 2735 Ma U-Pb zircon ages for the Rae domain, including: crystallization ages (squares), xenocrystic zircon ages (diamonds), and detrital zircon ages (circles), as well as Nd model ages (large boxes). The Rae domain U-Pb geochronological database has been subdivided into: (1) southwest Rae (Saskatchewan); (2) central Rae west of supracrustals (Nunavut and Northwest

Territories); (3) central Rae PAg/WLg (Nunavut – region southwest of Committee Bay and underlying the supracrustal belts); and (4) northeast Rae MRg (Nunavut - northern Baffin Island region). References: (1) southwest Rae (Persons *et al.*, 1988; Hanmer *et al.*, 1994; Hartlaub *et al.*, 2004); (2) central Rae west of supracrustals (Henderson & Loveridge, 1990; Henderson & Thériault, 1994; Thériault *et al.*, 1994); (3) central Rae PAg/WLg (Ashton, 1988; Davis & Zaleski, 1998; Zaleski *et al.*, 2001*a*); and (4) northeast Rae MRg (Jackson *et al.*, 1990; Wodicka *et al.*, 2002; Bethune & Scammell, 2003).

Fig. 2-11. U-Pb zircon crystallization ages for > 2500 Ma and < 2700 Ma plutonic rocks within the Rae domain (2σ age uncertainty ≤ 10 Ma only). A ca. 2629 Ma rhyolite interbedded with orthoquartzite and iron formation from the central Rae (Zaleski *et al.*, 2001*a*) and the maximum depositional ages for subarkose arenite HS0-329 and quartz arenite TM-11 are shown for comparison. References include from southwest to northeast: (1) Beaverlodge domain, southwest Rae (Van Schmus *et al.*, 1986); (2) east Athabasca mylonite triangle, snowbird tectonic zone, southwest Rae (Hanmer *et al.*, 1994); (3) central/northeastern Rae (LeCheminant & Roddick, 1991); (4) Chantrey Inlet area, northeastern Rae (Frisch & Parrish, 1992); (5) Woodburn Lake group, central Rae (Ashton, 1988; Roddick *et al.*, 1992; Davis & Zaleski, 1998); (6) Prince Albert group, central/northeastern Rae (Table 1 in Skulski *et al.*, 2003*a*; this study).

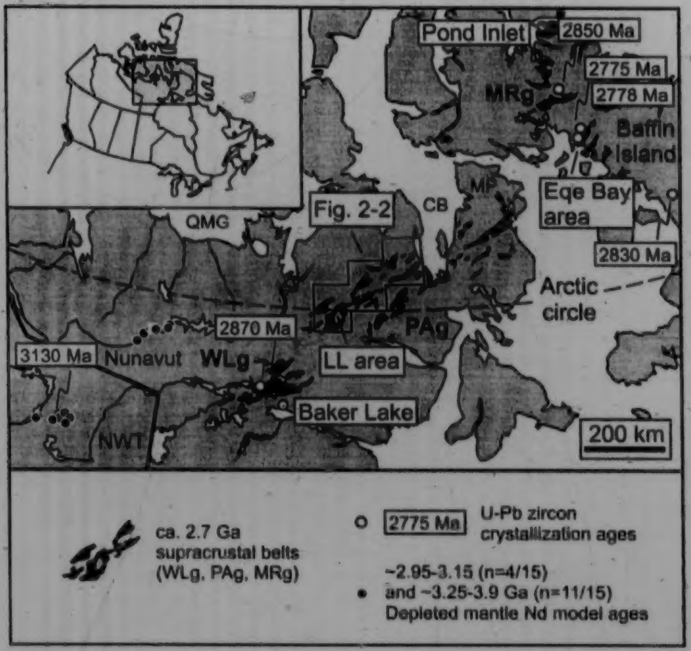
Pond Inlet
2850 Ma
2775 Ma
MRg
2778 Ma
Baffin Island
MP
Eqe Bay area
Fig. 2-2
CB
QMG
2830 Ma
Arctic circle
2870 Ma
PAg
3130 Ma
Nunavut
WLg
LL area
Baker Lake
NWT
200 km
ca. 2.7 Ga supracrustal belts (WLg, PAg, MRg)
○ 2775 Ma U-Pb zircon crystallization ages
~2.95-3.15 (n=4/15)
● and ~3.25-3.9 Ga (n=11/15) Depleted mantle Nd model ages

Figure 2-1

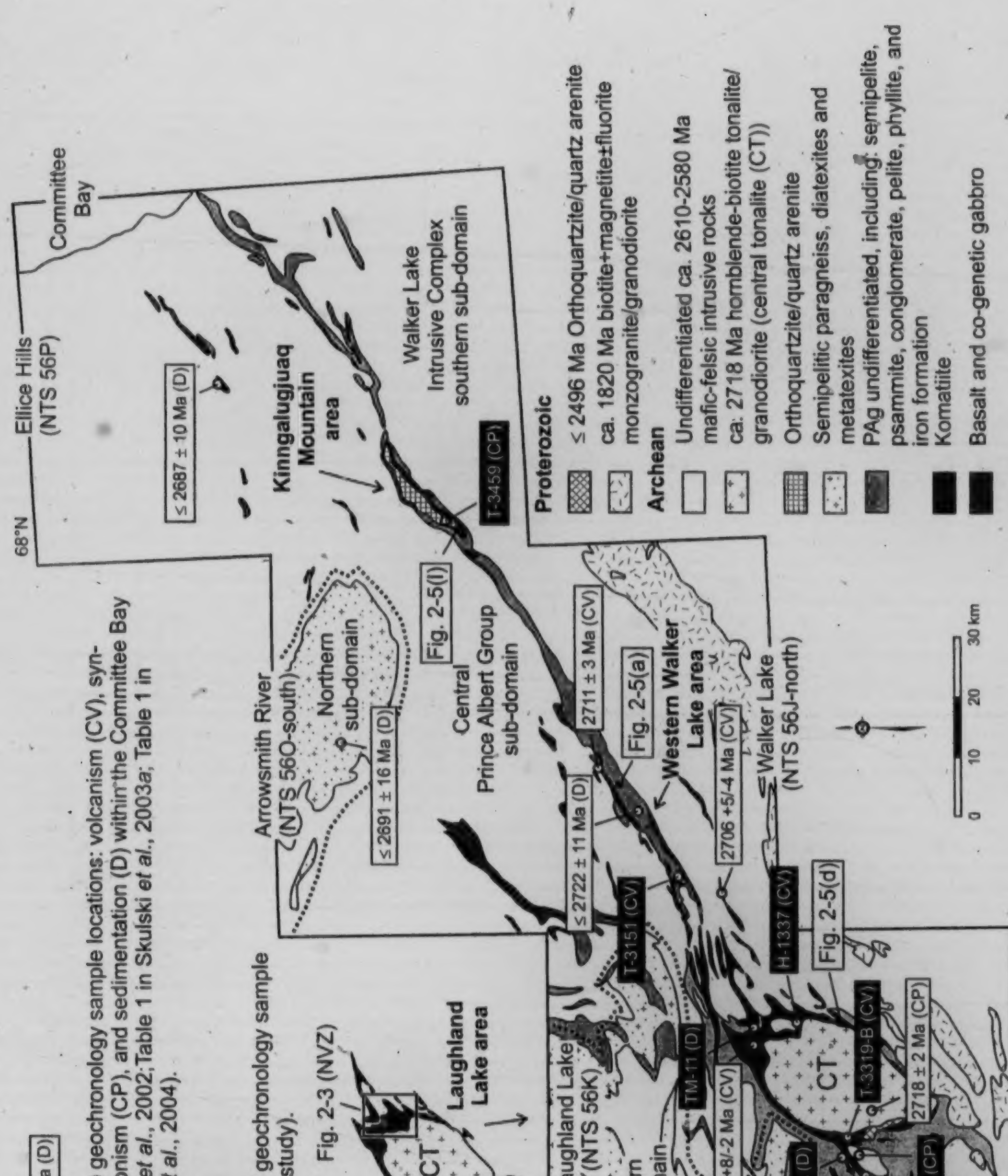
≤ 2722 ± 11 Ma (D)
U-Pb (zircon) geochronology sample locations: volcanism (CV), syn-volcanic plutonism (CP), and sedimentation (D) within the Committee Bay belt (Skulski et al., 2002; Table 1 in Skulski et al., 2003a; Table 1 in Sandeman et al., 2004).
H-1337 (CV)
U-Pb (zircon) geochronology sample location (this study).
Fig. 2-3 (NVZ)
CT
Laughland Lake area
Fig. 2-4 (SVZ)
94°W
68°N
Ellice Hills (NTS 56P)
Committee Bay
≤ 2687 ± 10 Ma (D)
Kinngalugjuaq Mountain area
Walker Lake Intrusive Complex southern sub-domain
T-3459 (CP)
Arrowsmith River (NTS 56O-south)
Northern sub-domain
≤ 2691 ± 16 Ma (D)
Fig. 2-5(l)
Central Prince Albert Group sub-domain
2711 ± 3 Ma (CV)
Fig. 2-5(a)
Western Walker Lake area
2706 +5/-4 Ma (CV)
Walker Lake (NTS 56J-north)
≤ 2722 ± 11 Ma (D)
T-3151 (CV)
H-1337 (CV)
Fig. 2-5(d)
Laughland Lake (NTS 56K)
Northern sub-domain
TM-11 (D)
2732 +8/-2 Ma (CV)
TM0-106-A (D)
T-3319-B (CV)
CT
2718 ± 2 Ma (CP)
HS0-329 (D)
HS0-334 (CP)
0 10 20 30 km
Proterozoic
≤ 2496 Ma Orthoquartzite/quartz arenite
ca. 1820 Ma biotite+magnetite±fluorite monzogranite/granodiorite
Archean
Undifferentiated ca. 2610-2580 Ma mafic-felsic intrusive rocks
ca. 2718 Ma hornblende-biotite tonalite/granodiorite (central tonalite (CT))
Orthoquartzite/quartz arenite
Semipelitic paragneiss, diatexites and metatexites
PAg undifferentiated, including: semipelite, psammite, conglomerate, pelite, phyllite, and iron formation
Komatiite
Basalt and co-genetic gabbro

Figure 2-2.

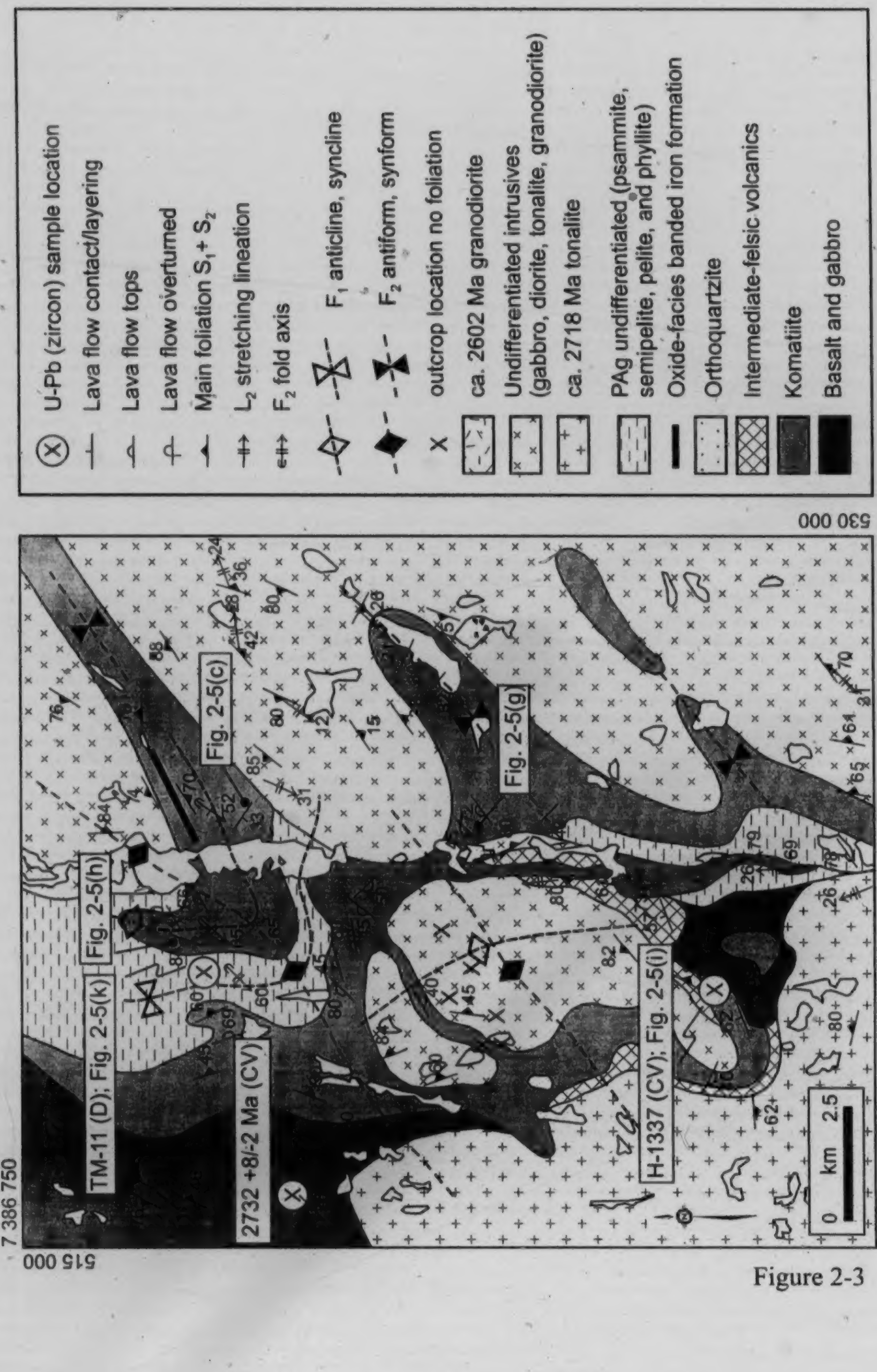
U-Pb (zircon) sample location
Lava flow contact/layering
Lava flow tops
Lava flow overturned
Main foliation $S_1 + S_2$
L_2 stretching lineation
F_2 fold axis
F_1 anticline, syncline
F_2 antiform, synform
outcrop location no foliation
ca. 2602 Ma granodiorite
Undifferentiated intrusives (gabbro, diorite, tonalite, granodiorite)
ca. 2718 Ma tonalite
PAg undifferentiated (psammite, semipelite, pelite, and phyllite)
Oxide-facies banded iron formation
Orthoquartzite
Intermediate-felsic volcanics
Komatiite
Basalt and gabbro
7 386 750
515 000
530 000
7 368 750
TM-11 (D); Fig. 2-5(k)
Fig. 2-5(h)
Fig. 2-5(c)
Fig. 2-5(g)
2732 +8/-2 Ma (CV)
H-1337 (CV); Fig. 2-5(i)
0 km 2.5

Figure 2-3

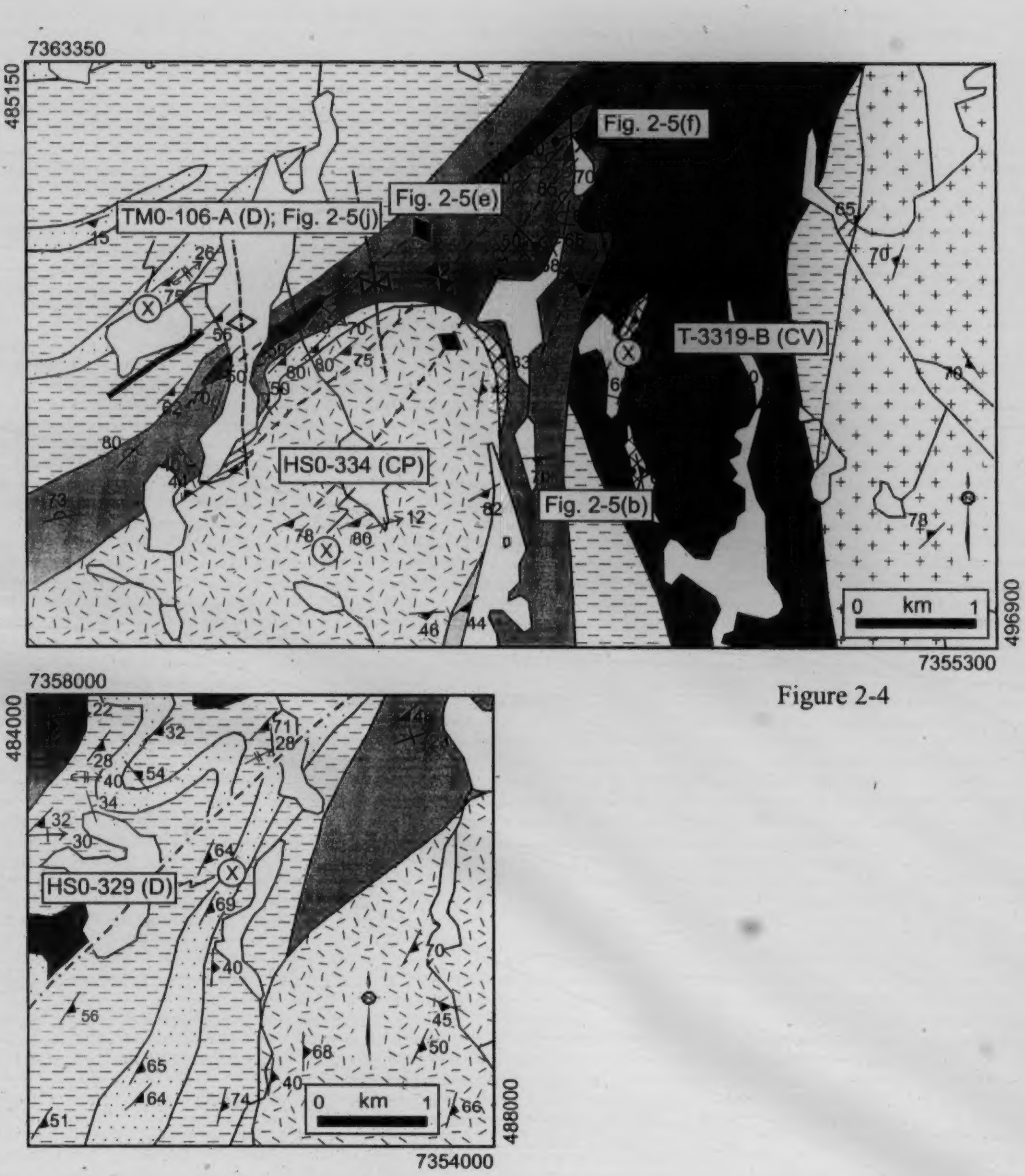
7363350
485150
Fig. 2-5(f)
Fig. 2-5(e)
TM0-106-A (D); Fig. 2-5(j)
T-3319-B (CV)
HS0-334 (CP)
Fig. 2-5(b)
0 km 1
496900
7355300
7358000
484000
HS0-329 (D)
0 km 1
488000
7354000

Figure 2-4

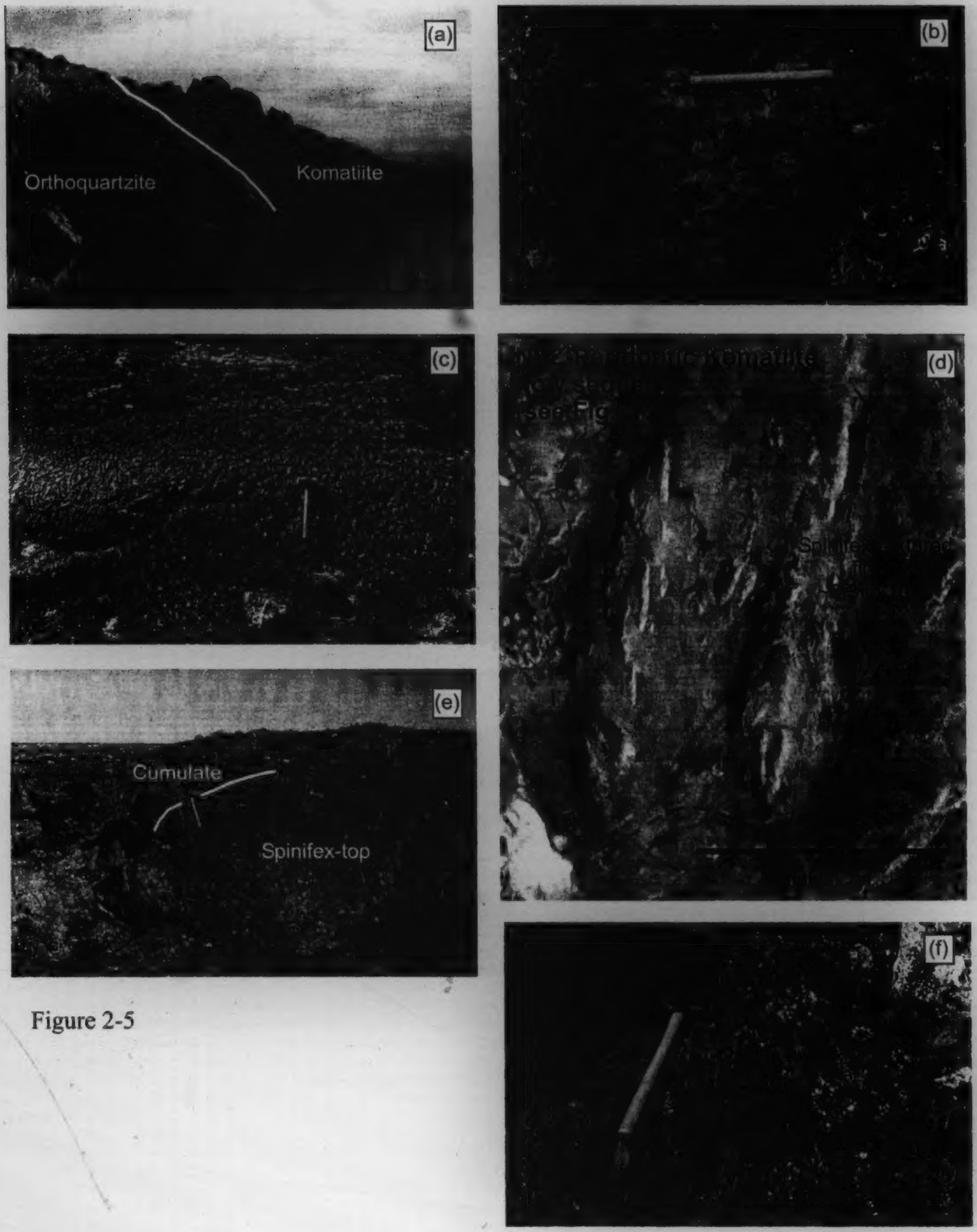
(a)
Orthoquartzite
Komatiite
(b)
(c)
(d)
see Fig
(e)
Cumulate
Spinifex-top
(f)

Figure 2-5

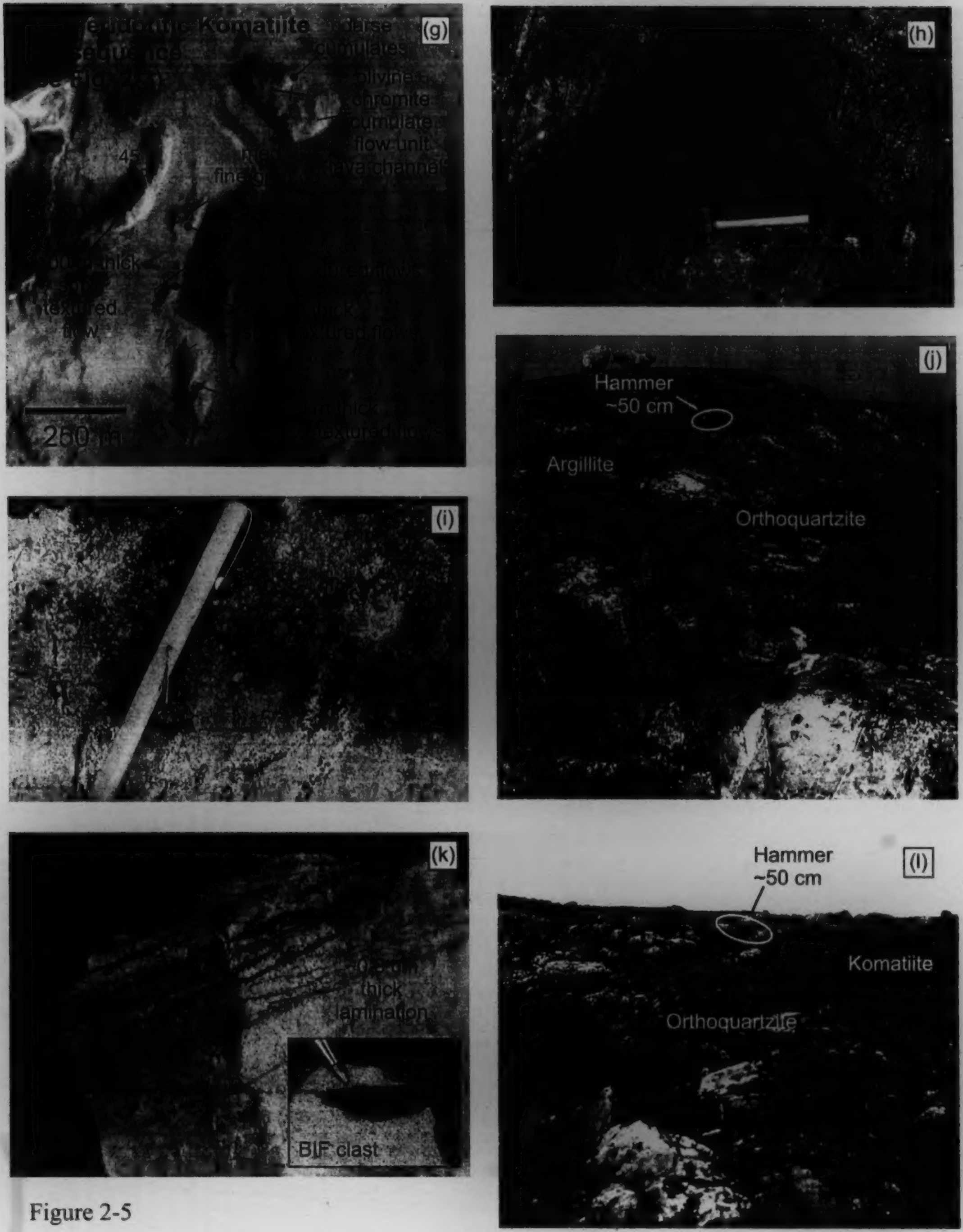
Komatiite
sequence
coarse
cumulates
olivine
chromite
cumulate
flow unit
lava channel
45
fine
thick
textured
flow
textured flows
thick
textured flows
thick
textured flows
250 m
(g)
(h)
Hammer
~50 cm
Argillite
Orthoquartzite
(j)
(i)
(k)
0.5 cm
thick
lamination
BIF clast
Hammer
~50 cm
(l)
Komatiite
Orthoquartzite

Figure 2-5

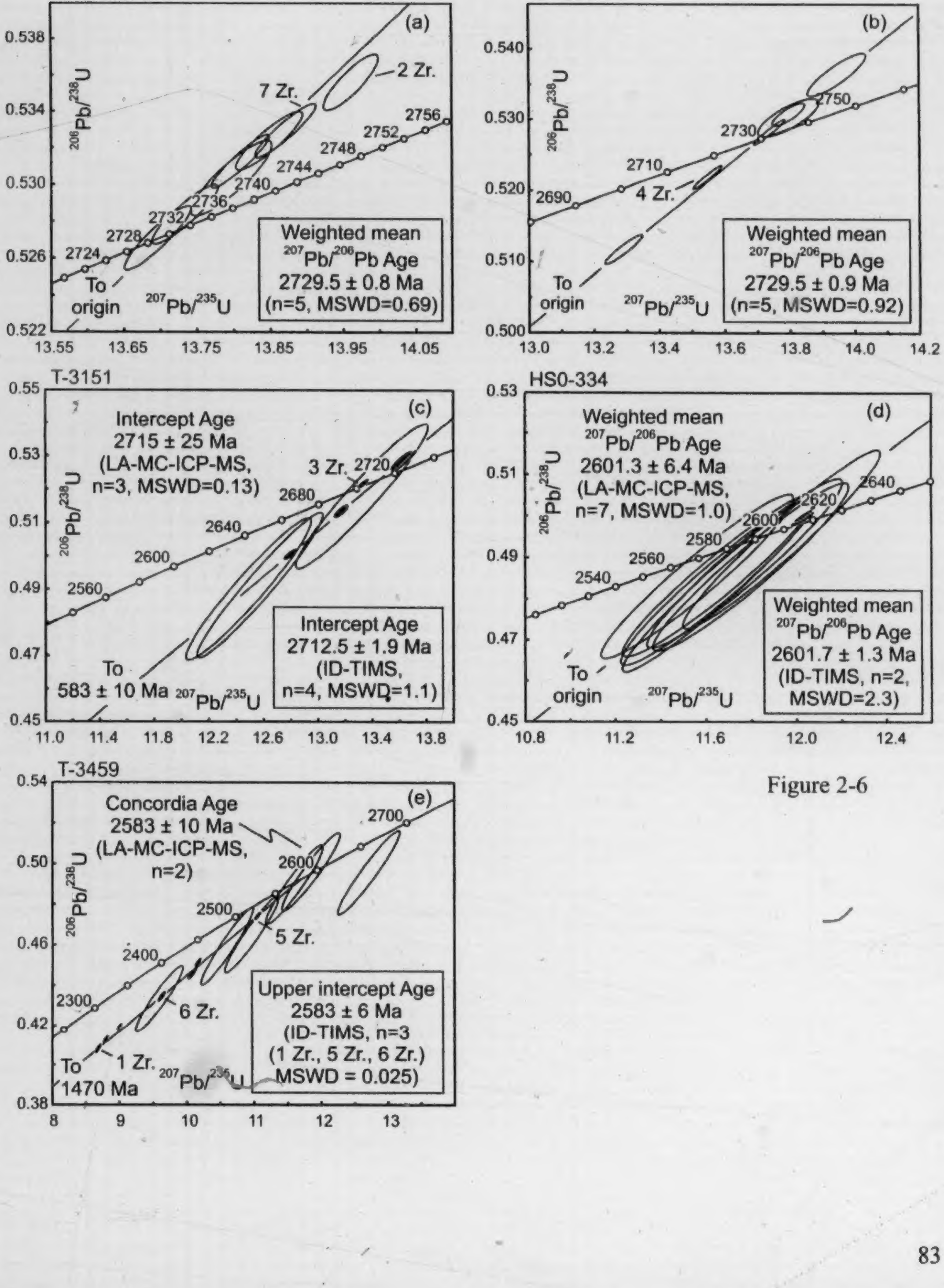
T-3319-B
(a)
7 Zr.
2 Zr.
2724
2728
2732
2736
2740
2744
2748
2752
2756
To origin
$^{206}Pb/^{238}U$
$^{207}Pb/^{235}U$
Weighted mean
$^{207}Pb/^{206}Pb$ Age
2729.5 ± 0.8 Ma
(n=5, MSWD=0.69)
0.522
0.526
0.530
0.534
0.538
13.55
13.65
13.75
13.85
13.95
14.05
H-1337
(b)
2690
2710
2730
2750
4 Zr.
To origin
Weighted mean
$^{207}Pb/^{206}Pb$ Age
2729.5 ± 0.9 Ma
(n=5, MSWD=0.92)
0.500
0.510
0.520
0.530
0.540
13.0
13.2
13.4
13.6
13.8
14.0
14.2
T-3151
(c)
Intercept Age
2715 ± 25 Ma
(LA-MC-ICP-MS,
n=3, MSWD=0.13)
3 Zr.
2720
2680
2640
2600
2560
To
583 ± 10 Ma
Intercept Age
2712.5 ± 1.9 Ma
(ID-TIMS,
n=4, MSWD=1.1)
0.45
0.47
0.49
0.51
0.53
0.55
11.0
11.4
11.8
12.2
12.6
13.0
13.4
13.8
HS0-334
(d)
Weighted mean
$^{207}Pb/^{206}Pb$ Age
2601.3 ± 6.4 Ma
(LA-MC-ICP-MS,
n=7, MSWD=1.0)
2540
2560
2580
2600
2620
2640
To origin
Weighted mean
$^{207}Pb/^{206}Pb$ Age
2601.7 ± 1.3 Ma
(ID-TIMS, n=2,
MSWD=2.3)
0.45
0.47
0.49
0.51
0.53
10.8
11.2
11.6
12.0
12.4
T-3459
(e)
Concordia Age
2583 ± 10 Ma
(LA-MC-ICP-MS,
n=2)
2700
2600
2500
2400
2300
5 Zr.
6 Zr.
1 Zr.
To
1470 Ma
Upper intercept Age
2583 ± 6 Ma
(ID-TIMS, n=3
(1 Zr., 5 Zr., 6 Zr.)
MSWD = 0.025)
0.38
0.42
0.46
0.50
0.54
8
9
10
11
12
13

Figure 2-6

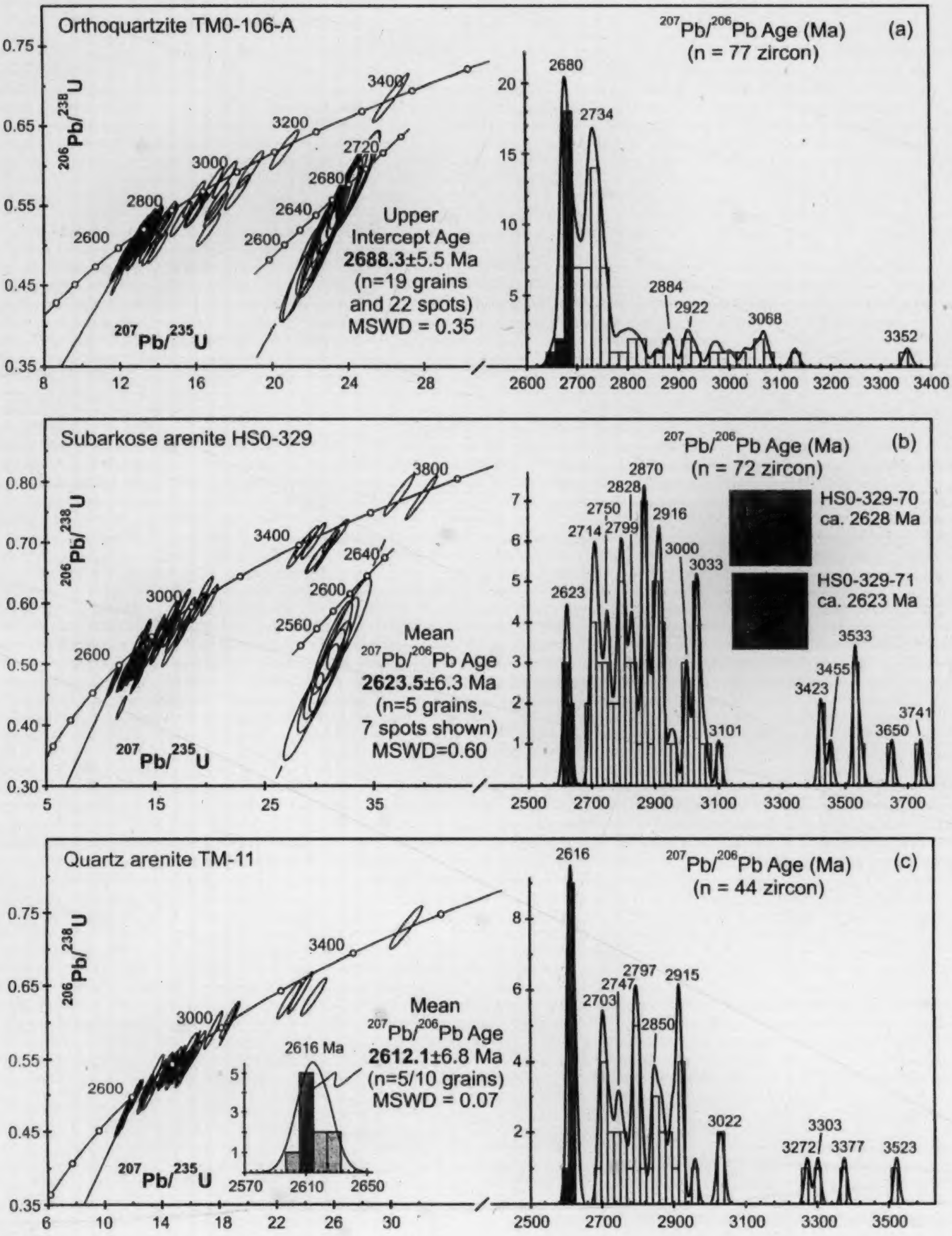
Orthoquartzite TM0-106-A
$^{207}Pb/^{206}Pb$ Age (Ma)
(n = 77 zircon)
(a)
$^{206}Pb/^{238}U$
$^{207}Pb/^{235}U$
0.75
0.65
0.55
0.45
0.35
8
12
16
20
24
28
2600
2800
3000
3200
3400
2600
2640
2680
2720
Upper Intercept Age
2688.3±5.5 Ma
(n=19 grains and 22 spots)
MSWD = 0.35
2680
2734
2884
2922
3068
3352
20
15
10
5
2600
2700
2800
2900
3000
3100
3200
3300
3400
Subarkose arenite HS0-329
$^{207}Pb/^{206}Pb$ Age (Ma)
(n = 72 zircon)
(b)
0.80
0.70
0.60
0.50
0.40
0.30
5
15
25
35
2600
3000
3400
3800
2560
2600
2640
Mean
$^{207}Pb/^{206}Pb$ Age
2623.5±6.3 Ma
(n=5 grains,
7 spots shown)
MSWD=0.60
2623
2714
2750
2799
2828
2870
2916
3000
3033
3101
3423
3455
3533
3650
3741
HS0-329-70
ca. 2628 Ma
HS0-329-71
ca. 2623 Ma
7
6
5
4
3
2
1
2500
2700
2900
3100
3300
3500
3700
Quartz arenite TM-11
$^{207}Pb/^{206}Pb$ Age (Ma)
(n = 44 zircon)
(c)
0.75
0.65
0.55
0.45
0.35
6
10
14
18
22
26
30
2600
3000
3400
2616 Ma
5
3
1
2570
2610
2650
Mean
$^{207}Pb/^{206}Pb$ Age
2612.1±6.8 Ma
(n=5/10 grains)
MSWD = 0.07
2616
2703
2747
2797
2850
2915
3022
3272
3303
3377
3523
8
6
4
2
2500
2700
2900
3100
3300
3500

Figure 2-7

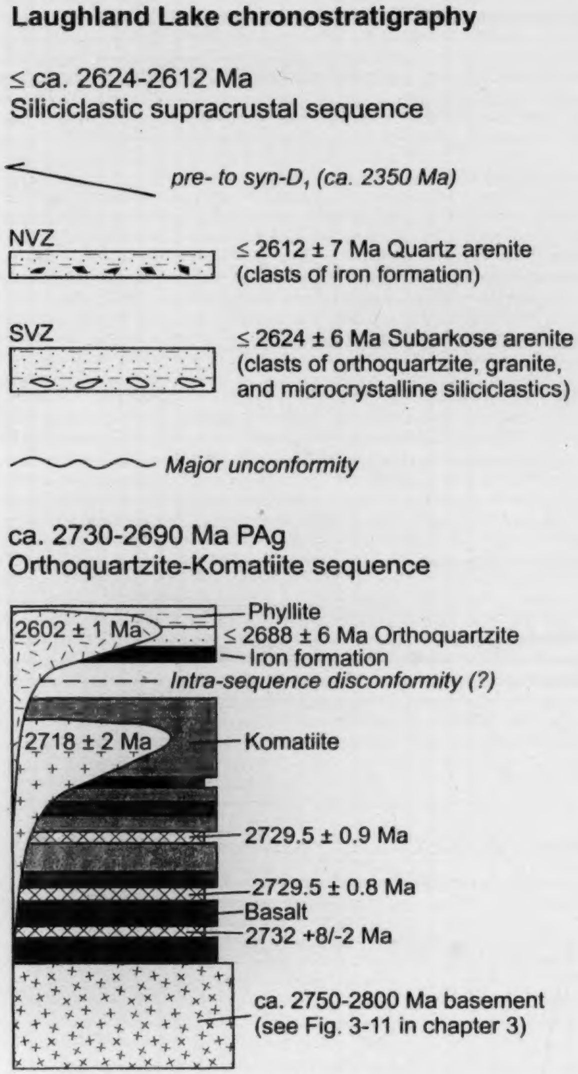
Laughland Lake chronostratigraphy
≤ ca. 2624-2612 Ma
Siliciclastic supracrustal sequence
pre- to syn-D_1 (ca. 2350 Ma)
NVZ
≤ 2612 ± 7 Ma Quartz arenite
(clasts of iron formation)
SVZ
≤ 2624 ± 6 Ma Subarkose arenite
(clasts of orthoquartzite, granite,
and microcrystalline siliciclastics)
Major unconformity
ca. 2730-2690 Ma PAg
Orthoquartzite-Komatiite sequence
Phyllite
2602 ± 1 Ma
≤ 2688 ± 6 Ma Orthoquartzite
Iron formation
Intra-sequence disconformity (?)
2718 ± 2 Ma
Komatiite
2729.5 ± 0.9 Ma
2729.5 ± 0.8 Ma
Basalt
2732 +8/-2 Ma
ca. 2750-2800 Ma basement
(see Fig. 3-11 in chapter 3)

Figure 2-8

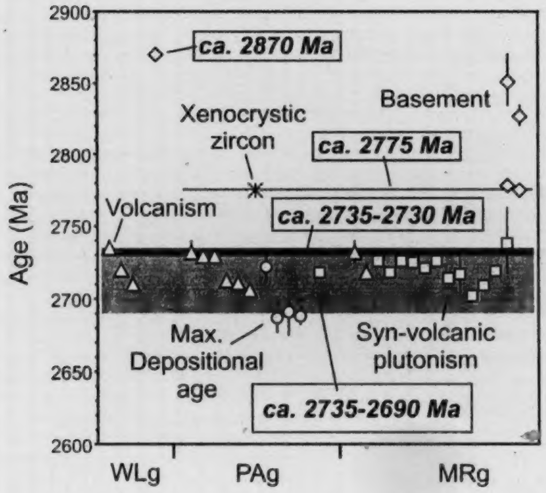
ca. 2870 Ma
Basement
Xenocrystic zircon
ca. 2775 Ma
Volcanism
ca. 2735-2730 Ma
Max. Depositional age
Syn-volcanic plutonism
ca. 2735-2690 Ma
Age (Ma)
2900
2850
2800
2750
2700
2650
2600
WLg
PAg
MRg

Figure 2-9

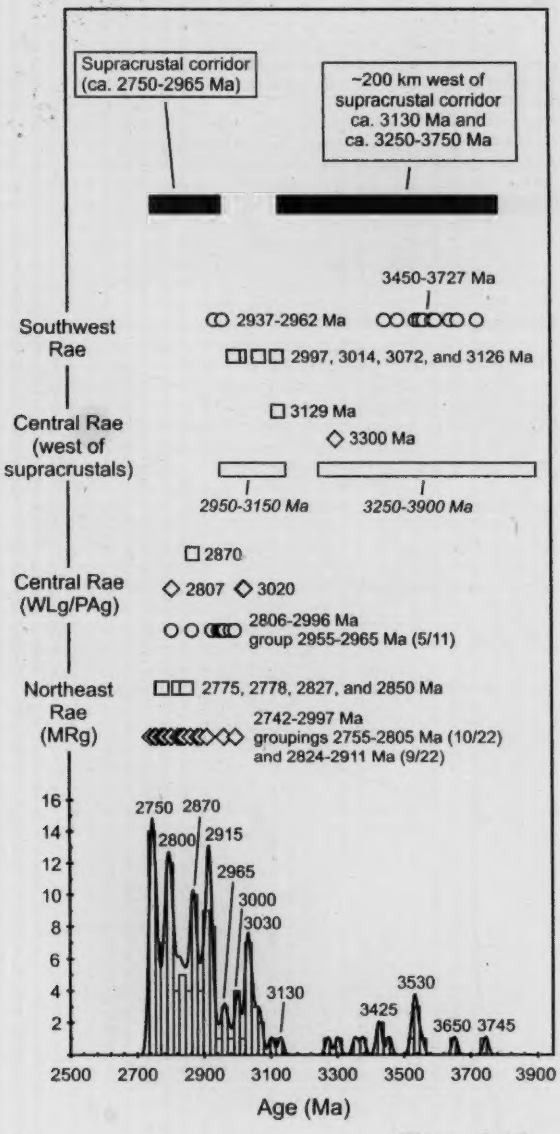
Supracrustal corridor (ca. 2750-2965 Ma)
~200 km west of supracrustal corridor ca. 3130 Ma and ca. 3250-3750 Ma
Southwest Rae
3450-3727 Ma
2937-2962 Ma
2997, 3014, 3072, and 3126 Ma
Central Rae (west of supracrustals)
3129 Ma
3300 Ma
2950-3150 Ma
3250-3900 Ma
Central Rae (WLg/PAg)
2870
2807
3020
2806-2996 Ma
group 2955-2965 Ma (5/11)
Northeast Rae (MRg)
2775, 2778, 2827, and 2850 Ma
2742-2997 Ma
groupings 2755-2805 Ma (10/22)
and 2824-2911 Ma (9/22)
16
14
12
10
8
6
4
2
2750
2870
2800
2915
2965
3000
3030
3130
3425
3530
3650
3745
2500
2700
2900
3100
3300
3500
3700
3900
Age (Ma)

Figure 2-10

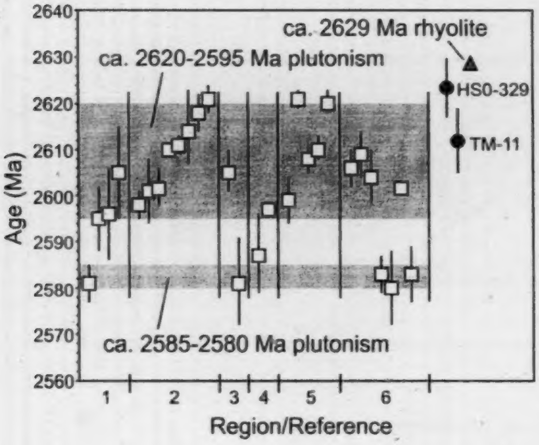
2640
2630
2620
2610
2600
2590
2580
2570
2560
Age (Ma)
ca. 2629 Ma rhyolite
ca. 2620-2595 Ma plutonism
HS0-329
TM-11
ca. 2585-2580 Ma plutonism
1
2
3
4
5
6
Region/Reference

Figure 2-11

REFERENCES

Arndt, N. T., Naldrett, A. J. & Pyke, D. R. (1977). Komatiitic and Iron-rich Tholeiitic Lavas of Munro Township, Northeast Ontario. *Journal of Petrology* **18**, 319-369.

Arndt, N. T. & Nisbet, E. G. (1982). What is a komatiite? In: Arndt, N. T. & Nisbet, E. G. (eds) *Komatiites*. London, UK: George Allen & Unwin, Ltd., pp. 19-27.

Ashton, K. E. (1988). Precambrian geology of the southeastern Amer Lake area (66H/1); near Baker Lake, N.W.T. Ph.D. thesis, Queen's University, Kingston, Ont.

Berman, R. G., Sanborn-Barrie, M., Stern, R. A. & Carson, C. J. (2005). Tectonometamorphism at *ca*. 2.35 and 1.85 Ga in the Rae Domain, western Churchill Province, Nunavut, Canada: insights from structural, metamorphic and *in situ* geochronological analysis of the southwestern Committee Bay Belt. *Canadian Mineralogist* **43**, 409-442.

Bethune, K. M. & Scammell, R. J. (2003). Geology, geochronology, and geochemistry of Archean rocks in the Eqe Bay area, north-central Baffin Island, Canada: constraints on the depositional and tectonic history of the Mary River Group of northeastern Rae Province. *Canadian Journal of Earth Sciences* **40**, 1137-1167.

Carson, C. J., Berman, R. G., Stern, R. A., Sanborn-Barrie, M., Skulski, T. & Sandeman, H. A. I. (2004). Age constraints on the Paleoproterozoic tectonometamorphic history of the Committee bay region, western Churchill Province, Canada: evidence from zircon and in situ monazite SHRIMP geochronology. *Canadian Journal of Earth Sciences* **41**, 1049-1076.

Davis, W. J. & Zaleski, E. (1998). Geochronological investigations of the Woodburn Lake Group, western Churchill Province, Northwest Territories: preliminary results. In: Radiogenic age and isotopic studies: Report 11. Geological Survey of Canada, Current Research 1998-F, pp. 89-97.

Frisch, T. (1982). Precambrian geology of the Prince Albert hills, western Melville Peninsula, Northwest Territories. Geological Survey of Canada, Bulletin 346.

Frisch, T. & Parrish, R. R. (1992). U-Pb zircon ages from the Chantrey Inlet area, northern District of Keewatin, Northwest Territories. In: Radiogenic age and isotopic studies: Report 5. Geological Survey of Canada, Paper 91-2, pp. 35-41.

Hanmer, S., Parrish, R., Williams, M. L. & Kopf, C. (1994). Striding-Athabasca mylonite zone: Complex Archean deep-crustal deformation in the East Athabasca mylonite triangle, northern Saskatchewan. *Canadian Journal of Earth Sciences* **31**, 1287-1300.

Hartlaub, R. P., Heaman, L. M., Ashton, K. E. & Chacko, T. (2004). The Archean Murmac Bay Group: evidence for a giant Archean rift in the Rae Province, Canada. *Precambrian Research*. **131**, 345-372.

Heaman, L. M., Erdmer, P. & Owen, J. V. (2002). U-Pb geochronologic constraints on the crustal evolution of the Long Range Inlier, Newfoundland. *Canadian Journal of Earth Sciences*. **39**, 845-865.

Henderson, J. B. & Loveridge, W. D. (1990). Inherited Archean zircon in the Proterozoic Thelon Tectonic Zone: U-Pb geochronology of the Campbell granite, south of McDonald fault, District of Mackenzie, Northwest Territories. In: Radiogenic age and isotopic studies: Report 3. Geological Survey of Canada, Paper 89-2, pp. 63-70.

Henderson, J. B. & Thériault, R. J. (1994). U-Pb zircon evidence for circa 3.1 Ga crust south of the McDonald Fault, northwestern Canadian Shield, Northwest Territories. In: Radiogenic age and isotopic studies: Report 8. Geological Survey of Canada, Current Research 1994-F, pp. 43-47.

Heywood, W. W. (1961). Geological notes, Northern District of Keewatin. Geological Survey of Canada, Paper 61-18.

Heywood, W. W. (1967). Geological notes, northeastern District of Keewatin and southern Melville Peninsula, District of Franklin, Northwest Territories (part 46, 47, 56, 57). Geological Survey of Canada, Special Paper 66-40.

Jackson, G. D. (1966). Geology and mineral possibilities of the Mary River region, northern Baffin Island. *Canadian mining Journal* **87**, 57-61.

Jackson, G. D., Hunt, P. A., Loveridge, W. D. & Parrish, R. R. (1990). Reconnaissance geochronology of Baffin Island, N.W.T. In: Radiogenic age and isotopic studies: Report 3. Geological Survey of Canada, Paper 89-2, pp. 123-148.

Jackson, G. D. & Taylor, F. C. (1972). Correlation of major Aphebian rock units in the Canadian Shield. *Canadian Journal of Earth Sciences* **9**, 1650-1699.

Jaffey, A. H., Flynn, K. F., Glendenin, L. E., Bentley, W. C. & Essling, A. M. (1971). Precision measurement of half-lives and specific activities of ^{235}U and ^{238}U. *Physics Review* **4**, 1889-1906.

Johnstone, S. E., Lin, S. & Sandeman, H. (2002). Significance of the Walker Lake shear zone with respect to regional deformation in the Committee Bay belt, central mainland, Nunavut. In: Current Research. Geological Survey of Canada, Paper 2002-C15.

Kjarsgaard, B. A., Kerswill, J. A. & Jenner, G. A. (1997). Lihostratigraphic and metallogenic implications of komatiite-banded iron formation-felsic volcanic rocks of the Archean Woodburn Lake group, Pipedream Lake, central Churchill Province, Northwest Territories. In: Current Research. Geological Survey of Canada, Paper 1997-C, pp. 101-110.

Krogh, T. E. (1973). A low-contamination method for hydrothermal decomposition of zircon and extraction of U and Pb for isotopic age determinations. *Geochimica et Cosmochimica Acta* **37**, 485-494.

Krogh, T. E. (1982). Improved accuracy of U-Pb zircon ages by the creation of more concordant systems using an air abrasion technique. *Geochemica et Cosmochimica Acta* **46**, 637-649.

Le Bas, M. J. (2000). IUGS Reclassification of the High-Mg and Picritic Volcanic Rocks. *Journal of Petrology* **41**, 1467-1470.

LeCheminant, A. N. & Roddick, J. C. (1991). U-Pb zircon evidence for widespread 2.6 Ga felsic magmatism in the central Disrict of Keewatin, N.W.T. In: Radiogenic age and isotopic studies: Report 4. Geological Survey of Canada, Paper 90-2, pp. 91-99.

Ludwig, K. R. (1992). ISOPLOT – a plotting and regression program for radiogenic isotope data, version 2.57. U.S. Geological Survey Open File report 91, p. 445.

MacHattie, T. G., Heaman, L., Sandeman, H., Sanborn-Barrie, M., Skulski, T. & Creaser, R. A. (2002*a*). Stratigraphic relations between basalt, komatiite and quartzite in the Archean Prince Albert Group, Committee Bay greenstone belt, central mainland

Nunavut, Canada. In: Program with Abstracts, Yellowknife Geoscience Fourm, Yellowknife, N.W.T.

MacHattie, T. (2002*b*). Physical volcanology of komatiite in the Laughland and Walker Lake areas, Committee Bay belt, Nunavut. In: Current Research. Geological Survey of Canada, Paper 2002-C14.

MacHattie, T. G., Heaman, L., Creaser, R. A., Skulski, T. & Sandeman, H. (2003*a*). Geochemical and Nd isotopic signature of mafic and ultramafic magmatism in the Archean Prince Albert Group, Committee Bay greenstone belt, central mainland Nunavut, Canada. In: Program with Abstracts, Yellowknife Geoscience Fourm, Yellowknife, N.W.T.

MacHattie, T. G., Heaman, L., Creaser, R. A., Skulski, T. & Sandeman, H. (2003*b*). Chemical and stratigraphic relationships between basalt and komatiite in the Archean Prince Albert group, Churchill Province, Nunavut. In: Program with Abstracts, Geological Association of Canada-Mineralogical Association of Canada annual meeting, Vancouver, B.C.

Persons, S. S. (1988). U-Pb geochronology of Precambrian Rocks in the Beaverlodge Area, Northwestern Saskatchewan. M.Sc. thesis, University of Kansas.

Roddick, J. C., Henderson, J. R. & Chapman, H. J. (1992). U-Pb ages from the Archean Whitehills-Tehek lakes supracrustal belt, Churchill Province, District of Keewatin, Northwest Territories. In: Radiogenic age and isotopic studies: Report 6. Geological Survey of Canada, Paper 92-2, pp. 31-40.

Sanborn-Barrie, M., Sandeman, H., Skulski, T., Brown, J., Young, M., MacHattie, T., Deyell, C., Carson, C., Panagapko, D. & Byrne, D. (2003). Structural geology of the northeastern Committee Bay belt, Ellce Hills area, central Nunavut. In: Current Research. Geological Survey of Canada, Paper 2003-C23.

Sanborn-Barrie, M., Skulski, T., Sandeman, H., Berman, R., Johnstone, S., MacHattie, T. & Hyde, D. (2002). Structural and metamorphic geology of the Walker Lake-Arrowsmith River area, Committee Bay belt, Nunavut. In: Current Research. Geological Survey of Canada, Paper 2002-C12.

Sandeman, H. A., Brown, J. A., Greiner, E., Hyde, D., Johnstone, S., MacHattie, T. G., Studnicki-Gizbert, C. & Plaza, D. (2001*a*). Geology, Laughland Lake, Nunavut. Geological Survey of Canada, Open File Map 4190, scale 1:100 000.

Sandeman, H. A., Brown, J., Studnicki-Gizbert, C., MacHattie, T., Hyde, D., Johnstone, S., Greiner, E. & Plaza, D. (2001*b*). Bedrock mapping in the Committee Bay Belt, Laughland Lake area, central mainland, Nunavut. In: Current Research. Geological Survey of Canada, Paper 2001-C12.

Sandeman, H. A., Skulski, T. & Sanborn-Barrie, M. (2004). Geology, Ellice Hills, Nunavut. Geological Survey of Canada, Open File Map1794, scale 1:100 000.

Sandeman, H. A., Studnicki-Gizbert, C., Brown, J. & Johnstone, S. (2001*c*). Regional structural and metamorphic geology of the Committee Bay belt, Laughland Lake area, central mainland, Nunavut. In: Current Research. Geological Survey of Canada, Paper 2001-C13.

Schau, M. (1977). Komatiites and quartzites in the Archean Prince Albert Group. In: Baragar, W. R. A., Coleman, L. S. & Hall, J. M. (eds) *Volcanic Regimes in Canada*. Geological Association of Canada Special Publication 16, pp. 341-354.

Schau, M. (1982). Geology of the Prince Albert Group in parts of Walker Lake and Laughland Lake map areas, District of Keewatin. Geological Survey of Canada, Bulletin 337.

Scott, D. J., St-Onge, M. R. & Corrigan, D. (2003). Geology of the Archean Rae Craton and Mary River Group and the Paleoproterozoic Piling Group, central Baffin Island, Nunavut. In: Current Research. Geological Survey of Canada, Paper 2003-C26.

Simonetti, A., Heaman, L. M., Hartlaub, R. P., Creaser, R. A., MacHattie, T. G. & Böhm, C. (2005). U-Pb dating by laser ablation-MC-ICP-MS using a new multiple ion counting-faraday collector array. *J. Anal. At. Spectrom.* **20**, 677-686.

Skulski, T., Sanborn-Barrie, M. & Sandeman, H. (2003*a*). Geology, Walker Lake and Arrowsmith River Area, Nunavut. Geological Survey of Canada, Open File Map 3777, scale 1:100 000.

Skulski, T., Sandeman, H., MacHattie, T., Sanborn-Barrie, M., Rayner, N., & Byrne, D. (2003*b*). Tectonic setting of 2.73-2.7 Ga Prince Albert Group, Churchill Province, Nunavut. In: Program with Abstracts, Geological Association of Canada-Mineralogical Association of Canada annual meeting, Vancouver, B.C.

Skulski, T., Sandeman, H., Sanborn-Barrie, M., MacHattie, T., Hyde, D., Johnstone, S., Panagapko, D. & Byrne, D. (2002). Contrasting crustal domains in the Committee Bay belt, Walker Lake-Arrowsmith River area, central Nunavut. In: Current Research. Geological Survey of Canada, Paper 2002-C11.

Skulski, T., Sandeman, H., Sanborn-Barrie, M., MacHattie, T., Young, M., Carson, C., Berman, R., Brown, J., Rayner, N., Panagapko, D., Byrne, D. & Deyell, C. (2003*c*). Bedrock geology of the Ellice Hills map area and new constraints on the regional geology of the Committee Bay area, Nunavut. In: Current Research. Geological Survey of Canada, Paper 2003-C22.

Stacey, J. S. & Kramers, J. D. (1975). Approximation of terrestrial lead isotope evolution by a two-stage model. *Earth and Planetary Science Letters* **26**, 207-221.

Thériault, R. J., Henderson, J. B. & Roscoe, S. M. (1994). Nd isotopic evidence for early to mid-Archean crust from high grade gneisses in the Queen Maud Block and south of the McDonald Fault, western Churchill Province, Northwest Territories. In: Radiogenic age and isotopic studies: Report 8. Geological Survey of Canada, Current Research 1994-F, pp. 37-42.

Van Schmus, W. R., Persons, S. S., Macdonald, R. & Sibbald, T. I. I. (1986). Preliminary results from U-Pb geochronology of the Uranium City Region. In: Summary of Investigations. Saskatchewan Geological Survey, Saskatchewan Energy and Mines, Miscellaneous Report 86-4, pp. 108-111.

Wodicka, N., St-Onge, M. R., Scott, D. J. & Corrigan, D. (2002). Preliminary report on the U-Pb geochronology on the northern margin of the Trans-Hudson Orogen, central Baffin Island, Nunavut. In: Radiogenic age and isotopic studies: Report 15. Geological Survey of Canada, Current Research 2002-F7.

Young, M. D., Sandeman, H., Berniolles, F. & Gertzbein, P. M. (2004). A preliminary stratigraphic and structural geology framework for the Archean Mary River Group, northern Baffin Island (NTS 37G), Nunavut. In: Current Research. Geological Survey of Canada, Paper 2004-C1.

Zaleski, E., Davis, W. J. & Sandeman, H. A. (2001*a*). Continental extension, mantle magmas and basement-cover relationships. In: Extended Abstracts, Proceedings of the 4th International Archean Symposium, Perth, Australia, pp. 374-376.

Zaleski, E., L'Heureux, R. L., Duke, N., Wilkinson, L. & Davis, W. J. (1999). Komatiitic and felsic volcanic rocks overlain by quartzite, Woodburn Lake group, Meadowbank River area, western Churchill Province, Northwest Territories (Nunavut). In: Current Research. Geological Survey of Canada, Paper 1999-C, pp. 9-18.

Zaleski, E., Pehrsson, S. J., Davis, W. J., Greiner, E., L'Heureux, R., Duke, N. & Kerswill, J. A. (2001*b*). Geology, Half Way Hills to Whitehills Lake area, Nunavut. Geological Survey of Canada, Open File Map 3697, scale 1:50 000.

Chapter 3. The Archean Prince Albert group (PAg), Central and Northeastern Rae domain, Nunavut, Canada: Evidence for an Extensional Continental Margin Setting

INTRODUCTION

The volcanic and sedimentary sequences preserved in Archean greenstone belts record tectonic and magmatic processes operative on the early Earth. Geochemical, petrological and isotopic studies of mafic and ultramafic rocks have provided invaluable insights into the thermal state (Nisbet *et al.*, 1993; Grove *et al.*, 1999) and chemical composition (Chase & Patchett, 1988; Stein & Hofmann, 1994) of the Archean mantle. Overwhelmingly, but not exclusively, the formation of Archean mafic-ultramafic volcanic successions have been linked with mantle plumes (e.g. Campbell *et al.*, 1989; Campbell & Griffiths, 1993; Herzberg, 1995; Arndt *et al.*, 1997; Walter, 1998; Sproule *et al.*, 2002). In plume models, volcanic successions are interpreted as either remnants of accreted oceanic plateau (e.g. Storey *et al.*, 1991; Arndt *et al.*, 1997; Puchtel *et al.*, 1998; Kerr *et al.*, 2000), or alternatively, if evidence of a continental influence is present, such as the preservation of zircon xenocrysts in mafic or ultramafic lavas (e.g. Compston *et al.*, 1986), comparisons are drawn with continental flood basalt provinces and continental rifting (Nelson, 1992; Blake, 1993; Blenkinsop *et al.*, 1993; Hunter *et al.*, 1998; Arndt, 1999; Cousens, 2000). A potential limitation of some studies concerned with the geodynamic setting(s) of mafic-ultramafic volcanic successions, and the interrelated conditions of melt generation within the mantle, is that geodynamic models are often based upon the interpretation of geochemical data obtained from mafic and/or ultramafic magmas. Many mafic-ultramafic volcanic successions also possess intercalated felsic volcanic rocks and chemical and/or clastic sedimentary rocks that retain valuable information concerning the setting of volcanism (e.g. ca. 2.7 Ga Ngezi Group, Belingwe greenstone belt; Wilson *et al.*, 1995; Hunter *et al.*, 1998) but are often ignored. Moreover, because tectonic processes operate on large (spatial and temporal) scales, the regional chronostratigraphic context of a particular mafic-ultramafic volcanic succession, and a knowledge of the full extent and duration of both the succession and regional scale magmatism are essential to developing sound geodynamic models.

This chapter and the following one (see Chapter 4) present the first geochemical and isotopic data for mafic, ultramafic and felsic volcanic rocks collected from a recently discovered, exceptionally well-preserved, and extensive (> 300 km^2 and up to ~3 km thick) ca. 2.7 Ga volcanic succession dominated by large volumes of komatiite located within the Canadian Arctic. Detailed mapping and sampling of this volcanic succession in conjunction with high-precision U-Pb zircon age dating of intercalated felsic volcanic rocks has established the relative and absolute volcanic stratigraphy and a ca. 2730 Ma age for mafic-ultramafic volcanism (see Chapter 2). On a more regional scale, this volcanic succession forms the basal sequence to the Prince Albert group (PAg), a ~600 km long (Fig. 3-1), clastic-dominated supracrustal belt located within the central/northeastern Rae domain of the northeastern Canadian Shield that is characterized by a unique orthoquartzite-komatiite lithological association (Schau, 1977; 1982).

New U-Pb zircon age constraints from a ~300 km long segment of the PAg (see Fig. 2-9 in Chapter 2) have confirmed earlier suppositions (e.g. Jackson & Taylor, 1972) that the PAg is a component of a much larger (~1400 km long and up to ~400 km wide) northeasterly-trending network of orthoquartzite-komatiite associated supracrustal belts located within the central and northeastern Rae domain (Fig. 3-1). Moreover, these data indicate that the initiation of magmatism along this ~1400 km long corridor was nearly synchronous; occurring within a narrow, < 5 m.y. window between ca. 2735-2730 Ma (see Fig. 2-9 in Chapter 2 and references therein). The extensive and well-preserved ca. 2730 Ma mafic-ultramafic volcanic succession of the lower PAg provides important insights into the tectonic and magmatic processes responsible for the formation of this vast mafic-ultramafic magmatic province. In this Chapter we present the geochemistry and Nd isotope compositions for intermediate-felsic, mafic and ultramafic volcanic rocks of the lower PAg to constrain its tectonic setting and the nature of the PAg basement. In addition, U-Pb age results are presented for xenocrystic zircon recovered from two dacite units. The petrogenesis of intercalated felsic volcanic rocks is investigated and some of the genetic relationships between basalt and komatiite are established. The chemical stratigraphy and spatial/temporal relationships between contaminated and uncontaminated rocks provides insights into the complex interactions between mantle-derived magmas and the crust.

REGIONAL ARCHEAN GEOLOGY OF THE CENTRAL AND NORTHEASTERN RAE DOMAIN

The Archean geological record preserved within the central and northeastern Rae domain of the northern Canadian Shield in Nunavut (Fig. 3-1) is dominated by Neorchean crust formed directly or indirectly in association with one of two, temporally and compositionally distinct, regionally recognized large igneous provinces. The most prominent magmatic province within the region, and the focus of this study, is a ca. 2735-

2690 Ma (see Fig. 2-9 in Chapter 2), predominantly mafic-ultramafic in composition, and forms the volcanic component of an extensive, ~1400 km long and up to ~400 km wide, northeasterly-trending network of co-genetic, clastic-dominated supracrustal belts (Fig. 3-1). These belts are characterized, in part, by their unique orthoquartzite-komatiite lithological associations as well as locally substantial volumes of komatiite (Schau, 1977, 1982; Chapter 2 and references therein). The younger, less prominent, but considerably more voluminous magmatic province within the region is ca. 2620-2580 Ma (e.g. LeCheminant & Roddick, 1991), and is comprised of intermediate-felsic plutonic rocks which dominate the crust within and adjacent to the crustal corridor containing the ca. 2735-2690 Ma supracrustal belts.

Although rare, relicts of crust older than ca. 2735 Ma are recognized within the central and northeastern Rae domain. Within the Baker Lake area in mainland Nunavut, and on northern Baffin Island, ca. 2775-2870 Ma intermediate-felsic plutonic rocks are recognized as basement components to the WLg and MRg (Fig. 3-1; Jackson *et al.*, 1990; Zaleski *et al.*, 2001; Wodicka *et al.*, 2002; Bethune & Scammell, 2003). Crust older than ca. 2870 Ma within the region is situated ~200-300 km west-southwest of the WLg and southern PAg segments, where a ~300 km segment of older to ancient crust (Fig. 3-1) is imaged by: (1) undated granitoids that possess depleted mantle Nd model ages between ca. 2.95-3.90 Ga (Thériault *et al.*, 1994); (2) a ca. 3.13 Ga granitoid spatially associated with the latter (Henderson & Thériault, 1994); and (3) a single ca. 3.3 Ga zircon xenocryst recovered from a Proterozoic granitoid within the same area (Henderson & Loveridge, 1990). Within the supracrustal corridor, this older to ancient crust is well-recognized by a persistent ca. 2.9-3.8 Ga detrital zircon signal within siliciclastic supracrustal rocks of the PAg, as well as those ≤ 2620-2610 Ma in age which unconformably overly the PAg (see Fig. 2-10 in Chapter 2; Skulski *et al.*, pers. com.). Only a small number of zircon xenocrysts older than the current maximum age for the basement to the supracrustal belts (ca. 2870 Ma; Zaleski *et al.*, 2001) have been identified within ca. 2.7-2.73 Ga volcanic rocks of the MRg (n=3/22 between ca. 2.91-3.0 Ga; Bethune & Scammell, 2003).

GENERAL GEOLOGY OF THE COMMITTEE BAY AREA AND CHRONOSTRATIGRAPHY OF THE PAG

The Rae domain southwest of Committee Bay (Fig. 3-1) is a northeasterly-trending region of crust underlain by greenschist- to middle amphibolite-facies sedimentary and volcanic rocks of the PAg, rare intermediate syn-volcanic plutonic rocks, and abundant, cross-cutting, ca. 2610-2580 Ma intermediate-felsic plutonic rocks (see Skulski *et al.*, 2003*c*; Chapter 2). Two episodes of Paleoproterozoic tectonometamorphism are recognized: (1) D_1-M_1 is associated with the formation of north-striking, easterly-dipping fabrics and the formation of upright to westerly-vergent F_1 folds and is constrained to ca. 2350 Ma (Berman *et al.*, 2005); and (2) D_2-M_2 which produced the prominent northeast-striking, southeast-dipping structural fabric and associated northwesterly-vergent folds and is constrained to ca. 1850 Ma (Carson *et al.*, 2004; Berman *et al.*, 2005). The tectonometamorphic reworking of the Committee Bay region has been attributed to collisional events on the western Rae margin (D_1-M_1), and within the Trans-Hudson Orogen (D_2-M_2) to the south (Sanborn-Barrie *et al.*, 2003; Carson *et al.*, 2004; Berman *et al.*, 2005), respectively.

Regional mapping and U-Pb zircon age dating of intermediate-felsic volcanic rocks, syn-volcanic plutonic rocks, and siliciclastic sedimentary rocks within the PAg (Fig. 3-2) suggests at least three chronostratigraphic sequences can be defined (Fig. 3-3). These include: (1) a lower, ca. 2730 Ma mafic-ultramafic volcanic succession (this study) dominated by komatiite, lesser basalt, and rare intermediate-felsic volcanic rocks and iron formation; (2) a middle, ca. 2710 Ma sequence consisting of intercalated ultramafic-felsic volcanic rocks, siliciclastic sediments and iron formation; and (3) an upper, ≤ ca. 2690 Ma sequence dominated by siliciclastic sedimentary rocks with lesser iron formation and komatiite (see Skulski *et al.*, 2003*c*; Chapter 2).

STRATIGRAPHY, VOLCANOLOGY, AND PETROGRAPHIC ASPECTS OF MAFIC, ULTRAMAFIC, AND INTERMEDIATE-FELSIC VOLCANIC ROCKS WITHIN THE LOWER PAG

Detailed mapping and high-precision U-Pb zircon age dating of felsic volcanic rocks within the lower PAg, as well as a detailed account of the physical volcanology within the lower PAg are reported in Chapter 2 and are summarized below. The lower PAg is located within the Laughland Lake area and on the opposing, northeast and southwest margins of a cross-cutting, ca. 2718 Ma tonalite/granodiorite pluton (Fig. 3-2; Skulski *et al.*, 2002), in areas informally referred to as the northeast (NVZ) and southwest volcanic zones (SVZ), respectively (see Chapter 2). Within both zones, an unequal distribution of mafic and ultramafic volcanic rocks provided the basis for a subdivision of the lower PAg into a lower, ~1 km thick volcanic horizon comprised predominantly of basalt (~4-13 wt.% MgO) and an upper, more voluminous, ~2 km thick horizon dominated by komatiite ($\geq$ 25 wt.% MgO) with lesser volumes of intercalated basalt (mainly ~8-13 wt.% MgO). High-precision U-Pb zircon ages of 2729.5 ± 0.8 Ma obtained for dacite within the basalt horizon and 2729.5 ± 0.9 Ma for dacite within the komatiite horizon (Fig. 3-2 and 3-3) confirmed that, although sharply defined in the field, the compositional transition from basalt- to komatiite-dominated volcanism occurred rapidly (Chapter 2).

As rocks within the N- and SVZ have been subjected to greenschist- to amphibolite-facies metamorphism, the primary mineralogy of mafic and ultramafic volcanic rocks has been completely replaced by secondary mineral assemblages. Original pyroxene crystals are replaced by amphiboles (tremolite-actinolite) and olivine by either serpentine or chlorite. In most instances, however, this replacement is clearly pseudomorphic in nature such that the original texture and mineralogy can be readily recognized at the scale of the thin section to outcrop (e.g. see Chapter 2). For these reasons, reference will be made to the primary mineralogy in the following discussion.

Basalt

Basaltic rocks, when texturally intact, are composed of variable amounts of stubby to acicular (up to > 500 μm in longest dimension) clinopyroxene, interstitial anhedral plagioclase, and minor amounts of Fe-Ti oxides (e.g. Fig. 3-4(a)). Within the exceptionally well-preserved basalt sample TM0-239-B, pyroxene crystals (now actinolite) ranging between > 1 mm to < 100 μm in the longest dimension possess readily identifiable compositional zoning (Fig. 3-4(a)).

Komatiite

Komatiite flows within the lower PAg consist of both spinifex-textured and spinifex-free lava flows that range from < 0.3 to > 100 m in total thickness (see Chapter 2). Samples in this study were collected from the southeastern portion of the NVZ (Fig. 3-2), and from spinifex-textured flows that are < 2 m thick. Most samples included quenched lava flow tops and/or fine grained random and platy olivine spinifex, although some cumulates were also collected. Lava flow tops are typically < 5 cm thick and consist of a network of polyhedral fractures and numerous ~0.5-2.5 cm spheroids of rapidly cooled komatiite set in a devitrified glassy matrix containing numerous cuspate glassy shards. Spinifex-textures developed in the upper portions of these flows consist of combinations of random to acicular and bladed olivine crystals (e.g. Fig. 3-4(b)) separated by plumose to spherulitic clinopyroxene, dendritic chromite, and interstitial glass. The cumulate-textured samples consist mainly of polyhedral olivine and lesser interstitial glass, chromite and minor sulfide.

Intermediate-felsic volcanic rocks

Intermediate-felsic volcanic rocks (andesite-dacite; ~60-70 wt.% SiO_2 and ≤ to 5 wt.% $Na_2O + K_2O$ (Table 3-1)) are a comparatively minor manifestation of the volcanism within the lower PAg, although occur within both volcanic zones and horizons (Fig. 3-2). Within the SVZ basalt horizon, andesite-dacite lavas (samples T-3321 and T-3319-B) are associated with intermediate volcanic breccias containing cm-sized fragments of basalt (e.g. Fig. 2-5(b) in Chapter 2). Andesite sample T-3321 contains < 1 cm long hornblende and plagioclase phenocrysts whereas dacite T-3319-B is characterized by its distinctive <

0.5 cm blue-grey quartz phenocrysts. Within the NVZ komatiite horizon, plagioclase-phyric dacite (sample H-1337; see Fig. 2-5(i) in Chapter 2) is associated with intermediate, heterolithic volcanic breccias containing both basaltic and felsic volcanic rock fragments.

GEOCHEMISTRY

The major and trace element compositions of mafic, ultramafic, and felsic volcanic rocks collected within the lower PAg and discussed in this study are listed in Table 3-1 and plotted in Figs. 3-5 to 3-9. The analytical methods, instrumentation used, and an assessment of precision and accuracy of geochemical data are discussed in Appendix A. The trace element compositions of the lavas are emphasized in this study for the following reasons: (1) elevated $(Th/Nb)_N$ ratios (≥ to >> 1) with or without concomitant light rare earth element (LREE) enrichment is the principal and, in fact, only basis by which the mafic-ultramafic volcanic rocks included in this study can be distinguished from similarly differentiated magmas within the lower PAg (e.g. Fig. 3-5 and later discussion); and (2) trace elements allow for a further subdivision of the high $(Th/Nb)_N$ volcanic rocks not possible using major elements (e.g. Fig. 3-6).

The trace elements emphasized in this study include: Th, Nb, P, Zr, Hf, Ti, Y and the rare earth elements (REE), which have been shown to be some of the least-mobile trace elements at low to moderate metamorphic grades (e.g. Lécuyer *et al.*, 1994). That said, no trace element can be considered completely immobile, a caveat especially true for metamorphosed Archean komatiite (see Lahaye *et al.*, 1995; Lahaye & Arndt, 1996). Because, trace element mobility involving the aforementioned trace elements does appear to have occurred in some samples discussed in this study, throughout the discussion an emphasis is placed on the overall trace element patterns/signatures displayed by a significant number of widely dispersed samples that, in all likelihood, is not possible to produce via fluid alteration processes. This approach is also used when discussing major element variation.

Trace elements

As a group, the mafic, ultramafic and intermediate-felsic volcanic rocks discussed in this chapter possess a rather unique trace element signature that distinguishes them from the majority of mafic and ultramafic lavas found within the lower PAg. They possess noticeably elevated Th (+/- LREE) relative to Nb, features which can be produced via crustal contamination. To distinguish between lavas with a recognizable potential to have interacted with typical continental crust from uncontaminated or minimally contaminated lavas, the most sensitive trace element ratio for monitoring crustal contamination is the primitive mantle normalized $(Th/Nb)_N$ ratio (e.g. Jochum *et al.*, 1991). We use $(Th/Nb)_N$ to discriminate between potentially contaminated and minimally to uncontaminated lavas, and thus, subdivide the lower PAg volcanism into two first-order geochemical groups, high and low $(Th/Nb)_N$ magmas, respectively (Fig. 3-5).

Using a primitive mantle normalized $(Th/Nb)_N$ ratio of ~1 as an approximate guide/cutoff, high $(Th/Nb)_N$ magmas recognized within the lower PAg (Fig. 3-5) include all the intermediate-felsic volcanic rocks ($(Th/Nb)_N \geq 1.9$), a significant portion of basalt ($(Th/Nb)_N \geq 1.3$) and only a small fraction of the komatiite ($(Th/Nb)_N \geq 1$). The high

$(Th/Nb)_N$ magmas can be further subdivided using their major (e.g. intermediate-felsic, mafic, and ultramafic) and trace element compositions, in particular their combined $(Th/Nb)_N$, $(Ce/Sm)_N$, and $(Gd/Yb)_N$ systematics.

Basalt

The lower PAg high $(Th/Nb)_N$ basalt samples can be subdivided into two distinct geochemical groups (group-1 and -2) based on their combined $(Th/Nb)_N$, $(Ce/Sm)_N$, and $(Gd/Yb)_N$ compositions. Group-1 basalt samples have a wide range in MgO content (mainly ~8-13 but up to ~19 wt.%; Table 3-1) and uniform primitive mantle normalized incompatible trace element patterns (Fig. 3-6) . These basalts are characterized by modest degrees of LREE- ($(Ce/Sm)_N$ ~1.3-1.5) and middle rare earth element (MREE)-enrichment $(Gd/Yb)_N$ ~1.2-1.5), moderately elevated $(Th/Nb)_N$ ratios (~1.3-1.7), and well-developed negative high-field-strength element (HFSE) anomalies at Nb, P and Ti relative to the bounding REE (Fig. 3-6).

The samples included in group-2 possess a more restricted range in MgO content (~7-9 wt.%; Table 3-1) and incompatible trace element compositions that are unlike any of the group-1 samples (Figs. 3-6 to -8). Compared to group-1 basalts, the group-2 basalt samples are characterized by highly variable $(Ce/Sm)_N$ (~0.8-1.3; Fig. 3-7(a)) and relatively high $(Th/Nb)_N$ (~1.7-8.8; Fig. 3-8). Samples within this group also display a minimal MREE-enrichment ($(Gd/Yb)_N$ ~1.1-1.2) compared with similarly differentiated group-1 samples (~1.3-1.5; Fig. 3-7(b)).

Komatiite

Similar to the subdivision of basalt, high $(Th/Nb)_N$ (i.e. >1) komatiite can be divided into two geochemical groups (group-1 and -2) based on distinctive trace element compositions (Fig. 3-6). The group-1 komatiite samples were collected from a single outcrop containing a several ~1-2 m thick spinifex-textured flows, and include samples of flow tops, random and plate spinifex, and one cumulate (Table 3-1). The group-1 komatiite are characterized by moderate LREE-depletion ($(Ce/Sm)_N$ ~0.6-0.8), minimal MREE-enrichment ($(Gd/Yb)_N$ ~1.1-1.2) and variable $(Th/Nb)_N$ ratios ranging from values of ~1 up to 1.5 (Fig. 3-6). The group-2 komatiite samples were also collected from a single outcrop containing a number of ~1-2 m thick spinifex-textured flows, and include four cumulate samples. The group-2 komatiite are distinguished from their group-1 counterparts by a greater degree of LREE-enrichment (e.g. $(Ce/Sm)_N$ ~0.9-1.3 versus ~0.6-0.8; Fig. 3-7a), overlapping but generally higher $(Th/Nb)_N$ ratios (~1.2-2.4 versus ~1.0-1.5), and pronounced HREE-enrichment ($(Gd/Yb)_N$ ~0.7-0.9 versus ~1.1-1.2; Fig. 3-7(b)). Although significantly more pronounced for the group-2 komatiite, most group-1 and -2 komatiite possesses positive HFSE anomalies at P, Zr, Hf, and Ti relative to the bounding REE (Fig. 3-6).

Intermediate-felsic volcanic rocks

The intermediate-felsic volcanic rocks all possess highly enriched incompatible trace element profiles punctuated by pronounced negative HFSE anomalies relative to the bounding REE at Nb, P and Ti (Fig. 3-6). These lavas are easily distinguished from their high $(Th/Nb)_N$ mafic and ultramafic counterparts by their elevated incompatible trace element contents (e.g. $(Ce)_N$ ~19-26 versus $\leq$ 10; Fig. 3-6) and more pronounced LREE-enrichment ($(Ce/Sm)_N$ ~2.4-2.6 versus ≤ 1.5; Fig. 3-7a) and HREE-depletion ($(Gd/Yb)_N$ ~1.7-2.0 versus ≤ 1.5; Fig. 3-7b).

Major elements

Selected major and minor element MgO variation diagrams for the high $(Th/Nb)_N$ volcanic rocks involving SiO_2, TiO_2, Al_2O_3, Fe_2O_3(T) and CaO are plotted in Fig. 3-9 along with the larger data set for low $(Th/Nb)_N$ basalt and komatiite collected within the lower PAg (shown as crosses in Fig. 3-9; Table 4-1 in Chapter 4). The linear regressions labeled all komatiite on the TiO_2, Al_2O_3 and CaO variation diagrams include all low $(Th/Nb)_N$ samples collected within the lower PAg (~22-40 wt.% MgO; Table 4-1 in Chapter 4).

Basalt

The distinctive trace element compositions that provided the basis for subdividing the high $(Th/Nb)_N$ basalt into two groups (e.g. Fig. 3-6), is not manifested in their major element compositions (Fig. 3-9). Apart from the overall wider range in MgO content displayed by the group-1 basalt (extending up to ~19 wt.%), equivalently differentiated group-1 and -2 basalt cannot be easily distinguished from most other low $(Th/Nb)_N$ basalt within the volcanic succession (Fig. 3-9). The major exception being the high TiO_2 contents of several of the low $(Th/Nb)_N$ basalt.

In general, the salient major element parameters that characterize the majority of group-1 and -2 basalt possessing MgO contents between ~7-13 wt.% include, relatively low SiO_2 (~48-53 wt.%) and TiO_2 (~0.7-1.0 wt.%), Al_2O_3 contents (~12-16 wt.%) that are negatively correlated with MgO, and variable CaO (~9-13 wt.%) and Fe_2O_3(T) contents (~10-14 wt.%) that do not correlate with MgO (Fig. 3-9). The two high-MgO group-1 basalt samples (~18-19 wt.%) are co-linear with lower MgO magmas on MgO variation diagrams involving TiO_2, Al_2O_3 and CaO (Fig. 3-9), but possess distinctly lower SiO_2 (~42-44 wt.%) and higher Fe_2O_3(T) contents (~16-17 wt.%).

Komatiite

As observed for basalt, the group-1 and -2 komatiite possess major element compositions that, to a large extent, overlap significantly with those of low $(Th/Nb)_N$ komatiite. However, some samples, particularly the group-2 komatiite, display some significant differences with respect to the larger komatiite data set for low $(Th/Nb)_N$ komatiite, differences which suggest significant major element mobility (Fig. 3-9).

The group-1 komatiite samples possess MgO contents between ~27-31 wt.%, and are collinear with most low $(Th/Nb)_N$ komatiite on MgO variation diagrams involving Al_2O_3 and TiO_2. These trends project toward reasonable x-axis intercepts of ~48-53 wt.% MgO suggesting olivine fractionation (removal or accumulation) control upon the concentration of these elements. Although some scatter is apparent in Fe_2O_3(T), the group-1 komatiite also overlap significantly with low $(Th/Nb)_N$ komatiite with respect to SiO_2 and CaO. The group-2 komatiite samples possess higher MgO than the group-1 komatiite (~31-35 wt.%), however, plot noticeably below the MgO-Al_2O_3 and MgO-TiO_2 regressions involving low $(Th/Nb)_N$ komatiite (Fig. 3-9) suggesting loss of MgO and/or TiO_2 and Al_2O_3. These samples also possess very high Fe_2O_3(T) and low SiO_2, compositions which are unlike any other komatiite within the lower PAg. As with most other high-MgO (>30 wt.%) komatiite, the group-2 samples appear to record systematic CaO-loss as the anomalous x-axis intercept on the MgO-CaO regression of low $(Th/Nb)_N$ komatiite (~42 wt.% MgO) is inconsistent with other chemical evidence for olivine control (Fig. 3-9).

Intermediate-felsic volcanic rocks

The intermediate-felsic volcanic rocks are easily distinguished from low-MgO basalt within the lower PAg by their high silica (~60-70 wt.%), and low $Fe_2O_3(T)$ (~5-8 wt.%) and CaO (~4-7 wt.%) contents, however, possess similar TiO_2 and Al_2O_3 contents (Fig. 3-9).

Nd isotopic data

The Nd isotopic data obtained in this study are listed in Table 3-2 and plotted in Fig. 3-10(a and b). The analytical methods, instrumentation used, and an assessment of precision and accuracy of geochemical data are discussed in Appendix A. Although a wide range in $^{147}Sm/^{144}Nd$ separates felsic, mafic, and ultramafic volcanic rocks (~0.12-0.25), all $\varepsilon Nd(2730\ Ma)$ values are positive and display a minimal amount of variation (< 2 epsilon units), ranging between +1.0 to +2.9 (Fig. 3-10a). Excluding the group-2 komatiite sample TM0-263-HS ($\varepsilon Nd(2730\ Ma)$ of +1.0), most samples are more tightly clustered, ranging between +1.6 and +2.9 (Fig. 3-10a). Taken together, these samples (9/10) yield a mean $\varepsilon Nd(2730\ Ma)$ value of +2.4 ± 1.0 (2σ standard deviation). In Fig. 3-10(b) the measured $^{143}Nd/^{144}Nd$ and $^{147}Sm/^{144}Nd$ ratios for all high $(Th/Nb)_N$ volcanic rocks are plotted on an isochron diagram. For plotting purposes, external errors include an assigned ~0.2 % error on $^{147}Sm/^{144}Nd$ and ± 0.000015 for $^{143}Nd/^{144}Nd$ (see Appendix A). A regression including the samples with εNd(2730 Ma) values between +1.6 and +2.9 yields a model-3 (MSWD = 11.2) errorchron age of 2724 ± 84 Ma, a result in excellent agreement within the known ca. 2730 Ma age for these volcanic rocks as determined by high-precision U-Pb zircon age dating of the felsic volcanic rocks T-3319-B and H-1337 (see Fig. 2-6 in Chapter 2).

U-PB ZIRCON ISOTOPIC RESULTS

During the selection of zircon for U-Pb dating by isotope dilution-thermal ionization mass spectrometry (ID-TIMS) of dacite H-1337 and T-3319-B (Chapter 2) several grains were suspected to have a xenocrystic origin based on their distinctive morphology, size, and colour characteristics. In particular, dacite H-1337 contained a significant quantity and diverse spectrum of the potentially pre-magmatic grains and, as such, was the main focus of the U-Pb zircon age dating. A representative selection of the potential zircon xenocrysts as well as grains considered indistinguishable from those previously analysed by ID-TIMS were selected and analysed from both felsic volcanic rocks (n=34 zircon; Table 3-3). The U-Pb results for both samples are plotted together on a concordia diagram and probability density histogram of $^{207}Pb/^{206}Pb$ age in Fig. 3-11. Several grains were analysed in multiple spots (n=6; Table 3-3); for these zircon, only the most concordant analyses are plotted on the concordia diagram and a mean $^{207}Pb/^{206}Pb$ age per grain was calculated and plotted on the $^{207}Pb/^{206}Pb$ age histogram. Selected post-ablation zircon images for dacite H-1337 and dacite T-3319-B (all with ~40 μm diameter ablation pits) are also displayed in Fig. 3-11.

The 34 zircon grains analysed include 28 from dacite H-1337 and 6 from dacite T-3319-B and both yielded remarkably similar age results (Table 3-3; Fig. 3-11). The U-Pb analyses display slight to moderate amounts of discordance (~4-15 %) and ^{207}Pb/^{206}Pb ages range between ca. 2722-2949 Ma. The zircon ^{207}Pb/^{206}Pb ages do not systematically correlate with the degree of discordance, however, the 5 oldest grains (> 2850 Ma in age) are amongst the most discordant (~12-15 %). The majority of zircon grains analysed have ^{207}Pb/^{206}Pb ages that are more tightly clustered between 2722 and 2810 Ma (~85 %). Within this range, two distinct age populations occur, one at ca. 2735 and the other at ca. 2775 Ma (Fig. 3-11). The ca. 2735 Ma age population consists of clear, colourless, subhedral prismatic zircon crystals (e.g. H-1337 grains #10, 14, and 15; Fig. 3-11) that are indistinguishable from those analysed by ID-TIMS and are interpreted to record the 2730 Ma crystallization ages obtained for the volcanic rocks by ID-TIMS (see Fig. 2-6 in Chapter 2). The oldest (> 2850 Ma) grains form two small age groups, one at ca. 2870 (n=3) and the other at ca. 2950 Ma (n=2).

The majority of pre-ca. 2730 Ma zircon xenocrysts from both samples possess ^{207}Pb/^{206}Pb ages that cluster between ca. 2750-2800 Ma (Table 3-3). These zircon grains are morphologically diverse (Fig. 3-11) and include large (several hundred μm long), pale pink zircon with subhedral external forms (e.g. grains #6, 9, and 13), relatively small, clear and colourless, strongly resorbed zircon (e.g. H-1337 grains #27 and 28, and T-3319-B grains #1, 2, and 3), and large, platy zircon fragments (e.g. grain #19). The small number of older zircon recovered from dacite H-1337 (e.g. 5 grains > 2850 Ma) are variable in size, morphology, and colour (Fig. 3-11) and include a highly fractured grain fragment (e.g. grain # 7), a long (~300 μm) subhedral prismatic grain (e.g. grain #24;

image not shown), and a fractured subrounded grain (e.g. grain #20). Considering the average 2σ external error of ~20 m.y. for $^{207}Pb/^{206}Pb$ ages reported in this study, the origin of zircon grains #11 (2743 Ma) and #18 (2746 Ma) is equivocal.

NATURE OF THE PAG BASEMENT AND THE ORIGIN OF THE INTERMEDIATE-FELSIC VOLCANIC ROCKS

The documentation of zircon xenocrysts within dacite T-3319-B and H-1337 (Fig. 3-11) provides direct, unequivocal evidence that the intercalated intermediate volcanic rocks, and by inference the basalt and komatiite within the lower PAg, were erupted upon a pre-existing substrate of continental crust. By integrating the age information obtained from the zircon xenocrysts with the major, trace element, and Nd isotopic compositions of the intermediate-felsic magmas, important insights into nature of the PAg basement can be obtained.

Xenocrystic zircon constraints

The zircon crystals analysed in this study consist of two principal types, primary magmatic zircon interpreted to have crystallized directly from the felsic magmas at ca. 2730 Ma, and older xenocrystic zircon. The dominant population of xenocrystic zircon grains analysed in this study are only slightly older than the 2730 Ma primary magmatic zircon. It is the origin of these zircon grains, those that comprise the prominent ca. 2750-2800 Ma population and the two older ca. 2870 Ma and 2950 Ma populations that are discussed below.

Moderate to extensive rounding coupled with frosted surface textures, typical of zircon that have experienced significant sedimentary transport, is noticeably lacking from the xenocrysts analysed in this study, in fact, many possess euhedral to subhedral external forms (e.g. H-1337 zircon #6, #9 and #13; Fig. 3-11). The variable morphology of the zircon xenocrysts, particularly those of the prominent ca. 2750-2800 Ma population is consistent with: (1) multiple modes of incorporation of the zircon xenocrysts; and (2) sourcing from igneous rocks of variable age.

The resorbed 2750-2800 Ma zircon xenocrysts are interpreted to indicate a period of zircon undersaturation within the magma and dissolution possibly related to partial melting of ca. 2750-2800 Ma crustal rocks. In contrast, the unresorbed zircon may have been encased in small crustal xenoliths/xenocrysts during the crystallization of the felsic magmas or possibly accidentally incorporated during late stage contamination. A lack of observable magmatic overgrowths on any xenocrystic zircon suggests a relatively short magmatic residence time for the xenocrysts. The older > 2850 Ma xenocrysts do not possess any unique features that provide evidence for their mode of incorporation. For the most part they are fractured, poor quality grain fragments (Fig. 3-11) and their origin is uncertain.

Major and trace element constraints

The major and trace element compositions of the intermediate-felsic volcanic rocks within the lower PAg suggest they have a unique origin with respect to the larger volumes of basalt and komatiite. Importantly, the degree of incompatible trace element fractionation observed in these magmas is unmatched by any high $(Th/Nb)_N$ basalt or komatiite (e.g. $(Ce/Sm)_N$ of ~2.4-2.6 versus ≤ to << 1.5; Fig. 3-7(a)). This precludes an origin for the intermediate-felsic magmas via crystal differentiation from a parental basalt or komatiite currently recognized within the lower PAg. Moreover, because magmatism within the volcanic succession is dominated by mantle-derived, incompatible trace element depleted, low $(Th/Nb)_N$ mafic and ultramafic magmas (e.g. Fig. 3-5), the excess LREE-enrichment and elevated $(Th/Nb)_N$ possessed by the intermediate-felsic magmas are unlikely to have a mantle origin. These observations, along with the presence of numerous ca. 2750-2800 Ma zircon xenocrysts are, however, consistent with an intra-crustal origin for these magmas.

If the intermediate-felsic magmas were generated by partial melting of continental crust, their chemical compositions can be used to constrain the composition of their source(s) depending on the degree of melting and subsequent differentiation. For example, exceptionally high degrees of crustal melting concomitant with the infiltration of large volumes of komatiite should produce primary crustal melts that more closely resemble their source in terms of major and trace element contents and incompatible trace element ratios than lower degree partial melts. Andesite T-3321 (~60 wt.% SiO_2) is presumed to more closely reflect the composition of its source because it is less differentiated than either dacite T-3319-B or H-1337 (up to ~70 wt.% SiO_2). In Fig. 3-12, the primitive mantle normalized extended trace element profile for andesite T-3321 and the average for dacite T-3319-B and H-1337 are plotted with compositional estimates for the upper and lower crust (Taylor & McLennan, 1985), average Neoarchean TTG-type crust (Condie, 2005), and the average juvenile quartz diorite (e.g. εNd(1850 Ma) of +5) from the ca. 1850-1865 Ma Wathaman batholith (MacHattie, 2002).

Although slightly more differentiated (based on the SiO_2 and incompatible element content), andesite T-3321 is remarkably similar in composition to estimates for average lower crust (Fig. 3-12). It possesses only marginally higher SiO_2 (~60 versus 55 wt.%) and greater LREE-enrichment ($(Ce/Sm)_N$ ~2.4 versus 1.8), and nearly identical $(Th/Nb)_N$ (~1.9 versus 1.5). In contrast, the more differentiated upper crust and TTG compositional estimates (~66-68 wt.% SiO_2) are both significantly more enriched in the most incompatible trace elements than either andesite T-3321 or the average dacite (Fig. 3-12). Moreover, TTG-type crust has a significantly higher $(Th/Nb)_N$ ratio (~11 versus $\leq$ 3) and is characterized by strong HREE-depletion, features not displayed by the intermediate-felsic volcanic rocks. As a group, the intermediate-felsic magmas and the Wathaman batholith volcanic arc quartz diorite are also remarkably similar in terms of SiO_2 as well as the abundance and magnitude of incompatible trace element fractionations, in particular with respect to negative HFSE anomalies at Nb, P, (+/- Zr and Hf) and Ti (Fig. 3-12).

Based on these compositional similarities, the primary process responsible for generating intermediate-felsic volcanic rocks within the lower PAg is interpreted to be partial melting of mafic-intermediate lower crustal rocks. The overall geochemical similarity between andesite T-3321 and the estimated composition of the lower crust (Fig. 3-12) suggests that the degree of crustal melting must have been very high, and suggestion that could be explained by pooling of high temperature komatiite at the crust-mantle boundary. The major and trace element compositional similarities between the intermediate-felsic volcanic rocks with established suprasubduction zone magmas (Fig.

3-12) suggests the lower PAg basement may have formed in a similar tectonic environment.

Nd isotopic constraints

If the assertion that the intermediate-felsic volcanic rocks were generated by lower crustal melting is correct, the suprachondritic whole rock initial Nd isotopic compositions of the volcanic rocks (e.g. mean εNd(2730 Ma) of +2.8; Table 3-2) require this crust to be young and juvenile. In order to reconcile the Nd isotopic data with the major and minor xenocrystic zircon age populations, only the youngest ca. 2750-2800 Ma population appears to have accurately imaged the basement, and that the older xenocrysts either: (1) do not reflect actual components of the igneous basement directly underlying the lower PAg (i.e. they may have been scavenged from unrecognized supracrustal rocks); (2) they are present but volumetrically insignificant and did not participate significantly in the production of the intermediate-felsic magmas; and/or (3) they are present but are not LREE-enriched. To graphically illustrate these options a simple model portraying the Nd isotopic evolution of a model depleted mantle and crust extracted from this model mantle at ca. 2775, 2870 and 2950 Ma (TTG-type and lower crust) is depicted in Fig. 3-13. The model depleted mantle is a second-order polynomial fit employing an εNd(0 Ma) value of +10, an εNd(4550 Ma) value of 0, an εNd(1850 Ma) of +5 (Chauvel *et al.*, 1987; Whalen *et al.*, 1999; MacHattie, 2002), and an εNd(2700 Ma) value of +2.4 (Ayer *et al.*, 2002; Polat & Münker, 2004).

The results of this simple modeling are straightforward and easily interpreted. A LREE-enriched crust extracted from the depleted mantle at ca. 2775 Ma will not evolve to an appreciably lower Nd isotopic composition than its depleted mantle source. At best, a difference of ~0.7 epsilon units can be obtained between a highly enriched TTG-type crust and the depleted mantle over such a short time period. A less-enriched composition, such as the lower crust, would differ even less from its depleted mantle source (~0.4 epsilon units) given only ~45 m.y. to evolve (Fig. 3-13). These values are indistinguishable considering the external errors on the Nd isotopic measurements of ~0.3-0.5 epsilon units (see Appendix A), and demonstrate that it is not possible to distinguish between primary ca. 2730 Ma depleted mantle derived magmas and volcanic rocks derived by melting of ca. 2775 Ma crust using Nd isotopes alone. Thus, the prominent ca. 2750-2800 Ma xenocrystic zircon population, major and trace element compositions, and suprachondritic initial Nd of the intermediate-felsic volcanic rocks collectively suggest they were derived via partial melting of lower continental crust with a mean age of ca. 2775 Ma which, in all likelihood, was extracted from the mantle at that time.

The Nd isotopic evolution depicted in Fig. 3-13 also precludes, beyond any reasonable doubt, the existence of significant quantities of LREE-enriched crust ≥ 2870 Ma in age directly beneath the lower PAg. Intermediate-felsic magmas derived entirely from juvenile ≥ 2870 Ma crust should possess εNd(2730 Ma) values at least ~1.4 epsilon units lower than the contemporaneous depleted mantle (Fig. 3-13), and not values which overlap with it. Overall, the Nd isotopic constraints combined with the small number of ≥ 2870 Ma zircon xenocrysts (n=5) is more easily reconciled if the older zircon xenocrysts were scavenged from unrecognized supracrustal rocks. This conclusion is in agreement with the Nd isotopic results obtained for both ca. 1.8 and 2.6 Ga I-type granitoid plutonic rocks which intrude portions of the PAg that yield predominantly ≤ 2.85 Ga depleted mantle Nd model ages (Skulski *et al.*, 2003*b*).

TRACE ELEMENT MODELING OF CRUST-MANTLE MIXING

Based on the evidence presented above, a continental setting is envisaged for volcanism within the lower PAg. Therefore, crustal contamination is likely the dominant process responsible for generating high $(Th/Nb)_N$ basalt and komatiite, particularly as these lavas are intercalated with larger volumes of low $(Th/Nb)_N$ basalt and komatiite (e.g. Fig. 3-5). In the following discussion, an attempt is made to replicate the unique trace element signatures of high $(Th/Nb)_N$ basalt and komatiite by employing simple two-component mixing models. For crustal end-members, andesite T-3321, the average dacite (T-3319-B and H-1337), and average Late Archean TTG (Condie, 2005) are utilized. For the parental magmas, low $(Th/Nb)_N$ komatiite and basalt within the lower PAg are utilized (see Table 3-4). For parental komatiites, averages for spinifex-textured lavas are used (see Table 3-4) and the three-fold subdivision of these low $(Th/Nb)_N$ komatiite employed in Chapter 4, using $(Gd/Yb)_N$ is followed here. This subdivision is particularly important because $(Gd/Yb)_N$ ratios for spinifex-textured low $(Th/Nb)_N$ komatiite vary continuously between ~0.8-1.3 and, as will be shown below, parental magmas possessing variable $(Gd/Yb)_N$ are required to explain the variation observed in high $(Th/Nb)_N$ magmas. The three-fold subdivision using $(Gd/Yb)_N$ includes HREE-enriched (~0.8-0.9), HREE-depleted (~1.2-1.3), and HREE-unfractionated (~1.0-1.1) parental magmas. For parental basalt, an average for incompatible trace element depleted, low $(Th/Nb)_N$ basalt is employed (see Table 3-4).

The trace element contents, and in particular the ratios $(Th/Nb)_N$, $(Ce/Sm)_N$ and $(Gd/Yb)_N$ are emphasized in the modeling because the magnitude of change in these ratios resulting from crustal contamination is highly variable but systematic (e.g. change in $(Th/Nb)_N > (Ce/Sm)_N >> (Gd/Yb)_N$) and is advantageous for assessing both the appropriate parental magma composition (e.g. HREE-depleted or -enriched komatiite) and crustal contaminant involved (e.g. TTG or lower crust). Modeling involving Nd isotopes has not been conducted because the mean εNd(2730 Ma) of virtually all high $(Th/Nb)_N$ volcanic rocks of +2.4 (Fig. 3-10(a)) is indistinguishable from the contemporaneous depleted mantle (e.g. see Ayer *et al.*, 2002; Polat & Münker, 2004) and/or the juvenile ca. 2750-2800 Ma crust suggested to underlie the lower PAg. The group-2 komatiite sample TM0-263-HS has a slightly lower εNd(2730 Ma) value of +1.0, which could reflect the involvement of older crust (e.g. > to >> 2800 Ma). However, the small amounts of crustal contamination (< 2 wt.%) necessary to explain the distinctive incompatible trace element signature of the group-2 komatiites, would require the involvement of exceptionally old crust to explain the Nd isotopic data. As there is strong evidence to suggest pervasive major element mobility has affected the group-2 komatiite (see Fig. 3-9), the Nd isotopic composition of this sample is considered suspect.

Group-1 basalt

The group-1 basalt possess relatively uniform trace element compositions (e.g. Figs. 3-6 to 3-8) considering their wide range in MgO (mainly ~8-13 but up to ~19 wt.%). This observation is inconsistent with the assimilation of crust concomitant with fractional crystallization. If this were the case, the most differentiated lavas should record higher degrees of crustal contamination, and thus higher $(Th/Nb)_N$ and $(Ce/Sm)_N$, features that are not displayed by the group-1 basalt (e.g. uniform $(Ce/Sm)_N$ in Fig. 3.7(a)). The uniform trace element composition of the group-1 basalt is more consistent with bulk mixing producing a contaminated parental magma (required to be ≥ 19 wt.% MgO) which, subsequent to mixing with crust, underwent significant olivine-dominated crystal fractionation to generate the more differentiated members of this group (e.g. those with MgO as low as ~8 wt.%). The $(Th/Nb)_N$ and $(Ce/Sm)_N$ ratios of the group-1 basalt are intermediate between all low $(Th/Nb)_N$ komatiite and andesite T-3321 (Fig. 3-8) suggesting that mixing between a komatiite and andesite magma may have been involved in their generation. A mixing relationship involving 15 wt.% andesite T-3321 and 85 wt.% average HREE-depleted komatiite (Fig. 3-14(a and b) and 3-15(a)) provides a remarkable convergence with respect to the combined $(Th/Nb)_N$, $(Ce/Sm)_N$, and $(Gd/Yb)_N$ ratios of the average group-1 basalt. This mixture yields $(Th/Nb)_N$, $(Ce/Sm)_N$, and $(Gd/Yb)_N$ ratios for a resultant magma of ~1.5, 1.3 and 1.4, values which are indistinguishable from those displayed by the average group-1 basalt of ~1.5, 1.4 and 1.4, respectively (Fig. 3-15(a)). In addition, the negative Nb, P, and Ti anomalies characterized by the group-1 basalt are manifested to similar extents in this mixture. The addition of 15 wt.% andesite T-3321 lowers the MgO content of the parental komatiite only marginally (~25 to ~22 wt.%), and is consistent with the requirement that the parental group-1 magma possess ≥ 19 wt.% MgO. However, significant crystal differentiation is required in order to generate the lower MgO members within this group, an aspect of group-1 basalt generation that will be addressed in a later section.

Group-2 basalt

The group-2 basalt possess heterogeneous $(Ce/Sm)_N$ and $(Th/Nb)_N$, however, remarkably uniform $(Gd/Yb)_N$ suggesting that, at least in part, the heterogeneity observed for the more incompatible trace elements might reflect compositional differences in the contaminants involved. Collectively the group-2 basalts are characterized by lower $(Ce/Sm)_N$ and higher $(Th/Nb)_N$ than the group-1 basalt (e.g. Fig. 3-8), a feature that suggests they have experienced lower degrees of contamination and that, on average, the contaminant(s) involved possessed higher $(Th/Nb)_N$ and $(Ce/Sm)_N$ than andesite T-3321.

The mean $(Gd/Yb)_N$ ratio of the group-2 basalt of ~1.1 is identical to that of the average low $(Th/Nb)_N$ depleted basalt suggesting, along with the LREE-depletion displayed by two of the four group-2 basalts, that it is a suitable parental magma. In Fig. 3-14(a and b), portions of three mixing curves are shown involving the average depleted basalt; one with average Late Archean TTG (Condie, 2005), a second using a modified version of this average in which the Th concentration has been increased by a factor of 1.25 (e.g. $(Th/Nb)_N$ of ~14 versus 11), and a third involving the average dacite. With respect to their combined $(Th/Nb)_N$, $(Ce/Sm)_N$, and $(Gd/Yb)_N$ systematics and trace element contents, two of the group-2 basalt samples (CS0-315 and -264-B) can be readily explained by mixing ~3-9 wt.% of the marginally modified TTG-type crust with the average depleted basalt (Fig. 3-14(a and b) and 3-15(b)). To explain the elevated $(Ce/Sm)_N$ and $(Th/Nb)_N$ of sample HS0-302 via crustal contamination of the average depleted basalt requires a contaminant more similar to the average dacite than TTG-type crust (Fig. 3-14(a)). The addition of ~10 wt.% of the average dacite can adequately reproduce the combined $(Th/Nb)_N$, $(Ce/Sm)_N$ and $(Gd/Yb)_N$ systematics and incompatible trace element contents of sample HS0-302 (Fig. 3-14(a and b) and 3-15(c)). No mixing relationship involving any plausible crustal contaminant can explain the anomalously elevated $(Th/Nb)_N$ ratio of the group-1 sample CS0-316 of ~8.8 (Fig. 3-14(a and b)). Basalt samples CS0-315 and -316 were collected from the same area and display identical primitive mantle normalized incompatible trace element profiles (Fig. 3-15(d)), so the higher Th concentration in sample CS0-316 is best explained by subsequent Th addition.

Group-1 komatiite

On average, the group-1 komatiite possess only slightly elevated $(Th/Nb)_N$ compared to the primitive mantle (~1.2) and are LREE-depleted ($(Ce/Sm)_N$ ~0.7), features suggesting very low degrees of contamination. The average $(Gd/Yb)_N$ ratio (~ 1.1) of the group-1 komatiite and a similar incompatible trace element profile suggest that the average HREE-unfractionated komatiite is a suitable parental magma (e.g. Fig. 3-15(e)). Mixing 99.5 wt.% of this komatiite with 0.5 wt.% TTG-type crust can reproduce the trace element signature of the group-1 komatiite (Fig. 3-15(e)).

Group-2 komatiite

On average, the group-2 komatiite possess higher $(Th/Nb)_N$ and $(Ce/Sm)_N$, and significantly lower $(Gd/Yb)_N$ than the group-1 komatiite. The low $(Gd/Yb)_N$ ratios (~0.8) indicate a parental magma similar to the average HREE-enriched komatiite (~0.8-0.9), as does their significant positive HFSE anomalies at Hf and Zr (e.g. Fig. 3-15(f)). Mixing 98 wt.% of the average HREE-enriched komatiite and 2 wt.% TTG-type crust yields a magma with the elevated $(Th/Nb)_N$ and $(Ce/Sm)_N$ possessed by the average group-2 komatiite (Fig. 3-14(f)). However, subsequent to contamination, olivine-accumulation is required in order to lower the incompatible trace element abundances of the contaminated magma to those observed in the group-2 komatiite. The apparent major element mobility displayed by the group-2 komatiite does not allow for the amount of olivine accumulation to be assessed, however, olivine accumulation is a process consistent with the group-2 samples being collected from the basal (largely cumulate) portions of spinifex-textured flows.

INSIGHTS INTO THE MAGMATIC DEVELOPMENT OF THE LOWER PAG

As concluded above, the intermediate-felsic volcanic rocks within the lower PAg were generated by partial melting of lower crustal rocks, and the incompatible trace element signatures of high $(Th/Nb)_N$ basalt and komatiite can be explained by ~2-15 wt.% contamination of low $(Th/Nb)_N$ basalt and komatiite recognized within the volcanic succession. Perhaps most insightful, the high $(Th/Nb)_N$ andesite and the average HREE-depleted komatiite end-member are required to generate the group-1 basalt, the predominant and most widely distributed high $(Th/Nb)_N$ basalt. Primarily using this geochemical/genetic relationship, fundamental constraints can now be placed upon portions of magmatic development of the lower PAg and insights into the nature of the relationship(s) between basalt and komatiite.

HREE-depleted komatiite, group-1 basalt, and primitive andesite association

The independent geochemical findings that: (1) the most primitive high $(Th/Nb)_N$ andesite is a partial melt of lower continental crust; (2) high-degrees of melting are required; (3) the group-1 basalt were contaminated with ~15 wt.% melt component similar in composition to primitive andesite; and (4) the parental magma to the group-1 basalt was the average HREE-depleted komatiite end-member, all suggest that the generation of lower crustal melt and the group-1 basalt are spatially, temporally, and genetically related. The simplest interpretation is that the heat required to melt the lower crust and generate the primitive andesite was supplied by emplacement/pooling of the HREE-depleted komatiite end-member near the crust-mantle boundary, that these melts mixed to form a contaminated parental ultramafic magma, and that the differentiation of this parental magma, a requirement to produce the lowest MgO group-1 basalt, occurred at this boundary.

Constraints for the differentiation process involved in generating the group-1 basalt can be obtained from examining the co-variation of the incompatible elements CaO, Al_2O_3, and TiO_2 with MgO (Fig. 3-16). Despite some scatter, possibly a result of non-liquid compositions and/or major element mobility, the average group-1 basalt and the contaminated and uncontaminated HREE-depleted komatiite are broadly co-linear on these variation diagrams. This relationship suggests that the variable extraction of a bulk cumulate assemblage consisting of ~70 wt.% olivine and ~30 wt.% clinopyroxene controlled the incompatible element variation. The average group-1 basalt (~12.5 wt.% MgO) can be generated from the contaminated HREE-depleted komatiite (~22 wt.% MgO) by ~35-40 wt.% crystal fractionation of this mineral assemblage. Note that up to ~55 wt.% crystallization is required to generate lavas with MgO contents as low as ~8 wt.% (Fig. 3-16). In agreement with these constraints, similar results are obtained from modeling of incompatible trace elements (Fig. 3-15(a)).

Group-2 basalt and group-1 and -2 komatiite

With the exception of sample HS0-302, the group-2 basalt can be suitably generated by contamination of the average depleted basalt with relatively small amounts (~3-9 wt.%) of a TTG-type crustal component (Fig. 3-14(a and b)). The involvement of such a highly-enriched crustal contaminant, coupled with the relatively small amounts of crust involved suggests a random/accidental contamination process that, in all likelihood, occurred during high-level transport and/or eruption of the parental magma. Despite some scatter, the group-2 basalt also possess major element compositions that are remarkably similar to the average depleted basalt (Fig. 3-16), similarities that would are consistent with minor amounts of crustal contamination.

Similar to the random/accidental upper crustal contamination suggested for the group-2 basalt above, the close spatial/temporal relationship between group-1 and -2 komatiite and absence of similar, high $(Th/Nb)_N$ komatiite magmas elsewhere within the volcanic succession (e.g. Fig. 3-5) suggests that contamination was also accidental, and potentially related to the local substrate onto which they were erupted. Despite the fact that the group-1 and -2 komatiites require distinct parental magmas (e.g. HREE-unfractionated and HREE-enriched; see Fig. 3-15(e and f)) their incompatible trace element signatures can both be modeled by small amounts of crustal contamination (~0.5-2 wt.%) involving a TTG-type crust, a result consistent with local contamination.

NEW CONSTRAINTS FOR THE REGIONAL SETTING OF MAFIC ULTRAMAFIC MAGMATISM WITHIN THE CENTRAL AND NORTHEASTERN RAE DOMAIN

The geochemical and isotopic data obtained for high $(Th/Nb)_N$ mafic, ultramafic, and intermediate-felsic volcanic rocks of the PAg presented in this study have established that ca. 2730 Ma mafic-ultramafic volcanism within the lower PAg formed upon a pre-existing substrate of Rae continental crust. This buried crust, is best imaged by the whole rock Nd isotopic composition and U-Pb ages of xenocrystic zircon within intermediate-felsic volcanic rocks, and is constrained to be juvenile and ca. 2750-2800 Ma. Importantly, the age, juvenile character, and distinctive geochemical signature of the PAg basement now allows more exacting constraints to be placed upon the regional setting of ca. 2735-2690 Ma mafic-ultramafic magmatism within the central and northeastern Rae domain. These data allow for a refinement of the extensional continental setting proposed in Chapter 2, a setting in which extension and magmatism were focused along the continental margin.

The recognition of ca. 2750-2800 Ma crust is critical to understanding the setting of ca. 2735-2690 Ma mafic-ultramafic magmatism. Regional evidence for ca. 2750-2800 Ma crust within the supracrustal corridor includes: (1) directly dated ca. 2775 and 2778 Ma plutonic rocks within the Eqe Bay area on northern Baffin Island (Fig. 3-1; Bethune & Scammell, 2003); (2) a prominent population of precisely dated (~1-2 Ma 2σ uncertainties), ca. 2755-2805 Ma zircon xenocrysts (n=10/22) contained within ca. 2730-2700 Ma felsic volcanic rocks of the MRg located within the Eqe Bay area (Bethune & Scammell, 2003); (3) the prominent ca. 2750-2800 Ma xenocrystic zircon population contained within ca. 2730 Ma felsic volcanic rocks of the lower PAg identified in this study (Fig. 3-11); and (4) a major population of ca. 2750-2800 Ma detrital zircon (~1/3 of 121 pre-ca. 2735 Ma zircon) identified within siliciclastic supracrustal rocks that unconformably overlie the lower PAg within the Laughland Lake area (see Fig. 2-10 in Chapter 2).

The occurrence of ca. 2750-2800 Ma crust beneath the lower PAg within the Laughland Lake area and MRg on Baffin Island not only supports the regional correlation of these supracrustal belts (see Chapter 2), it indicates that ca. 2750-2800 Ma crust has a significant minimum strike length of ~800 km (Fig. 3-1). Although major, trace element, and Nd isotopic data are unavailable for the ca. 2750-2800 Ma basement to the MRg, beneath the lower PAg it is constrained to be juvenile and to possess a suprasubduction zone geochemical signature (e.g. Fig. 3-12). These signatures suggest the ca. 2750-2800 Ma basement represents either the most outboard portion of continental margin volcanic arc or an intra-oceanic arc accreted to older Rae crust sometime prior to ca. 2735 Ma. In either scenario, a continental margin setting for ca. 2735-2690 Ma mafic-ultramafic magmatism is implied.

Due to the presence of ca. 3.25-3.90 Ga crust (inferred from Nd model ages) in close proximity to the supracrustal corridor (~200 km; Fig. 3-1), the occurrence of ancient ca. 3.3-3.8 Ga detrital zircons within siliciclastic sedimentary rocks within the middle and upper PAg is not surprising (e.g. see Fig. 2-7 in Chapter 2; Skulski *et al.*, pers. comm.). The presence of these zircon suggests that during deposition of siliciclastic sedimentary rocks within the middle and upper PAg, the ancient Rae crust as well as components at least as young as ca. 3.13 Ga were, as they are now, located to the west of the supracrustal corridor (Fig. 3-1). If the ca. 2750-2800 Ma basement was, as suggested above, formed outboard of the older Rae crust within an intra-oceanic volcanic arc, the current lack of evidence for old crust within the supracrustal corridor, and the preferential formation of the supracrustal belts upon the youngest and most juvenile crust, would simply reflect their formation at the continental margin.

The distinctly linear disposition of the supracrustal network and the abrupt initiation of regional mafic-ultramafic magmatism suggesting lithospheric extension preceded and facilitated the initiation of magmatism can also be reconciled in a continental margin setting undergoing extension. We suggest that the focusing of strain within pre-existing, linear, and regional scale structures inherent to the Rae continental margin exerted a controlling influence upon the regional distribution of mafic-ultramafic magmatism and siliciclastic sedimentation between ca. 2735-2690 Ma.

CONCLUSIONS

(1) The documentation of a prominent, ca. 2750-2800 Ma xenocrystic zircon population within two ca. 2730 Ma, high $(Th/Nb)_N$ felsic volcanic rocks intercalated with basalt and komatiite within the lower PAg has confirmed that this dominantly mafic-ultramafic volcanic succession formed upon a pre-existing substrate of continental crust. The major, trace element, and Nd isotopic compositions of these felsic and associated intermediate volcanic rocks suggests that they were derived via partial melting of juvenile, ca. 2750-2800 Ma lower continental crust.

(2) Geochemical modeling indicates that the small volumes of high $(Th/Nb)_N$ (≥ to >> 1) basalt and komatiite within the lower PAg can be explained by crustal contamination of low $(Th/Nb)_N$ basalt and komatiite recognized within the volcanic succession. The parental uncontaminated magmas involved were incompatible trace element depleted, HREE-depleted to -enriched komatiite ($(Gd/Yb)_N$ ~0.8-1.3) and incompatible trace element depleted, minimally HREE-depleted basalt ($(Gd/Yb)_N$ ~1.1-1.2).

(3) Two principal types of contaminants and related processes/locations of contamination are required: (1) larger and more pervasive contamination of komatiite occurring at the crust-mantle boundary via the addition of primitive lower crustal melts; and (2) minimal to moderate high-level contamination of basalt and komatiite during transport through the crust and/or during eruption at the surface via the addition of highly enriched TTG-type contaminant.

(4) The most abundant and widespread high $(Th/Nb)_N$ magmas are the group-1 basalt (~8-19 wt.% MgO) which were generated at the crust-mantle boundary via the addition of ~15 wt.% of a primitive andesite melt produced by partial melting of ca. 2750-2800 Ma lower crust in response to the emplacement an incompatible element depleted, minimally HREE-depleted ($(Gd/Yb)_N$ ~1.2-1.3) parental komatiite (~25 wt.% MgO). Significant olivine and clinopyroxene crystal differentiation at the crust-mantle boundary (~35-40 wt.%) is required to generated the average group-1 basalt from its contaminated parental komatiite. The lesser amounts of the group-2, high $(Th/Nb)_N$ basalt were largely

generated via the addition of ~2-10 wt.% TTG-type crust to incompatible element depleted basalt.

(5) The rare, highly localized occurrence of high $(Th/Nb)_N$ komatiite being restricted to a single flow sequence can be explained by minimal contamination of komatiite (≤ 2 wt.%) via the addition of a TTG-type crustal contaminant suggesting contamination occurred at the site of eruption.

(6) The distinctive bi-modal basalt-komatiite association (~4-13 and ≥ 25 wt.% MgO) which characterizes the lower PAg is, at least partially, an artifact of crystal differentiation of high-MgO komatiite at the crust mantle boundary and is inconsistent with shallow-level differentiation of komatiite magmas.

(7) The current data suggests that the ca. 2735-2690 Ma supracrustal belts within the central and northeastern Rae domain characterized by orthoquartzite-komatiite associations are co-genetic and formed along a ~1400 km long and up to ~400 km wide extensional basin positioned within/along the Rae continental margin.

APPENDIX A. SAMPLE PREPARATION AND ANALYTICAL METHODS

For major and trace element geochemistry, rock samples were cleaned of all visible alteration and reduced to sub-cm sized chips using a jaw crusher. The small rock chips were then hand picked and powdered using an agate mill. The majority of the geochemical analyses presented in this contribution had their major and selected minor and trace elements (SiO_2-Co; Table 3-1) determined on fused glass discs using a Philips PW2440 X-ray fluorescence mass spectrometer in the geochemical laboratories of the Earth and Planetary Sciences department at the University of McGill, Montreal. The accuracy of the XRF data is estimated to be < 1 % for all elements and method precision is within 0.5 % for all elements at concentration levels ≥ 10x the detection limit based on repeated measurement of international rock powders. The basalt samples all possess concentration levels > to >> than 10x the detection for elements analysed by XRF with the exception of some of the trace elements, including Ni, Cr and V. For komatiite, all elemental concentrations are ≥ to >> 10x the detection limit with the exception of Na_2O and K_2O. The loss on ignition (LOI) was determined gravimetrically. For the geochemical samples that had major elements determined by XRF, the trace elements Co, Cr, Ni, Sc, V, Zn, and Ga were determined by inductively coupled plasma-atomic emission spectrometry (ICP-AES) and Nb, Th, Y, Hf, Zr and the REE by inductively coupled plasma-mass spectrometry (ICP-MS) at the geochemical laboratories of the Geological Survey of Canada in Ottawa. For all trace element analyses, rock powders were dissolved using a combination of nitric, perchloric and hydrofluoric acids followed by a lithium metaborate fusion of any residual material. The detection limits, and duplicate dissolutions/analyses for komatiite and basalt conducted during the period of this study are reported in Table 4-A-1 in Chapter 4. The accuracy and precision as judged by the analysis of in-house and international standard reference materials are generally < 5 % (2σ relative standard deviation) when concentrations are ≥ 10x the limit of detection. The reproducibility of basalt and komatiite powders is ≤ to << 10 % ((total difference/mean) x 100) for all trace elements at the concentration levels of samples reported here.

Four of the basalt samples (CS0-316, -315, -264-B, and HS0-302; Table 3-1) had their major and trace elements determined by ICP-MS at Activation Laboratories in Ancaster, Ontario. For major element determinations rock powders were fused by mixing the samples with a flux and fused in an induction furnace. The molten melt is poured into a solution of 5 % nitric acid containing an internal standard and mixed until dissolved and analysed on a Thermo Jarrell-Ash ENVIRO II ICP. The accuracy and precision of the major and minor elements SiO_2, Al_2O_3, Fe_2O_3, MgO, CaO and TiO_2 are within 2 % and MnO, Na_2O, K_2O and P_2O_5 within 2-7 % based on long-term lab averages of an international basalt standard with a similar composition to the samples analysed in this study. For trace elements, rock powders were prepared as above and spiked with internal standards and analysed using a Perkin Elmer SCIEX ELAN 6000 ICP-MS. Similarly, with reference to international basalt standard materials the trace elements have an estimated accuracy and precision within ~5-10 % and many are < 5 %.

All Sm-Nd and U-Pb zircon isotopic analyses were preformed at the University of Alberta Radiogenic Isotope Facility, Edmonton, Alberta. For Sm-Nd isotopes, rock powders (prepared as above) were weighed into Teflon vials and spiked with a mixed ^{149}Sm-^{150}Nd tracer solution. The sample-spike mixture was dissolved and homogenized in a mixture of concentrated HF and HNO_3 acid for a period of 5-7 days at ~160 °C. Sm and Nd were concentrated and purified by following the analytical procedure described in Creaser *et al.* (1997). Sm isotopic ratios were measured on a multi-collector sector-54 thermal ionization mass spectrometer (TIMS) operated in multidynamic mode and Nd isotopic ratios were acquired using a NuPlasma multicollector-inductively coupled plasma-mass spectrometer (MC-ICP-MS). For Nd isotopic acquisition, the analysis of unknown sample solutions was alternated with a 200 ppb solution of an in-house Nd Alfa isotopic standard solution (accepted $^{143}Nd/^{144}Nd$ = 0.512265 based on calibration to the La Jolla standard). Within a given analytical session the Nd-Alfa solution has an external reproducibility within ± 0.000015 and the long term lab average (n=256) has $^{143}Nd/^{144}Nd$ = 0.512240 ± 0.000020. The sample-standard bracketing technique was used to correct for instrumental drift during the analytical session. Solutions prepared from the same rock powder and analysed during separate analytical sessions always reproduce within their in-run precision. The uncertainty in $^{147}Sm/^{144}Nd$ based on analysis of basalt standard BCR-1 is ~0.2 %. Duplicate analyses of separate komatiite rock powders taken from the same vial reproduce $^{147}Sm/^{144}Nd$ within ~0.2-0.3 % and εNd(2730 Ma) values within ~0.3 (Chapter 4). Typically, Archean rocks reproduce εNd(T) values within < 0.4 epsilon units (see Yamashita & Creaser, 1999).

For U-Pb samples clean palm-sized rock fragments were jaw crushed and pulverized to fine powder using a Bico disc mill. The fine powder (generally < 100 mesh) was passed over a Wilfley Table to obtain a heavy mineral concentrate. Zircons were liberated from the dried concentrate by magnetic (Frantz isodynamic separator) and density (methylene iodide) based techniques. U-Pb age determinations by LA-MC-ICP-MS were obtained using a NuPlasma MC-ICP-MS coupled to a New Wave Research Nd:YAG (λ = 213 nm) laser ablation system. The details of the U-Pb zircon dating technique by LA-MC-ICP-MS at the University of Alberta are outlined in Simonetti *et al.* (2005) and briefly summarized below. Selected zircons from the sample and an in-house zircon standard were mounted and polished together in an epoxy puck. Ablation was conducted using a laser energy output of ~2 J/cm^2 and laser spot size of ~40 μm (diameter). An individual ablation run consisted of a ~30 sec. blank measurement prior to aspiration of a 1 ppb Tl solution into the plasma source using a desolvating nebulizer (DSN-100) during ablation. The simultaneous measurement of U (faraday collectors), Pb (ion counters) and Tl (faraday collectors) isotopes is conducted during a ~30 sec. ablation run. A common Pb correction was necessary for only a very small number of analyses and its application is discussed in Simonetti *et al.* (2005). A typical external reproducibility (2σ) of ~0.5-0.7 % for ^{207}Pb/^{206}Pb and ~3 % for ^{206}Pb/^{238}U (and ^{206}Pb/^{238}U) is obtained for international zircon standards (Simonetti *et al.*, 2005) and is applied to the measured isotopic data reported in this study. Very few analyses had errors that exceeded this external reproducibility. The ^{238}U (1.55125×10^{-10} a^{-1}) and ^{235}U (9.8485×10^{-10} a^{-1}) decay constants used in age calculations are those determined by Jaffey *et al.* (1971). Age calculations (ID-TIMS and LA-MC-ICP-MS) were preformed using the Isoplot version 3.00 software (Ludwig, 1992; 2003). Error ellipses and quoted ages on concordia diagrams are at the 2σ level of uncertainty. Error due to uncertainty in U decay constants has not been included.

Table 3-1. Major, minor and trace element oxides (except Cr_2O_3 -ppm) and LOI are in wt.% and all other elements are in ppm. Oxides (and Ni) have been normalized to 100% anhydrous. Basalt horizon (B); komatiite horizon (K); komatiite (kom.); flow top (f. top); plate spinifex (p. spfx.); random spinifex (r. spfx.); basal cumulate (b. cum.).

Table 3-2. Nd isotopic ratios normalized to $^{146}Nd/^{144}Nd = 0.7219$. Uncertainty reported in the Nd isotopic ratio is $2\sigma/\sqrt{n}$ analytical error in the last decimal place, where *n* is the number of measured isotopic ratios. Initial εNd values (2730 Ma) calculated using present day CHUR parameters of $^{143}Nd/^{144}Nd = 0.512638$ and $^{147}Sm/^{144}Nd = 0.1967$.

Table 3-3. Counts per second (cps); counts per second radiogenic (cps rad.). The percent discordance (% disc.) is calculated using the $^{206}Pb/^{238}U$ and $^{207}Pb/^{206}Pb$ ages.

Table 3-4. Low $(Th/Nb)_N$ komatiite and basalt averages are from samples listed in Table 4-1 in Chapter 4. HREE-enriched komatiite (n=6; HS0-091-SP1, HS0-091-SP1A, HS0-091-SP1B, HS0-091-SP2, TM0-228-C, and TM0-231-F), HREE-unfractionated (unfract.) komatiite (n=4; HS0-091-SP3, TM-1, TM-1A, and TM0-285-F8 (no Hf and Zr from this sample), HREE-depleted komatiite (n=4; TM0-011-F, TM0-011-G, TM0-011-H, and TM0-239-12), depleted basalt (n=3; TM-7-D, TM0-239-E, and TM0-239-F).

Table 3-1. Major and trace element compositions of PAg felsic-ultramafic volcanic rocks.

Sample	T-3319-B	T-3321	H-1337	TM0-239-B	TM0-239-D	TM0-239-A	TM0-239-C	TM-1-H	TM-1-G	TM0-285-C-3	TM0-285-C
Rock type	dacite	andesite	dacite	basalt	basalt	basalt	basalt	basalt	basalt	basalt	basalt
Zone	SVZ	SVZ	NVZ	NVZ	NVZ	NVZ	NVZ	NVZ	NVZ	SVZ	SVZ
Horizon	B	B	K	K	K	K	K	K	K	K	K
Group	n/a	n/a	n/a	1	1	1	1	1	1	1	1
SiO_2	63.66	60.30	70.12	51.87	50.75	51.44	50.38	42.07	44.16	48.18	49.29
TiO_2	0.73	1.00	0.57	0.83	0.82	1.02	0.84	0.64	0.56	0.67	0.79
Al_2O_3	15.12	16.29	13.88	12.54	12.84	14.33	13.46	12.12	10.48	11.83	12.75
Fe_2O_3	6.50	7.93	4.56	11.27	11.70	11.63	11.48	16.73	15.71	11.36	10.04
MnO	0.13	0.13	0.12	0.18	0.18	0.15	0.15	0.33	0.33	0.25	0.17
MgO	3.57	3.05	1.71	9.27	9.87	7.97	9.87	19.32	18.63	13.05	12.31
CaO	6.69	6.93	3.82	9.03	10.10	8.90	9.95	7.37	8.64	10.02	12.02
Na_2O	2.18	3.27	4.52	4.65	3.37	4.24	3.52	0.90	0.98	4.08	1.30
K_2O	1.27	0.89	0.56	0.17	0.17	0.21	0.16	0.07	0.09	0.23	1.01
P_2O_5	0.13	0.20	0.13	0.10	0.08	0.10	0.09	0.05	0.07	0.07	0.07
Cr_2O_3	110	22	70	838	906	48	711	3412	2868	2200	2105
Ni	75	19	24	155	156	78	127	622	565	388	438
V	110	130	75	211	232	270	238	193	203	190	228
Co	23	23	13	50	46	49	55	95	92	59	65
LOI	4.13	2.08	0.23	0.49	0.63	0.61	0.64	5.05	4.11	1.62	1.56
Total	100.3	100.3	100.1	100.5	100.6	100.7	100.2	100.6	100.6	100.3	100.0
Co	23	23	11	46	46	48	51	95	87	58	61
Cr	83	29	49	627	674	65	540	2250	1900	1570	1520
Ni	77	26	27	152	159	80	129	600	535	354	394
Sc	15	14	10	32	36	36	37	36	32	32	37
V	107	133	76	213	233	278	238	196	203	195	233
Zn	84	99	64	94	85	70	71	154	144	79	61
Ga	18	21	17	16	15	17	17	13	11	13	14
Nb	8.5	8.8	8.1	3.8	3.2	3.7	3.4	2.4	2.2	3.5	3.0
Th	3.2	2.0	2.9	0.75	0.54	0.61	0.54	0.50	0.45	0.67	0.51
Y	21	21	15	18	19	21	20	14	15	18	16
Hf	4.0	2.6	4.1	1.9	1.5	1.7	1.6	1.5	1.3	1.9	1.5
Zr	152	99	165	74	58	63	60	56	46	71	54
La	20	18	15	6.0	6.6	6.8	4.8	4.1	4.5	3.8	6.1
Ce	43	40	32	14	15	17	13	10	11	12	14
Pr	5.1	5.0	3.5	2.0	2.1	2.4	1.8	1.4	1.5	1.8	1.9
Nd	20	20	14	8.9	9.5	11	8.4	6.3	6.9	8.6	9.1
Sm	4.2	4.1	3.0	2.3	2.5	2.7	2.3	1.7	1.8	2.3	2.3
Gd	3.8	3.9	2.9	2.9	3.1	3.5	3.1	2.2	2.2	2.9	2.9
Tb	0.63	0.62	0.48	0.50	0.52	0.58	0.52	0.39	0.39	0.49	0.50
Dy	3.5	3.5	2.5	3.1	3.3	3.7	3.4	2.5	2.5	3.0	2.8
Ho	0.68	0.66	0.49	0.64	0.67	0.76	0.71	0.52	0.52	0.64	0.60
Er	1.9	1.7	1.3	1.7	1.7	2.0	1.9	1.4	1.4	1.7	1.6
Tm	0.28	0.26	0.18	0.25	0.27	0.30	0.29	0.22	0.22	0.26	0.23
Yb	1.8	1.6	1.2	1.7	1.8	2.0	1.9	1.4	1.5	1.7	1.6
Lu	0.27	0.23	0.18	0.25	0.26	0.30	0.27	0.21	0.22	0.25	0.24
$(Th/Nb)_N$	3.12	1.88	2.96	1.63	1.40	1.36	1.31	1.72	1.69	1.58	1.41
$(Ce/Sm)_N$	2.48	2.36	2.59	1.48	1.45	1.53	1.37	1.43	1.48	1.26	1.48
$(Gd/Yb)_N$	1.71	1.98	1.96	1.38	1.40	1.42	1.32	1.27	1.19	1.38	1.47

Table 3-1. continued

Sample	TM0-285-D-1	CS0-316	CS0-315	HS0-302	CS0-264-B	TM0-263-C-1	TM0-263-J-1	TM0-263-G-1	TM0-263-D-1	TM0-263-F-1	TM0-263-J-2
Rock type	basalt	basalt	basalt	basalt	basalt	kom.	kom.	kom.	kom.	kom.	kom.
						f. top	f. top	f. top	f. top	f. top	r. spfx.
	SVZ	NVZ	NVZ	SVZ	NVZ	NVZ	NVZ	NVZ	NVZ	NVZ	NVZ
Horizon	K	B	B	B	K	K	K	K	K	K	K
Group	1	2	2	2	2	1	1	1	1	1	1
SiO_2	48.54	48.02	49.47	48.25	52.77	44.13	45.35	44.15	44.58	44.89	45.69
TiO_2	0.67	0.85	0.84	1.02	0.80	0.34	0.35	0.35	0.32	0.34	0.36
Al_2O_3	12.19	15.84	14.98	16.15	14.58	6.90	6.86	6.98	6.58	6.85	7.14
Fe_2O_3	10.87	12.52	12.19	13.54	10.24	11.85	10.89	11.62	11.17	10.98	10.34
MnO	0.22	0.21	0.20	0.20	0.13	0.15	0.15	0.15	0.16	0.15	0.15
MgO	13.00	8.56	7.43	8.21	7.88	30.76	30.15	31.04	30.39	30.57	29.37
CaO	9.61	11.85	12.86	10.18	10.71	5.00	5.39	4.85	5.92	5.32	6.03
Na_2O	4.17	1.93	1.84	2.19	2.56	0.23	0.24	0.20	0.26	0.25	0.28
K_2O	0.43	0.16	0.12	0.18	0.23	0.02	0.02	0.02	0.02	0.02	0.03
P_2O_5	0.09	0.06	0.07	0.08	0.09	0.04	0.03	0.04	0.03	0.03	0.03
Cr_2O_3	1777					4077	4243	4179	4002	4199	4323
Ni	371					1725	1625	1833	1713	1749	1537
V	188					119	116	132	115	126	123
Co	51					100	92	104	93	94	90
LOI	2.25	1.84	1.17	1.16	0.76	8.72	8.14	8.88	8.92	8.42	7.67
Total	100.3	99.3	98.8	98.9	99.5	100.5	100.6	100.5	100.4	100.5	100.7
Co	53	91	117	102	122	99	90	98	92	96	83
Cr	1250	168	188	197	482	2630	2720	2660	2530	2700	2800
Ni	333	114	127	133	149	1530	1440	1630	1480	1560	1370
Sc	31					20	22	20	20	21	23
V	189	273	286	320	252	125	122	133	116	126	126
Zn	69	70	94	113	69	76	80	76	75	74	73
Ga	13	17	16	19	17	7.4	7	7.1	6.7	7.2	7.3
Nb	4.1	0.80	0.65	1.68	1.57	0.50	0.49	0.49	0.50	0.51	0.55
Th	0.64	0.85	0.19	0.35	0.90	0.09	0.08	0.07	0.07	0.07	0.07
Y	19	17.7	17.7	20.8	16.8	7.0	6.7	6.1	7.3	6.7	7.7
Hf	1.9	1.4	1.4	1.5	1.6	0.58	0.64	0.52	0.42	0.50	0.60
Zr	69	51	51	60	68	26	27	20	14	19	21
La	3.9	2.6	2.3	4.2	4.2	0.7	0.6	0.5	0.7	0.5	0.6
Ce	13	6.0	5.9	9.3	10.2	1.8	1.5	1.5	1.9	1.4	1.7
Pr	2.0	1.01	0.96	1.52	1.43	0.28	0.25	0.23	0.30	0.24	0.28
Nd	9.6	5.1	4.8	6.8	6.4	1.5	1.4	1.4	1.6	1.4	1.7
Sm	2.5	1.76	1.76	2.29	1.96	0.60	0.57	0.53	0.64	0.60	0.69
Gd	3.0	2.5	2.5	2.9	2.4	0.92	0.88	0.82	0.96	0.85	1.00
Tb	0.50	0.50	0.50	0.56	0.47	0.18	0.17	0.16	0.18	0.17	0.20
Dy	3.1	3.1	3.2	3.5	3.0	1.1	1.1	1.0	1.2	1.1	1.3
Ho	0.63	0.67	0.69	0.79	0.62	0.24	0.23	0.21	0.25	0.23	0.26
Er	1.7	1.9	1.9	2.2	1.8	0.66	0.62	0.61	0.67	0.64	0.71
Tm	0.26	0.26	0.28	0.32	0.25	0.11	0.10	0.09	0.10	0.10	0.11
Yb	1.7	1.8	1.9	2.1	1.7	0.68	0.60	0.60	0.68	0.65	0.65
Lu	0.27	0.29	0.28	0.32	0.24	0.11	0.09	0.09	0.10	0.10	0.10
$(Th/Nb)_N$	1.29	8.80	2.42	1.71	4.74	1.49	1.35	1.18	1.16	1.14	1.05
$(Ce/Sm)_N$	1.26	0.82	0.81	0.99	1.26	0.73	0.64	0.69	0.72	0.57	0.60
$(Gd/Yb)_N$	1.43	1.11	1.08	1.09	1.16	1.10	1.19	1.11	1.14	1.06	1.25

Table 3-1. continued

Sample	TM0-263-I-1	TM0-263-J-3	TM0-263-H	TM0-263-A	TM0-263-HS	TM0-263-G	TM0-263-C	TM0-263-E
Rock type	kom.	kom.	kom.	kom.	kom.	kom.	kom.	kom.
	f. top	p. spfx.	p. spfx.	b. cum.	b. cum.	b. cum.	b. cum.	b. cum.
	NVZ	NVZ	NVZ	NVZ	NVZ	NVZ	NVZ	NVZ
Horizon	K	K	K	K	K	K	K	K
Group	1	1	1	1	2	2	2	2
SiO_2	46.37	45.80	45.16	44.02	42.89	42.93	42.06	43.00
TiO_2	0.37	0.34	0.40	0.23	0.22	0.18	0.19	0.20
Al_2O_3	7.54	7.14	7.79	4.71	4.90	3.82	3.83	4.09
Fe_2O_3	8.84	10.11	12.12	13.27	16.49	15.67	15.82	13.99
MnO	0.15	0.15	0.16	0.18	0.17	0.18	0.19	0.22
MgO	29.07	29.77	26.58	31.35	30.93	34.84	35.20	35.41
CaO	6.70	5.75	6.75	5.52	3.65	1.71	2.11	2.48
Na_2O	0.32	0.30	0.40	0.14	0.24	0.11	0.06	0.05
K_2O	0.02	0.02	0.03	0.01	0.01	0.01	0.01	0.01
P_2O_5	0.03	0.04	0.04	0.02	0.02	0.02	0.02	0.02
Cr_2O_3	4385	4306	4445	3267	2858	2826	2791	3070
Ni	1495	1548	1281	2136	1969	2438	2264	2219
V	117	133	155	111	110	92	81	76
Co	83	84	85	122	128	132	127	122
LOI	7.57	7.86	6.21	10.18	8.82	10.78	11.61	11.51
Total	100.7	100.4	100.1	100.4	101.0	100.9	100.7	100.2
Co	80		85	120	125	134	125	127
Cr	2810		3070	2130	1930	1890	1830	2010
Ni	1330		1120	1780	1700	2070	1880	1840
Sc	23		26	17	14	13	12	13
V	118		160	111	115	98	86	81
Zn	73		70	71	83	87	83	81
Ga	7.5		7.6	5.2	6.3	4.7	4.5	4.5
Nb	0.64		0.58	0.3	0.24	0.21	0.25	0.27
Th	0.08		0.08	0.05	0.07	0.06	0.06	0.04
Y	7.9		8.3	7.4	5.1	2.8	3.3	3.5
Hf	0.60		0.65	0.41	0.37	0.30	0.30	0.36
Zr	24		24	14	14	11	11	12
La	0.8		0.8	0.7	0.8	0.4	0.6	0.4
Ce	2.0		2.6	1.9	1.6	1.0	1.3	1.0
Pr	0.31		0.39	0.30	0.23	0.14	0.18	0.16
Nd	1.7		2.2	1.7	1.1	0.6	0.8	0.7
Sm	0.68		0.75	0.61	0.38	0.21	0.25	0.26
Gd	0.97		1.10	0.98	0.60	0.33	0.40	0.44
Tb	0.20		0.21	0.19	0.11	0.06	0.07	0.08
Dy	1.3		1.4	1.1	0.72	0.42	0.49	0.53
Ho	0.26		0.31	0.28	0.17	0.10	0.12	0.13
Er	0.71		0.81	0.71	0.46	0.30	0.33	0.36
Tm	0.11		0.12	0.11	0.07	0.05	0.05	0.06
Yb	0.69		0.83	0.74	0.54	0.37	0.41	0.41
Lu	0.10		0.13	0.12	0.09	0.06	0.07	0.07
$(Th/Nb)_N$	1.03		1.14	1.38	2.41	2.36	1.99	1.23
$(Ce/Sm)_N$	0.71		0.84	0.75	1.02	1.15	1.26	0.93
$(Gd/Yb)_N$	1.14		1.07	1.07	0.90	0.72	0.79	0.87

Table 3-2. Sm and Nd isotopic compositions of PAg felsic-ultramafic volcanic rocks.

Sample	Rock type	MgO (wt.%)	$(Th/Nb)_N$	$(Ce/Sm)_N$	$(Gd/Yb)_N$	Sm (ppm)	Nd (ppm)	$^{147}Sm/^{144}Nd$	$^{143}Nd/^{144}Nd$	εNd(T)
Intermediate-Felsic volcanic rocks										
T-3319-B	dacite	3.57	3.12	2.48	1.71	3.7	18.1	0.1239	0.511463 ± 9	2.7
H-1337	dacite	1.71	2.96	2.59	1.96	2.2	11.7	0.1160	0.511331 ± 8	2.9
Group-1 basalt										
TM0-239-A	basalt	7.97	1.36	1.53	1.42	2.9	10.3	0.1674	0.512237 ± 10	2.5
TM0-285-C	basalt	12.31	1.41	1.48	1.47	2.2	8.0	0.1674	0.512190 ± 9	1.6
TM-1-G	basalt	18.63	1.69	1.48	1.19	1.7	6.2	0.1636	0.512126 ± 10	1.6
Group-2 basalt										
CS0-315	basalt	7.43	2.42	0.81	1.08	1.9	5.4	0.2116	0.513046 ± 4	2.8
CS0-264-B	basalt	7.88	4.74	1.26	1.16	2.2	7.7	0.1754	0.512356 ± 4	2.0
HS0-302	basalt	8.21	1.71	0.99	1.09	2.2	7.2	0.1854	0.512573 ± 5	2.7
Group-1 komatiite										
TM0-263-J-2	kom. r. spfx.	29.37	1.05	0.60	1.25	0.60	1.5	0.2475	0.513678 ± 7	2.4
Group-2 komatiite										
TM0-263-HS	kom. b. cum.	30.93	2.41	1.02	0.90	0.40	1.2	0.2127	0.512976 ± 10	1.0

Table 3-3. U-Pb zircon isotopic data obtained by laser ablation-MC-ICP-MS.

Zr. #	^{204}Pb cps	^{206}Pb cps rad.	^{207}Pb/^{206}Pb	error (1σ)	^{207}Pb/^{235}U	error (1σ)	^{206}Pb/^{238}U	error (1σ)	^{207}Pb/^{206}Pb age	error (1σ)	% disc.
Dacite H-1337											
1-a	0	132488	0.1933	0.0010	12.9351	0.1941	0.4875	0.0083	2771	8	9.2
1-b	20	137791	0.1929	0.0010	12.2450	0.1837	0.4626	0.0080	2767	9	13.7
2	0	146036	0.1913	0.0011	12.1685	0.1826	0.4635	0.0077	2753	9	13.0
3	0	71156	0.1972	0.0011	12.7265	0.1909	0.4703	0.0075	2803	9	13.6
4	5	44483	0.2157	0.0013	15.1289	0.2270	0.5082	0.0085	2949	10	12.4
5	0	123194	0.1954	0.0010	13.2129	0.1982	0.4904	0.0081	2788	9	9.4
6	14	134903	0.1928	0.0011	12.6724	0.1901	0.4759	0.0079	2766	9	11.2
7	0	110912	0.2054	0.0011	14.0343	0.2106	0.4953	0.0087	2869	9	11.7
8	0	105649	0.1980	0.0011	13.1272	0.1970	0.4806	0.0085	2810	9	12.0
9-a	0	111072	0.1947	0.0010	11.8107	0.1772	0.4400	0.0075	2782	9	18.5
9-b	0	117041	0.1929	0.0010	13.2090	0.1982	0.4957	0.0086	2767	9	7.6
10-a	2	247152	0.1888	0.0010	12.7086	0.1907	0.4882	0.0080	2732	8	7.5
10-b	0	240553	0.1886	0.0010	12.0955	0.1815	0.4651	0.0075	2730	9	11.8
10-c	0	420790	0.1871	0.0009	12.4238	0.1864	0.4815	0.0082	2717	8	8.1
11	9	169226	0.1901	0.0010	13.2992	0.1995	0.5048	0.0081	2743	9	4.8
12-a	2	134443	0.1935	0.0010	13.2020	0.1981	0.4924	0.0080	2772	9	8.4
12-b	0	131291	0.1938	0.0010	12.8195	0.1923	0.4774	0.0085	2774	8	11.2
13	14	118696	0.1960	0.0010	13.1305	0.1970	0.4835	0.0082	2793	9	10.9
14	0	260795	0.1882	0.0010	12.5159	0.1878	0.4800	0.0078	2726	9	8.8
15	0	351613	0.1877	0.0010	12.4318	0.1865	0.4780	0.0079	2722	8	9.0
16	0	57911	0.2047	0.0012	13.7477	0.2062	0.4846	0.0078	2864	9	13.4
17	0	100247	0.1928	0.0011	12.8222	0.1924	0.4798	0.0081	2766	9	10.5
18	0	189107	0.1904	0.0010	12.9907	0.1949	0.4923	0.0082	2746	9	7.3
19	0	100891	0.1955	0.0013	13.3104	0.1997	0.4903	0.0080	2789	11	9.4
20	5	30738	0.2154	0.0017	14.9390	0.2241	0.4997	0.0087	2947	13	13.8
21	0	99995	0.1930	0.0014	12.8705	0.1931	0.4784	0.0078	2768	12	10.8
22	0	265267	0.1882	0.0010	12.7489	0.1913	0.4888	0.0078	2726	8	7.1
23-a	0	165484	0.1901	0.0010	12.6095	0.1892	0.4783	0.0077	2743	9	9.8
23-b	4	218114	0.1887	0.0010	12.5524	0.1883	0.4801	0.0080	2731	8	9.0
23-c	0	169260	0.1898	0.0010	12.8208	0.1923	0.4879	0.0076	2740	9	7.9
24	0	34391	0.2070	0.0011	13.9883	0.2098	0.4877	0.0078	2882	9	13.5
25	0	121149	0.1949	0.0011	12.7534	0.1913	0.4719	0.0078	2784	9	12.6
26	0	202252	0.1893	0.0010	12.2774	0.1842	0.4681	0.0077	2736	8	11.5
27	0	45606	0.1934	0.0012	11.7809	0.1767	0.4390	0.0073	2771	10	18.3
28	0	104526	0.1950	0.0011	12.7323	0.1910	0.4710	0.0078	2785	9	12.8
Dacite T-3319-B											
1	9	201772	0.1929	0.0010	13.6860	0.2053	0.5145	0.0079	2767	9	4.0
2	0	191618	0.1958	0.0010	14.0794	0.2112	0.5215	0.0085	2792	8	3.8
3	19	142576	0.1960	0.0010	13.8561	0.2079	0.5126	0.0082	2794	9	5.5
4-a	0	226547	0.1929	0.0010	13.5758	0.2037	0.5103	0.0085	2767	8	4.8
4-b	0	231972	0.1928	0.0010	13.4117	0.2012	0.5046	0.0079	2766	8	5.8
5	0	206000	0.1937	0.0010	13.7113	0.2057	0.5135	0.0079	2774	9	4.5
6	2	650016	0.1892	0.0010	13.1408	0.1971	0.5037	0.0084	2736	8	4.7

Table 3-4. Average compositions of low $(Th/Nb)_N$ komatiite and basalt.

Rock	Avg. HREE-enriched kom.	Avg. HREE-unfract. kom.	Avg. HREE-depleted kom.	Avg. depleted basalt
SiO_2	45.30	44.69	44.19	48.65
TiO_2	0.33	0.40	0.46	0.77
Al_2O_3	7.29	8.05	7.97	13.41
Fe_2O_3	11.36	12.88	13.71	13.80
MnO	0.15	0.15	0.17	0.19
MgO	28.94	26.87	25.36	9.27
CaO	5.76	6.09	7.18	9.10
Na_2O	0.25	0.25	0.33	4.39
K_2O	0.02	0.02	0.02	0.31
P_2O_5	0.03	0.04	0.04	0.06
Cr_2O_3	4114	4486	4328	694
Ni	1564	1227	1353	97
V	134	151	149	268
Co	90	93	100	62
LOI	7.78	6.61	5.80	0.66
Total	100.7	100.3	100.3	100.5
Co	93	98	96	61
Cr	2670	3008	3055	344
Ni	1418	1148	1053	106
Sc	24	27	27	39
V	135	157	166	272
Zn	72	73	75	74
Ga	7	8	8	14
Nb	0.4	0.6	0.8	1.3
Th	0.03	0.06	0.07	0.11
Y	6.7	8.3	9.7	19.0
Hf	0.53	0.64	0.76	1.13
Zr	19.00	23.00	26.75	38.67
La	0.35	0.63	0.80	1.40
Ce	1.0	1.75	2.33	4.50
Pr	0.18	0.31	0.43	0.79
Nd	1.07	1.78	2.50	4.43
Sm	0.48	0.69	0.98	1.70
Gd	0.80	1.12	1.48	2.60
Tb	0.16	0.21	0.27	0.47
Dy	1.10	1.43	1.65	3.17
Ho	0.24	0.30	0.35	0.69
Er	0.67	0.81	0.94	1.83
Tm	0.11	0.13	0.15	0.28
Yb	0.75	0.86	0.95	1.90
Lu	0.12	0.13	0.15	0.28
$(Th/Nb)_N$	0.66	0.81	0.76	0.69
$(Ce/Sm)_N$	0.50	0.62	0.58	0.64
$(Gd/Yb)_N$	0.87	1.06	1.27	1.11

Fig. 3-1. Distribution of Neoarchean, ca. 2735-2690 Ma supracrustal belts (see Fig. 2-9 in Chapter 2 and references therein) characterized by orthoquartzite-komatiite lithological associations within the central and northeastern Rae domain of Nunavut including, from southwest to northeast, the Woodburn Lake group (WLg), Prince Albert group (PAg), and Mary River group (MRg), respectively. Also shown are the locations of Neo- to Mesoarchean aged, ca. 2775-2870 Ma basement components of the WLg and MRg (Jackson *et al.*, 1990; Wodicka *et al.*, 2002; Zaleski *et al.*, 2001; Bethune & Scammell, 2003), and undated granitoids that yielded predominantly "ancient" (Paleo-to Eoarchean) depleted mantle Nd model ages clustering between ca. 3.25-3.9 Ga (Thériault *et al.*, 1994). The undivided Archean aged crust (grey fill) within and external to the supracrustal belt corridor is dominated by Neoarchean, ca. 2620-2580 Ma intermediate-felsic plutonic rocks (see MacHattie *et al.*, in preparation *a* and references therein). The extent of the regional bedrock mapping conducted southwest of Committee Bay between 2000 and 2002 is outlined (Fig. 3-2; see Skulski *et al.*, 2003*c*) as is the location of this study, within the southwestern portion of the PAg in the Laughland Lake area (LL area). Committee Bay (CB); Melville Peninsula (MP); Northwest Territories (NWT); Queen Maud Gulf (QMG).

Fig. 3-2. General geological map of the Committee Bay region delineating the supracrustal rocks of the PAg from granitoid rocks. Substantial occurrences of basalt, komatiite and orthoquartzite have been separated from undifferentiated PAg when possible. The U-Pb (zircon) ages for volcanism, syn-volcanic plutonism, and

sedimentation (max. age) are indicated as are the locations of geochemical and Nd isotopic samples. Map simplified after Skulski *et al.* (2003*c*).

Fig. 3-3. Schematic composite PAg stratigraphy illustrating the subdivision into lower (ca. 2730 Ma), middle (ca. 2710 Ma) and upper (≤ ca. 2690 Ma) chronostratigraphic sequences, respectively. References for U-Pb (zircon) ages are listed in Fig. 3-2.

Fig. 3-4. (a) Plane polarized light photomicrograph of basalt sample TM0-239-B containing equant to skeletal, compositionally zoned clinopyroxene and anhedral plagioclase. Some minor Fe-Ti-oxides are also visible. (b) Fine grained, random olivine spinifex-textured komatiite sample TM0-263-J-2 (ball point pen for scale).

Fig. 3-5. Plot of MgO (wt.%) versus $(Th/Nb)_N$ (primitive mantle normalized) for peridotitic komatiite, basalt, and intermediate-felsic volcanic rocks collected within the ca. 2730 Ma mafic-ultramafic volcanic succession of the lower PAg. High $(Th/Nb)_N$ volcanic rocks (circles) possessing $(Th/Nb)_N \geq 1$ are discussed in this study.

Fig. 3-6. Primitive mantle normalized (McDonough & Sun, 1995) extended trace element diagram illustrating the major/trace element subdivision of high $(Th/Nb)_N \geq 1$ volcanic rocks including, (from top) andesite and dacite, group-1 basalt, group-2 basalt, group-1 komatiite, and group-2 komatiite, respectively.

Fig. 3-7. (a) MgO (wt.%) versus $(Ce/Sm)_N$, and (b) MgO (wt.%) versus $(Gd/Yb)_N$ for high $(Th/Nb)_N$ volcanic rocks (symbols as in Fig. 3-6).

Fig. 3-8. Plot of $(Th/Nb)_N$ versus $(Ce/Sm)_N$ for high $(Th/Nb)_N$ volcanic rocks. Average low $(Th/Nb)_N$ komatiite (cross) includes all peridotitic komatiite shown in Fig. 3-5 (see Table 4-1 in Chapter 4).

Fig. 3-9. Plots of MgO (wt.%) versus selected major and minor element(s) involving SiO_2, TiO_2, Al_2O_3, $Fe_2O_3(T)$ and CaO for $(Th/Nb)_N \geq 1$ volcanic rocks (symbols as in Fig. 3-6). Included are the data for low $(Th/Nb)_N$ basalt and komatiite for comparison (crosses; see Table 4-1 in Chapter 4). Mineral compositions plotted on the SiO_2, TiO_2, Al_2O_3 and CaO variation diagrams include the average olivine (n=9) and high-Ca clinopyroxene (n=10) analysed from peridotitic komatiite flows (~25-26 wt.% MgO for spinifex-textured samples) from Munro Township (Table 2 and 3 of Arndt *et al.*, 1977). See text for details of the regressions shown on the TiO_2, Al_2O_3, and CaO variation diagrams.

Fig. 3-10. (a) Plot of $^{147}Sm/^{144}Nd$ versus εNd(2730 Ma). The mean for 9/10 samples (excluded group-2 komatiite sample TM0-263-HS) of +2.4 ± 1.0 (2σ std. dev.) is shown (symbols as in Fig. 3-6). (b) Sm-Nd isochron diagram. The regression shown is for 9/10 samples (excluded group-2 komatiite sample TM0-263-HS) yields an "errorchron" model-3 age of 2724 ± 84 Ma (Isoplot software version 3.0; see Ludwig, 1992). Assigned external errors of 0.2 % for $^{147}Sm/^{144}Nd$ and 0.000015 for $^{143}Nd/^{144}Nd$ have been applied to the data.

Fig. 3-11. Concordia diagram and probability density histogram of $^{207}Pb/^{206}Pb$ age (bin width is 18 m.y.) for xenocrystic zircon separated from dacite T-3319-B and dacite H-1337. For zircon analysed in multiple spots (e.g. grain #10a and c from sample H-1337) a weighted mean $^{207}Pb/^{206}Pb$ age is used for the histogram and the most concordant analyses plotted on the concordia diagram. Zircon images were taken post-ablation and laser pits are ~40 μm in diameter. The U-Pb zircon crystallization ages shown for these samples were obtained by ID-TIMS (see Chapter 2).

Fig. 3-12. Primitive mantle normalized (McDonough & Sun, 1995) extended trace element plot comparing primitive andesite (sample T-3321) and the average dacite (samples T-3319-B and H-1337) with various crustal compositions including, estimates for the average upper and lower continental crust (Taylor & McLennan, 1985), an average composition for Late Archean TTG (Condie, 2005), and an average for suprasubduction zone generated quartz diorites from the Trans-Hudson orogen (MacHattie, 2002).

Fig. 3-13. Nd isotopic composition of low and high $(Th/Nb)_N$ volcanic rocks (this study; see Table 4-2 in Chapter 4) analysed from the lower PAg compared the Nd isotopic evolution of a hypothetical, Late Archean depleted mantle and LREE-enriched, ca. 2775, 2870 and 2950 Ma crust extracted from this mantle. See text for details.

Fig. 3-14. Plots of $(Th/Nb)_N$ versus $(Ce/Sm)_N$ and $(Gd/Yb)_N$ for the average group-1 basalt and individual group-2 basalts. Compositions used in mixing calculations include: average depleted basalt within the lower PAg (Table 3-4); average HREE-depleted komatiite within the lower PAg (Table 3-4); average Late Archean TTG (Condie, 2005); a modified version of this average (see legend); the average lower PAg dacite (samples T-3319-B and H-1337); and andesite sample T-3321.

Fig. 3-15. (a-f) Primitive mantle normalized (McDonough & Sun, 1995) extended trace element plots summarizing the results of the two-component mixing models shown in Fig. 3-14 as well as modeling specific to the group-1 and -2 komatiite. With respect to the latter, averages for HREE-unfractionated and HREE-enriched komatiites were used for the parental magmas (see Table 3-4) and TTG crust for the contaminant. In (a), the olivine and clinopyroxene partition coefficients used to model crystal fractionation are composites from (Salters *et al.* (2002); McDade *et al.* (2003); Zanetti *et al.* (2004); Salters & Longhi (1999)). The composite partition coefficients are listed in Table 4-3 (Chapter 4) as Ol. and Cpx.-1, respectively.

Fig. 3-16. MgO (wt.%) variation diagrams involving CaO, Al_2O_3, and TiO_2 displaying the group-1 and -2 basalt, andesite T-3321, the average group-1 basalt, the average depleted basalt (see Table 3-4), the average HREE-depleted komatiite (see Table 3-4), and the average HREE-depleted komatiite contaminated with 15 wt.% andesite. The mineral compositions shown include average olivine (n=9) and high-Ca clinopyroxene

(n=10) analysed from peridotitic komatiite flows (~25-26 wt.% MgO for spinifex-textured samples) from Munro Township (Table 2 and 3 of Arndt *et al.*, 1977). The regressions shown involve a cumulate mineral assemblage consisting of ~70 wt.% olivine and ~30 wt.% clinopyroxene, the contaminated and uncontaminated average HREE-depleted komatiite, and the average group-1 basalt.

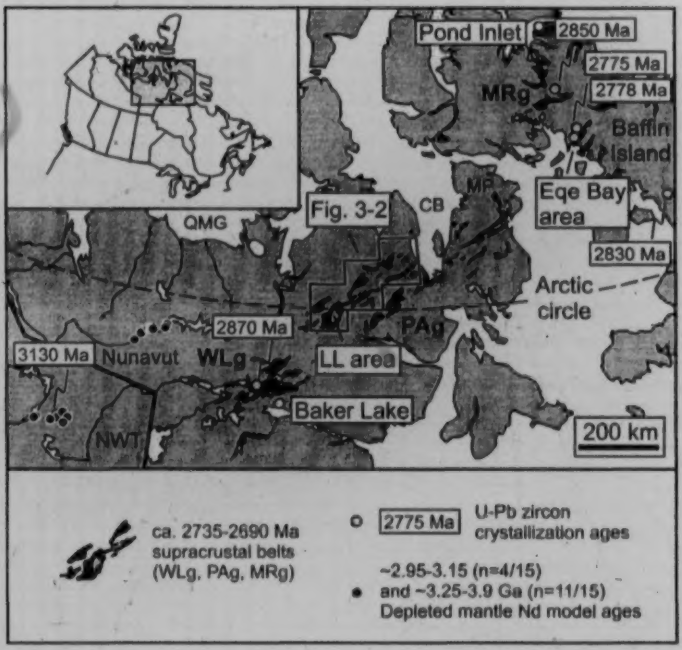
Pond Inlet
2850 Ma
2775 Ma
2778 Ma
MRg
Baffin Island
MP
CB
Eqe Bay area
Fig. 3-2
QMG
2830 Ma
Arctic circle
2870 Ma
PAg
3130 Ma
Nunavut
WLg
LL area
Baker Lake
NWT
200 km
ca. 2735-2690 Ma supracrustal belts (WLg, PAg, MRg)
2775 Ma
U-Pb zircon crystallization ages
~2.95-3.15 (n=4/15) and ~3.25-3.9 Ga (n=11/15) Depleted mantle Nd model ages

Figure 3-1

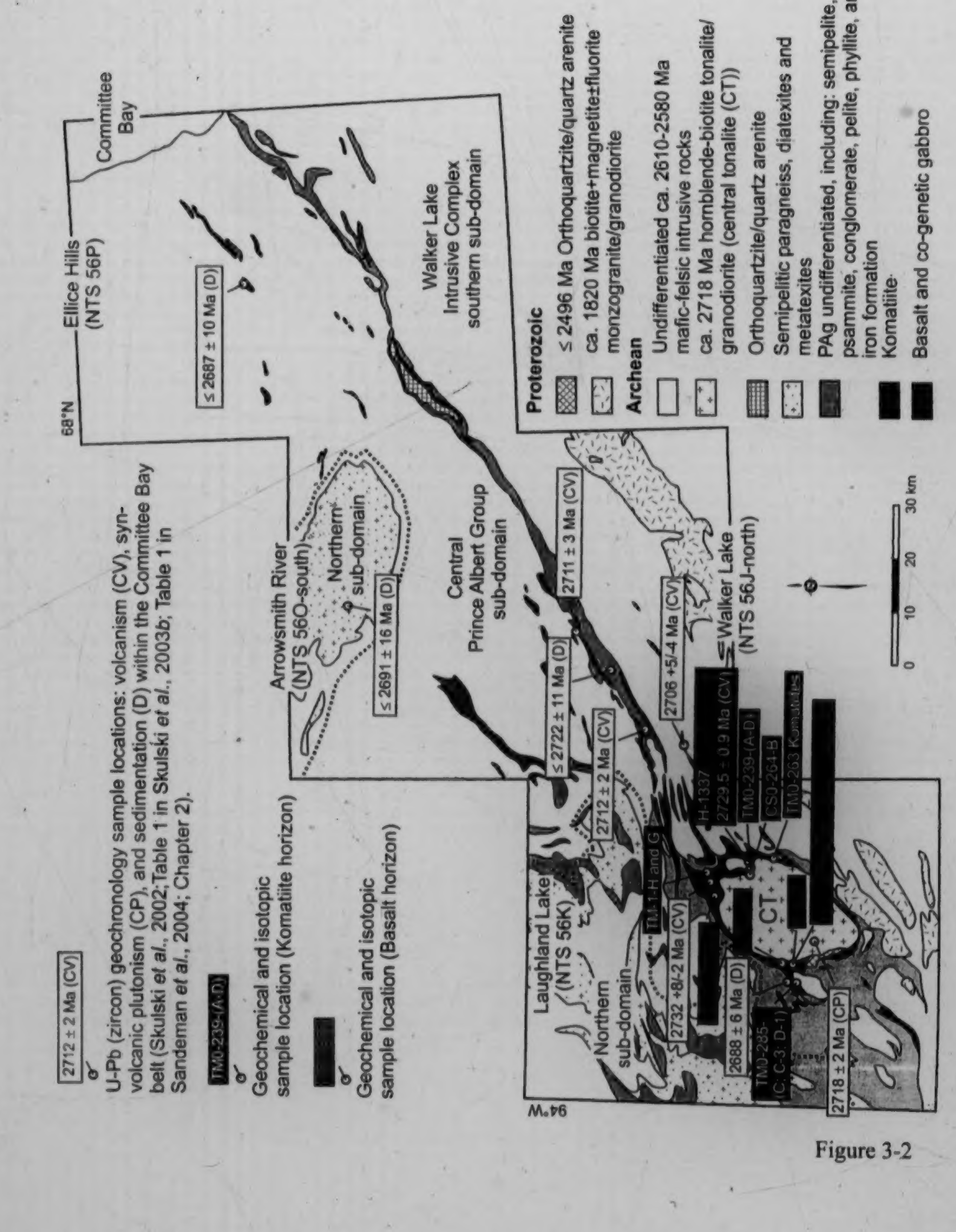
2712 ± 2 Ma (CV)
U-Pb (zircon) geochronology sample locations: volcanism (CV), syn-volcanic plutonism (CP), and sedimentation (D) within the Committee Bay belt (Skulski et al., 2002; Table 1 in Skulski et al., 2003b; Table 1 in Sandeman et al., 2004; Chapter 2).
TM0-239-(A-D)
Geochemical and isotopic sample location (Komatiite horizon)
Geochemical and isotopic sample location (Basalt horizon)
Proterozoic
≤ 2496 Ma Orthoquartzite/quartz arenite
ca. 1820 Ma biotite+magnetite±fluorite monzogranite/granodiorite
Archean
Undifferentiated ca. 2610-2580 Ma mafic-felsic intrusive rocks
ca. 2718 Ma hornblende-biotite tonalite/granodiorite (central tonalite (CT))
Orthoquartzite/quartz arenite
Semipelitic paragneiss, diatexites and metatexites
PAg undifferentiated, including: semipelite, psammite, conglomerate, pelite, phyllite, and iron formation
Komatiite
Basalt and co-genetic gabbro
Committee Bay
Ellice Hills (NTS 56P)
68°N
≤ 2687 ± 10 Ma (D)
Walker Lake Intrusive Complex southern sub-domain
Arrowsmith River (NTS 56O-south)
Northern sub-domain
≤ 2691 ± 16 Ma (D)
Central Prince Albert Group sub-domain
2711 ± 3 Ma (CV)
≤ 2722 ± 11 Ma (D)
2706 +5/-4 Ma (CV)
Walker Lake (NTS 56J-north)
0 10 20 30 km
Laughland Lake (NTS 56K)
Northern sub-domain
2712 ± 2 Ma (CV)
TM-1-H and G
H-1337
2729.5 ± 0.9 Ma (CV)
TM0-239-(A-D)
CS0-264-B
TM0-263 Komatiites
2732 +8/-2 Ma (CV)
CT
2688 ± 6 Ma (D)
TM0-285-(C, C-3, D-1)
2718 ± 2 Ma (CP)
94°W

Figure 3-2

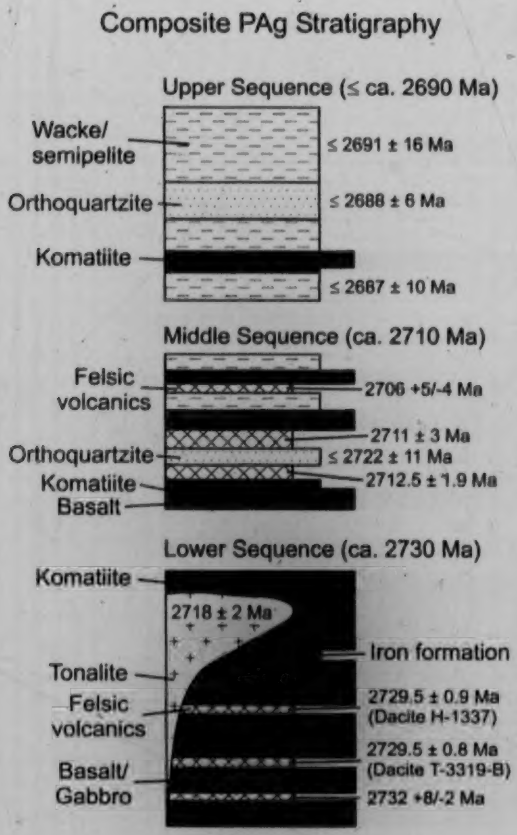

Composite PAg Stratigraphy
Upper Sequence (≤ ca. 2690 Ma)
Wacke/ semipelite
≤ 2691 ± 16 Ma
Orthoquartzite
≤ 2688 ± 6 Ma
Komatiite
≤ 2687 ± 10 Ma
Middle Sequence (ca. 2710 Ma)
Felsic volcanics
2706 +5/-4 Ma
2711 ± 3 Ma
Orthoquartzite
≤ 2722 ± 11 Ma
Komatiite
2712.5 ± 1.9 Ma
Basalt
Lower Sequence (ca. 2730 Ma)
Komatiite
2718 ± 2 Ma
Iron formation
Tonalite
Felsic volcanics
2729.5 ± 0.9 Ma (Dacite H-1337)
2729.5 ± 0.8 Ma (Dacite T-3319-B)
Basalt/ Gabbro
2732 +8/-2 Ma

Figure 3-3

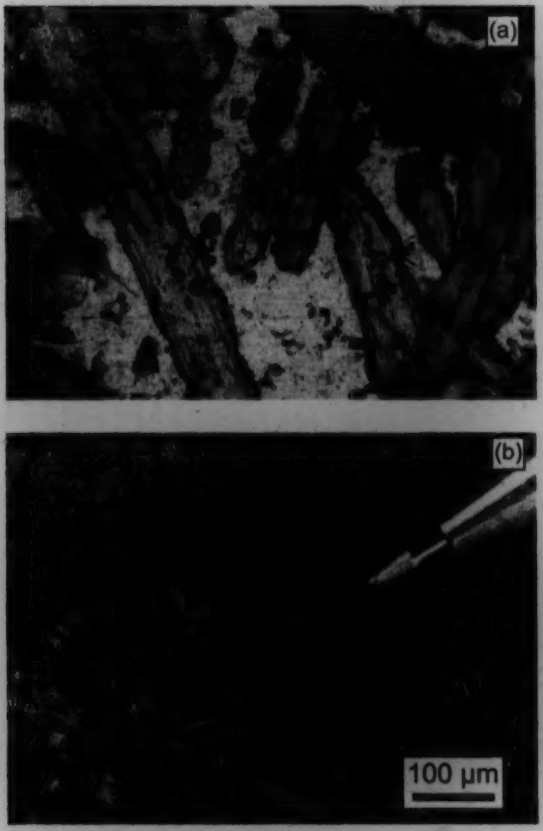

Figure 3-4

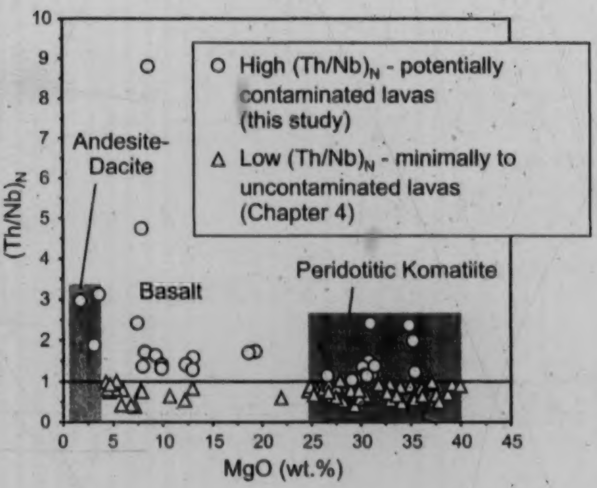
10
9
8
7
6
5
4
3
2
1
0
(Th/Nb)$_N$
0
5
10
15
20
25
30
35
40
45
MgO (wt.%)
Andesite-Dacite
Basalt
Peridotitic Komatiite
○ High (Th/Nb)$_N$ - potentially contaminated lavas (this study)
△ Low (Th/Nb)$_N$ - minimally to uncontaminated lavas (Chapter 4)

Figure 3-5

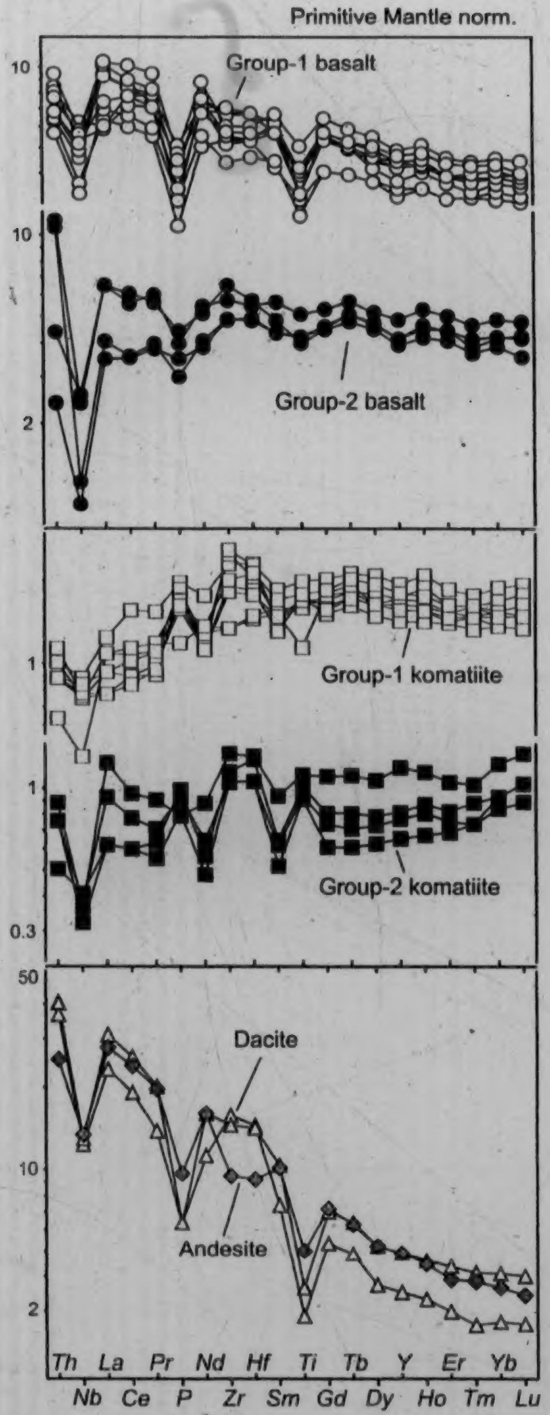
Primitive Mantle norm.
10
Group-1 basalt
10
2
Group-2 basalt
1
Group-1 komatiite
1
0.3
Group-2 komatiite
50
Dacite
10
Andesite
2
Th
Nb
La
Ce
Pr
P
Nd
Zr
Hf
Sm
Ti
Gd
Tb
Dy
Y
Ho
Er
Tm
Yb
Lu

Figure 3-6

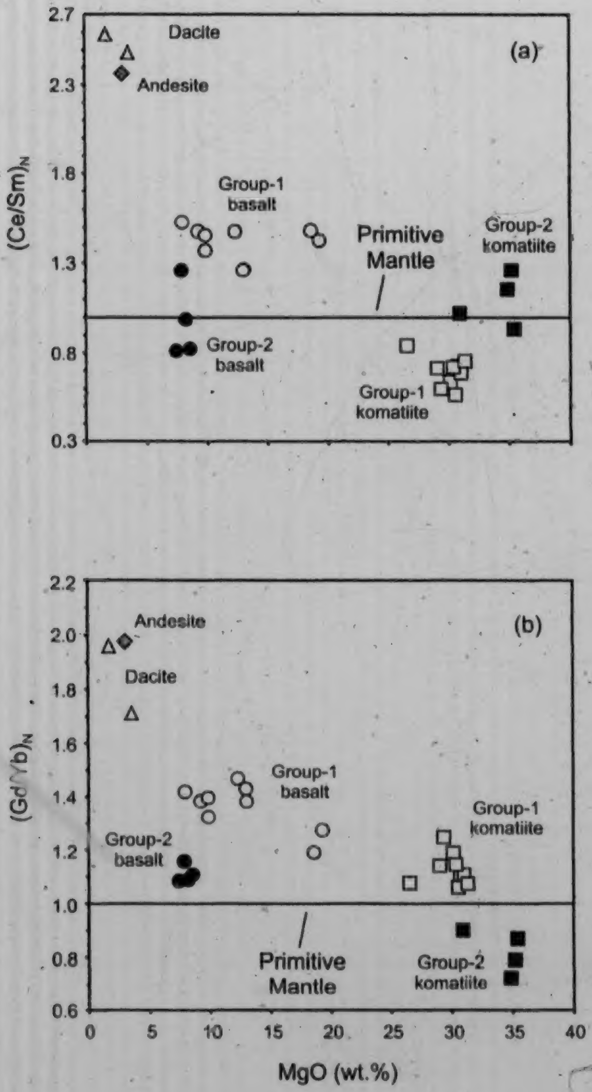

(a)
2.7
2.3
1.8
1.3
0.8
0.3
(Ce/Sm)$_N$
Dacite
Andesite
Group-1 basalt
Primitive Mantle
Group-2 komatiite
Group-2 basalt
Group-1 komatiite
(b)
2.2
2.0
1.8
1.6
1.4
1.2
1.0
0.8
0.6
(Gd/Yb)$_N$
Andesite
Dacite
Group-1 basalt
Group-1 komatiite
Group-2 basalt
Primitive Mantle
Group-2 komatiite
0
5
10
15
20
25
30
35
40
MgO (wt.%)

Figure 3-7

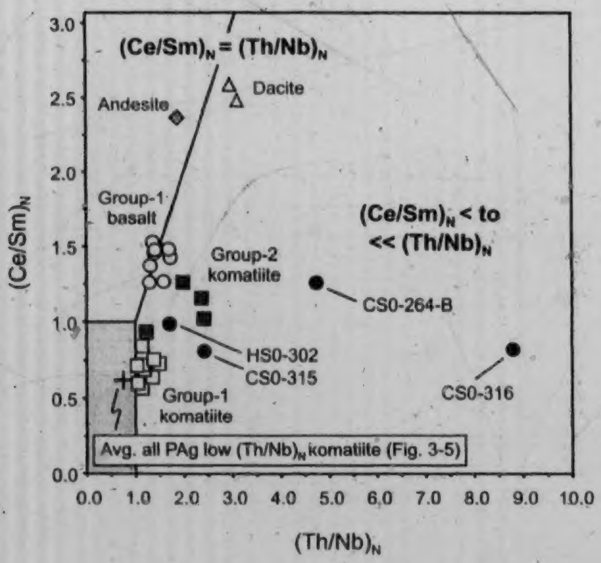
(Ce/Sm)$_N$ = (Th/Nb)$_N$
Dacite
Andesite
Group-1 basalt
Group-2 komatiite
(Ce/Sm)$_N$ < to << (Th/Nb)$_N$
CS0-264-B
HS0-302
CS0-315
CS0-316
Group-1 komatiite
Avg. all PAg low (Th/Nb)$_N$ komatiite (Fig. 3-5)
(Ce/Sm)$_N$
(Th/Nb)$_N$
0.0
0.5
1.0
1.5
2.0
2.5
3.0
0.0
1.0
2.0
3.0
4.0
5.0
6.0
7.0
8.0
9.0
10.0

Figure 3-8

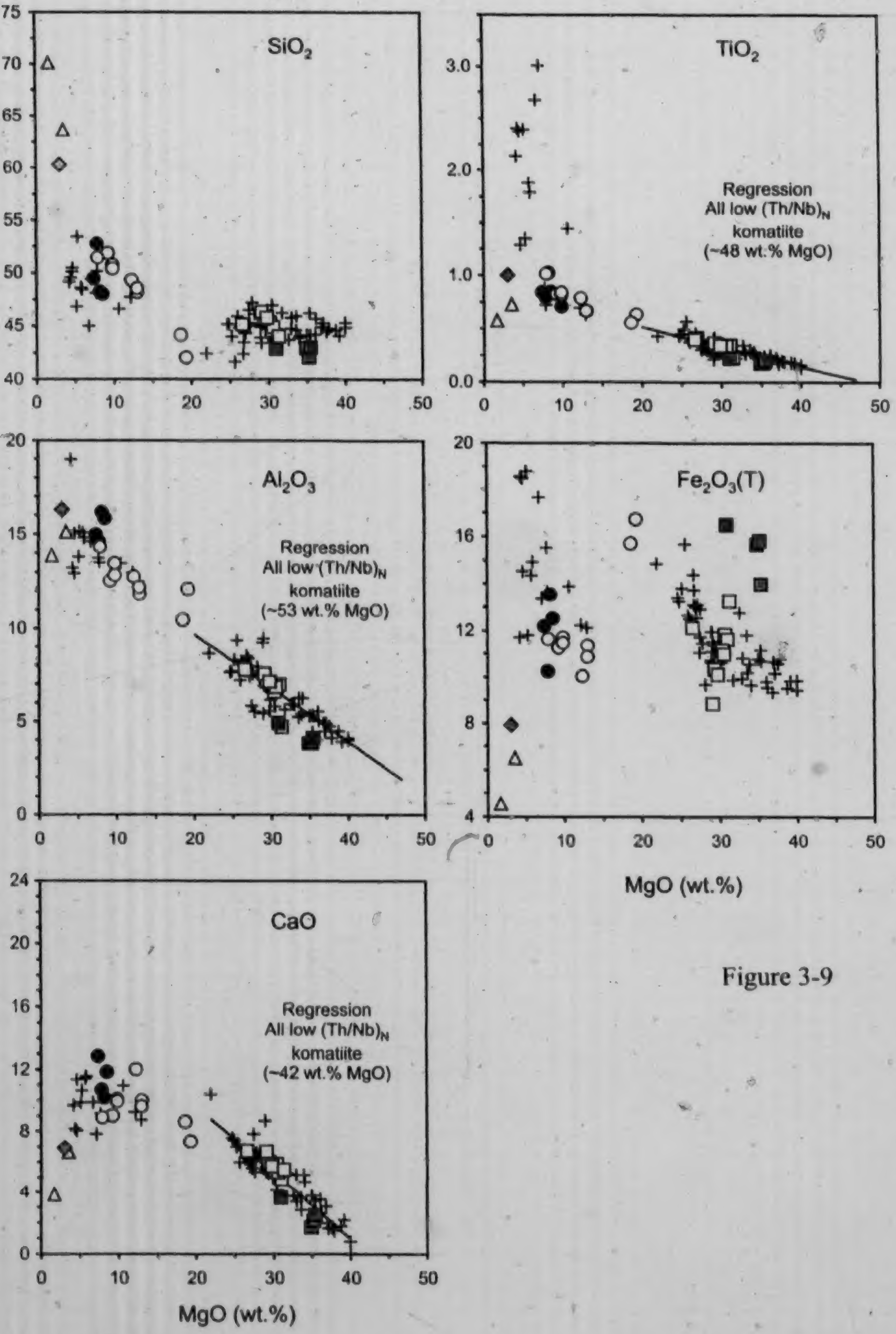
SiO$_2$
TiO$_2$
Regression
All low (Th/Nb)$_N$
komatiite
(~48 wt.% MgO)
Al$_2$O$_3$
Regression
All low (Th/Nb)$_N$
komatiite
(~53 wt.% MgO)
Fe$_2$O$_3$(T)
CaO
Regression
All low (Th/Nb)$_N$
komatiite
(~42 wt.% MgO)
MgO (wt.%)
MgO (wt.%)
75
70
65
60
55
50
45
40
3.0
2.0
1.0
0.0
20
15
10
5
0
20
16
12
8
4
24
20
16
12
8
4
0
0
10
20
30
40
50

Figure 3-9

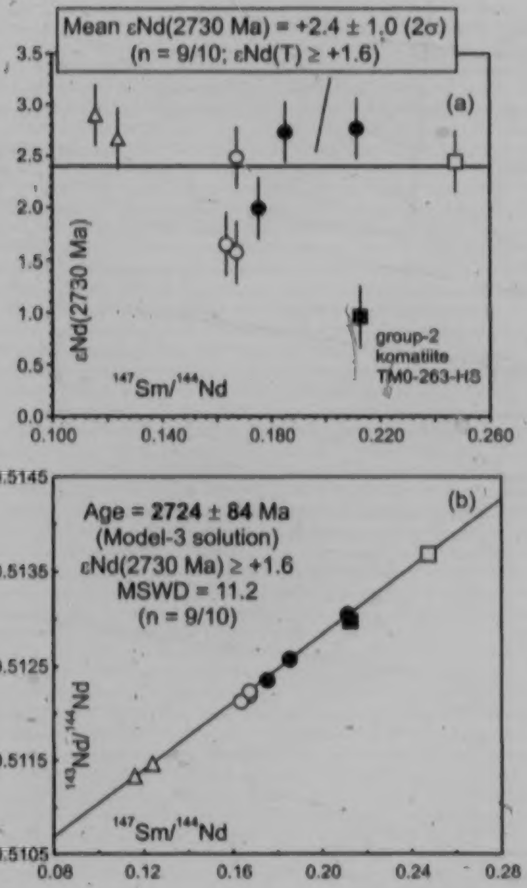
Mean εNd(2730 Ma) = +2.4 ± 1.0 (2σ)
(n = 9/10; εNd(T) ≥ +1.6)
(a)
εNd(2730 Ma)
147Sm/144Nd
group-2
komatiite
TM0-263-HS
0.0
0.5
1.0
1.5
2.0
2.5
3.0
3.5
0.100
0.140
0.180
0.220
0.260
(b)
Age = 2724 ± 84 Ma
(Model-3 solution)
εNd(2730 Ma) ≥ +1.6
MSWD = 11.2
(n = 9/10)
143Nd/144Nd
147Sm/144Nd
0.5105
0.5115
0.5125
0.5135
0.5145
0.08
0.12
0.16
0.20
0.24
0.28

Figure 3-10

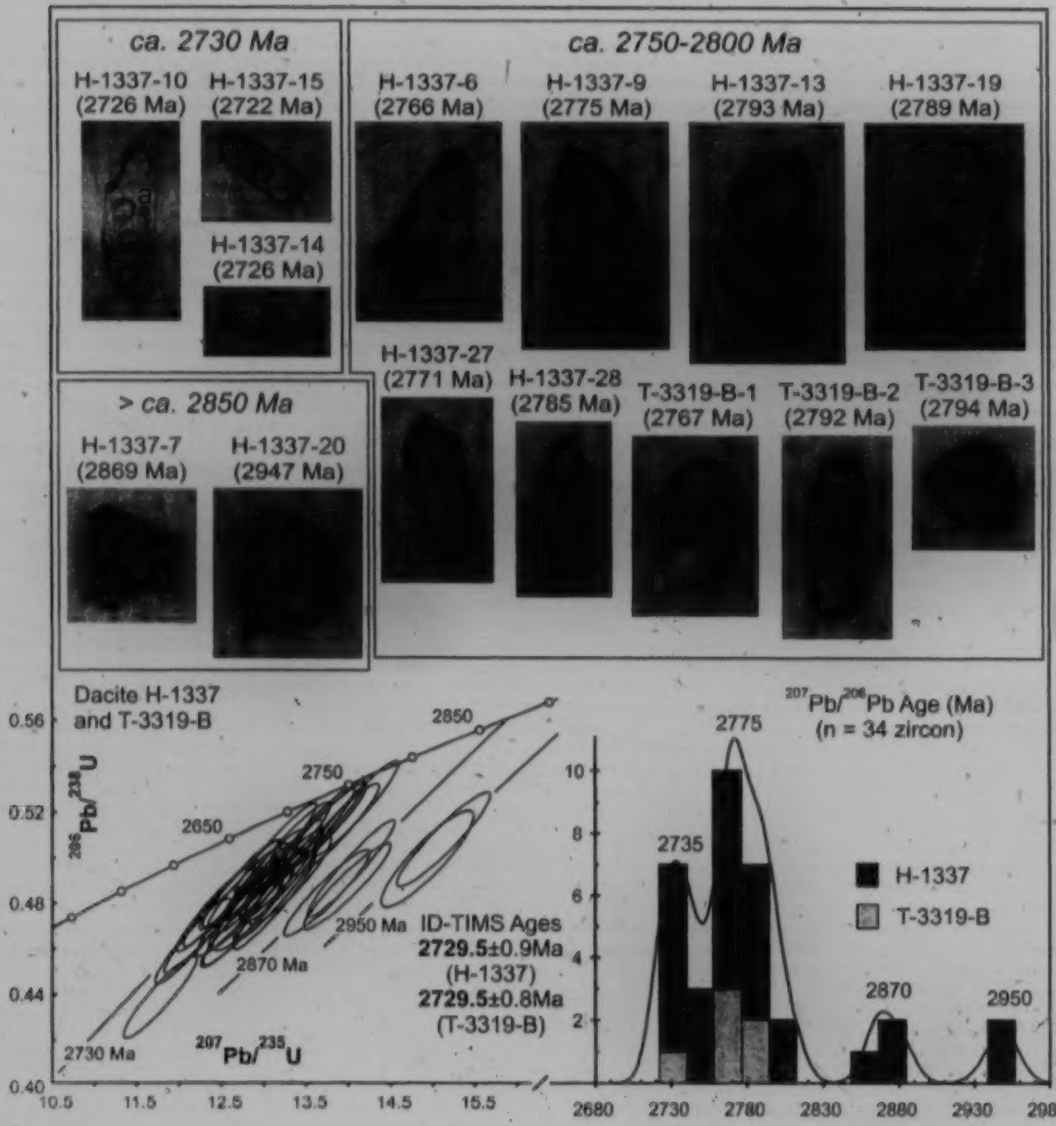
ca. 2730 Ma
H-1337-10 (2726 Ma)
H-1337-15 (2722 Ma)
H-1337-14 (2726 Ma)
ca. 2750-2800 Ma
H-1337-6 (2766 Ma)
H-1337-9 (2775 Ma)
H-1337-13 (2793 Ma)
H-1337-19 (2789 Ma)
H-1337-27 (2771 Ma)
H-1337-28 (2785 Ma)
T-3319-B-1 (2767 Ma)
T-3319-B-2 (2792 Ma)
T-3319-B-3 (2794 Ma)
> ca. 2850 Ma
H-1337-7 (2869 Ma)
H-1337-20 (2947 Ma)
Dacite H-1337 and T-3319-B
$^{206}Pb/^{238}U$
$^{207}Pb/^{235}U$
0.56
0.52
0.48
0.44
0.40
10.5
11.5
12.5
13.5
14.5
15.5
2850
2750
2650
2950 Ma
2870 Ma
2730 Ma
ID-TIMS Ages
2729.5±0.9Ma (H-1337)
2729.5±0.8Ma (T-3319-B)
$^{207}Pb/^{206}Pb$ Age (Ma) (n = 34 zircon)
2775
2735
2870
2950
10
8
6
4
2
H-1337
T-3319-B
2680
2730
2780
2830
2880
2930
2980

Figure 3-11

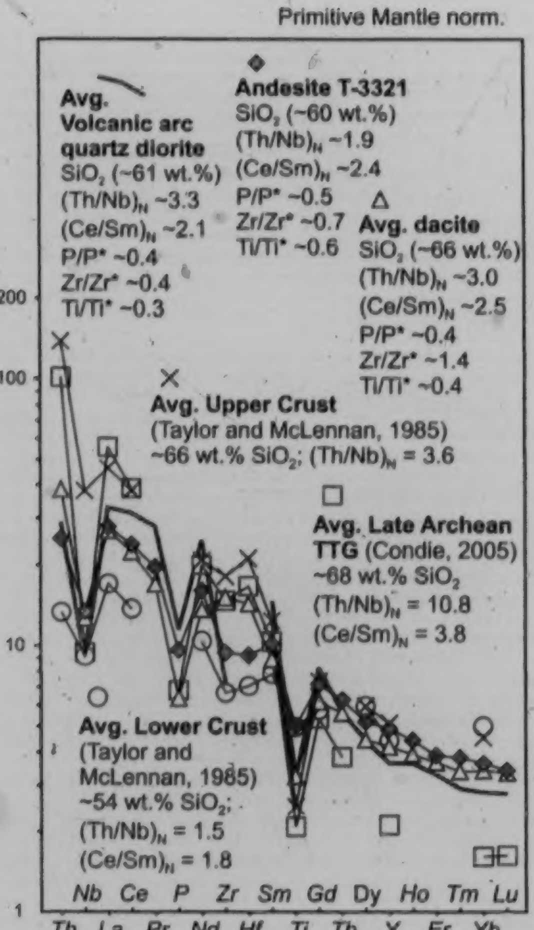
Primitive Mantle norm.
Avg. Volcanic arc quartz diorite
SiO₂ (~61 wt.%)
(Th/Nb)N ~3.3
(Ce/Sm)N ~2.1
P/P* ~0.4
Zr/Zr* ~0.4
Ti/Ti* ~0.3
Andesite T-3321
SiO₂ (~60 wt.%)
(Th/Nb)N ~1.9
(Ce/Sm)N ~2.4
P/P* ~0.5
Zr/Zr* ~0.7
Ti/Ti* ~0.6
Avg. dacite
SiO₂ (~66 wt.%)
(Th/Nb)N ~3.0
(Ce/Sm)N ~2.5
P/P* ~0.4
Zr/Zr* ~1.4
Ti/Ti* ~0.4
Avg. Upper Crust
(Taylor and McLennan, 1985)
~66 wt.% SiO₂; (Th/Nb)N = 3.6
Avg. Late Archean TTG (Condie, 2005)
~68 wt.% SiO₂
(Th/Nb)N = 10.8
(Ce/Sm)N = 3.8
Avg. Lower Crust
(Taylor and McLennan, 1985)
~54 wt.% SiO₂;
(Th/Nb)N = 1.5
(Ce/Sm)N = 1.8
200
100
10
1
Nb Ce P Zr Sm Gd Dy Ho Tm Lu
Th La Pr Nd Hf Ti Tb Y Er Yb

Figure 3-12

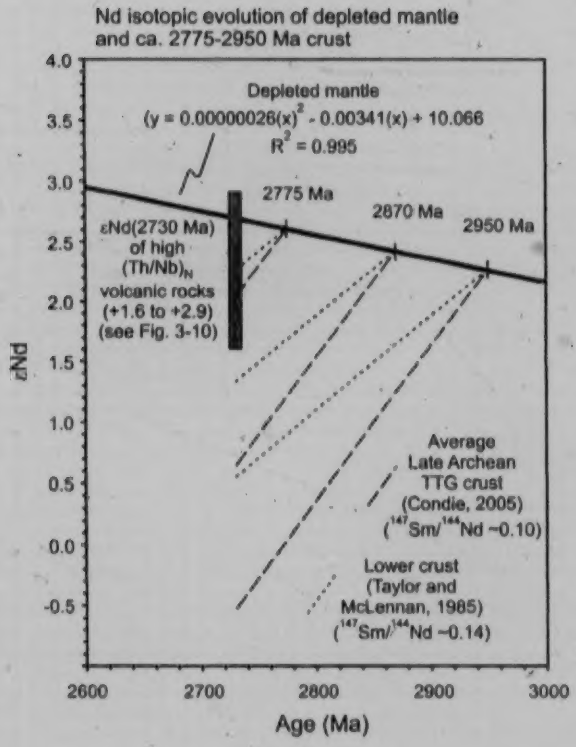
Nd isotopic evolution of depleted mantle and ca. 2775-2950 Ma crust
Depleted mantle
(y = 0.00000026(x)^2 - 0.00341(x) + 10.066
R^2 = 0.995
2775 Ma
2870 Ma
2950 Ma
εNd(2730 Ma) of high (Th/Nb)N volcanic rocks (+1.6 to +2.9) (see Fig. 3-10)
Average Late Archean TTG crust (Condie, 2005) (147Sm/144Nd ~0.10)
Lower crust (Taylor and McLennan, 1985) (147Sm/144Nd ~0.14)
εNd
4.0
3.5
3.0
2.5
2.0
1.5
1.0
0.5
0.0
-0.5
2600
2700
2800
2900
3000
Age (Ma)

Figure 3-13

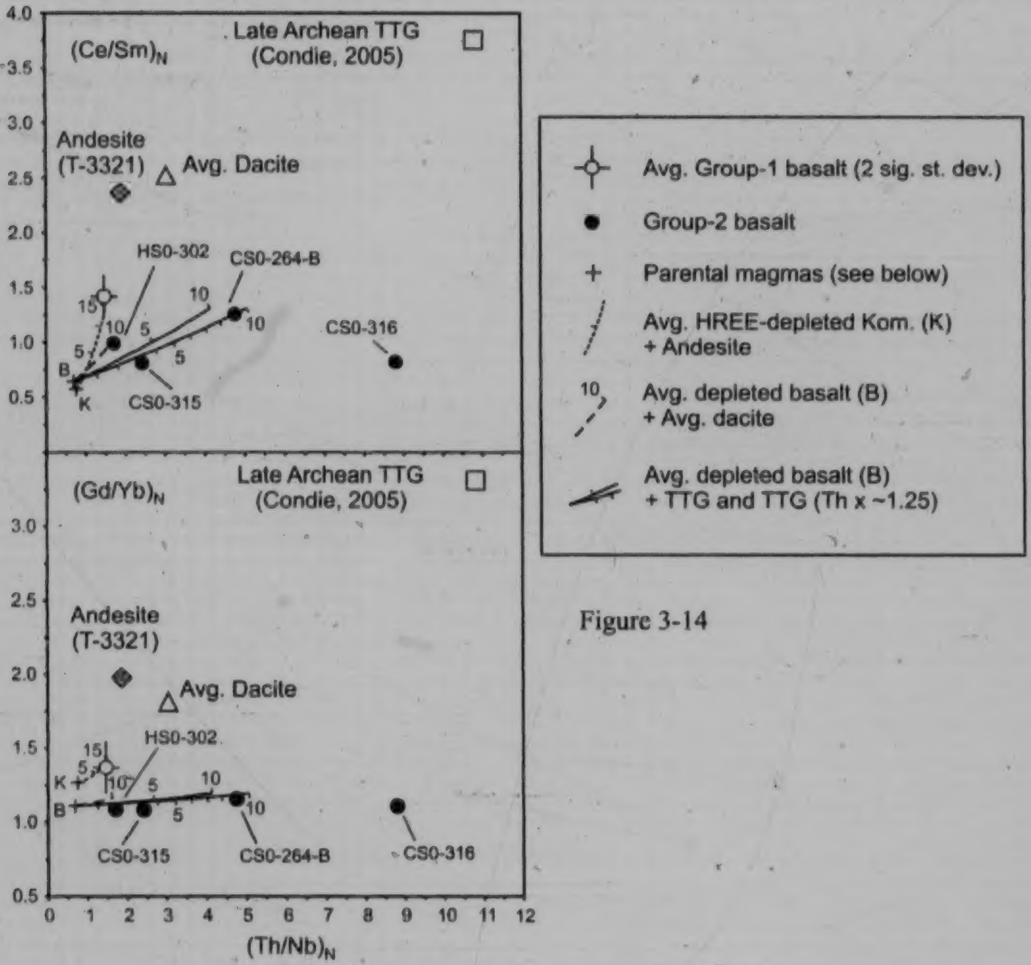
(Ce/Sm)N
Late Archean TTG (Condie, 2005)
Andesite (T-3321)
Avg. Dacite
HS0-302
CS0-264-B
CS0-316
CS0-315
15
10
5
B
K
4.0
3.5
3.0
2.5
2.0
1.5
1.0
0.5
(Gd/Yb)N
Late Archean TTG (Condie, 2005)
Andesite (T-3321)
Avg. Dacite
HS0-302
CS0-315
CS0-264-B
CS0-316
3.0
2.5
2.0
1.5
1.0
0.5
0
1
2
3
4
5
6
7
8
9
10
11
12
(Th/Nb)N
Avg. Group-1 basalt (2 sig. st. dev.)
Group-2 basalt
Parental magmas (see below)
Avg. HREE-depleted Kom. (K) + Andesite
Avg. depleted basalt (B) + Avg. dacite
Avg. depleted basalt (B) + TTG and TTG (Th x ~1.25)

Figure 3-14

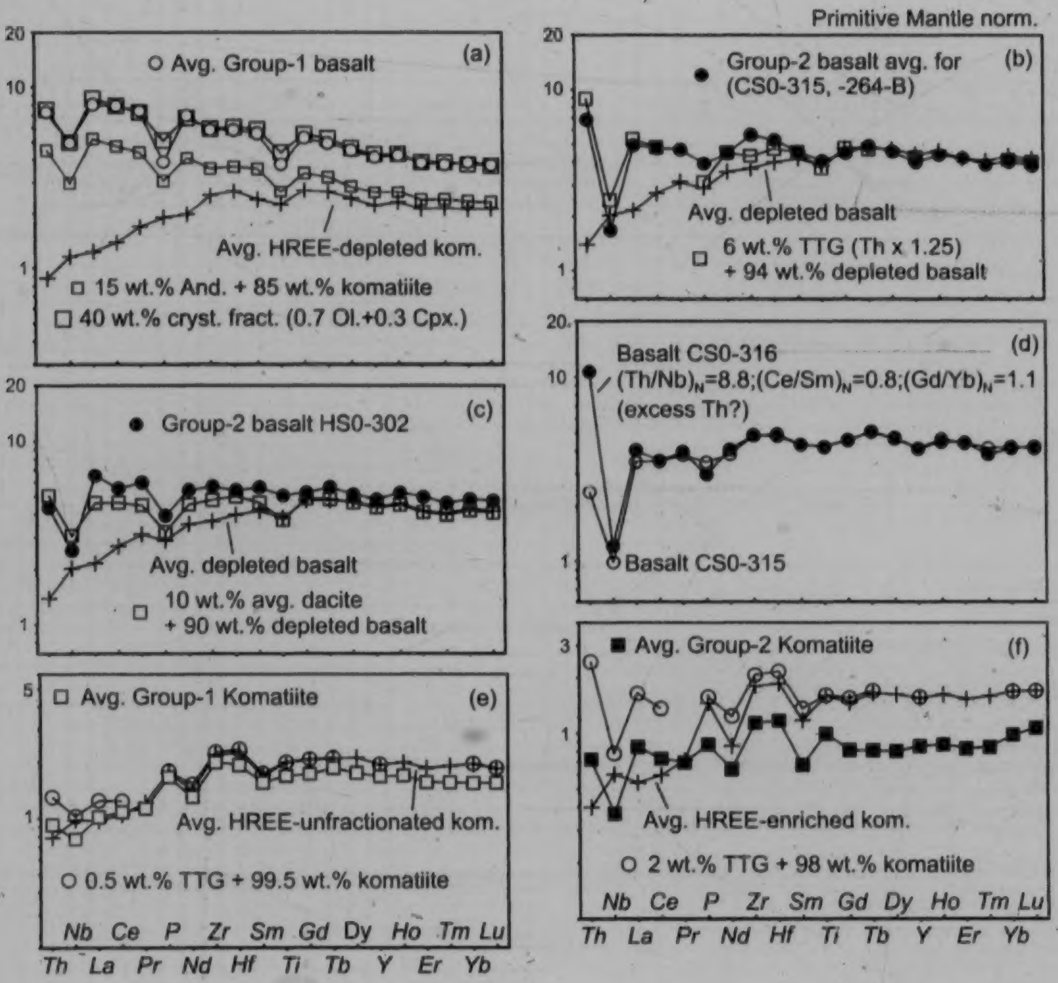
Primitive Mantle norm.
(a)
○ Avg. Group-1 basalt
Avg. HREE-depleted kom.
□ 15 wt.% And. + 85 wt.% komatiite
□ 40 wt.% cryst. fract. (0.7 Ol.+0.3 Cpx.)
(b)
● Group-2 basalt avg. for (CS0-315, -264-B)
Avg. depleted basalt
□ 6 wt.% TTG (Th x 1.25) + 94 wt.% depleted basalt
(c)
● Group-2 basalt HS0-302
Avg. depleted basalt
□ 10 wt.% avg. dacite + 90 wt.% depleted basalt
(d)
Basalt CS0-316
(Th/Nb)N=8.8;(Ce/Sm)N=0.8;(Gd/Yb)N=1.1
(excess Th?)
Basalt CS0-315
(e)
□ Avg. Group-1 Komatiite
Avg. HREE-unfractionated kom.
○ 0.5 wt.% TTG + 99.5 wt.% komatiite
(f)
■ Avg. Group-2 Komatiite
Avg. HREE-enriched kom.
○ 2 wt.% TTG + 98 wt.% komatiite
20
10
1
5
3
Nb Ce P Zr Sm Gd Dy Ho Tm Lu
Th La Pr Nd Hf Ti Tb Y Er Yb

Figure 3-15

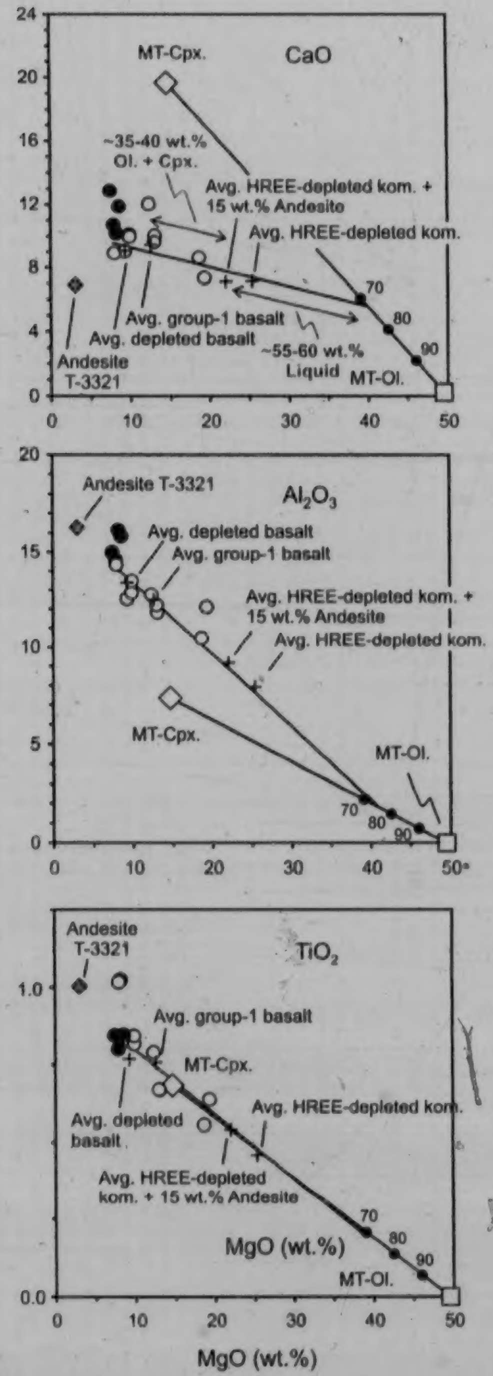
CaO
MT-Cpx.
~35-40 wt.%
Ol. + Cpx.
Avg. HREE-depleted kom. +
15 wt.% Andesite
Avg. HREE-depleted kom.
70
80
90
Avg. group-1 basalt
Avg. depleted basalt
~55-60 wt.%
Liquid
MT-Ol.
Andesite
T-3321
24
20
16
12
8
4
0
0
10
20
30
40
50
Al$_2$O$_3$
Andesite T-3321
Avg. depleted basalt
Avg. group-1 basalt
Avg. HREE-depleted kom. +
15 wt.% Andesite
Avg. HREE-depleted kom.
MT-Cpx.
MT-Ol.
70
80
90
20
15
10
5
0
0
10
20
30
40
50
TiO$_2$
Andesite
T-3321
Avg. group-1 basalt
MT-Cpx.
Avg. depleted
basalt
Avg. HREE-depleted kom.
Avg. HREE-depleted
kom. + 15 wt.% Andesite
70
80
90
MgO (wt.%)
MT-Ol.
1.0
0.0
0
10
20
30
40
50
MgO (wt.%)

Figure 3-16

REFERENCES

Arndt, N. T. (1999). Why was flood volcanism on submerged continental platforms so common in the Precambrian? *Precambrian Research* **97**, 155-164.

Arndt, N. T., Albarède, F. & Nisbet, E. G. (1997). Mafic and Ultramafic Magmatism. In: de Wit, M. J. & Ashwal, L. D. (eds) *Greenstone Belts*. Oxford: Oxford University Press, pp. 233-254.

Arndt, N. T., Naldrett, A. J. & Pyke, D. R. (1977). Komatiitic and Iron-rich Tholeiitic Lavas of Munro Township, Northeast Ontario. *Journal of Petrology* **18**, 319-369.

Arndt, N. T. & Nisbet, E. G. (1982). What is a komatiite? In: Arndt, N. T. & Nisbet, E. G. (eds) *Komatiites*. London, UK: George Allen & Unwin, Ltd., pp. 19-27.

Ayer, J., Amelin, Y., Corfu, F., Kamo, S., Ketchum, J., Kwok, K., Trowell, N. (2002). Evolution of the southern Abitibi greenstone belt based on U-Pb geochronology: autochthonous volcanic construction followed by plutonism, regional deformation and sedimentation. *Precambrian Research* **115**, 63-95.

Berman, R. G., Sanborn-Barrie, M., Stern, R. A. & Carson, C. J. (2005). Tectonometamorphism at *ca*. 2.35 and 1.85 Ga in the Rae Domain, western Churchill Province, Nunavut, Canada: insights from structural, metamorphic and *in situ* geochronological analysis of the southwestern Committee Bay Belt. *Canadian Mineralogist* **43**, 409-442.

Bethune, K. M. & Scammell, R. J. (2003). Geology, geochronology, and geochemistry of Archean rocks in the Eqe Bay area, north-central Baffin Island, Canada: constraints on the depositional and tectonic history of the Mary River Group of northeastern Rae Province. *Canadian Journal of Earth Sciences* **40**, 1137-1167.

Blake, T. S. (1993). Late Archaean crustal extension, sedimentary basin formation, flood basalt volcanism and continental rifting: the Nullagine and Mount Jope Supersequences Western Australia. *Precambrian Research* **60**, 185-241.

Blenkinsop, T. G., Fedo, C. M., Bickle, M. J., Eriksson, K. A., Martin, A., Nisbet, E. G. & Wilson, J. F. (1993). Ensialic origin for the Ngezi Group, Belingwe greenstone belt, Zimbabwe. *Geology* **21**, 1135-1138.

Campbell, I. H. & Griffiths, R. W. (1993). The evolution of the mantle's chemical structure. *Lithos* **30**, 389-399.

Campbell, I. H., Griffiths, R. W. & Hill, R. I. (1989). Melting in an Archaean mantle plume: heads it's basalts, tails it's komatiites. *Nature* **339**, 697-699.

Carson, C. J., Berman, R. G., Stern, R. A., Sanborn-Barrie, M., Skulski, T. & Sandeman, H. A. I. (2004). Age constraints on the Paleoproterozoic tectonometamorphic history of the Committee bay region, western Churchill Province, Canada: evidence from zircon and in situ monazite SHRIMP geochronology. *Canadian Journal of Earth Sciences* **41**, 1049-1076.

Chase, C. G. & Patchett, P. J. (1988). Stored mafic/ultramafic crust and early Archean mantle depletion. *Earth and Planetary Science Letters* **91**, 66-72.

Chauvel, C., Arndt, N. T., Kielinzcuk, S. & Thom, A. (1987). Formation of Canadian 1.9 Ga old continental crust I: Nd isotopic data. *Canadian Journal of Earth Sciences* **24**, 396-406.

Compston, W., Williams, I. S., Campbell, I. H. & Gresham, J. J. (1986). Zircon xenocrysts from the Kambalda volcanics, age constraints and direct evidence for older continental crust below the Kambalda-Norseman greenstones. *Earth and Planetary Science Letters* **76**, 299-311.

Condie, K. C. (2005). TTGs and adakites: are they both slab melts? *Lithos* **80**, 33-44.

Cousens, B. L. (2000). Geochemistry of the Archean Kam Group, Yellowknife Greenstone Belt, Slave Province, Canada. *Journal of Geology* **108**, 181-197.

Davis, W. J. & Zaleski, E. (1998). Geochronological investigations of the Woodburn Lake Group, western Churchill Province, Northwest Territories: preliminary results. In: Radiogenic age and isotopic studies: Report 11. Geological Survey of Canada, Current Research 1998-F, pp. 89-97.

Grove, T. L., Parman, S. W. & Dann, J. C. (1999). Conditions of magma generation for Archean komatiites from the Barberton Mountainland, South Africa. In: Fei, Y., Bertka, C. M. & Mysen, B. O. (eds) *Mantle Petrology: Field Observations and High Pressure Experimentation: A Tribute to Francis R. (Joe) Boyd.* The Geochemical Society, Special Publication No. 6, pp. 155-167.

Henderson, J. B. & Loveridge, W. D. (1990). Inherited Archean zircon in the Proterozoic Thelon Tectonic Zone: U-Pb geochronology of the Campbell granite, south of McDonald fault, District of Mackenzie, Northwest Territories. In: Radiogenic age and isotopic studies: Report 3. Geological Survey of Canada, Paper 89-2, pp. 63-70.

Henderson, J. B. & Thériault, R. J. (1994). U-Pb zircon evidence for circa 3.1 Ga crust south of the McDonald Fault, northwestern Canadian Shield, Northwest Territories. In: Radiogenic age and isotopic studies: Report 8. Geological Survey of Canada, Current Research 1994-F, pp. 43-47.

Herzberg, C. (1995). Generation of plume magmas through time: an experimental perspective. *Chemical Geology* **126**, 1-16.

Hunter, M. A., Bickle, M. J., Nisbet, E. G., Martin, A. & Chapman, H. J. (1998). Continental extensional setting for the Archean Belingwe Greenstone Belt, Zimbabwe. *Geology* **26**, 883-886.

Jackson, G. D., Hunt, P. A., Loveridge, W. D. & Parrish, R. R. (1990). Reconnaissance geochronology of Baffin Island, N.W.T. In: Radiogenic age and isotopic studies: Report 3. Geological Survey of Canada, Paper 89-2, pp. 123-148.

Jackson, G. D. & Taylor, F. C. (1972). Correlation of major Aphebian rock units in the Canadian Shield. *Canadian Journal of Earth Sciences* **9**, 1650-1699.

Jaffey, A. H., Flynn, K. F., Glendenin, L. E., Bentley, W. C. & Essling, A. M. (1971). Precision measurement of half-lives and specific activities of ^{235}U and ^{238}U. *Physics Review* **4**, 1889-1906.

Jochum, K. P., Arndt, N. T. & Hofmann, A. W. (1991). Nb-Th-La in komatiites and basalts: constraints on komatiite petrogenesis and mantle evolution. *Earth and Planetary Science Letters* **107**, 272-289.

Kerr, A. C., White, R. V. & Saunders, A. D. (2000). LIP Reading: Recognizing Oceanic Plateaux in the Geological Record. *Journal of Petrology* **41**, 1041-1056.

Lahaye, Y. & Arndt, N. (1996). Alteration of a Komatiite Flow from Alexo, Ontario, Canada. *Journal of Petrology* **37**, 1261-1284.

Lahaye, Y., Arndt, N., Byerly, G., Chauvel, C., Fourcade, S. & Grau, G. (1995). The influence of alteration on the trace-element and Nd isotopic compositions of komatiites. *Chemical Geology* **126**, 43-64.

LeCheminant, A. N. & Roddick, J. C. (1991). U-Pb zircon evidence for widespread 2.6 Ga felsic magmatism in the central Disrict of Keewatin, N.W.T. In: Radiogenic age and isotopic studies: Report 4. Geological Survey of Canada, Paper 90-2, pp. 91-99.

Lécuyer, C., Grau, G., Anhaeusser, C. R. & Fourcade, S. (1994). The origin of fluids and the effects of metamorphism on the primary chemical compositions of Barberton komatiites: New evidence from geochemical (REE) and isotopic (Nd, O, H, ^{39}Ar/^{40}Ar) data. *Geochimica et Cosmochimica Acta* **58**, 969-984.

Ludwig, K. R. (1992). ISOPLOT – a plotting and regression program for radiogenic isotope data, version 2.57. U.S. Geological Survey Open File report 91, p. 445.

MacHattie, T. G. (2002). Petrogenesis of the Wathaman Batholith and LaRonge Domain plutons in the Reindeer Lake Area, Trans-Hudson Orogen, Saskatchewan. M.Sc. thesis, Memorial University of Newfoundland, St. John's, Nfld.

McDade, P., Blundy, J. D. & Wood, B. J. (2003). Trace element partitioning on the Tinaquillo Lherzolite solidus at 1.5 GPa. *Physics of the Earth and Planetary Interiors* **139**, 129-147.

McDonough, W. F. & Sun, S.-s. (1995). The Composition of the Earth. *Chemical Geology* **120**, 223-253.

Nelson, D. R., Trendall, A. F., de Laeter, J. R., Grobler, N. J. & Fletcher, I. R. (1992). A comparative study of the geochemical and isotopic systematics of late Archaean flood basalts from the Pilbara and Kaapvaal Cratons. *Precambrian Research* **54**, 231-256.

Nisbet, E. G., Cheadle, M. J., Arndt, N. T. & Bickle, M. J. (1993). Constraining the potentential temperature of the Archean mantle: A review of the evidence from komatiites. *Lithos* **30**, 291-307.

Polat, A. & Münker, C. (2004). Hf-Nd isotope evidence for contemporaneous subduction processes in the source of late Archean arc lavas from the Superior Province. *Chemical Geology* **213**, 403-429.

Puchtel, I. S., Hofmann, A. W., Mezger, K., Jochum, K. P., Shchipansky, A. A. & Samsonov, A. V. (1998). Oceanic plateau model for continental crustal growth in the Archaean: A case study from the Komstomuksha greenstone belt, NW Baltic Shield. *Earth and Planetary Science Letters* **155**, 57-74.

Salters, V. J. M. & Longhi, J. (1999). Trace element partitioning during the initial stages of melting beneath mid-ocean ridges. *Earth and Planetary Science Letters* **166**, 15-30.

Salters, V. J. M., Longhi, J. E. & Bizimis, M. (2002). Near mantle solidus trace element partitioning at pressures up to 3.4 GPa. *Geochemistry Geophysics Geosystems* **3**, 2001GC000148.

Sanborn-Barrie, M., Sandeman, H., Skulski, T., Brown, J., Young, M., MacHattie, T., Deyell, C., Carson, C., Panagapko, D. & Byrne, D. (2003). Structural geology of the northeastern Committee Bay belt, Ellce Hills area, central Nunavut. In: Current Research. Geological Survey of Canada, Paper 2003-C23.

Sanborn-Barrie, M., Skulski, T., Sandeman, H., Berman, R., Johnstone, S., MacHattie, T. & Hyde, D. (2002). Structural and metamorphic geology of the Walker Lake-Arrowsmith River area, Committee Bay belt, Nunavut. In: Current Research. Geological Survey of Canada, Paper 2002-C12.

Sandeman, H. A., Brown, J., Studnicki-Gizbert, C., MacHattie, T., Hyde, D., Johnstone, S., Greiner, E. & Plaza, D. (2001). Bedrock mapping in the Committee Bay Belt, Laughland Lake area, central mainland, Nunavut. In: Current Research. Geological Survey of Canada, Paper 2001-C12.

Schau, M. (1977). Komatiites and quartzites in the Archean Prince Albert Group. In: Baragar, W. R. A., Coleman, L. S. & Hall, J. M. (eds) *Volcanic Regimes in Canada*. Geological Association of Canada Special Publication 16, pp. 341-354.

Schau, M. (1982). Geology of the Prince Albert Group in parts of Walker Lake and Laughland Lake map areas, District of Keewatin. Geological Survey of Canada, Bulletin 337.

Simonetti, A., Heaman, L. M., Hartlaub, R. P., Creaser, R. A., MacHattie, T. G. & Böhm, C. (2005). U-Pb dating by laser ablation-MC-ICP-MS using a new multiple ion counting-faraday collector array. *J. Anal. At. Spectrom*, **20**, 677-686.

Skulski, T., Sanborn-Barrie, M. & Sandeman, H. (2003*a*). Geology, Walker Lake and Arrowsmith River Area, Nunavut. Geological Survey of Canada, Open File Map 3777, scale 1:100 000.

Skulski, T., Sandeman, H., MacHattie, T., Sanborn-Barrie, M., Rayner, N., & Byrne, D. (2003*b*). Tectonic setting of 2.73-2.7 Ga Prince Albert Group, Churchill Province, Nunavut. In: Program with Abstracts, Geological Association of Canada-Mineralogical Association of Canada annual meeting, Vancouver, B.C.

Skulski, T., Sandeman, H., Sanborn-Barrie, M., MacHattie, T., Hyde, D., Johnstone, S., Panagapko, D. & Byrne, D. (2002). Contrasting crustal domains in the Committee Bay belt, Walker Lake-Arrowsmith River area, central Nunavut. In: Current Research. Geological Survey of Canada, Paper 2002-C11.

Skulski, T., Sandeman, H., Sanborn-Barrie, M., MacHattie, T., Young, M., Carson, C., Berman, R., Brown, J., Rayner, N., Panagapko, D., Byrne, D. & Deyell, C. (2003*c*). Bedrock geology of the Ellice Hills map area and new constraints on the regional geology of the Committee Bay area, Nunavut. In: Current Research. Geological Survey of Canada, Paper 2003-C22.

Sproule, R. A., Lesher, C. M., Ayer, J. A., Thurston, P. C., Herzberg, C. T. (2002). Spatial and temporal variations in the geochemistry of komatiites and komatiitic basalts in the Abitibi greenstone belt. *Precambrian Research* **115**, 153-186.

Stein, M. & Hofmann, A. W. (1994). Mantle plumes and episodic crustal growth. *Nature* **372**, 63-68.

Storey, M., Mahoney, J. J., Kroenke, L. W. & Saunders, A. D. (1991). Are oceanic plateaus sites of komatiite formation? *Geology* **19**, 376-379.

Taylor, S. R. & McLennan, S. M. (1985). The Continental Crust: its Composition and Evolution. Blackwell, Oxford.

Thériault, R. J., Henderson, J. B. & Roscoe, S. M. (1994). Nd isotopic evidence for early to mid-Archean crust from high grade gneisses in the Queen Maud Block and south of the McDonald Fault, western Churchill Province, Northwest Territories. In: Radiogenic age and isotopic studies: Report 8. Geological Survey of Canada, Current Research 1994-F, pp. 37-42.

Walter, M. J. (1998). Melting of Garnet Peridotite and the Origin of Komatiite and Depleted Lithosphere. *Journal of Petrology* **39**, 29-60.

Whalen, J. B., Syme, E. C. & Stern, R. A. (1999). Geochemical and Nd isotopic evolution of Paleoproterozoic arc-type granitoid magmatism in the Flin Flon Belt, Trans-Hudson orogen, Canada. *Canadian Journal of Earth Sciences* **36**, 227-250.

Wilson, J. F., Nesbitt, R. W. & Fanning, M. (1995). Zircon geochronology of Archaean felsic sequences in the Zimbabwe Craton: A revision of greenstone stratigraphy and a model for crustal growth. In: Coward, M. P. & Ries, A. C. (eds) *Early Precambrian processes*. London: Geological Society of London Special Publication, pp. 109-126.

Wodicka, N., St-Onge, M. R., Scott, D. J. & Corrigan, D. (2002). Preliminary report on the U-Pb geochronology on the northern margin of the Trans-Hudson Orogen, central Baffin Island, Nunavut. In: Radiogenic age and isotopic studies: Report 15. Geological Survey of Canada, Current Research 2002-F7.

Yamashita, K. & Creaser, R. A. (1999). Geochemical and Nd isotopic constraints for the origin of Late Archean turbidites from the Yellowknife area, Northwest Territories, Canada. *Geochimica et Cosmochimica Acta*. **63**, 2579-2598.

Zaleski, E., Davis, W. J. & Sandeman, H. A. (2001). Continental extension, mantle magmas and basement-cover relationships. In: Extended Abstracts, Proceedings of the 4th International Archean Symposium, Perth, Australia, pp. 374-376.

Zanetti, A., Tiepolo, M., Oberti, R. & Vannucci, R. (2004). Trace-element partitioning in olivine: modeling of a complete data set from a synthetic hydrous basanite melt. *Lithos* **75**, 39-54.

Chapter 4. Generation of Archean Al-undepleted komatiite: Insights from ca. 2730 Ma mafic-ultramafic magmas within the lower Prince Albert group, Nunavut, Canada

INTRODUCTION

The existence of Late Archean (ca. 2.7 Ga) komatiite with very high-MgO contents (up to ~25-29 wt.%) has been well-established by detailed petrological and geochemical studies conducted on a handful of exceptionally well-preserved and globally distributed (from Canada, Africa and Australia) occurrences (Nisbet *et al.*, 1993). Since the MgO content of a "liquid" is a direct function of its temperature, these lavas would have erupted at the surface with temperatures between ~1520-1580 °C (Nisbet *et al.*, 1993) and, as such, are the hottest magmas known to have erupted on Earth. Chemically, these Archean high-MgO komatiite magmas are examples of the so called aluminum-undepleted (Nesbitt *et al.*, 1979) or "Munro-type" (Arndt, 1994) compositional variety of komatiite which are typically characterized, along with their high-MgO contents, by the following chemical features: (1) relatively low incompatible trace element abundances (e.g. $(Yb)_N$ ~1-2); (2) depletion in the most incompatible trace elements (e.g. $(Ce/Yb)_N < 1$)); (3) Al_2O_3/TiO_2 (wt.%) ratios similar to the primitive mantle (e.g. ~19-20); and (4) derivation from a mantle source region characterized by long-term depletion in Nd/Sm and Hf/Lu relative to the bulk earth (i.e. suprachondritic initial Nd and Hf isotopic compositions). Because this "type" of komatiite is the dominant manifestation of ultramafic magmatism occurring within ca. 2.7 Ga greenstone belts (e.g. Sproule *et al.*, 2002) it is imperative that their petrogenesis, along with generally larger volumes of associated tholeiitic basalt be accurately evaluated so that the thermal, chemical, petrological, and geodynamical significance of Al-undepleted komatiite and associated basalt magmatism at ca. 2.7 Ga be correctly interpreted.

High-pressure melting experiments employing relatively fertile, nominally anhydrous peridotites (e.g. lherzolites KLB-1 and KR-4003) indicate that in order to generate typical Al-undepleted Archean komatiite magmas, high degrees of melting are required (Takahashi & Scarfe, 1985; Takahashi, 1986; Herzberg, 1995; Herzberg & Zhang, 1996; Walter, 1998). Largely because of the high eruption and inferred mantle source temperatures, geodynamic models of high-MgO komatiite magma generation have almost universally been linked with mantle plumes (Campbell *et al.*, 1989; Campbell & Griffiths, 1993; Herzberg, 1995; Arndt *et al.*, 1997; Tomlinson *et al.*, 1999). In plume-based models, komatiite-bearing volcanic successions are either interpreted as remnants of accreted oceanic plateau (Storey *et al.*, 1991; Arndt *et al.*, 1997; Puchtel *et al.*, 1998; Kerr *et al.*, 2000), or alternatively, if evidence of a continental influence is present, comparisons are drawn with continental flood basalt provinces and continental rifting (Compston *et al.*, 1986; Nelson, 1992; Blake, 1993; Blenkinsop *et al.*, 1993; Hunter *et al.*, 1998; Arndt, 1999; Cousens, 2000; Bolhar *et al.*, 2003; Shimizu *et al.*, 2004; 2005). However, in many instances the presence of komatiite is the only evidence suggestive of the possible involvement of mantle plumes and, as such, the physical, chemical and thermal structure of inferred Archean mantle plumes is correspondingly poorly constrained. It is also unclear in many of these studies to what extent, if any, processes within the overriding lithosphere have in influencing potential mantle plumes, apart from simply acting as a barrier to continued decompression melting and as a contaminant to high-temperature magmas.

In this contribution we present major, trace element and Nd and Hf isotope geochemistry for uncontaminated komatiite and basalt from the lower Prince Albert group (PAg), a newly discovered, ca. 2730 Ma mafic-ultramafic volcanic succession dominated by Al-undepleted komatiite and located within the central/northeastern Rae domain of Nunavut, Canada (Fig. 4-1). The geochemical signals persevered within the lower PAg magmas provide a unique and detailed glimpse into the detailed setting and petrogenesis of Al-undepleted komatiite, the physical structure of thermally anomalous mantle upwellings (plumes), and insights into the broader scale thermal and chemical structure of the Archean mantle. A prominent role for the lithosphere is also established, and the importance of the juxtaposition of thick and thin lithosphere in both focusing mantel upwellings and also facilitating the achievement of exceptionally high extents of melting and prolific komatiite magmatism is demonstrated.

REGIONAL ARCHEAN GEOLOGY OF SUPRACRUSTAL BELTS WITHIN THE CENTRAL AND NORTHEASTERN RAE DOMAIN AND SETTING OF MAFIC-ULTRAMAFIC MAGMATISM

The central and northeastern Rae domain is a northeasterly-trending region of Archean crust located within the northernmost Canadian Shield in Nunavut. It contains an extensive, ~1400 km long and up to ~400 km wide, northeasterly-trending network of ca. 2.7 Ga clastic-dominated supracrustal belts characterized by their distinctive lithological associations of orthoquartzite and iron formation with komatiite (Fig. 4-1). From southwest to northeast the supracrustal network includes the Woodburn Lake (WLg), Prince Albert (PAg), and Mary River groups (MRg), respectively. These supracrustal belts are now recognized to be components of a much larger, co-genetic supracrustal network in which the predominant mafic-ultramafic and associated felsic volcanism began abruptly between ca. 2735-2730 Ma and persisted for ~40-45 m.y. until ca. 2690 Ma (see Fig. 2-9 and discussion in Chapter 2).

An extensional continental margin setting for the supracrustal belts within the central and northeastern Rae domain was proposed in Chapter 3 based upon three principal lines of evidence: (1) the rapid initiation of volcanism between ca. 2735-2730 Ma along the full ~1400 km strike length of the supracrustal network suggesting that lithospheric extension must have preceded and facilitated the initiation of volcanism; (2) the focused formation of the supracrustal belts upon relatively young (≤ 2.87 Ga) and juvenile crust adjacent to significantly more ancient crustal components to the west (≥ 3.13 Ga up to 3.3-3.8 Ga), and that are only well-recognized within the supracrustal corridor as detrital zircon; and (3) the juvenile, ca. 2750-2800 Ma basement to the lower PAg has major and trace element geochemical similarities to magmas formed in suprasubduction zone settings, and is interpreted to have formed within an intra-oceanic volcanic arc that was accreted to the older Rae crust between ca. 2750-2735 Ma (Chapter 3).

GENERAL GEOLOGY AND CHRONOSTRATIGRAPHY OF THE PAG

The general geology of the Rae domain southwest of Committee Bay (Fig. 4-1) containing supracrustal rocks of the PAg has been subdivided into three, northeast-trending crustal sub-domains based on lithological associations and/or metamorphic grade (Fig. 4-2; Sandeman *et al.*, 2001; Skulski *et al.*, 2002; 2003*c*). The central PAg sub-domain, is underlain by greenschist- to middle amphibolite-facies sedimentary and volcanic rocks of the PAg, rare intermediate syn-volcanic plutonic rocks, and voluminous cross-cutting, ca. 2610-2580 Ma intermediate-felsic plutonic rocks (Skulski *et al.*, 2003*a*; Chapter 2). The northern sub-domain consists of upper amphibolite-facies migmatitic paragneiss, metatexite and diatexite of the PAg intruded by ca. 2610-2580 Ma plutonic rocks (Sanborn-Barrie *et al.*, 2002; Sandeman *et al.*, 2001; Carson *et al.*, 2004). The southern sub-domain is entirely plutonic (Walker Lake intrusive complex of Sandeman *et al.*, 2001) and is dominated by ca. 2610 Ma K-feldspar megacrystic granodiorite and lesser, post-tectonic, ca. 1820 Ma biotite-magnetite-fluorite granite (Skulski *et al.*, 2003*c*). The major northeast-striking, southeast-dipping structural fabric of rocks exposed within the Committee Bay region (area depicted in Fig. 4-2) was produced during D_2-M_2 tectonometamorphism that culminated at ca. 1850 Ma (Carson *et al.*, 2004; Berman *et al.*, 2005). Earlier, pre-D_2 fabrics are predominantly north-striking, easterly-dipping, and associated with upright to westerly-vergent F_1 folds. The timing of D_1-M_1 is constrained to ca. 2350 Ma (Berman *et al.*, 2005). The ca. 2350 Ma and ca. 1850 Ma reworking of the region has been linked with orogenesis to the west (D_1-M_1), and to the south (D_2-M_2) (Sanborn-Barrie *et al.*, 2003; Carson *et al.*, 2004; Berman *et al.*, 2005), respectively.

Regional mapping and U-Pb zircon age dating of intermediate-felsic volcanic rocks and detrital zircon age dating of siliciclastic sedimentary rocks within the PAg (Fig. 4-2; Skulski *et al.*, 2002; Table 1 in Skulski *et al.*, 2003*a*; Table 1 in Sandeman *et al.*, 2004; Chapter 2) has provided the basis for its preliminary subdivision into three chronostratigraphic sequences (Fig. 4-3). These sequences include: (1) a lower, ca. 2730 Ma volcanic succession comprised of mafic, ultramafic, and rare intermediate-felsic volcanic rocks; (2) a middle, ca. 2710 Ma sequence comprised of siliciclastic sedimentary rocks and iron formation intercalated with mafic, ultramafic, and intermediate-felsic volcanic rocks; and (3) an upper, ≤ 2690 Ma sequence dominated by siliciclastic sedimentary rocks with occurrences of iron formation and komatiite. The lowermost PAg is constrained to have formed upon a relatively young and juvenile substrate of ca. 2750-2800 Ma crust as evidenced from xenocrystic zircons contained within ca. 2730 Ma felsic volcanic rocks, and the combined major, trace element, and Nd isotopic systematics of the lavas (see Chapter 3).

STRATIGRAPHY AND PETROLOGY OF THE LOWER PAG MAFIC AND ULTRAMAFIC VOLCANIC ROCKS

The mafic-ultramafic volcanic succession comprising the lower PAg is located within the southwest portion of the belt within the Laughland Lake area where it is well-exposed in two separate areas located upon the opposing southwest and northeast margins of the central tonalite (Fig. 4-2). These areas are informally referred to as the northeast (Fig. 4-4; NVZ) and southwest (Fig. 4-5; SVZ) volcanic zones, respectively. Together they expose ~300 km^2 of a volcanic stratigraphy that is dominated by high-MgO (≥ 25 wt.%) komatiite flows, lesser aphyric basalt (~4-13 wt.% MgO), and rare intermediate-felsic volcanic rocks and breccias (e.g. Fig. 4-7). Detailed mapping and geochemical sampling within the northeast and southwest volcanic zones (Figs. 4-4 and 4-5 and Fig. 3-2 in Chapter 3) has shown the lower PAg to be divisible into a lower, ~1 km thick horizon comprised of basalt overlain by a more voluminous, ~2 km thick volcanic horizon dominated by komatiite, but containing lesser amounts of basalt. High-precision

U-Pb zircon ages for felsic volcanic rocks intercalated with basalt within the SVZ (2729.5 ± 0.8 Ma; Fig. 4-5) and komatiite within the NVZ (2729.5 ± 0.9 Ma; Fig. 4-4) confirm the rapid transition from basalt- to komatiite-dominated volcanism (Chapter 2).

Komatiite

Two principal types of komatiite are recognized within the lower PAg, olivine spinifex-textured flows and non-spinifex-textured, polyhedral olivine-phyric flows and/or sills. The prominent spinifex-textured flows range in thickness from those as thin as ~0.3 m to those that approach ~100 m in total thickness, however, most are between ~2-10 metres thick. Olivine spinifex zones consist of random, acicular, and bladed olivine separated by plumose to spherulitic clinopyroxene, dendritic chromite, and glass (Fig. 4-6(a and b)). The tops of olivine spinifex-textured flows are a few to 10's of cm thick and consist of a complex network of polyhedral fractures separating cm- to sub-cm-sized spheroids of quenched komatiite and glassy shards. The bases of these flows are olivine-phyric and consist of variable amounts of loosely to closely packed, elongated to stubby olivine and minor chromite encased in a glassy matrix (Fig. 4-6(c)).

Komatiite flows/sills(?) lacking spinifex zones and/or recognizable flow tops are locally abundant within the lower PAg and, for the most part, are indistinguishable from the basal olivine-phyric zones of spinifex-textured flows. One noteworthy occurrence of olivine-phyric komatiite sampled as part of this study (flow #6 in Table 4-1) consists of alternating layers (metre- to 10's of metre-scale) of fine- to coarse-grained olivine-phyric komatiite in which the near vertical layering is at a very high angle to underlying and flanking spinifex-textured flows (Fig. 4-6(d)). This unit also contains numerous patches and layers of elongated (~5-15 cm) and branching harrisitic-olivine, a texture interpreted to be related to growth along the substrates of komatiite lava channels (e.g. Hill *et al.*, 1995; Perring *et al.*, 1995).

Basalt

Mafic magmatism within the basalt horizon is largely in the form of aphyric massive flows, however, co-genetic, medium- to coarse-grained gabbroic pods and sills are locally abundant. Basaltic rocks are commonly comprised of stubby to acicular (up to 500 μm) clinopyroxene crystals set in a matrix of plagioclase, and containing minor Fe-Ti oxides (Fig. 4-6(e)). Basaltic rocks within the komatiite horizon are, for the most part, petrologically indistinguishable from those described from the lower basalt horizon where massive, aphyric flows predominate. However, some flows do possess clinopyroxene spinifex-textured zones containing abundant and highly acicular clinopyroxene arranged into divergent cone-shaped aggregates up to 20-30 cm long.

GEOCHEMISTRY

Preliminaries

In Chapter 3, direct (xenocrystic zircon) and indirect (geochemical) evidence suggested that the lower PAg formed upon a substrate of juvenile, ca. 2750-2800 Ma continental crust. The amount of crustal contamination is detected by noticeable modifications to the incompatible trace element signatures of some basalt and komatiite and the primitive mantle normalized $(Th/Nb)_N$ ratio was used to subdivide the lower PAg magmas into two broad groups (Fig. 4-7): high $(Th/Nb)_N$ magmas ($\geq$ to $>>1$), interpreted to have interacted with or be directly generated from continental crust (Chapter 3); and low $(Th/Nb)_N$ magmas ($\leq$ to $<<$ 1), interpreted to represent uncontaminated or "minimally" contaminated magmas (this Chapter). The subdivision of low $(Th/Nb)_N$ basalt and komatiite employed in this study utilizes the mantle normalized ratios of light, middle, and heavy rare earth elements (LREE, MREE and HREE), although for komatiite only the MREE and HREE are used (e.g. $(Gd/Yb)_N$). In the following discussion, the trace element compositions and subdivisions of low $(Th/Nb)_N$ basalt and komatiite are presented first, followed by the major element data.

Trace elements and subdivision – mafic magmatism

As a group, low $(Th/Nb)_N$ basalt within the lower PAg (~4-13 wt.% MgO; Table 4-1) are characterized by an exceptional, relatively orderly, chemical variability with respect to incompatible trace element contents and ratios (e.g. Fig 4-8 to 4-10). Primarily for presentation of the data, they have been subdivided into four trace element groupings using $(Ce/Yb)_N$. These groups include three that display variable LREE-enrichment and HREE-depletion: the highly enriched group-1 basalt ($(Ce/Yb)_N$ ~7-9), moderately enriched group-2 basalt ($(Ce/Yb)_N$ ~2-4), and minimally enriched group-3 basalt ($(Ce/Yb)_N$ ~1.2-1.4). These groups are predominantly found within the basalt horizon. The fourth group, the depleted basalt, is comprised magmas that display LREE-depletion and minimal to moderate HREE-depletion ($(Ce/Yb)_N$ ~0.6-0.8). This group is found within the komatiite horizon.

Highly enriched group-1 basalt (EB-1)

The highly enriched group-1 basalt (EB-1) is comprised of three samples collected within the SVZ komatiite horizon (Table 4-1 and Fig. 4-5). When plotted on a primitive mantle normalized extended element diagram (Fig. 4-8) the elevated LREE contents of the EB-1 relative to Th and the HREE produces distinctive hump-shaped patterns. The degree of HREE-depletion relative to both the LREE and MREE ($(Ce/Yb)_N$ ~7-9 and $(Gd/Yb)_N$ ~2-3) is notably greater than that of any other basalt within the lower PAg (Fig. 4-9). The EB-1 are also characterized by low high-field-strength element (HFSE) contents relative to the REE (Fig. 4-8 and 4-10), and possess P/P*, Zr/Zr*, Hf/Hf*, and Ti/Ti* ratios that are < 1 (avg. ~0.4-0.7; Table 4-1). Most EB-1 possess low $(Th/Nb)_N$ ratios (~0.4-0.6) and positive Nb/Nb* between ~1.1-1.5 (Fig. 4-10). One sample, however, (T-3318-A) possesses a distinctly higher $(Th/Nb)_N$ ratio (~1) and corresponding low Nb/Nb* of ~0.7.

Moderately enriched group-2 basalt (EB-2)

The moderately enriched group-2 basalt (EB-2) is comprised of three samples collected within the SVZ, two from the basalt horizon and one from the komatiite horizon (Table 4-1 and Fig. 4-5). When plotted on a primitive mantle normalized extended element diagram (Fig. 4-8) the elevated LREE contents of the EB-2 relative to Th and the HREE produces hump-shaped patterns similar to, but less pronounced than the EB-1. The degree of HREE-depletion is also more subdued than the EB-1 ($(Ce/Yb)_N$ ~2-4 and $(Gd/Yb)_N$ ~2) as is the degree of LREE-enrichment ($(Ce/Sm)_N$ ~1.1-1.7; Fig. 4-9). The EB-2 are also characterized by low HFSE contents (Fig. 4-8 and 4-10) and with few exceptions (P/P* and Ti/Ti* of sample TM0-285-D4) the EB-2 possess P/P*, Zr/Zr*, Hf/Hf*, and Ti/Ti* ratios that are < 1 (avg. ~0.6-0.8; Table 4-1). Most EB-2, also possess low to very low $(Th/Nb)_N$ ratios (~0.4) and positive Nb/Nb* (~1.5-1.6). One sample, however, (T-3319-A) possesses a distinctly higher $(Th/Nb)_N$ ratio (~1) and corresponding low Nb/Nb* of ~0.8.

Minimally enriched group-3 basalt (EB-3)

The minimally enriched group-3 basalt (MEB) is comprised of five samples collected within the SVZ, four basalts from the basalt horizon, and a coarse grained gabbro (sample HS0-091-I) from the komatiite horizon (Table 4-1 and Fig. 4-5). On a primitive mantle normalized extended element diagram (Fig. 4-8) the EB-3 display remarkably similar patterns characterized by moderate enrichment in LREE and MREE relative to HREE ($(Ce/Yb)_N$ ~1.2-1.4 and $(Gd/Yb)_N$ ~1.2-1.3) and minimal fractionation of LREE relative to MREE ($(Ce/Sm)_N$ ~0.9-1.0). Similar to the EB-1 and -2, the EB-3 possess low HFSE contents relative to the REE and P/P*, Zr/Zr*, Hf/Hf*, and Ti/Ti* (avg. ~0.8-0.9). The EB-3, possess $(Th/Nb)_N$ ratios between ~0.7-0.9 and minimally fractionated Nb/Nb* between ~0.9-1.2.

Depleted basalt (DB)

The depleted basalt (DB) is comprised of four samples collected within the NVZ komatiite horizon (Table 4-1 and Fig. 4-4). On a primitive mantle normalized extended element diagram (Fig. 4-8) the DB display very similar patterns characterized by LREE-depletion relative to both the MREE and HREE ($(Ce/Sm)_N$ ~0.6-0.9 and $(Ce/Yb)_N$ ~0.6-0.8) and minimal to moderate HREE-depletion ($(Gd/Yb)_N$ ~1.0-1.2). Relative to the REE the HFSE are relatively unfractionated (e.g. P/P*, Zr/Zr*, Hf/Hf*, and Ti/Ti* avg. ~0.9-1.1). The DB possess low to moderate $(Th/Nb)_N$ ratios (~0.5-0.8) and Nb/Nb* between ~1-1.3.

Trace elements and subdivision – ultramafic magmatism

Similar to basalt, low $(Th/Nb)_N$ komatiite (~22-40 wt.% MgO; Fig. 4-7) are characterized by an exceptional, but orderly, variability with respect to incompatible trace element contents and ratios. However, in contrast to basalt, low $(Th/Nb)_N$ komatiite are depleted in highly incompatible elements (e.g. $(Ce/Sm)_N < 1$; Fig. 4-9) and are characterized by significant variation in MREE and HREE, not LREE. As $(Gd/Yb)_N$ is both insensitive to crustal contamination (see modeling in Appendix D) and olivine fractionation (see modeling in Appendix E), it is a useful parameter for subdividing komatiite. Four geochemical groups have been defined based on variation in $(Gd/Yb)_N$: group-A (~1.2-1.3), group-B (~1.0-1.1), group-C (~0.8-0.9), and group-D (~0.5-0.7).

Group-A komatiite

The group-A komatiite consist of 8 samples of spinifex-textured and olivine-phyric komatiite collected from 8 spinifex-textured flows within the NVZ (see Fig. 4-4). On a primitive mantle normalized extended element diagram (Fig. 4-8) the average group-A komatiite is characterized by moderate to minimal depletion in LREE relative to MREE and Th relative to Nb ($(Ce/Sm)_N$ ~0.6 (0.5-0.7) and $(Th/Nb)_N$ ~0.8 (0.6-1.0)) and enrichment in MREE relative to HREE (e.g. $(Gd/Yb)_N$ ~1.2-1.3). Overall the group-A komatiite display minimal to moderate HFSE fractionations relative to the REE and the average group-A komatiite possesses a Nb/Nb* of ~1.1, P/P* of ~1, Zr/Zr* and Hf/Hf* of ~1.2-1.3, and Ti/Ti* of ~0.9 (Fig. 4-8 and 4-10).

Group-B komatiite

The group-B komatiite consist of 13 samples of spinifex-textured and olivine-phyric komatiite collected from 13 spinifex- and non spinifex-textured flows within the NVZ and SVZ (see Fig. 4-4). On a primitive mantle normalized extended element diagram (Fig. 4-8) the average group-B komatiite is characterized by moderate to minimal depletion in LREE relative to MREE and Th relative to Nb ($(Ce/Sm)_N$ ~0.7 (0.5-1.0) and $(Th/Nb)_N$ ~0.8 (0.6-0.9)) and minimal fractionation of MREE relative to HREE (e.g. $(Gd/Yb)_N$ ~1.0-1.1). The group-B komatiite possess moderate to pronounced positive HFSE anomalies relative to the REE, and the average group-B komatiite possesses a Nb/Nb* of ~1.1, P/P* of ~1.3, Zr/Zr* and Hf/Hf* of ~1.6, and Ti/Ti* of ~1.1 (Fig 4-8 and 4-10).

Group-C komatiite

The group-C komatiite consist of 25 samples of spinifex-textured and olivine-phyric komatiite collected from 13 spinifex- and non spinifex-textured flows within the NVZ and SVZ (see Fig. 4-4). Multiple samples were collected from 5 of the 13 flows (#2 through 6 in Table 4-1). On a primitive mantle normalized extended element diagram (Fig. 4-8) the average group-C komatiite is characterized by moderate to minimal depletion in LREE relative to MREE and Th relative to Nb ($(Ce/Sm)_N$ ~0.6 (0.4-0.8) and $(Th/Nb)_N$ ~0.7 (0.4-0.9)) and depletion in MREE relative to HREE (e.g. $(Gd/Yb)_N$ ~0.8-

0.9). The group-C komatiite possess pronounced positive HFSE anomalies relative to the bounding REE (Fig. 4-8), and on average possesses a Nb/Nb* of ~1.3, P/P*, Zr/Zr* and Hf/Hf* of ~1.8-1.9, and Ti/Ti* of ~1.2 (Fig. 4-8 and 4-10).

Group-D komatiite

The group-D komatiite consist of 7 samples of olivine-phyric komatiite collected from 3 spinifex- and non spinifex-textured flows within the NVZ and SVZ (see Fig. 4-4). Multiple samples (n=6/7) were collected from the spatially associated spinifex-textured flow #4 or lava channel (flow #6) located within the NVZ (see Fig. 4-6(d)). Notably, both of these flows also contain samples included within the group-C komatiite (Table 4-1). On a primitive mantle normalized extended element diagram (Fig. 4-8) the average group-D komatiite is characterized by moderate to minimal depletion in LREE relative to MREE and Th relative to Nb ($(Ce/Sm)_N$ ~0.8 (0.7-0.9) and $(Th/Nb)_N$ ~0.9 (0.5-1.0)) and strong HREE-enrichment relative to the MREE (e.g. $(Gd/Yb)_N$ ~0.5-0.7). With the exception of a modest Nb/Nb* of ~1.1, the average group-D komatiite possesses pronounced positive HFSE anomalies, and P/P* of ~2, Zr/Zr* and Hf/Hf* of ~2.6, and Ti/Ti* of ~1.6 (Fig. 4-8 and 4-10).

Major elements

Major and minor element MgO variation diagrams for low $(Th/Nb)_N$ basalt and komatiite including SiO_2, TiO_2, Al_2O_3, $Fe_2O_3(T)$, CaO, and ratios thereof (e.g. Al_2O_3/TiO_2 wt. ratio) are displayed in Fig. 4-11. In Fig. 4-12, the major and minor element compositions of spinifex-textured and selected low-MgO olivine-phyric samples from the group-A, -B, and -C komatiite are plotted against $(Gd/Yb)_N$. These samples are interpreted to more closely approximate the compositions of the komatiite liquids and illustrate important major and minor element compositional differences between HREE-enriched and HREE-depleted komatiite.

Mafic magmatism

The significant variation in incompatible trace element composition displayed by low $(Th/Nb)_N$ basalt is not manifested into discernable differences in major element composition (Fig. 4-11). Only the elevated TiO_2 contents of the enriched basalts ($\geq$ 1.3 wt.%) can be used to distinguish them from depleted basalt (~0.6-0.9 wt.%). With respect to MgO, the DB are marginally more primitive (~8-13 wt.%) than the majority of the enriched basalts (~4-7 wt.%) and in terms of SiO_2, most low $(Th/Nb)_N$ basalt are indistinguishable (~47-50 wt.%). With respect to MgO-Al_2O_3 systematics, most low $(Th/Nb)_N$ basalt are co-linear, and as MgO decreases from ~13-4 wt.%, Al_2O_3 increases from ~12-15 wt.% (Fig. 4-11). The Fe_2O_3 contents vary substantially within all groups, ranging between ~12-19 wt.%. The CaO contents are also variable, although more so for the enriched basalts (~8-12 wt.%) that the DB (~9 wt.%). With respect to Al_2O_3/TiO_2 ratios, the DB possess distinctly higher ratios than the enriched basalts (~16-20 versus ~5-12), a difference attributable to variable TiO_2 contents (Fig. 4-11).

Ultramafic magmatism

Overall, most low $(Th/Nb)_N$ komatiite (~22-40 wt.% MgO) display relatively well-correlated MgO-TiO_2 and MgO-Al_2O_3 systematics (e.g. R^2 ~0.7-0.8) that project toward x-axis intercepts of ~50 wt.% MgO (Fig. 4-11). This suggests olivine fractionation, either removal and/or accumulation, was an important process controlling incompatible element variation, and is consistent with the observation that olivine is the only major cumulate mineral phase recognized. The MgO-CaO systematics of low $(Th/Nb)_N$ komatiite appear inconsistent with olivine fractionation (x-axis intercept of ~42 wt.% MgO; Fig. 4-11), however, this can be attributed to systematic CaO-loss from high-MgO olivine-phyric komatiite. A significant number of high-MgO (~33-40 wt.%) olivine-phyric samples possess anomalously low $CaO/Al_2O_3 < 0.1$ to 0.6 (n=16/31) compared to most spinifex-textured samples (CaO/Al_2O_3 ~0.7-1.0 (n=18/22). CaO-loss from these samples is confirmed from a well-correlated (R^2 ~0.80) MgO-Al_2O_3 regression and x-axis intercept of ~50 wt.% MgO (not shown). Significant scatter is apparent in the MgO-SiO_2 plot suggesting variable SiO_2-loss and -gain. Although also somewhat scattered, the majority of samples (n=49/53) possess $Fe_2O_3(T)$ contents between ~10-14 wt.%, including most spinifex-textured samples (n=20/22). The Al_2O_3/TiO_2 (wt. ratio) of low $(Th/Nb)_N$ komatiite is variable and controlled by TiO_2 content. The group-A komatiite possess the lowest Al_2O_3/TiO_2 ratios between ~17-18, most group-B (n=9/13) possess higher ratios of ~19-21, the group-C (n=18/25) between ~22-24, and the majority of group-D samples (n=5/7) between ~22-27 (Fig. 4-11 and Table 4-1).

In Fig. 4-12, $(Gd/Yb)_N$ is plotted against MgO, $Fe_2O_3(T)$, TiO_2, Al_2O_3, SiO_2, and CaO for spinifex-textured and selected low-MgO olivine-phyric samples (n=2). The two olivine-phyric samples are from group-C (TM0-231-F and TM0-228-C) and have been included because of their geochemical similarities to spinifex-textured samples within their group and lack of chemical evidence for olivine accumulation. Because of obvious and suspected major element mobility and/or excessive olivine fractionation, some samples have been omitted from the regressions shown in Fig. 4-12. These include the anomalously low-MgO group-C spinifex-textured sample HS0-091-SP1 (~22 wt.%), the anomalous group-B sample TM0-011-E (Fe_2O_3(T), TiO_2, Al_2O_3, SiO_2), and three group-C spinifex-textured samples from flow #3 (TM0-226-B, -C, and -D; Table 4-1). These samples display within-flow major and minor element variations inconsistent with olivine fractionation (Fig. 4-12). With the aforementioned samples omitted, it is clear that differences in MgO, Fe_2O_3(T) and TiO_2 content are closely associated with variation in $(Gd/Yb)_N$. The correlation of these elements with $(Gd/Yb)_N$ suggests that end-member ultramafic liquids can be qualitatively defined and include a HREE-enriched liquid possessing $(Gd/Yb)_N$ as low as ~0.8, high-MgO (~29 wt.%), and low Fe_2O_3(T) (~11 wt.%) and TiO_2 (~0.3 wt.%), and a HREE-depleted liquid possessing $(Gd/Yb)_N$ as high as ~1.3 and characterized by comparatively low-MgO (~25 wt.%), and high Fe_2O_3(T) (~14 wt.%) and TiO_2 (~0.45 wt.%). No correlation exists between $(Gd/Yb)_N$ and SiO_2, and Al_2O_3 and CaO are poorly positively correlated with $(Gd/Yb)_N$.

Nd isotopes

The Sm-Nd isotopic data obtained for 7 basalt and 17 komatiite samples from all eight groups are listed in Table 4-2 and plotted on an isochron diagram in Fig. 4-13(a). The majority of low $(Th/Nb)_N$ basalt and komatiite possess εNd(2730 Ma) values that cluster between +1.7 and +3.0 (n=19/24), despite a considerable range in $^{147}Sm/^{144}Nd$ (~0.11-0.28). Superimposed on this prominent Nd isotopic signal are five komatiite samples from group-B, -C, and -D that possess εNd(2730 Ma) values minimally (+3.4 to +4.3) to significantly (+6.4 to +7.2) greater than the +3.0 maxima in εNd(T) suggested by other low $(Th/Nb)_N$ komatiite (Table 4-2). When low $(Th/Nb)_N$ basalt and komatiite with εNd(2730 Ma) values between +1.7 and +3.0 are regressed on a Sm-Nd isochron diagram (Fig. 4-13(a)) they yield a Model-3 solution age of 2730 ± 30 Ma (MSWD = 4.8). Clearly this is a meaningful result considering the U-Pb zircon age determinations for felsic volcanic rocks within the basalt and komatiite horizon of 2729.5 ± 0.8 and 2729.5 ± 0.9 Ma (Chapter 2). A mean εNd(2730 Ma) value for these 19 samples of +2.4 ± 0.7 (2σ std. dev.) is considered a good approximation of the dominant Nd isotopic signature of lower PAg magmatism.

Hf isotopes

The Lu-Hf isotopic data obtained for 8 basalt and 6 komatiite from all groups except the group-D komatiite are listed along with the Sm-Nd isotopic data in Table 4-2, and plotted on a Lu-Hf isochron diagram in Fig. 4-13(b). Similar to εNd(2730 Ma), the εHf(2730 Ma) values for most low $(Th/Nb)_N$ basalt and komatiite are remarkably uniform despite a modest range in $^{176}Lu/^{177}Hf$ (~0.009-0.04). Basalt possess tightly clustered εHf(2730 Ma) values between +4.3 and +4.9 and komatiite, with the exception of samples TM0-226-B and HS0-091-SP2, display a similar range, between +3.9 and +5.2 (Table 4-2). Sample TM0-226-B has a significantly elevated εHf(2730 Ma) value of +8.5 and sample HS0-091-SP2 has an anomalously low value of -0.9. When low $(Th/Nb)_N$ basalt and komatiite with εHf(2730 Ma) values between +4.3 and +5.3 (n=12/14 samples) are plotted on a Lu-Hf isochron diagram (Fig. 4-13(b)) they yield a Model-1 solution age of 2715 ± 26 Ma (MSWD = 1.1) when a ^{176}Lu decay constant of 1.866×10^{-11} a^{-1} is used (Scherer *et al.*, 2001; Söderlund *et al.*, 2004). This age is in excellent agreement with the aforementioned ca. 2730 Ma U-Pb zircon age constraints, and a mean εHf(2730 Ma) value for the 12 samples of +4.6 ± 0.6 (2σ std. deviation) is considered a good approximation of the dominant Hf isotopic signature of lower PAg magmatism.

ISOTOPIC COMPOSITION OF THE MANTLE SOURCE

The majority of low $(Th/Nb)_N$ basalt and komatiite analysed in this study possess uniform initial Nd (εNd(2730 Ma) of +2.4 ± 0.7) and Hf (εHf(2730 Ma) of +4.6 ± 0.6) isotopic compositions. This uniformity is striking considering the significant chemical variation displayed by the samples (e.g. ^{147}Sm/^{144}Nd ~0.12-0.28; $(Gd/Yb)_N$ ~0.5-3.2; MgO ~4-40 wt.%). These isotopic data indicate that the mantle source for most low $(Th/Nb)_N$ basalt and komatiite was characterized by a long-term and relatively uniform depletion in Nd/Sm and Hf/Lu relative to the bulk silicate earth. A similar range in εNd(2730 Ma) was also found for high $(Th/Nb)_N$ intermediate-felsic volcanic rocks and contaminated basalt and komatiite within the lower PAg, as well as low $(Th/Nb)_N$, ca. 2690 Ma komatiite within the upper PAg (see Fig. 4-14(a and b)); Chapter 3, MacHattie *et al.*, unpublished data). This isotopic uniformity, irrespective of age or amount of crustal involvement, further underscores the uniform extent of long-term incompatible trace element depletion of the mantle source of PAg komatiite, the juvenile nature of the basement, and the longevity of the processes involved in generating komatiite from this depleted mantle.

In a global context, the isotopic composition of the mantle imaged by the majority of low and high $(Th/Nb)_N$ PAg magmas is similar to other ca. 2.7 Ga juvenile volcanic and plutonic rocks (e.g. Dupré *et al.*, 1984 (Canada); Lesher & Arndt, 1995 (Australia)). In particular, the extensive Nd and Hf isotopic data set available from ca. 2.7 Ga supracrustal belts of the Superior Province within the southern Canadian Shield are remarkably similar (e.g. Dupré *et al.*, 1984, Machado *et al.*, 1986, Corfu & Noble, 1992; Corfu & Stott, 1993, 1996; Ayer *et al.*, 2002; Polat & Münker, 2004). In the most recent Nd-Hf isotopic investigation of ca. 2.7 Ga volcanic rocks from the Abitibi belt (Polat & Münker, 2004) new Hf isotopic data and those obtained in earlier studies (Corfu and Noble, 1992; Blichert-Toft & Arndt, 1999; Vervoort & Blichert-Toft, 1999) were compiled and recast using a U-Pb calibrated ^{176}Lu decay constant (e.g. Scherer *et al.*, 2001). This compilation indicates that the initial Hf isotopic composition of the depleted mantle beneath the Superior Province is characterized by a mean εHf(2.7 Ga) value of +4.2 ± 0.5. Various Nd isotopic compilations (e.g. Ayer *et al.*, 2002; Polat & Münker, 2004) are all in agreement that this mantle possesses a complimentary depleted Nd isotopic signature characterized by a mean εNd(2.7 Ga) value of +2.5 ± 0.5. These isotopic compositions are identical to the mean εNd(T) and εHf(T) that characterize the majority of low $(Th/Nb)_N$ basalt and komatiite within the lower PAg suggesting that large portions of the Archean mantle were uniformly depleted in incompatible trace elements.

In contrast to most low or high $(Th/Nb)_N$ magmas within the PAg, some komatiite possess minimal to significantly more radiogenic initial Nd (n=5 with εNd(2730)Ma between +3.4 up to +7.2). Within this sub-group, two samples analysed for their Hf isotopic compositions also possess anomalous initial Hf (εHf(2730)Ma of +8.5 and -0.9).

Importantly, four of these samples were collected from the same series of outcrops (e.g. HS0-091-FCR, -G, -SP3, -SP2) situated within the core of a Paleoproterozoic F_2-fold (D_2-M_2 tectonometamorphism occurred between ca. 1850-1820 Ma; Carson *et al.*, 2003; Berman *et al.*, 2004) within the SVZ (Fig. 4-5). This, combined with the highly variable dispersal of these samples toward higher εNd(2730 Ma) values than the +2.8 to +3.0 maxima recognized for other volcanic rocks suggests these samples may have experienced localized, fluid-related isotopic exchange. One or more of the younger tectonomagmatic event(s) recognized within the area including, regional ca. 2.6 Ga plutonism, ca. 2350 Ma (D_1-M_1) or ca. 1850-1820 Ma (D_2-M_2) tectonometamorphism (Carson *et al.*, 2003; Berman *et al.*, 2004) may have been involved.

DEFINING BASALT AND KOMATIITE COMPOSITIONAL CONTINUA

As discussed above, the significant incompatible trace element fractionation characterizing low $(Th/Nb)_N$ basalt and komatiite within the lower PAg cannot be attributed to long-term mantle source heterogeneity. Importantly, the most extreme chemical fractionations observed, those involving the relative fractionation of the REE (e.g. $(Ce/Yb)_N$ and $(Gd/Yb)_N$) and REE and HFSE (e.g. P/P* and Hf/Hf*) display nearly continuous variation (Figs. 4-9 to 4-10). It is this systematic variation that suggests two geochemical continua exist, one comprised of basalt, and the other komatiite. Below we examine the continua in greater detail, define the end-members, and discuss the approach that will be taken to model their generation. Some initial modeling was necessary to assess geochemical variation superimposed upon the larger-scale variation inherent to the continua. This modeling is relegated to the appendices and includes: (1) assessing analytical precision affects on highly incompatible trace element ratios (see Appendix A and B through E); (2) assessing the reliability of HFSE concentrations (Appendix B); (2) modeling $(Th/Nb)_N$ and Nb/Nb* variation resulting from crustal contamination (Appendix C); (3) modeling of olivine accumulation upon $(Gd/Yb)_N$ and identification of the most HREE-enriched komatiite end-member (Appendix D); and (4) plagioclase and pyroxene crystal fractionation for the EB-3 and identification of anomalously differentiated basalt samples (Appendix E).

Basalt compositional continuum

The basalt compositional continuum is readily recognized from the combined $(Ce/Yb)_N$-$(Ce)_N$ and $(Ce/Yb)_N$-$(Yb)_N$ systematics of the four principal basalt groups. Importantly, the exceptional correlation of $(Ce/Yb)_N$ with $(Ce)_N$ that defines the continua can be produced by mixing the highly enriched (EB-1) and depleted (DB) basalt end-members (Fig. 4-15(a)). In this model, the minimally and moderately enriched basalt (EB-2 and -3) can be produced by mixing ~70-90 wt.% depleted basalt with ~10-30 wt.% enriched basalt (Fig. 4-15(a)). The marginally higher HREE contents of the EB-2 and EB-3 than those of the EB-1 and DB (Fig. 4-15(b)) can be simply attributed to a slightly greater degree of differentiation (Fig. 4-15(c)). Thus, the basalt compositional continuum can be defined by mixing of the highly enriched and depleted basalt end-members

Komatiite compositional continuum

The komatiite compositional continuum is readily recognized from the major and trace element co-variation of spinifex-textured and low-MgO olivine-phyric samples depicted in Fig. 4-12 and, similar to basalt, this co-variation can be produced by mixing involving end-members. However, accurately defining the HREE-enriched end-member in the komatiite continuum is complicated by the fact that spinifex-textured or near liquid samples of the strongly HREE-enriched group-D komatiite have not been recognized and/or sampled. Importantly though, modeling olivine accumulation (Appendix D) indicates that the low $(Gd/Yb)_N$ of the group-D komatiite cannot be changed by this process and a parental magma possessing a $(Gd/Yb)_N$ ratio at least as low as ~0.63 (group average) is required. From the MgO-$(Gd/Yb)_N$ systematics of komatiite liquids defined in Fig. 4-12, the group-D komatiite liquid is suggested to have possessed ~31 wt.% MgO (Fig. 4-16(a)). Un-mixing komatiite liquids yields identical results, and un-mixing ~30 wt.% of the HREE-enriched group-A komatiite liquid from the HREE-enriched group-C liquid (liquids are averages of samples in Fig. 4-12 (see caption)) yields a komatiite liquid possessing ~31 wt.% MgO and a $(Gd/Yb)_N$ ratio of ~0.63. Applying this method to more elements allows the full extended trace element profile for the group-D liquid to be defined (Fig. 4-16(b)). This composition is interpreted to closely reflect the true composition of the group-D komatiite liquid end-member (see Appendix D), and the komatiite compositional continuum can be defined by mixing of this strongly HREE-enriched end-member with the HREE-depleted group-A liquid end-member.

Approach to modeling basalt and komatiite petrogenesis

In order to understand how the basalt and komatiite compositional continua may have been created, it is first imperative that constraints be placed upon the generation of the respective end-members. In the following discussion the origin of the depleted and highly enriched end-members in the basalt continuum are evaluated first, followed by the HREE-depleted and HREE-enriched end-members in the komatiite continuum.

DEPLETED BASALT GENERATION

The similar $(Ce/Sm)_N$, $(Gd/Yb)_N$, P/P*, Zr/Zr*, Hf/Hf*, Ti/Ti*, and Al_2O_3/TiO_2 of the DB and group-A komatiite (Figs. 4-8 to 4-10) suggest they may be related through crystal differentiation. On an MgO versus CaO variation diagram (Fig. 4-17(a)), a regression involving the average low- (~8 wt.%) and high-MgO (~12-13 wt.%) DB and group-A komatiite liquid is exceptionally well-correlated ($R^2 = 0.95$) and intercepts the olivine-clinopyroxene tie-line shown at ~70 wt.% olivine and ~30 wt.% clinopyroxene. This correlation suggests that ~50 wt.% of a bulk cumulate mineral assemblage consisting predominantly of olivine must be removed from the group-A komatiite liquid to generate DB with MgO contents between ~8-13 wt.%. Similar, well-correlated regressions are found for Al_2O_3 and TiO_2 (not shown) and yield identical estimates for the amount of crystal fractionation required. Furthermore, the REE profile and contents of the average low-MgO (~8 wt.%) DB can be reproduced by ~50 wt.% olivine-dominated crystal fractionation from a group-A spinifex-textured komatiite (Fig. 4-17(b)).

HIGHLY ENRICHED BASALT GENERATION

The generation of the highly enriched basalt end-member is closely tied to other members in the continuum. Two observations suggest that like the depleted basalt, the highly enriched basalt was generated by crystal differentiation from a parental ultramafic magma. Firstly, the co-linear MgO-Al_2O_3 systematics of enriched and depleted basalts with the group-A komatiite (Fig. 4-18) suggests olivine-dominated crystal fractionation from parental ultramafic magma(s) similar in composition to the group-A komatiite liquid may have been involved in the production of enriched basalts. Secondly, the distinctive primitive mantle normalized incompatible trace element signature of the highly enriched basalt end-member, including the combination of significant incompatible element enrichment (e.g. $(Ce/Yb)_N$ ~7), pronounced negative HFSE anomalies (e.g. Hf/Hf* of ~0.5), and low $(Th/Nb)_N$ (~0.5) necessitate a unique origin. They suggest low degrees of melting, a source depleted in highly incompatible trace elements, and significant amounts of garnet retention in the residue.

The garnet-peridotite melting experiments of Walter (1998) conducted using the nominally anhydrous natural peridotite KR-4003 can provide constraints for the origin of the enriched basalts and their highly enriched end-member. These experiments are particularly relevant because low-degree (~10 wt.%) garnet-saturated melt compositions were produced over a considerable, ~4-7 GPa pressure interval. Importantly, with increasing pressure, the Al_2O_3 contents of low-degree garnet-saturated melts decrease systematically from ~10 wt.% at ~4 GPa to ~5 wt.% at ~7 GPa (Fig. 4-19(a)) suggesting Al_2O_3 can be used as a barometer of garnet-peridotite melting. This decrease in Al_2O_3 is accompanied by an increase in MgO from ~20 up to ~24 wt.%, and when the melt compositions are regressed on an MgO versus Al_2O_3 plot, they intersect the crystal fractionation array of the group-A komatiite liquid and depleted basalt at a high angle between ~4 and 4.5 GPa (Fig. 4-19(b)). This finding suggests the co-linearity of enriched and depleted basalts may be due to the involvement of a parental ultramafic magma component to the enriched basalts that was produced by low degrees of garnet-peridotite melting at ~4.25 GPa.

Using MgO-Al_2O_3 and MgO-CaO systematics, a parental ultramafic liquid possessing ~20 wt.% MgO and ~9 wt.% Al_2O_3 and CaO (avg. of Walter's runs 40.07 and 45.03 (Fig. 4-19(a and c)) would have to undergo ~50 wt.% crystal fractionation in order to generate an enriched basalt possessing ~5-7 wt.% MgO (Fig. 4-19(b and d)). Unfortunatey, it is not possible to accurately assess the bulk olivine/clinopyroxene ratio of this assemblage because of significant scatter in CaO. Nevertheless, as assemblage consisting of ~60 wt.% olivine and 40 wt.% clinopyroxene yields a crystal fractionation pathway that is sub-parallel to that defined for the group-A komatiite liquid and depleted basalt, and that intersects several high-CaO enriched basalt (Fig. 4-19(b and d)). Importantly, the higher clinopyroxene component of this assemblage would be consistent with the higher CaO of the group-E komatiite liquid compared to group-A which could produce the depleted basalt by removal of a bulk assemblage consisting of ~70 wt.% olivine and ~30 wt.% clinopyroxene (Fig. 4-19(d)). Using the 60:40 mineral assemblage, partition coefficients from the literature (Table 4-3), and assuming ~50 wt.% crystal fractionation, the incompatible trace element contents of the highly enriched basalt end-member can be restored to abundances appropriate for a primary ultramafic magma possessing ~20 wt.% MgO to model partial melting (see Fig. 4-22(a-d)). In the following discussion this restored, highly enriched ultramafic melt composition will be referred to as the group-E komatiite liquid.

The input parameters for modeling partial melting include, the high-pressure modal mineralogy of the KR-4003 (Fig. 4-20; Walter, 1998) and the non-modal melt reactions derived from these experiments, various partition coefficients from the literature (e.g. Fig. 4-21(a and b) and Table 4-3), and estimates for composition of the depleted MORB (Salters & Stracke, 2004; Workman & Hart, 2005) and primitive mantle (McDonough & Sun, 1995). Because of the number of variables, several non-modal batch melting models of garnet-peridotite were constructed (see Fig. 4-22(a-d)). This iterative approach is useful for determining the most important variables, and combination thereof, necessary to produce the distinctive incompatible trace element profile of the group-E komatiite. The model melt that matches the group-E komatiite liquid characteristics best (Fig. 4-22(d)) is a ~2 wt.% non-modal melt of an incompatible element depleted MORB-like source in which the modal mineralogy is equivalent to that of the KR-4003 peridotite at ~4.25 GPa (Fig. 4-20), the partition coefficients for the solidus pyroxene are more similar to the average ~2.4-3.4 GPa orthopyroxene (Pyx.-1) than ~2.4-3.4 GPa clinopyroxene (Pyx.-2), and HREE-partition coefficients for the solidus garnet are ~65 % lower (Gt.-1) than those of solidus garnet at ~3.2-3.4 GPa (see Fig. 4-21(a and b)).

Although the major element compositions of the low degree ~4 to 4.5 GPa melts in Walter's (1998) experiments average ~12 wt.% melting (not ~2 wt.%), it appears that extrapolating Walter's (1998) experimental data to lower degrees of melting may not greatly influence MgO, Al_2O_3, and CaO (e.g. see Fig. 4-19(a and c)). Importantly, shifts in the concentrations of these major elements of a few wt.% for will not significantly influence the results of the major element modeling. Overall, the major and trace element constraints are in excellent agreement that the highly enriched basalt end-member was produced by crystal fractionation from a parental group-E komatiite liquid that possessed ~20 wt.% MgO, and was generated by low degrees of melting at ~4.25 GPa.

HREE-DEPLETED GROUP-A KOMATIITE GENERATION

The higher MgO content of the group-A komatiite liquid compared with that of group-E (~25 versus ~20 wt.%), its significantly greater depletion in highly incompatible trace elements, and lower extent of HREE-depletion (Fig. 4-22(a-d)) suggest the generation of the group-A komatiite liquid involved higher-degrees of melting. The ~8 wt.% Al_2O_3 content of the group-A komatiite liquid suggests it may have been generated between ~4.5-5 GPa pressure (see Fig. 4-19(a)). As this pressure range is only marginally higher than that suggested for production of the group-E komatiite liquid, modeling the generation of the group-A komatiite liquid is attempted using the same partition coefficients, modal mineralogy, melting reaction, and depleted MORB mantle starting composition used to model the group-E komatiite liquid (Fig. 4-22(a-c)). Overall, a ~25 wt.% non-modal batch melt can reproduce the incompatible trace element profile of the group-A komatiite liquid remarkably well in terms of $(Ce/Yb)_N$, $(Ce)_N$ and $(Yb)_N$ (Fig. 4-22(a-c)). The marginally higher Th, Zr, and Hf of the group-A komatiite liquid compared to the model melt can be explained by minor amounts of crustal contamination (Th) and/or normal analytical uncertainty (Th, Zr, and Hf; see Appendix B and C).

The average SiO_2, Al_2O_3, MgO, FeO, and CaO of melts approximating ~25 wt.% melting at ~4.5, 5, and 6 GPa derived from Walter's (1998) runs 45.03, 45.02, 60.01 and 60.05, and a 60:40 mixture thereof, are compared with the group-A komatiite liquid in Table 4-4. In broad agreement with the trace element modeling, the Al_2O_3, MgO, and

FeO of a ~25 wt.% melt of garnet-peridotite at ~5 GPa is similar to the composition to the group-A komatiite liquid. As SiO_2 is suspect in all PAg komatiite (e.g. Fig. 4-11) the minor differences in SiO_2 (~2 wt.%) are equivocal, however, a ~1 wt.% lower CaO content for the group-A liquid may be significant as a lower CaO content could suggest higher degrees of melting (e.g. Fig. 4-19(c)).

HREE-ENRICHED GROUP-D KOMATIITE GENERATION

To model the generation of the group-D komatiite liquid, its composition needs to be defined. As discussed in detail in Appendix D, assuming the komatiite compositional continuum was generated by mixing, the simplest, least subjective, and accurate manner in which to derive the group-D liquid composition is to un-mix ~30 wt.% of the group-A liquid from that of group-C until the resultant magma possess a $(Gd/Yb)_N$ ratio of ~0.63. This group-D komatiite liquid (Fig. 4-21(a)) should also possess an exceptionally high MgO content of ~31 wt.%, and low $Fe_2O_3(T)$ (~10 wt.%), TiO_2 (~0.25 wt.%), and CaO (~5 wt.%) contents, either using the un-mixing calculation, or the correlations between these elements with $(Gd/Yb)_N$ as shown in Fig. 4-12.

In Walter's (1998) melting experiments, the CaO content of melts generated between ~3-7 GPa decrease steadily with increasing degree of melting, importantly though, CaO content is relatively insensitive to pressure (Fig. 4-19(c)). As such, the low-CaO and high-MgO contents inferred the group-D liquid require exceptionally high extents of melting of a source with a bulk composition similar to the KR-4003 lherzolite (Fig. 4-23), considerably greater than the low-degree ~4.25 GPa melt or the group-A komatiite liquid. For example, a melt possessing a MgO content as high as ~31 wt.%

would require > 50 wt.% melting and be in equilibrium with residues comprised of orthopyroxene and/or olivine (Walter, 1998). However, simply increasing the degree of melting of the same source used to model the highly enriched and group-A komatiite cannot produce a group-D liquid. This is because the incompatible trace element composition of a low or high-degree melt in equilibrium with orthopyroxene and/or olivine must closely reflect the composition of its source, and thus the strong HREE-enrichment and pronounced positive HFSE anomalies that characterize the group-D komatiite liquid (Fig. 4-16(b)) preclude derivation from a source possessing an incompatible trace element composition similar to the depleted MORB mantle. Importantly, the trace element modeling of garnet-peridotite melting between ~4-5 GPa employing the depleted MORB mantle starting composition of Salters & Stracke (2004) and Workman & Hart (2005) generates residual mantle with incompatible trace element characteristics similar to the group-D komatiite liquid (Fig. 4-24(a)). These residues are minimally to significantly more HREE-enriched and refractory than the initial source composition and possess pronounced positive HFSE anomalies.

If the source for the group-D komatiite liquid is indeed the residual mantle generated during the melt extraction which produced the highly enriched and group-A komatiite, MgO-CaO systematics (Fig. 4-23) can be used to approximate the total amount of melting required to generate the group-D komatiite from the original source (KR-4003 lherzolite). Overall, ~60-65 wt.% total melting would be necessary to generate an ultramafic melt possessing ~31 wt.% MgO from this lherzolite and would require equilibrium with a low-CaO harzburgite or dunite residual mineral assemblage (Fig. 4-23). Relative to a residual mantle generated by ~25 wt.% partial melting at ~4.5 GPa from the KR-4003 lherzolite (avg. residue of ~12 and 37 wt.% melting; Table 4-5), a composition which should approximate the residue produced by extraction of the group-A komatiite liquid, ~30-35 wt.% additional melting would be required to generate the group-D komatiite liquid (Fig. 4-23). In Fig. 4-24(b), a ~30 wt.% non-modal batch melt of the group-A komatiite liquid residue is shown for a starting mineral assemblage consisting of ~70 wt.% olivine and ~30 wt.% orthopyroxene, respectively. Note that using this mode and Walter's (1998) orthopyroxene-dominated melt reaction (Fig. 4-22(b); 0.03(Ol.) + 0.97(Opx.) = 1.0(melt)), only ~30 wt.% melting can be achieved before orthopyroxene exhaustion.

As expected, the model melt is indistinguishable from the original source with respect to the relative fractionation of incompatible trace elements and all are enriched relative to the source to an extent proportional to the degree of melting (~3.3 or 1/(melt fraction); Fig. 4-25). Although the model melt and the group-D komatiite liquid are similar with respect to some of the least incompatible trace elements (e.g. $(Yb)_N$ ~1.5), their moderate to highly incompatible trace element contents differ greatly (Fig. 4-25). Importantly though, the relative difference between the group-D komatiite liquid and the model melt (group-D liquid/model melt) is highly systematic (Fig. 4-23). The relative difference is nearly perfectly inversely proportional to the bulk partition coefficients used to model the melting (Fig. 4-23). Thus, the difference in the degree of incompatible trace element fractionation observed between the group-D komatiite liquid and the ~30 wt.% model melt is proportional to the degree of fractionation expected for a theoretical, 0 wt.% melt of the bulk source (1/bulk Kd's) and/or orthopyroxene (1/opx. Kd's), i.e. $Cl/Co = 1/D$ as the degree of melting approaches 0 wt.%. Importantly, melt fractions even as low as ~1 wt.% cannot generate incompatible trace element fractionation relative to the original source (Cl/Co) that approach the magnitude observed (Fig. 4-23).

Although the nature of these fractionations are not yet fully understood, their systematic nature and clear relationship with orthopyroxene partitioning suggests they are unlikely to be a coincidental artifact of the modeling, or assumptions inherent to defining the group-D komatiite liquid, instead this suggests an origin for these fractionations related to melting. The major and least incompatible trace element data (e.g. MgO, CaO, and Yb) are in agreement that ~30 wt.% re-melting of the refractory residue generated by the extraction of the group-A komatiite is required to generate the group-D komatiite liquid (Fig. 4-21(b)). To reconcile the more highly incompatible trace element systematics, a more complex melting model which takes into consideration the detailed spatial and temporal manner in which the migrating melt and matrix interact, precisely how melt aggregation occurs, and the manner in which small and large melt fractions contribute during this process appears to be required. More efficient delivery of the most highly incompatible trace elements to the top of the melt column could explain these data, a situation that may be analogous to the theoretical melt percolation models of Navon & Stolper (1987) in which chromatographic effects within the melt column are postulated to be capable of inducing extreme fractionations of incompatible trace elements similar to those predicted for exceptionally low degrees of melting.

ORIGIN OF THE COMPOSITIONAL CONTINUA AND TWO-STAGE MAGMATIC DEVELOPMENT OF THE LOWER PAG

Establishing that the highly enriched and depleted end-members in the basalt compositional continuum were generated by similar extents of crystal differentiation from parental komatiite magmas suggests the minimally to moderately enriched members of the continuum have a similar origin. In Fig. 4-26(a) a mixing curve involving the group-A and group-E komatiite liquids is shown along with trajectories appropriate for simply reversing the olivine and clinopyroxene crystal differentiation required to generate these intermediate members from ultramafic magmas produced by mixing involving the end-members. Reversing the differentiation to the point where these members possess $(Lu)_N$ of ~2.3 (avg. for group-A and -E komatiite liquid; see Fig. 4-26(b)) suggests that approximately ~60-65 wt.% crystal differentiation from parental ultramafic magmas dominated by a group-A end-member component ($\geq$ 70 wt.%) could explain the generation of the minimally and moderately enriched basalt (Fig. 4-26(a and b)). The compositional continuum comprised of incompatible trace element depleted komatiite magmas can be readily explained by mixing involving end-members, in this case the group-A and group-D komatiite liquids (e.g. Fig. 4-16(a and b)). Importantly, the mixing of ultramafic magmas within this continuum that possess $(Gd/Yb)_N$ ratios that vary by up to ~0.4 (~0.5-0.9), encompassing approximately half of the variation observed in this ratio of ~0.8 (~0.5-1.3), has been documented within the group-C/-D flows #4 and #6 (Fig. 4-6(d); and modeling in Appendix D). Importantly, an origin for the two continua via mixing involving ultramafic end-members requires only three primary magmas, the group-A, -E, and -D liquids, respectively. In order to reconcile the relative eruption order of members within the two respective continua with constraints for the origin of the group-A, -E, and -D liquids, the magmatic development of the lower PAg must have involved two distinct stages of melting and mixing, with or without crystal differentiation, separated by a minimal hiatus.

The initial phase of magmatism within the lower PAg (stage 1) is recorded in the lower basalt horizon. This horizon, with the exception of rare crustally-derived intermediate-felsic volcanic rocks (Chapter 3) is exclusively comprised of derivative magmas that define the basalt compositional continuum. Geochemical sampling of both low and high $(Th/Nb)_N$ magmas indicates that the complete continuum of depleted (only recognized as high $(Th/Nb)_N$ basalt) to highly enriched magmas is present within this horizon and, as such, requires their parental ultramafic magmas to be present at shallow lithospheric depths simultaneously during its construction. The exclusive occurrence of stage 1 magmas within the basalt horizon can be explained if the group-A and -E komatiite liquids were the first magmas generated during mantle upwelling and arrive at the lithosphere. As magmas within this horizon are differentiated ($\leq$ 11 wt.% MgO), significant crystal differentiation (~50 wt.%) of the parental group-A and -E liquids at depth is required prior to their eruption. The parental ultramafic magma end-members are first, however, required to mix in order to generate the compositional continuum, therefore magma mixing is constrained to have occurred either during melt generation and migration within the mantle and/or during collection and pooling at lithospheric mantle depths. An interconnected magma plumbing system developed at shallow depths is implied and one in which the group-A liquid stalled and began differentiation at the crust-mantle boundary, whereas the group-E liquid end-member at a somewhat greater depth. The incomplete homogenization of these stage 1 magmas during mixing processes and their stalling at or below the crust-mantle boundary may reflect the density differences predicted between these parental ultramafic magmas and continental crust. The ascent of the group-A komatiite, presumably the least dense stage 1 magma, to the crust-mantle boundary upon arrival of the stage 1 melts at the lithosphere is well-supported by geochemical evidence. At this boundary, melting, mixing, and crystal differentiation led to the production of three principal and distinctive derivative magmas, the intermediate-felsic volcanic rocks (lower crustal melting; Chapter 3), the group-1 high $(Th/Nb)_N$ basalt (crystal differentiation of crustal melt contaminated group-A komatiite; Chapter 3), and the depleted basalt (crystal differentiation of group-A komatiite), respectively.

The second stage of magmatism within the lower PAg (stage 2) is recorded in the upper komatiite horizon. This horizon is dominated by komatiite magmas that contain a significant component of the group-D komatiite liquid, and that were produced by mixing of the group-A and -D liquids. Because the group-D liquid was generated by re-melting of the residue produced by the extraction of the group-A liquid, the generation of the group-D liquid at its eruption within the komatiite horizon must constitute stage 2. Significantly, both the primary stage 1 and stage 2 magmas, as well as the stage 2 derivatives produced by the emplacement and differentiation of group-A liquid at the crust mantle-boundary (intermediate-felsic volcanic rocks, group-1 and -2 high $(Th/Nb)_N$ basalt, and depleted basalt), all occur within the upper komatiite horizon. This suggests that the arrival of the group-D komatiite liquid at shallow lithospheric depths occurred shortly after the stage 1 melts. However, the arrival of the group-D komatiite must have been retarded long enough for the basalt horizon to have formed and thus crystal differentiation of the stage 1 parental ultramafic magmas to already be near completion.

This hiatus is interpreted to record the time period separating the extraction of the group-A komatiite liquid from its mantle source (stage 1), and the initiation of the re-melting of this source and the production of the group-D komatiite liquid (stage 2). A relatively rapid transition from basalt to komatiite-dominated magmatism or, in other words, the eruption of derivative stage 1 and the undifferentiated stage 2 group-D komatiite is well supported by the high-precision U-Pb zircon ages obtained for felsic volcanic rocks within the volcanic succession. The dacite sample T-3319-B intercalated with basalt within the SVZ (Fig. 4-5) and dacite sample H-1337 intercalated with komatiite within the NVZ (Fig. 4-4) both yielded identical crystallization ages of 2729.5 ± 0.8 Ma and 2729.5 ± 0.9 Ma, respectively (Chapter 2). In essence, the time encapsulated within the volcanic stratigraphy at the basalt/komatiite horizon transition is only constrained by the time required for the residue of the group-A komatiite extraction to migrate to a depth at which it will achieve ~30 wt.% melting or, alternatively, the time required for the group-A komatiite and -E komatiite liquids to undergo ~50 wt.% crystal differentiation.

PHASE EQUILIBRIA CONSTRAINTS

As discussed above, the magmatic development of the lower PAg can be qualitatively described by two separate stages of mantle melting, involving three primary ultramafic magmas. Below we use phase equilibria constraints to semi-quantitatively assess: (1) the P-T trajectory of the parcel of mantle that produced the group-A (stage 1) and group-D komatiite liquids (stage 2) and thickness of the lithosphere during its upwelling; and (2) the relative temperature difference between the two mantle components required to produce the group-A and -E komatiite liquids during stage 1 melting.

The evidence for a rapid transition from stage 1 to stage 2 melting, separated by a minimal hiatus, is well-supported by all available field, geochemical, and age constraints. In order to facilitate a relatively rapid transition from stage 1 to stage 2 melting and for the "parcel" of mantle required to generate the group-A komatiite via ~25 wt.% melting to be re-melted by an additional ~30 wt.% require a thin lithosphere at the time of upwelling. The pressure at which this parcel of mantle achieved ~30 wt.% would constrain the maximum thickness of the lithosphere at the time of upwelling. The melting experiments of Wasylenki *et al.* (2003) conducted at ~1 GPa utilized a refractory peridotite composition (DMM-1; Table 4-5) that is broadly similar to residual mantle produced by ~25 wt.% melting at ~4.5 GPa as calculated from Walter's (1998) melting experiments (see Fig. 4-23 and Table 4-5). As such, DMM-1 is a composition that might approximate the source for the group-D komatiite liquid and provide constraints applicable to its low pressure generation. In agreement with their nearly identical compositions, the ~4.5 GPa residue (~65 wt.% olivine, ~29 wt.% pyroxene and ~7 wt.% garnet) is similar to DMM-1 (~63 wt.% olivine, ~28 wt.% orthopyroxene and ~8 wt.% clinopyroxene) in terms of olivine:pyroxene+garnet ratio (~65:35) and thus, should possess similar modes at low pressure. The clinopyroxene-absent melting reaction of 1.24 orthopyroxene equals 0.24 olivine and 1.0 melt determined by Wasyenki *et al.* (2003) indicates the normative mineral mode of this peridotite at ~16.6 wt.% melting of ~81.5 wt.% olivine and ~18.5 wt.% orthopyroxene (see Table 2 of Wasyenki *et al.*, 2003) can only sustain another ~15 wt.% melting before orthopyroxene-out, i.e. achieve ~31.5 wt.%

total melting at 1 GPa. This amount of melting is identical to that suggested to be required to produce the group-D komatiite liquid (Fig. 4-23). Wasylenki *et al.*'s (2003) melting experiments indicate that ~30 wt.% melting concomitant with orthopyroxene-out requires a temperature of ~1547 °C at 1 GPa.

On the temperature versus pressure diagram depicted in Fig. 4-27, attempts are made to integrate this constraint with those obtained from Walter's (1998) melting experiments and the solidus of peridotite KLB-1 (Herzberg *et al.*, 2000) in order to semi-quantitatively assess the pressure at which the refractory residue generated by the extraction of the group-A komatiite might have achieved ~30 wt.% melting. This requires constraints for the absolute pressure and temperature appropriate for group-A komatiite melt segregation and formation of the refractory residue, assumptions to be made about the P-T-trajectory of the refractory residue during its ascent, and the relative position of the ~30 wt.% melt contour of refractory peridotite at pressures > 1 GPa. The generation of the group-A komatiite requires ~25 wt.% melting at ~5 GPa pressure, and from Walter's (1998) melting experiments, this is achieved ~35 °C above the solidus. Relative to the solidus parametrization of Herzberg *et al.* (2000), this residual mantle would possess a temperature of ~1720 °C (Fig. 4-27), and relative to the KR-4003 solidus, a temperature of ~1675 °C. The temperature shown relative to the higher temperature KLB-1 peridotite solidus is preferred because it is more consistent with the high eruption temperature inferred for the group-D komatiite liquid of ~1615 °C based on an MgO content of ~31 wt.% (Nisbet *et al.*, 1993).

Assuming an adiabatic? cooling rate of 0.3 °C per km during ascent, the residual mantle generated by the extraction of the group-A komatiite would intersect a ~30 wt.%

melt contour inferred from Wasylenki *et al.*'s (2003) melting experiments, assuming a P-T-trajectory for the orthopyroxene-out reaction curve that is sub-parallel to that determined by Walter (1998) near ~2 GPa, or ~60 km (Fig. 4-27). We suggest that this depth should be considered a conservative estimate for the maximum thickness of the lithosphere for the following reasons: (1) the highest absolute temperature for the refractory peridotite source at ~5 GPa was chosen, i.e. relative to the KLB-1 solidus; (2) the mantle was assumed to cool minimally between ~2-5 GPa; (3) the residual mantle may have been more refractory than DMM-1; (4) melting may have been somewhat greater than ~30 wt.%; and (5) the major and trace element modeling of melting suggest that the limit of orthopyroxene stability in the melt interval was reached. Importantly, unless the depth to the lithosphere, the ultimate barrier to continued decompression melting, is precisely equivalent to the depth at which the upwelling refractory mantle achieved this limit (unlikely), it seems reasonable to conclude that the mantle upwelling did not exceed this limit. For these reasons, we suggest that the thickness of the lithosphere at the time of mantle upwelling must have been < 60 km.

In order to achieve the ~25 wt.% melting at ~5 GPa required to generate the group-A komatiite, the initiation of this stage of melting must have begun at a considerable depth. Kinzler & Grove (1992) have shown that the amount of decompression required to achieve a temperature ~35 °C above the solidus via continuous decompression melting within the spinel stability field requires ~1.8 GPa, assuming this constraint is also broadly applicable to the garnet stability field, the melting which produced the group-A komatiite may have begun at a depth of ~6.8 GPa (~210 km) prior to its segregation at ~5 GPa (Fig. 4-27). Relative to the KLB-1 solidus depicted in Fig. 4-

27, mantle intersecting the solidus at ~6.8 GPa would have a temperature of ~1795 °C, and a potential temperature of ~1725 °C assuming an adiabatic gradient of 0.3 °C per km. In contrast, the generation of the group-E komatiite liquid is consistent with near solidus melting at ~4.25 GPa, a difference which clearly indicates that depleted mantle of contrasting temperature was involved in the generation of the stage 1 magmas. If the steepness of the KLB-1 solidus parameterization of Herzberg *et al.* (2000) depicted in Fig. 4-27 is accurate and appropriate, and the ~6.8 GPa solidus intersection suggested for the group-A komatiite is correct, a ~150 °C difference in mantle potential temperature for the stage 1 mantle components is implied.

REGIONAL SETTING OF MAFIC-ULTRAMAFIC MAGMATISM AND THE IMPORTANCE OF PRE-EXISTING LITHOSPHERIC ARCHITECTURE AND STRUCTURES

As discussed previously (see Chapter 2 and 3) and reviewed earlier in this contribution, the mafic-ultramafic magmatism recorded within the lower PAg is part of a much larger mafic-ultramafic magmatic province formed over an extended, ~45 m.y. time period between ca. 2735-2690 Ma (Chapter 2 and references therein). This magmatism is confined within a ~1400 km long and up to ~400 km wide crustal corridor within the central and northeastern Rae domain (Fig. 4-1). The currently available field, geochemical, U-Pb zircon ages, and Nd isotopic data have been previously interpreted to suggest that regional mafic-ultramafic magmatism formed within an extensional continental margin setting (Chapter 3). Integrating the new petrological, geochemical, and temporal constraints obtained from modeling basalt and komatiite petrogenesis within the lower PAg not only reinforces this interpretation, but provides more detailed insight into the regional geodynamic controls upon mafic-ultramafic magmatism. Although not discussed in detail, the geochemical data we have obtained from mafic-ultramafic volcanic rocks collected from supracrustal strands located northeast of the lower PAg and predominantly from sequences comprising the middle and upper PAg display some rather striking compositional similarities when compared with those within the lower PAg.

It has been argued Chapter 2 and 3 that lithospheric extension occurred prior to the initiation of magmatism and was controlled by pre-existing regional structures parallel to, and genetically related to the age structure of the continental margin (see Fig. 2-10 and discussion in Chapter 3). If correct, this margin may have possessed a pre-existing lithospheric architecture comprised of thicker westerly hinterland, and young and juvenile, thinner easterly margin (Fig. 4-28). Such a setting and lithospheric architecture would be well-suited for the emplacement of the lower PAg magmas because of the requirement that the lithosphere be < 60 km thick beneath the lower PAg at ca. 2730 Ma. A thin lithosphere may have been present prior to magmatism because of an inherent lithospheric architecture enhanced by ongoing extension along the margin. In addition to simply providing space, the systematic and preferential eruption of mafic-ultramafic magmas between ca. 2735-2690 Ma within the supracrustal corridor suggests that indeed a large-scale lithospheric architecture controlled the distribution of magmatism and strongly influenced mantle upwelling. Within the lower PAg the eruption of the mafic-ultramafic magmas upon ca. 2750-2800 Ma crust, the youngest and most juvenile Rae basement recognized, and thus presumably the thinnest and most outboard crust comprising its margin. This observation is consistent with upwelling asthenosphere migrating to the shallowest depth possible, which may have been directly beneath the lower PAg. Similarly, at the regional scale, komatiite is the dominant manifestation of volcanism within the supracrustal corridor, a feature which is consistent with a relatively thin lithosphere beneath the corridor.

The major and incompatible trace element geochemistry of PAg komatiite and basalt collected from supracrustal strands located northeast of the Laughland Lake map area (e.g. see Fig. 4-2 and 4-3), and predominantly from the central Walker Lake (middle PAg - ca. 2710 Ma) and northeastern Ellice Hills strands (upper PAg - ca. 2690 Ma), provide compelling evidence for a similar melting history at the scale of the greenstone belt to that which we have described from the lower PAg. On the MgO versus $(Gd/Yb)_N$ and Hf/Hf* plots displayed in Fig. 4-29(a and b), the 48 samples of mafic and ultramafic volcanic rocks (< 55 wt.% SiO_2) spanning ~3-34 wt.% MgO collected from supracrustal strands northeast of the Laughland Lake map area are difficult to distinguish from those collected within the lower PAg. For example, all samples possessing < 20 wt.% MgO, i.e. broadly basaltic compositions, are minimally to moderately HREE-depleted ($(Gd/Yb)_N$ ~1.1-2.0) and possess minimal to negative HFSE anomalies (Hf/Hf* ~0.6-1.0), while komatiite magmas possessing ~22-34 wt.% are both HREE-depleted to -enriched ($(Gd/Yb)_N$ ~0.8-1.3) and possess minimal to positive HFSE anomalies (Hf/Hf* ~0.8-2.8) (Fig. 4-29(a and b)). These data suggest that the mantle upwelling and melting imaged within the lower PAg magmas is not unique. Numerous upwellings, undergoing similar low- and high-pressure melting histories, involving low and high-temperature mantle components must have experienced similar low-pressure mixing and differentiation processes.

In summary, the most suitable geodynamic model to explain the regional and volcanic succession scale geochemical, petrological, and chronological constraints for the PAg is an extensional continental margin setting in which, over a ~45 m.y. time period, discrete mantle upwellings were continually focused toward the most outboard, young and juvenile portions of this continental margin. The lower PAg, however, is particularly exceptional because it has recorded the complete melting history of one of these upwellings and in so doing, provides insights into the physical and thermal structure of the upwelling mantle which generated it.

THERMAL, PHYSICAL, AND CHEMCIAL STRUCTURE OF THERMALLY ANOMALOUS MANTLE UPWELLINGS AND THEIR ORIGIN

The precise thermal structure of the mantle upwelling imaged by the mafic and ultramafic magmas within the lower PAg is still uncertain, however, it must have been dominated by the high-temperature mantle component (see Fig. 4-27). This mantle achieved ~25 wt.% melting within the garnet stability field at ~5 GPa and a further ~30 wt.% melting at $\leq$ 2 GPa. In contrast, the low-temperature mantle component is only required to contribute ~2 wt.% melt at ~4 GPa. Such a negligible contribution for the low-temperature mantle component implies two possibilities: (1) either the low-temperature mantle was not physically part of the upwelling and may simply reflect incipient melting of ambient mantle near its solidus at ~4 GPa in response to thermal energy input from the high-degree stage 1 melt (group-A komatiite liquid) as it migrated within a channelized melt conduit through this lower temperature mantle; or (2) the low-temperature mantle was a relatively thin veneer of ambient mantle entrained along the periphery of the high-temperature upwelling. In either case, the predominance of high-temperature mantle component indicates that a thermal structure to the upwelling mantle is either so poorly manifested that it is negligible or, alternatively, non existent.

Irrespective of the thermal aspects of the upwelling, the distribution of geochemical signals with stratigraphic height within the lower PAg indicate that no new garnet-saturated melts (high- or low-temperature mantle derived) were being produced during the generation of the stage 2 group-D komatiite liquid at < 2 GPa. If this were so, the systematic difference between the group-D komatiite liquid and the ~30 wt.% model melt of harzburgite would not have been preserved (e.g. Fig. 4-24(b) and 4-25) and it seems unlikely that a group-D komatiite signature would be preserved at all if new garnet-saturated stage 1 melts were being produced. These observations suggest that the upwelling mantle which produced the lower PAg was a circumscribed parcel of mantle. Because this upwelling is dominated by a high-temperature component, the upwelling parcel of mantle imaged by magmas within the lower PAg may best be described thermal anomaly. The height of this anomaly is constrained to be < to << 90 km, the difference in the segregation depths for the high-degree stage 1 and 2 melts.

The lifespan of the thermal anomaly imaged within the lower PAg is only constrained to the time required for the parcel mantle to traverse the ~150 km interval between its deepest intersection with the peridotite solidus at ~6.8 GPa and the termination of melting at ~2 GPa. The high-precision U-Pb zircon age constraints indicate that a minimal time span, perhaps << 1 m.y., defines the transition from basalt-to komatiite dominated magmatism within the lower PAg and, as such, effectively dates the volcanic succession to ca. 2730 Ma. Arguably a tighter constraint for the lifespan of the thermal anomaly comes from the fact that the stage 1 melts were still differentiating during the arrival of the stage 2 melt and that they mixed and erupted together to form the komatiite horizon. This observation indicates that the lifespan of the thermal anomaly imaged within the lower PAg is only constrained to the time required for a komatiite melt to undergo ~50 wt.% crystal differentiation and produce a basalt. The overall lifespan of thermally anomalous mantle upwellings within the PAg, however, is considerably longer spanning ~40-45 m.y. To explain the geochemical signals preserved within all PAg basalt and komatiite (Fig. 4-29), numerous discrete thermal anomalies lasting ~1-2 m.y appear to be required. Collectively then, these anomalies should be considered components of a long-lived and broader mantle upwelling that spans the time interval between ca. 2735-2690 Ma.

A key component to understanding the origin these thermal anomalies is the fact that the low- and high-temperature mantle components imaged during stage 1 melting appear to be generated from a compositionally similar mantle. In Table 4-5 and Fig. 4-19(b and d)) it is clear that from a major element perspective, the relatively fertile peridotites KLB-1 and KR-4003 are indistinguishable from estimates for the primitive upper mantle (McDonough & Sun, 1995) or depleted MORB mantle (Salters & Stracke, 2004; Workman & Hart, 2005). Importantly, these relatively fertile peridotitic compositions are interpreted to be representative of the mean composition of the modern upper mantle and the primary reason that lherzolites KR-4003 and KLB-1 are routinely used in melting experiments. At the trace element level, several of the derivative stage 1 basalts, including the most enriched and depleted end-members, as well as some of the group-A komatiite, possess low $(Th/Nb)_N$ ratios between ~0.4-0.65 (see Appendix C). These particular samples are the least likely to have experienced any crustal contamination and the convergence in their $(Th/Nb)_N$ ratios, despite exceptional variations in $(Ce/Sm)_N$, $(Ce/Yb)_N$, Hf/Hf* and $(Gd/Yb)_N$, is striking. Importantly, the mean $(Th/Nb)_N$ and Nb/Nb* of ~0.5 and ~1.3 for these stage 1 magmas (n=7 samples) are identical to the average $(Th/Nb)_N$ and Nb/Nb* of the depleted MORB mantle (Salters & Stracke, 2004; Workman & Hart, 2005) of ~0.5 and ~1.3, respectively. This finding is especially important for two principal reasons: (1) the composition of the high- and low-temperature mantle components are indistinguishable; and (2) they are indistinguishable from the modern depleted upper mantle.

The evidence that a MORB-like mantle, in terms of its major and trace element composition was involved in generating the stage 1 melts is not surprising considering that their source, similar to the modern depleted upper mantle, must have been characterized by a uniform long-term depletion in Nd/Sm and Hf/Lu compared to the bulk earth. This finding, coupled with the fact that the source for the lower PAg magmas is indistinguishable from the ca. 2.7 Ga depleted upper mantle imaged by juvenile magmas within the southern Superior Province (Ayer *et al.*, 2002; Polat & Münker, 2004) suggest that the PAg mantle source originated within the upper mantle. The ~150 °C temperature difference between the low- and high-temperature mantle components (Fig. 4-27) suggests the low-temperature component may represent ambient upper mantle, and because both are representative of the upper mantle chemically, a mechanism/process seems necessary to “heat-up” the upper mantle. The suggestion that the low-temperature mantle component is ambient Archean upper mantle is well-supported by its estimated ~1580 °C potential temperature (allow for 0.3 °C per kilometer adiabatic ascent from ~4.25 GPa and ~1625 °C; Fig. 4-27) which is ~200 ° C hotter than some estimates for the potential temperature of the modern upper mantle at mid-ocean-ridges of ~1350-1400 °C (McKenzie & Bickle, 1988; Kinzler & Grove, 1992; Asimow *et al.*, 2001; Presnall *et al.*, 2002). This is also in excellent agreement with secular cooling models for the mantle since the late Archean which predict a temperature decrease over this time of ~200 ° C (Pollack, 1997).

In our opinion, two scenarios can describe the origin of the thermally anomalous mantle component, one is that thermal energy was transferred from the lower mantle to the upper mantle by upwellings initially generated at the core-mantle thermal boundary layer or, the uppermost mantle was heated due to thermal insulation by a thick (≥ 210 km; Fig. 4-27) and laterally extensive lithosphere. Although distinguishing between these two scenarios naturally involves considerable speculation, we consider the thermal insulation model to be the most problematical for the following reasons: (1) although it has been proposed that thermal insulation is capable of generating ΔT's of ~200 °C (e.g. Anderson, 1982; 1998), it is uncertain if such temperature anomalies can be produced/preserved in a hotter and more vigorously convecting Archean upper mantle; (2) thermal insulation models require a thick and laterally extensive lithosphere the size of a supercontinent (Gurnis, 1988; Anderson, 1994) and it is unknown if such a laterally extensive and thick lithosphere was present at ca. 2.7 Ga within the central and northeastern Rae domain; (3) the global production of high-temperature Al-undepleted komatiite from the depleted mantle at ca. 2.7 Ga, most of which are compositionally indistinguishable from the high-temperature stage 1 melt (i.e. Al-undepleted or Munro-type komatiite; e.g. Arndt, 1994) can be found in supracrustal belts where evidence for older and thicker lithosphere is absent (e.g. Abitibi greenstone belt; Ayer *et al*., 2002; Sproule *et al*., 2002); and (4) thermal insulation of ambient Archean mantle by a thick and laterally extensive lithosphere should have been equally capable of producing large amounts of Al-undepleted komatiite at time periods younger than ca. 2.7 Ga and cannot explain an apparent peak in their production at ca. 2.7 Ga (e.g. Condie, 2001)

For these reasons, we currently prefer a model in which thermal energy was transferred into the base of the upper mantle by lower mantle upwellings initiated at the core-mantle thermal boundary layer. As the composition of the lower mantle at the core-mantle boundary layer is uncertain, and because the chemical composition of the low- and high-temperature mantle components of the upwelling are chemically indistinguishable, a thermal, not chemical transfer between the lower and upper mantle seems to be required. If this model is correct, some pivotal questions still remain: (1) precisely how the physical form of these anomalies might be altered or possibly determined by their impact with the lithosphere; (2) how they physically interact with the low-temperature mantle during migration within the upper mantle; and (3) how many anomalies are required to be present during a particular period of magmatic activity within the corridor. Because multiple thermal anomalies are required to explain the geochemistry of ca. 2730-2690 Ma komatiite within the spatially limited PAg segment studied (~300 km of the ~1400 km strike length; Fig. 4-1), the acquisition of geochemistry from basalt and komatiite from chronologically well-constrained examples emplaced further along strike will be critical in addressing some of the remaining questions.

SUMMARY AND CONCLUSIONS

This study has demonstrated that high-MgO (~25-31 wt.%) Al-undepleted komatiite magmas produced at ca. 2.7 Ga require high degrees of peridotite melting (≥ 25 wt.% up to ~55-60 wt.%) that begins at ~7 GPa and terminates at pressures ≤ 2 GPa (orthopyroxene exhaustion). The mantle source for these high-MgO magmas is relatively fertile in terms of its major element composition and only minimally depleted in highly incompatible trace elements. The temperature of this mantle is anomalous and estimated to be ~150 °C greater than the ambient ca. 2.7 Ga mantle temperature. This ambient mantle is estimated to be ~200 °C hotter than the modern upper mantle and upon depressurization produces primary komatiitic magmas possessing minimum MgO contents of ~18-20 wt.%.

Thermally anomalous ca. 2.7 Ga mantle upwellings are discrete parcels of hot fertile mantle that originate from depths ≥ 200 km. The composition of these anomalies is identical to the ambient ca. 2.7 Ga mantle, and both are indistinguishable from the modern depleted upper mantle. This suggests that thermally anomalous mantle originates from within the upper mantle. The heating of the upper mantle is presumed to be from below, and potentially a result of thermal energy imparted from large-scale core-mantle boundary derived upwellings. At shallow depths (< 200 km), thermally anomalous mantle upwellings can be focused by pre-existing lithospheric architecture toward regions of thin lithosphere where maxima in melting and komatiite magma generation can be achieved.

APPENDIX A. SAMPLE PREPARATION AND ANALYTICAL METHODS

For major and trace element geochemistry, rock samples were cleaned of all visible alteration and reduced to sub-cm sized chips using a jaw crusher. The small rock chips were then hand picked and powdered using an agate mill. Fused glass discs were prepared from an aliquot of these powders and were analysed for major and selected minor and trace elements (SiO_2-Co; Table 4-1) using a Philips PW2440 X-ray fluorescence spectrometer at McGill University, Montreal. The accuracy of the XRF data is estimated to be < 1 % for all elements and method precision is within 0.5 % for all elements at concentration levels ≥ 10x the detection limit based on repeated measurement of international rock powders. The basalt samples all possess concentration levels > to >> than 10x the detection for elements analysed by XRF with the exception of some of the trace elements, including Ni, Cr and V. For komatiite, all elemental concentrations are ≥ to >> 10x the detection limit with the exception of Na_2O and K_2O. The loss on ignition (LOI) was determined gravimetrically.

The trace elements Co, Cr, Ni, V and Zn were determined by inductively coupled plasma-atomic emission spectrometry (ICP-AES) and Nb, Th, Y, Hf, Zr and the REE by ICP-mass spectrometry (ICP-MS) at the geochemical laboratories of the Geological Survey of Canada in Ottawa. For all analyses, rock powders were dissolved using a combination of nitric, perchloric and hydrofluoric acids followed by a lithium metaborate fusion of any residual material. The detection limits and results of duplicate dissolutions of whole rock komatiite and basalt samples are listed in Table 4-A-1. The accuracy and precision as evaluated by the analysis of in-house and international standard reference materials is generally < 5 % (2σ relative standard deviation) when concentrations are ~10x the limit of detection. The reproducibility of komatiite powders is < to << 10 % (% = (total difference/mean) x 100) for the REE and up to ~10-30 % for some high field strength elements (e.g. Hf and Th). Basaltic compositions generally reproduce extremely well for all trace elements in concentrations well above their detection limits (Table 4-A-1).

All Sm-Nd and U-Pb zircon isotopic analyses were preformed at the University of Alberta Radiogenic Isotope Facility, Edmonton, Alberta. For Sm-Nd isotope analyses, rock powders (prepared as above) were weighed into Teflon vials and spiked with a mixed ^{149}Sm-^{150}Nd tracer solution. The sample-spike mixture was dissolved and homogenized in a mixture of concentrated HF and HNO_3 acid for a period of 5-7 days at ~160 °C. Sm and Nd were concentrated and purified by following the analytical procedure described in Creaser *et al.* (1997). Sm isotopic ratios were measured on a multi-collector Sector-54 thermal ionization mass spectrometer (TIMS) operated in multi-dynamic mode. Nd isotopic ratios were acquired using a NuPlasma multicollector-inductively coupled plasma-mass spectrometer (MC-ICP-MS). For Nd, the isotopic analysis of unknown sample solutions was alternated with a 200 ppb solution of an in-house Nd Alfa isotopic standard solution (accepted ^{143}Nd/^{144}Nd = 0.512265 based on calibration to the La Jolla standard). Within a given analytical session the Nd-Alfa solution has an external reproducibility within ± 0.000015 and the long term lab average (n=256) has ^{143}Nd/^{144}Nd = 0.512240 ± 0.000020. The sample-standard bracketing technique was used to correct for instrumental drift during the analytical session. Solutions prepared from the same rock powder and analysed during separate analytical sessions always reproduce within their in-run precision. The uncertainty in $^{147}Sm/^{144}Nd$ based on analysis of basalt standard BCR-1 is ~0.2 %. Duplicate analyses of komatiite rock powders taken from the same vial reproduce $^{147}Sm/^{144}Nd$ within 0.2-0.3% (one sigma) and εNd(2730 Ma) values within 0.2-0.3 (Table 4-2). Typically, Archean rocks reproduce within < 0.4 epsilon units (e.g. Yamashita & Creaser, 1999).

For Lu-Hf isotopes, the chemical separation of Lu and Hf followed the procedure described in Bizzarro *et al.* (2003). Rock powders were weighed into graphite crucibles along with a metaborate flux and fused. The molten sample was rapidly transferred to a Teflon vial containing dilute HCl and a mixed ^{180}Hf-^{176}Lu tracer solution. The glass bead dissolution is rapid (~30 min.) and the resultant solutions are then loaded onto columns for separation and purification of Lu and Hf as outlined in Bizzarro *et al.* (2003). Procedural blanks of < 50 pg are considered negligible. Lu and Hf isotopic measurements were preformed on a NuPlasma MC-ICP-MS and follow the protocol outlined in Schmidberger *et al.* (2002). Repeat measurements (n=27) of a 50 ppb solution of the JMC 475 Hf isotopic standard during this study yielded the following average values: $^{176}Hf/^{177}Hf = 0.282160 \pm 20$, $^{178}Hf/^{177}Hf = 1.46728 \pm 7$, $^{180}Hf/^{177}Hf = 1.88677 \pm 21$ and $^{174}Hf/^{177}Hf = 0.00866 \pm 6$. Corrections for Lu and Yb isobaric interferences were monitored using the ^{175}Lu ion signal and any deviations from the accepted $^{174}Hf/^{177}Hf$ natural value (resulting from ^{174}Yb). Although a few samples required off-line corrections for minor Lu and Yb interferences, most yielded $^{174}Hf/^{177}Hf$ ratios of 0.00866, identical to the JMC Hf standard. Three duplicate analyses of basalt and komatiite powders taken from the same vial reproduce ^{176}Lu/^{177}Hf within ~0.3, 3 and 5 %, respectively (Table 4-2). The poor reproducibility of Lu/Hf for two samples is interpreted to result from sample heterogeneity as all duplicates reproduce initial εHf values within ~0.2.

APPENDIX B. ASSESSMENT OF HIGH-FIELD-STRENGTH ELEMENT ANOMALIES

In Fig. 4-B-1(a and b), quadrupole-ICP-MS data for Lu and Hf are plotted versus their respective concentrations as determined by ID-MC-ICP-MS. With respect to Lu, the two methods are in excellent agreement (Fig. 4-B-1(a)). Over the ~0.1-0.8 ppm range in Lu concentration, the maximum absolute difference between the two methods does not exceed ~0.02-0.03 ppm, and is close to the reproducibility for basalt and komatiite duplicates (quadrupole-ICP-MS up to ~0.02 ppm (Table 4-A-1); ID-MC-ICP-MS up to ~0.02 ppm (Table 4-2)). In contrast to Lu, the Hf concentrations obtained by the two methods are not in agreement for some samples. The enriched basalts containing > 2 ppm Hf yielded significantly higher Hf by ID-MC-ICP-MS (~0.3-0.9 ppm; Fig. 4-B-1(b)). This result is significant considering the reproducibility of Hf for samples containing < 2 ppm Hf is between ~0.06-0.08 ppm (by ID-MC-ICP-MS or quadrupole-ICP-MS). With the exception of komatiite sample TM0-228-A, basalt and komatiite with Hf concentrations < 2 ppm yielded similar Hf concentrations by both methods. The absolute difference in ppm ranges between ~0.02-0.19 and averages ~0.09 ppm, close to the reproducibility of each method.

The consistently higher Hf concentrations as determined by ID-MC-ICP-MS for basalt with elevated Hf (> 2 ppm) may be due to incomplete dissolution of a Hf-rich phase. Triplicate dissolutions of EB-1 sample T-3322-B are particularly informative. The duplicate analyses by quadrupole-ICP-MS yielded Hf concentrations of 3.6 and 3.9 ppm that are significantly different compared to the Hf reproducibility for duplicate analyses of depleted basalt and komatiite containing < 2 ppm Hf (up to ~0.08 ppm). The Hf concentration by ID-MC-ICP-MS of 4.4 ppm is even higher. In contrast, the Lu concentration of all three analyses is indistinguishable (0.30-0.32 ppm). These data strongly suggest that a Hf-rich phase was variably dissolved in the three separate dissolutions and that the ID-MC-ICP-MS data is closest to the true value.

In Fig. 4-B-2 the variation in Hf/Hf* resulting from interchanging Hf analysed by quadrupole-ICP-MS versus ID-MC-ICP-MS is semi-quantitatively examined. Two important analytically related features are evident: (1) the significant differences in Hf concentrations for the enriched basalt samples between the two methods have a minor effect on Hf/Hf*; and (2) most basalt and komatiite plot close to or on a 1:1 Hf/Hf* correlation line. For komatiite, a ±0.3 uncertainty in Hf/Hf* is shown for all samples and, with one exception, both methods agree within this assigned uncertainty. This uncertainty takes into account the reproducibility of Hf obtained for komatiite duplicates within the ~0.4-0.8 ppm range which averages ~0.06. For example, Hf/Hf* varies within ~0.6 if a ±0.06 ppm uncertainty is applied to komatiite samples with the lowest Hf concentrations (n=12 with ~0.4 ppm Hf). This degree of uncertainty seems reasonable considering the reproducibility of Hf concentrations by both methods. For example, the ~0.06 ppm difference in Hf concentration for komatiite sample TM0-011-F yields Hf/Hf* ratios that differ by ~0.2.

In Fig. 4-B-3(a and b) Ti/Ti* and Hf/Hf* are plotted versus P/P* for all basalt and komatiite analysed in this study and, with few exceptions, HFSE/REE fractionations are exceptionally well correlated. Significant deviations from the well-correlated array between P/P* and Hf/Hf* in Fig. 4-B-3(b) are found for seven komatiite samples, including TM0-228-A, and interpreted to possess anomalously high Hf. None of these samples can be explained by reasonable analytical uncertainties (e.g. all are >1 Hf/Hf* unit above the array). Although two samples (TM0-227-D and TM0-235-5) plot off both the P/P*-Ti/Ti* and P/P*-Hf/Hf* arrays, potentially suggesting that P/P* ratios are an issue for these samples not Hf/Hf*. Overall, the exceptional correlation of virtually all basalt and komatiite samples with respect to P/P*, Hf/Hf* (and Zr/Zr*), and Ti/Ti* suggests that the Hf (and Zr) of samples labeled in Fig. 4-B-3(b) are highly suspect.

APPENDIX C. ASSESSMENT OF CRUSTAL CONTAMINATION AND DETECTION LIMIT EFFECTS ON HIGHLY INCOMPATIBLE TRACE ELEMENT RATIOS

In Fig. 4-C-1(a), all low and high $(Th/Nb)_N$ volcanic rocks collected within the lower PAg are plotted on a $(Th/Nb)_N$ versus Nb/Nb* diagram. Over a considerable range in $(Th/Nb)_N$ and Nb/Nb*, all magmas are exceptionally well-correlated ($R^2 = 0.93$) and define a power law distribution. This distribution is interpreted, at least for the high $(Th/Nb)_N$ magmas, to reflect mixing between basalt and komatiite possessing low $(Th/Nb)_N$ and elevated Nb/Nb* with high $(Th/Nb)_N$ and low Nb/Nb* crust and/or crustally-derived melts (Chapter 3). For low $(Th/Nb)_N$ basalt and komatiite (Fig. 4-C-1(b)), the most depleted magmas from almost all geochemical groups possess $(Th/Nb)_N$

ratios between ~0.40-0.65, although, a significant number of samples possess elevated $(Th/Nb)_N$ and Nb/Nb*.

The effects of crustal contamination and/or analytical uncertainty in Th concentration upon $(Th/Nb)_N$ and Nb/Nb* are quantitatively examined in (Fig. 4-C-1(b-d)). The results of this modeling clearly indicate that minute amounts of crustal contamination can readily explain the within group variations and overall correlation observed in $(Th/Nb)_N$ and Nb/Nb* for most basalt and komatiite. The only exceptions include the two EB-1 samples which require significant amounts of crustal contamination to explain their elevated $(Th/Nb)_N$ ratios (Fig. 4-C-1(d)). The close spatial association of these particular samples with the high $(Th/Nb)_N$ dacite T-3319-B within the SVZ (Fig. 4-5) might suggest that these particular basalts mixed with intermediated-felsic melts within the upper crust. In addition to contamination, normal analytical uncertainty in Th concentration for samples with contents near the ~0.02 ppm detection limit can have a major effect on $(Th/Nb)_N$ and Nb/Nb* (Fig. 4-C-1(b)).

APPENDIX D. QUANTIFICATION OF THE MOST HREE-ENRICHED KOMATIITE LIQUID

The olivine-phyric komatiite samples collected from flow #4 and 6 (Fig. 4-6(d)) display significant variation in $(Gd/Yb)_N$ ~0.5-0.9 (Table 4-1) and thus contain both group-C and -D komatiite (Fig. 4-8). Because olivine accumulation within komatiite flows is capable of decreasing $(Gd/Yb)_N$ (e.g. Arndt and Lesher, 1992) modeling of olivine accumulation is examined as a possible mechanism to generate the group-D komatiite from a the group-C komatiite liquid. Based on $MgO-Al_2O_3$ and $MgO-TiO_2$

systematics (Fig. 4-D-1(a and b)) < 50 wt.% olivine addition to the group-C liquid is required to produce the average group-D komatiite. Using these constraints and two sets of olivine partition coefficients for the MREE and HREE, including those obtained in the Kambalda study highlighted above (Arndt and Lesher, 1992), the effects of olivine accumulation on $(Gd/Yb)_N$ can been quantitatively assessed (Fig. 4-D-1(c)). The results of the modeling indicate that the addition of ~50 wt.% olivine to the group-C liquid can only reasonably decrease $(Gd/Yb)_N$ by ~0.05 (Fig. 4-E-1(c)). Also inconsistent with olivine control upon $(Gd/Yb)_N$, the ~0.4 difference in $(Gd/Yb)_N$ for samples from both flows is not correlated with their limited range in MgO (~32-40 wt.%). The modeling results can be reconciled if incomplete magma mixing between variably HREE-enriched komatiite liquids occurred during the eruption and crystallization of these flows. This requires the existence of a group-D komatiite liquid end-member characterized by strong HREE-enrichment.

Employing the regressions in Fig. 4-12 and ultramafic liquid possessing a $(Gd/Yb)_N$ of ~0.6 should possess high-MgO (~31 wt.%) and very low $Fe_2O_3(T)$ (~10 wt.%) and TiO_2 (~0.25 wt.%). We chose to define the full incompatible trace element composition of the group-D komatiite liquid by un-mixing the group-A and -C liquids (Fig. 4-16). This method eliminates two problematical issues in attempting to define the incompatible trace element profile of this liquid by un-mixing olivine including: (1) the low incompatible element contents of some of the group-D komatiite samples that approach analytical detection limits (e.g. Th) and are thus unreliable; and (2) the group-D samples from flows #4 and 6 (n=6/7) possess anomalously elevated concentrations of highly incompatible trace elements (Fig. 4-D-2(a)). Although an apparent mean excesses in Th may be entirely analytical in nature, the elevated Nb and La-Nd of the group-D komatiite samples from these flows is surprising, in particular because it is not observed for the group-C samples within the same flow. This suggests that the incompatible elements were added to the group-D parental liquid prior to partitioning into the two flows. The Sm-Nd isotopic systematics of three group-D komatiite samples (εNd(2730 Ma) between +2 to +3; Table 4-2)) indicate that LREE addition occurred shortly before or was synchronous with the crystallization of flows.

In Fig. 4-D-2(b) the group-D liquid is shown along with the results of adding 1 wt.% TTG and 1.5 wt.% of the mean EB-1 and -2 to this liquid. It is apparent from these simple mixing models that small amounts of contamination of the group-D komatiite liquid enriched basalts can explain the relatively flat, primitive mantle normalized Nb and LREE (La-Nd) that characterizes the average group-D komatiite from flows #4 and 6 (Fig. 4-E-2(b)) whereas a TTG-type contaminant cannot. This contamination is suspected to have occurred as the group-D komatiite liquid was travelling within a lava channel (flow #6 in Fig. 4-6(d)) that flowed over and assimilated some of the lower basalts. This would explain how only the group-D samples from flows #4 and 6 were affected and suggests that the spinifex-textured flow #4 was, at least in part, supplied by highly depleted magmas traveling in the lava channel.

APPENDIX E. PLAGIOCLASE AND LOW-CAO PYROXENE (PIGEONITE) FRACTIONATION

The within-group variation in incompatible trace element content displayed by EB-3 is extreme and anomalous. On the MgO versus Yb plot in Fig. 4-9, the EB-3 posses consistently low MgO contents (~4.4-5.9 wt.%) and extremely variable Yb (e.g. ~2.6-5.4 ppm). The negative correlation between MgO and Yb displayed by most other basalt groups is broadly consistent with olivine and clinopyroxene crystal fractionation, however, the EB-3 variation in these elements cannot be explained by fractionation of these minerals. The variation in incompatible trace element content for the EB-3 is, however, closely tied to variations in Al_2O_3 and CaO. The association of low Al_2O_3 (and CaO) with EB-3 samples possessing elevated incompatible trace element contents suggests crystal fractionation involving plagioclase. On a Al_2O_3 versus CaO plot (Fig. 4-E-1(a)) the EB-3 are exceptional well correlated ($R^2 = 0.96$) and can be used along with the incompatible element contents of end-members within the group (Fig. 4-E-1(b)) to semi-quantitatively model this fractionation.

Assuming that the REE were equally highly incompatible during the proposed crystal fractionation, then ~50 wt.% crystal fractionation of the least differentiated EB-3 sample HS0-091-I is required to increase the REE abundances to the levels observed in samples T-3324-A and -B (Fig. 4-E-1(b)). With this constraint, and assuming plagioclase is a fractionating phase, pigeonite and augite must have also co-precipitated with plagioclase. In Fig. 4-E-1(a) appropriate plagioclase, pigeonite, and augite mineral compositions taken from literature suggest that the mineral assemblage may be approximated by ~45 wt.% plagioclase and ~55 wt.% pyroxene, and that the pyroxene assemblage is ~60 wt.% augite and ~40 wt.% pigeonite. Importantly, the co-precipitation of pigeonite and plagioclase with augite is expected to occur in differentiating komatiite magmas that have experienced earlier olivine and augite co-precipitation based upon experimental phase equilibrium studies (Kinzler & Grove, 1985).

Table 4-1. Major and trace element oxides (except Cr_2O_3 (ppm)) and LOI are in wt.% and all other elements in ppm. XRF data listed between SiO_2 and Ni have been normalized to 100 wt.% anhydrous. Group: highly enriched group-1 basalt (EB-1); moderately enriched group-2 basalt (EB-2); minimally enriched group-3 basalt (EB-3); depleted basalt (DB); group-A, -B, -C, and -D komatiite (A, B, C, and D). Horizon: basalt (B); komatiite (K). Zone: southwest volcanic zone (SVZ); northeast volcanic zone (NVZ). Rock type: pyroxene spinifex-textured basalt (p. spfx.); spinifex-texture komatiite (kom. ol. spfx.); polyhedral olivine-phyric komatiite (kom. ol. phy.). Flow type: aphyric basalt (aphy.); spinifex-textured komatiite flow (p. spfx.); non-spinifex-textured komatiite (n. spfx.). Flow number (flow no. (1-6)). Flow thickness in metres (thick). Subscript N (e.g. $(Ce/Yb)_N$) denotes normalization relative to primitive mantle (McDonough & Sun, 1995). The HFSE/HFSE* ratios (e.g. P/P*) measure their fractionation relative to the bounding trace elements as depicted in Fig. 4-8 (see Fig. 4-10).

Table 4-2. Uncertainty reported in the Nd and Hf isotopic ratios is $2\sigma/\sqrt{n}$ analytical error in the last decimal place, where *n* is the number of measured isotopic ratios. Nd isotopic ratios normalized to $^{146}Nd/^{144}Nd = 0.7219$ and initial εNd values (2730 Ma) calculated using present day CHUR parameters of $^{143}Nd/^{144}Nd = 0.512638$ and $^{147}Sm/^{144}Nd = 0.1967$. Hf isotopic ratios normalized to $^{179}Hf/^{177}Hf = 0.7325$ and initial εHf values (2730 Ma) calculated using present day CHUR parameters of $^{176}Hf/^{177}Hf = 0.282772$ and $^{176}Lu/^{177}Hf = 0.0332$ (Blichert-Toft & Albarède, 1997) and a decay constant for ^{176}Lu of

1.866 E-11 (Scherer *et al.*, 2001; Söderlund *et al.*, 2004). Age calculations were preformed using the Isoplot version 3.00 software (Ludwig, 1992).

Table 4-3. References: (1) Salters *et al.* (2002); (2) McDade *et al.* (2003); (3) Zanetti *et al.* (2004); (4) Salters & Longhi (1999); (5) Blundy *et al.* (1998); (6) Arth (1976); (7) van Westrenen *et al.* (1999); (8) Draper *et al.* (2003). The postulated ~4 GPa garnet (Gt.-1) is essentially a composite (average) of the 2.4-3.4 GPa garnets of Salters & Longhi (1999) and Salters *et al.* (2002), however, the partition coefficients for the compatible elements Y, Yb, and Lu were calculated by multiplying the average 3.2-3.4 GPa garnet of Salters *et al.* (2002) by 0.65. This represents the average decrease in these partition coefficients observed with increasing pressure from ~2.4-2.8 to 3.2-3.4 GPa. The italicized plagioclase, olivine, and clinopyroxene partition coefficients are all interpolated values assessed in relation to the bounding REE and HFSE for which portioning data are available. These partition coefficients are only employed in modeling fractional crystallization in order to maintain elemental continuity in REE and extended trace element diagrams between basalt and komatiite and not in modeling partial melting.

Table 4-4. The high degree (~25 wt.%) garnet peridotite melts (KR-4003) are averages of garnet-saturated runs conducted between ~4.5 and 6 GPa (Walter, 1998). The presumed ~5.0 GPa melt is a composite of the ~4.5 and 6 GPa melts and equivalent to 65 wt.% of the ~4.5 GPa melt and 35 wt.% of the 6 GPa melt, respectively. The Al-undepleted komatiite (Al-und. kom.) is from Wei *et al.*, (1990), a composition which displayed olivine, pyroxene, and garnet co-saturation near ~5.6 GPa. The group-A

komatiite liquid is an average of the four spinifex-textured samples within this group (Table 4-1).

Table 4-5. Minerals compositions and normative modes are those in equilibrium with ~12 and ~37 wt.% melt at ~4.5 GPa and taken from the garnet peridotite (KR-4003) melting experiments of Walter (1998). The compositions of the residues shown were calculated from these data. The peridotitic mantle compositions shown for comparison include: DMM-1 - Wasylenki *et al.* (2003); DMMa - Salters & Strake (2004); DMMb - Workman & Hart (2005); PM - McDonough & Sun (1995); KLB-1 - Walter (1998); KR-4003 - Walter (1998).

Table 4-A-1. Duplicate trace element analyses of komatiite and basalt. The % error is a relative error calculated as ((total difference/mean)*100). Detection limit (d.l.). The trace element ratios are calculated as those in Table 4-1.

Table 4-1. Major and trace element compositions of PAg mafic and ultramafic rocks.

Group	EB-1	EB-1	EB-1	EB-2	EB-2	EB-2	EB-3	EB-3	EB-3	EB-3
Horizon	B	B	B	B	B	K	B	B	B	B
Zone	SVZ	SVZ	SVZ	SVZ	SVZ	SVZ	SVZ	SVZ	SVZ	SVZ
Sample	T-3318-A	T-3322-A	T-3322-B	T-3318-B	T-3319-A	TM0-285-D4	T-3324-A	T-3324-B	T-3325-A	T-3325-B
Rock type	basalt	basalt	basalt	basalt	basalt	basalt	basalt	basalt	basalt	basalt
Flow type	aphy.	aphy.	aphy.	aphy.	aphy.	aphy.	aphy.	aphy.	aphy.	aphy.
Flow no.\thick	na	na	na	na	na	na	na	na	na	na
SiO_2	49.16	46.62	49.38	48.59	53.40	45.01	49.50	50.13	46.86	48.45
TiO_2	2.14	1.45	3.01	1.88	1.35	2.68	2.40	2.37	2.39	1.79
Al_2O_3	18.98	13.46	14.83	15.08	15.16	14.61	13.23	12.95	13.81	14.80
Fe_2O_3	11.70	13.88	13.37	14.35	11.80	17.65	18.55	18.48	18.77	14.92
MnO	0.21	0.23	0.18	0.22	0.18	0.21	0.25	0.26	0.23	0.23
MgO	4.25	10.66	7.16	5.80	5.30	6.75	4.40	4.62	5.17	5.93
CaO	9.68	10.96	7.85	11.42	10.64	9.87	8.18	8.05	9.87	11.58
Na_2O	2.17	2.16	2.46	2.20	1.43	2.53	2.97	2.63	2.40	1.83
K_2O	1.07	0.31	1.23	0.27	0.47	0.26	0.26	0.27	0.31	0.26
P_2O_5	0.64	0.19	0.51	0.17	0.21	0.41	0.26	0.23	0.18	0.17
Cr_2O_3	< 15	572	172	250	385	143	< 15	< 15	< 15	227
Ni	3	273	51	53	159	47	10	10	34	86
V	194	229	273	293	211	350	354	364	646	299
Co	34	61	42	43	39	45	49	35	47	40
LOI	4.61	2.72	1.29	0.76	8.41	0.62	0.26	0.27	0.65	1.52
Total	100.6	100.5	100.3	100.5	100.1	100.6	100.5	101.1	100.7	100.2
Co	33	59	45	44	44	47	48	48	53	44
Cr	17	411	152	200	268	143	53	50	37	189
Ni	16	269	64	69	149	70	37	39	64	98
Sc	22	29	29	39	26	37	42	44	48	37
V	195	228	270	298	214	343	356	371	679	312
Zn	133	142	160	128	134	139	168	176	151	154
Ga	24	17	21	20	18	21	21	21	21	19
Nb	16	13	19	7.6	7.5	11	9.9	9.3	5.8	5.3
Th	1.9	0.99	0.90	0.39	0.91	0.55	0.96	0.84	0.56	0.51
Y	33	24	31	31	19	27	59	53	40	35
Hf	4	1.8	3.6	2.2	2.3	2.2	3.7	3.5	2.5	2.1
Zr	165	68	140	82	93	88	128	122	86	79
La	31	18	21	6.7	11	11	10	9.2	6.5	5.8
Ce	79	48	63	21	27	30	28	25	18	16
Pr	11	6.8	9.4	3.3	3.6	4.3	4.3	3.7	2.8	2.4
Nd	45	29	43	17	16	21	21	19	14	13
Sm	9	5.9	9.5	4.7	3.9	5	6.7	5.8	4.5	4.2
Gd	7.5	5.1	8.4	5.4	3.8	5.6	8.4	7.3	5.8	5.2
Tb	1.1	0.75	1.2	0.91	0.64	0.87	1.5	1.4	1.0	0.92
Dy	5.9	4.1	6.0	5.2	3.5	4.9	9.2	8.2	6.2	5.6
Ho	1.1	0.82	1.1	1.0	0.68	0.96	2.0	1.7	1.3	1.2
Er	2.8	2.1	2.5	2.7	1.7	2.5	5.4	4.9	3.7	3.2
Tm	0.41	0.31	0.35	0.4	0.25	0.36	0.83	0.77	0.55	0.5
Yb	2.40	1.90	2.10	2.40	1.60	2.30	5.40	4.90	3.60	3.20
Lu	0.36	0.29	0.30	0.37	0.24	0.34	0.82	0.73	0.55	0.5
$(Th/Nb)_N$	0.98	0.63	0.39	0.42	1.00	0.41	0.80	0.75	0.80	0.80
$(Ce/Sm)_N$	2.13	1.97	1.61	1.08	1.68	1.45	1.01	1.04	0.97	0.92
$(Ce/Yb)_N$	8.67	6.65	7.90	2.30	4.44	3.43	1.37	1.34	1.32	1.32
$(Gd/Yb)_N$	2.53	2.18	3.24	1.82	1.93	1.97	1.26	1.21	1.31	1.32
Nb/Nb*	0.72	1.06	1.51	1.62	0.82	1.54	1.10	1.15	1.05	1.06
P/P*	0.78	0.37	0.69	0.61	0.77	1.19	0.75	0.76	0.79	0.83
Zr/Zr*	0.56	0.35	0.47	0.62	0.80	0.58	0.73	0.79	0.74	0.73
Hf/Hf*	0.5	0.3	0.4	0.6	0.7	0.5	0.79	0.84	0.79	0.72
Ti/Ti*	0.61	0.62	0.79	0.87	0.82	1.18	0.75	0.85	1.09	0.90
Al_2O_3/TiO_2	8.9	9.3	4.9	8.0	11.2	5.5	5.5	5.5	5.8	8.3
CaO/Al_2O_3	0.51	0.81	0.53	0.76	0.70	0.68	0.62	0.62	0.71	0.78

Table 4-1. Continued

Group	EB-3	DB	DB	DB	DB	A	A	A	A	A
Horizon	K	K	K	K	K	K	K	K	K	K
Zone	SVZ	NVZ	NVZ	NVZ	NVZ	NVZ	NVZ	NVZ	NVZ	NVZ
Sample	HSO-091-I	TM-7-D	TM-7-E	TM0-239-E	TM0-239-F	TMO-011-F	TMO-011-G	TMO-011-H	TMO-239-12	TMO-011-A
Rock type	gabbro	basalt	basalt	basalt	basalt	kom.	kom.	kom.	kom.	kom.
	na	p. spfx.	p. spfx.			ol. spfx.	ol. spfx.	ol. spfx.	ol. spfx.	ol. phy.
Flow type	na	spfx.	spfx.	aphy.	aphy.	spfx.	spfx.	spfx.	spfx.	spfx.
Flow no.\thick	na	1(<10)	1(<10)	na	na	na	na	na	na	na
SiO_2	50.46	47.70	48.37	48.10	50.14	45.15	44.02	45.17	42.41	46.53
TiO_2	1.29	0.70	0.63	0.88	0.73	0.45	0.49	0.43	0.46	0.33
Al_2O_3	15.03	12.96	12.50	13.75	13.53	7.70	8.31	7.65	8.23	5.56
Fe_2O_3	14.52	12.23	12.13	15.52	13.65	13.25	13.80	13.39	14.39	11.15
MnO	0.23	0.18	0.18	0.20	0.18	0.17	0.16	0.18	0.16	0.16
MgO	4.68	12.19	12.98	7.75	7.87	24.87	25.19	24.65	26.72	29.81
CaO	11.35	9.23	8.74	9.17	8.91	7.46	7.01	7.57	6.68	5.70
Na_2O	1.82	4.05	4.09	4.38	4.73	0.33	0.36	0.34	0.31	0.17
K_2O	0.51	0.54	0.17	0.19	0.19	0.02	0.02	0.02	0.03	0.02
P_2O_5	0.11	0.07	0.06	0.06	0.05	0.04	0.04	0.04	0.04	0.03
Cr_2O_3	71	1226	1115	< 15	162	4354	4665	4390	3902	3549
Ni	28	187	238	40	65	1229	1215	1230	1739	1763
V	324	224	209	315	264	151	172	149	124	114
Co	47	63	61	65	58	100	100	94	106	104
LOI	3.66	1.19	2.23	0.37	0.43	5.42	5.69	5.25	6.84	7.35
Total	100.1	100.4	100.4	100.6	100.5	100.5	100.1	100.2	100.4	100.6
Co	46	58	58	66	58	100	96	96	91	95
Cr	84	858	782	26	147	2910	3160	3010	3140	2350
Ni	44	186	230	57	75	1060	1050	1070	1030	1490
Sc	42	36	36	42	40	26	29	26	28	20
V	328	225	214	322	268	154	174	156	178	113
Zn	128	80	82	74	69	72	74	77	77	75
Ga	19	13	13	16	14	7.5	8.3	7.8	7.8	5.7
Nb	3.8	1.4	1.5	1.5	1.1	0.76	0.87	0.75	0.68	0.64
Th	0.42	0.09	0.15	0.14	0.1	0.08	0.07	0.07	0.06	0.06
Y	25	19	16	21	17	10	9.9	9.6	9.3	8.2
Hf	1.6	1.2	1.1	1.2	0.99	0.78	0.81	0.82	0.64	0.56
Zr	58	41	34	43	32	27	30	27	23	20
La	4.6	1.4	1.8	1.6	1.2	0.8	0.9	0.7	0.8	0.8
Ce	12	4.7	5.1	5.1	3.7	2.4	2.4	2.3	2.2	2.5
Pr	1.8	0.82	0.80	0.89	0.67	0.47	0.43	0.44	0.39	0.42
Nd	8.8	4.4	4.2	5.0	3.9	2.7	2.5	2.5	2.3	2.3
Sm	2.9	1.7	1.4	1.9	1.5	1.1	0.99	0.95	0.89	0.84
Gd	3.8	2.5	2.1	3.0	2.3	1.5	1.5	1.50	1.4	1.2
Tb	0.67	0.45	0.4	0.54	0.43	0.29	0.26	0.26	0.25	0.2
Dy	4.2	3.1	2.6	3.5	2.9	1.7	1.7	1.6	1.6	1.3
Ho	0.89	0.67	0.56	0.76	0.63	0.37	0.34	0.34	0.35	0.29
Er	2.4	1.8	1.6	2.0	1.7	1.0	0.91	0.90	0.96	0.76
Tm	0.38	0.29	0.25	0.3	0.24	0.15	0.15	0.14	0.15	0.12
Yb	2.60	1.9	1.7	2.1	1.7	0.97	0.93	0.92	0.96	0.78
Lu	0.4	0.29	0.24	0.31	0.25	0.14	0.15	0.15	0.14	0.12
$(Th/Nb)_N$	0.91	0.53	0.83	0.77	0.75	0.87	0.67	0.77	0.73	0.78
$(Ce/Sm)_N$	1.00	0.67	0.88	0.65	0.60	0.53	0.59	0.59	0.60	0.72
$(Ce/Yb)_N$	1.22	0.65	0.79	0.64	0.57	0.65	0.68	0.66	0.60	0.84
$(Gd/Yb)_N$	1.18	1.07	1.00	1.16	1.10	1.25	1.31	1.32	1.18	1.25
Nb/Nb*	0.94	1.36	1.00	1.09	1.10	1.04	1.20	1.17	1.07	1.01
P/P*	0.77	0.96	0.96	0.81	0.83	1.02	1.03	0.96	1.17	0.86
Zr/Zr*	0.78	1.02	0.95	0.95	0.90	1.06	1.29	1.19	1.09	0.98
Hf/Hf*	0.80	1.10	1.14	0.98	1.03	1.14	1.30	1.34	1.13	1.01
Ti/Ti*	0.91	0.79	0.86	0.86	0.91	0.82	0.94	0.85	0.96	0.76
Al_2O_3/TiO_2	11.7	18.6	19.8	15.7	18.6	17.1	16.9	17.6	17.9	17.1
CaO/Al_2O_3	0.76	0.71	0.70	0.67	0.66	0.97	0.84	0.99	0.81	1.03

Table 4-1. Continued

Group	A	A	A	B	B	B	B	B	B	B
Horizon	K	K	K	K	K	K	K	K	K	K
Zone	NVZ	NVZ	NVZ	SVZ	NVZ	NVZ	NVZ	NVZ	NVZ	NVZ
Sample	TMO-011-B	TMO-011-C	TMO-011-D	HSO-091-SP3	TM-1	TM-1A	TM-1B	TM-1C	TM-1D	TM-1E
Rock type	kom. ol. phy.	kom. ol. phy.	kom. ol. phy.	kom. ol. spfx.	kom. ol. spfx.	kom. ol. spfx.	kom. ol. spfx.	kom. ol. spfx.	kom. ol. spfx.	kom. ol. spfx.
Flow type	spfx.	spfx.	spfx.	spfx.	spfx.	spfx.	spfx.	spfx.	spfx.	spfx.
Flow no.\thick	na	na	na	na	na	na	na	na	na	na
SiO_2	44.61	43.73	47.22	44.32	44.57	45.05	44.95	45.23	43.48	45.92
TiO_2	0.30	0.35	0.33	0.39	0.41	0.41	0.39	0.39	0.44	0.37
Al_2O_3	5.23	5.92	5.52	8.38	7.93	7.71	7.97	7.42	8.51	7.22
Fe_2O_3	11.80	12.76	11.46	13.00	13.10	12.92	12.55	13.10	13.72	12.66
MnO	0.16	0.15	0.19	0.16	0.13	0.13	0.15	0.13	0.13	0.14
MgO	33.56	32.62	27.87	27.01	26.73	27.55	27.08	27.23	26.77	25.97
CaO	3.62	3.71	6.63	5.86	6.24	5.38	6.03	5.63	6.08	6.82
Na_2O	0.08	0.12	0.22	0.26	0.26	0.20	0.23	0.22	0.22	0.28
K_2O	0.02	0.02	0.02	0.02	0.03	0.02	0.02	0.02	0.02	0.01
P_2O_5	0.02	0.03	0.02	0.03	0.03	0.04	0.04	0.05	0.04	0.04
Cr_2O_3	3755	3828	3581	4496	4587	4577	4495	4403	4750	4269
Ni	2122	2032	1674	1142	1125	1374	1271	1393	1121	1372
V	96	106	126	159	153	143	142	149	161	147
Co	102	104	92	91	83	95	87	99	83	87
LOI	9.58	8.84	5.19	6.81	6.29	6.43	6.3	6.27	6.57	5.69
Total	100.8	100.7	100.4	100.1	100.4	100.5	100.2	100.3	100.9	100.7
Co	118	106	98	91	93	101				
Cr	2490	2530	2450	2990	3110	3090				
Ni	1790	1700	1460	991	1160	1340				
Sc	18	20	19	26	28	27				
V	102	111	122	164	166	148				
Zn	50	62	69	74	73	65				
Ga	5.9	6.3	6.1	8.7	8.1	8.2				
Nb	0.51	0.58	0.57	0.65	0.63	0.57				
Th	0.04	0.05	0.07	0.05	0.07	0.06				
Y	6.1	5.9	7.8	7.0	8.4	7.9				
Hf	0.51	0.62	0.72	0.64	0.64	0.64				
Zr	18	23	26	23	23	23				
La	0.6	0.6	0.7	0.6	0.8	0.6				
Ce	1.7	1.7	2.1	1.6	1.9	1.6				
Pr	0.28	0.27	0.35	0.26	0.33	0.27				
Nd	1.5	1.6	2	1.6	1.7	1.6				
Sm	0.57	0.55	0.75	0.58	0.66	0.65				
Gd	0.9	0.89	1.1	0.97	1.1	1.1				
Tb	0.15	0.15	0.21	0.18	0.2	0.2				
Dy	1.0	1.0	1.3	1.2	1.4	1.3				
Ho	0.21	0.21	0.27	0.26	0.29	0.28				
Er	0.55	0.56	0.74	0.66	0.8	0.79				
Tm	0.09	0.09	0.12	0.11	0.13	0.12				
Yb	0.58	0.59	0.74	0.75	0.81	0.79				
Lu	0.09	0.1	0.11	0.11	0.12	0.12				
$(Th/Nb)_N$	0.65	0.71	1.02	0.64	0.92	0.87				
$(Ce/Sm)_N$	0.72	0.75	0.68	0.67	0.70	0.60				
$(Ce/Yb)_N$	0.77	0.76	0.75	0.56	0.62	0.53				
$(Gd/Yb)_N$	1.26	1.22	1.21	1.05	1.10	1.13				
Nb/Nb*	1.14	1.16	0.89	1.29	0.92	1.04				
P/P*	1.02	1.22	0.79	1.32	1.16	1.72				
Zr/Zr*	1.32	1.66	1.44	1.62	1.47	1.53				
Hf/Hf*	1.39	1.66	1.48	1.67	1.52	1.58				
Ti/Ti*	0.99	1.15	0.84	1.21	1.13	1.12				
Al_2O_3/TiO_2	17.3	17.2	16.8	21.6	19.2	19.0	20.2	19.2	19.5	19.3
CaO/Al_2O_3	0.69	0.63	1.20	0.70	0.79	0.70	0.76	0.76	0.71	0.94

Table 4-1. Continued

Group	B	B	B	B	B	B	C	C	C	C
Horizon	K	K	K	K	K	K	K	K	K	K
Zone	NVZ	SVZ	NVZ	NVZ	NVZ	NVZ	SVZ	SVZ	SVZ	SVZ
Sample	TMO-011-E	TMO-285-F8	TMO-014-C	TMO-231-B	TMO-239-1	TMO-239-9	HSO-091-SP1	HSO-091-SP1A	HSO-091-SP1B	HSO-091-SP2
Rock type	kom. ol. spfx.	kom. ol. spfx.	kom. ol. phy.	kom. ol. phy.	kom. ol. phy.	kom. ol. phy.	kom. ol. spfx.	kom. ol. spfx.	kom. ol. spfx.	kom. ol. spfx.
Flow type	spfx.	spfx.	n. spfx.	n. spfx.	n. spfx.	n. spfe.	spfx.	spfx.	spfx.	spfx.
Flow no.\thick	na	na	na	na	na	na	na	na	na	na
SiO_2	41.65	44.81	44.77	43.91	46.51	45.31	42.44	45.13	45.09	45.74
TiO_2	0.57	0.40	0.27	0.27	0.31	0.35	0.43	0.33	0.32	0.33
Al_2O_3	9.38	8.19	5.93	5.38	5.84	6.15	8.66	7.09	6.91	7.42
Fe_2O_3	15.68	12.50	9.93	10.53	11.05	11.54	14.86	11.51	11.95	10.26
MnO	0.16	0.16	0.15	0.16	0.21	0.16	0.24	0.15	0.14	0.15
MgO	25.59	26.18	32.90	33.94	27.45	29.87	21.92	29.17	29.03	29.24
CaO	6.00	6.86	5.19	5.18	7.84	5.74	10.40	5.74	5.70	5.97
Na_2O	0.30	0.29	0.29	0.05	0.20	0.16	0.50	0.26	0.25	0.25
K_2O	0.02	0.02	0.02	0.01	0.01	0.02	0.03	0.02	0.02	0.03
P_2O_5	0.06	0.04	0.02	0.03	0.01	0.03	0.04	0.03	0.03	0.03
Cr_2O_3	5094	4285	3327	3169	3924	4462	4041	4186	4115	4300
Ni	1029	1269	1989	2194	1666	2234	740	1553	1547	1605
V	197	147	101	83	110	86	208	137	147	124
Co	102	102	88	94	88	113	94	89	86	91
LOI	6.3	6.89	9.5	16.12	9.02	7.47	5.27	7.61	7.4	7.45
Total	100.3	100.3	100.2	100.1	100.1	100.8	99.4	100.9	100.8	100.4
Co	103	107	89	97	92	101	100	101	85	88
Cr	3430	2840	2120	1890	2570	2630	2660	2720	2620	2710
Ni	898	1100	1630	1670	1400	1520	659	1610	1360	1380
Sc	33	28	18	15	19	21	32	24	24	25
V	203	148	101	86	109	121	206	158	144	119
Zn	84	79	59	57	78	66	80	74	71	78
Ga	9.3	7	5.9	4.4	7.1	6.7	8.2	6.7	6.8	7.2
Nb	0.9	0.72	0.35	0.48	0.55	0.56	0.56	0.37	0.36	0.39
Th	0.08	0.07	0.04	0.05	0.04	0.04	0.04	0.03	0.03	0.03
Y	10	10	6.4	5.8	7.6	6.8	12	5.7	5.6	7.5
Hf	1.0	1.3	0.5	0.41	0.43	0.58	0.72	0.53	0.48	0.47
Zr	38	52	19	15	15	18	24	20	16	17
La	0.9	0.5	0.5	0.7	0.6	0.4	0.5	0.3	0.3	0.3
Ce	2.4	1.9	1.3	1.9	2	1.4	1.7	0.8	0.8	1.0
Pr	0.45	0.37	0.21	0.3	0.33	0.26	0.31	0.15	0.15	0.18
Nd	2.6	2.2	1.1	1.6	1.9	1.5	1.7	0.9	0.9	1.1
Sm	0.99	0.86	0.46	0.46	0.67	0.58	0.85	0.42	0.42	0.51
Gd	1.4	1.3	0.78	0.74	1.0	0.98	1.5	0.71	0.71	0.87
Tb	0.26	0.25	0.16	0.14	0.19	0.18	0.27	0.14	0.15	0.18
Dy	1.8	1.8	1.0	0.89	1.3	1.2	1.9	1.0	0.97	1.3
Ho	0.36	0.36	0.24	0.21	0.27	0.25	0.41	0.21	0.21	0.27
Er	1.0	1.0	0.58	0.54	0.71	0.68	1.2	0.58	0.56	0.77
Tm	0.16	0.16	0.09	0.09	0.11	0.11	0.19	0.1	0.09	0.13
Yb	1.0	1.1	0.64	0.57	0.74	0.73	1.3	0.65	0.67	0.88
Lu	0.16	0.15	0.1	0.09	0.12	0.12	0.22	0.11	0.1	0.13
$(Th/Nb)_N$	0.74	0.80	0.95	0.86	0.60	0.59	0.59	0.67	0.69	0.64
$(Ce/Sm)_N$	0.59	0.54	0.69	1.00	0.72	0.59	0.48	0.46	0.46	0.48
$(Ce/Yb)_N$	0.63	0.45	0.53	0.88	0.71	0.50	0.34	0.32	0.31	0.30
$(Gd/Yb)_N$	1.13	0.96	0.99	1.05	1.10	1.09	0.94	0.89	0.86	0.80
Nb/Nb*	1.16	1.33	0.85	0.89	1.22	1.53	1.37	1.35	1.31	1.42
P/P*	1.40	1.23	1.38	1.22	0.45	1.27	1.56	2.31	2.15	1.65
Zr/Zr*	1.61	2.56	1.81	1.19	0.90	1.31	1.35	2.21	1.77	1.54
Hf/Hf*	1.57	2.38	1.77	1.20	0.96	1.57	1.51	2.17	1.97	1.58
Ti/Ti*	1.13	0.88	1.05	1.08	0.87	1.07	0.89	1.41	1.36	1.15
Al_2O_3/TiO_2	16.5	20.7	22.0	20.0	19.1	17.8	20.1	21.6	21.8	22.5
CaO/Al_2O_3	0.64	0.84	0.88	0.96	1.34	0.93	1.20	0.81	0.82	0.80

Table 4-1. Continued

Group	C	C	C	C	C	C	C	C	C	C
Horizon	K	K	K	K	K	K	K	K	K	K
Zone	SVZ	SVZ	NVZ	NVZ	NVZ	SVZ	SVZ	NVZ	NVZ	NVZ
Sample	HS0-091-FCR	HS0-091-FCP	TMO-226-B	TMO-226-C	TMO-226-D	HSO-091-A	HS0-091-FCB	TMO-226-A	TMO-227-A	TMO-227-B2
Rock type	kom. ol. spfx.	kom. ol. spfx.	kom. ol. spfx.	kom. ol. spfx.	kom. ol. spfx.	kom. ol. phy.	kom. ol. phy.	kom. ol. phy.	kom. ol. phy.	kom. ol. phy.
Flow type	spfx.	spfx.	spfx.	spfx.	spfx.	spfx.	spfx.	spfx.	spfx.	spfx.
Flow no.\thick	2(<2)	2(<2)	3(<2)	3(<2)	3(<2)	na	2(<2)	3(<2)	4(~10)	4(~10)
SiO_2	45.30	44.9	43.41	43.93	46.15	45.79	45.73	44.92	46.25	44.10
TiO_2	0.34	0.32	0.42	0.41	0.33	0.26	0.29	0.21	0.22	0.28
Al_2O_3	7.29	7.25	9.45	9.26	7.90	5.89	7.06	5.41	5.62	6.23
Fe_2O_3	11.37	11.96	11.09	10.72	9.67	10.82	10.54	10.62	9.87	9.65
MnO	0.14	0.14	0.09	0.09	0.10	0.14	0.15	0.18	0.17	0.18
MgO	29.33	28.95	29.05	28.94	28.18	32.98	29.85	28.95	31.75	34.07
CaO	5.35	5.62	5.35	5.49	6.51	3.38	5.52	8.69	5.31	4.71
Na_2O	0.23	0.24	0.44	0.43	0.55	0.14	0.21	0.47	0.23	0.15
K_2O	0.02	0.03	0.02	0.03	0.03	0.01	0.02	0.02	0.01	0.01
P_2O_5	0.03	0.03	0.04	0.04	0.03	0.03	0.03	0.02	0.02	0.03
Cr_2O_3	4483	4171	5030	5028	4086	3775	3987	3127	3316	3922
Ni	1586	1470	1355	1655	1389	1859	1815	1956	2164	1937
V	129	135	192	161	138	111	97	89	94	95
Co	91	87	71	76	75	96	106	106	96	83
LOI	7.58	7.39	7.48	7.52	6.74	9.13	7.61	8.76	9.77	12.04
Total	100.5	100.6	100.5	100.5	100.2	100.6	100.7	100.0	100.2	100.3
Co	96		72	86	74	89		97	93	84
Cr	2940		3250	3230	2670	2470		1960	2120	2430
Ni	1540		1150	1430	1190	1530		1590	1780	1550
Sc	25		29	26	24	20		16	15	20
V	126		201	163	144	113		87	98	94
Zn	82		64	62	58	70		62	61	61
Ga	7.5		8.9	8.6	7.3	5.5		5.1	5.6	5.6
Nb	0.35		0.46	0.46	0.48	0.31		0.32	0.27	0.35
Th	0.03		0.04	0.04	0.03	0.02		0.03	0.03	0.02
Y	5.8		7.5	7.2	8.4	4.3		8.3	5.7	5.6
Hf	0.61		0.57	0.58	0.53	0.39		0.39	0.34	0.4
Zr	22		18	20	18	13		14	12	14
La	0.3		0.4	0.3	0.4	0.2		0.6	0.3	0.3
Ce	0.8		1.2	1.1	1.2	0.6		1.6	0.9	0.9
Pr	0.14		0.22	0.21	0.22	0.11		0.26	0.15	0.16
Nd	0.8		1.3	1.2	1.4	0.6		1.5	0.8	1.0
Sm	0.45		0.51	0.49	0.56	0.29		0.55	0.32	0.39
Gd	0.75		0.82	0.82	0.97	0.49		0.9	0.59	0.68
Tb	0.15		0.18	0.17	0.2	0.1		0.18	0.13	0.14
Dy	1.0		1.1	1.1	1.3	0.71		1.2	0.84	0.82
Ho	0.22		0.26	0.24	0.3	0.15		0.26	0.19	0.2
Er	0.63		0.76	0.68	0.81	0.41		0.76	0.52	0.53
Tm	0.1		0.11	0.1	0.12	0.06		0.12	0.09	0.09
Yb	0.65		0.79	0.71	0.89	0.47		0.82	0.58	0.58
Lu	0.09		0.13	0.12	0.15	0.07		0.13	0.09	0.09
$(Th/Nb)_N$	0.71		0.72	0.72	0.52	0.53		0.78	0.92	0.47
$(Ce/Sm)_N$	0.43		0.57	0.54	0.52	0.50		0.71	0.68	0.56
$(Ce/Yb)_N$	0.32		0.40	0.41	0.35	0.34		0.51	0.41	0.41
$(Gd/Yb)_N$	0.94		0.84	0.94	0.88	0.85		0.89	0.82	0.95
Nb/Nb*	1.27		1.25	1.45	1.51	1.69		0.82	0.98	1.56
P/P*	2.55		2.25	1.99	1.53	2.67		0.81	1.92	2.24
Zr/Zr*	2.49		1.50	1.77	1.38	2.11		1.05	1.61	1.52
Hf/Hf*	2.56		1.76	1.90	1.51	2.35		1.08	1.69	1.61
Ti/Ti*	1.36		1.51	1.51	1.06	1.63		0.71	1.20	1.29
Al_2O_3/TiO_2	21.6	22.8	22.7	22.7	23.7	22.5	24.1	25.3	25.3	21.9
CaO/Al_2O_3	0.73	0.78	0.57	0.59	0.82	0.57	0.78	1.61	0.94	0.76

Table 4-1. Continued

Group	C	C	C	C	C	C	C	C	C	C
Horizon	K	K	K	K	K	K	K	K	K	K
Zone	NVZ	NVZ	NVZ	NVZ	NVZ	NVZ	NVZ	NVZ	NVZ	NVZ
Sample	TMO-227-E	TMO-228-A	TMO-228-B	TMO-228-C	TMO-228-D	TMO-229-B	TMO-229-E	TMO-229-G	TMO-231-F	TMO-239-5
Rock type	kom. ol. phy.	kom. ol. phy.	kom. ol. phy.	kom. ol. phy.	kom. ol. phy.	kom. ol. phy.	kom. ol. phy.	kom. ol. phy.	kom. ol. phy.	kom. ol. phy.
Flow type	spfx.	spfx.	spfx.	spfx.	spfx.	n. spfx.	n. spfx.	n. spfx.	n. spfx.	spfx.
Flow no.\thick	4(~10)	5(>100)	5(>100)	5(>100)	5(>100)	6(>100)	6(>100)	6(>100)	na	na
SiO_2	45.95	44.14	44.11	45.24	44.48	44.91	44.19	45.70	45.28	46.23
TiO_2	0.28	0.23	0.22	0.31	0.20	0.23	0.24	0.25	0.33	0.24
Al_2O_3	6.25	5.30	5.32	7.49	4.75	4.90	5.53	5.04	7.55	4.43
Fe_2O_3	10.19	10.78	10.68	11.38	10.56	9.34	9.79	9.55	11.72	11.14
MnO	0.15	0.14	0.15	0.16	0.13	0.11	0.10	0.10	0.17	0.13
MgO	33.59	34.98	35.37	29.35	37.55	36.84	36.07	36.14	27.56	35.32
CaO	2.82	3.75	3.41	5.24	1.68	3.06	3.51	2.61	6.56	1.80
Na_2O	0.13	0.09	0.13	0.24	0.03	0.07	0.06	0.04	0.27	0.07
K_2O	0.01	0.01	0.01	0.02	0.01	0.01	0.01	0.01	0.02	0.01
P_2O_5	0.03	0.02	0.03	0.03	0.02	0.03	0.03	0.03	0.03	0.02
Cr_2O_3	3869	3575	3491	3903	3484	2770	2422	3076	3696	4821
Ni	2149	2090	2108	1568	2361	2295	2238	2208	1527	1221
V	103	90	92	133	83	95	102	89	131	171
Co	100	92	90	92	98	90	93	89	88	94
LOI	9.54	11.61	11.55	8.51	11.78	11.48	12.14	11.66	8.15	9.53
Total	100.7	100.7	100.6	100.7	100.7	100.7	100.6	100.6	100.6	100.4
Co	97	94	100	90	98	86	92	87	99	112
Cr	2460	2220	2180	2540	2200	1780	1560	1930	2490	3040
Ni	1760	1680	1760	1320	1910	1850	1780	1760	1300	1940
Sc	20	17	17	23	15	17	17	16	23	17
V	107	94	92	130	84	97	101	90	134	90
Zn	58	60	68	61	63	55	47	51	67	65
Ga	5.7	4.6	4.7	6.8	4.3	4.4	5.2	4.5	6.7	4.9
Nb	0.36	0.28	0.30	0.41	0.25	0.36	0.40	0.39	0.49	0.38
Th	0.03	0.03	0.02	0.02	0.02	0.04	0.04	0.03	0.05	0.03
Y	4.7	4.5	4.6	7.1	3.3	5.3	5.6	5.1	8.4	3
Hf	0.53	0.69	0.38	0.55	0.6	0.44	0.41	0.42	0.53	0.48
Zr	19	26	14	21	23	15	14	15	18	18
La	0.3	0.2	0.3	0.3	0.2	0.3	0.4	0.3	0.6	0.2
Ce	0.6	0.6	0.6	0.9	0.5	1.0	1.1	0.9	1.7	0.6
Pr	0.11	0.12	0.12	0.19	0.09	0.16	0.19	0.15	0.28	0.11
Nd	0.7	0.8	0.7	1.1	0.5	0.9	1.1	0.9	1.6	0.6
Sm	0.31	0.30	0.28	0.45	0.21	0.35	0.40	0.34	0.62	0.24
Gd	0.53	0.53	0.52	0.76	0.37	0.59	0.63	0.57	0.99	0.39
Tb	0.11	0.11	0.10	0.16	0.07	0.12	0.13	0.12	0.2	0.07
Dy	0.71	0.68	0.63	1.0	0.48	0.8	0.83	0.77	1.3	0.49
Ho	0.16	0.17	0.15	0.24	0.11	0.18	0.19	0.18	0.3	0.11
Er	0.46	0.47	0.44	0.67	0.35	0.49	0.55	0.5	0.82	0.3
Tm	0.08	0.07	0.08	0.1	0.05	0.09	0.09	0.08	0.13	0.05
Yb	0.53	0.53	0.51	0.73	0.38	0.61	0.63	0.54	0.89	0.37
Lu	0.08	0.09	0.08	0.12	0.06	0.10	0.10	0.09	0.14	0.05
$(Th/Nb)_N$	0.69	0.89	0.55	0.40	0.66	0.92	0.83	0.64	0.84	0.65
$(Ce/Sm)_N$	0.47	0.48	0.52	0.48	0.58	0.69	0.67	0.64	0.66	0.61
$(Ce/Yb)_N$	0.30	0.30	0.31	0.32	0.35	0.43	0.46	0.44	0.50	0.43
$(Gd/Yb)_N$	0.81	0.81	0.83	0.84	0.79	0.78	0.81	0.86	0.90	0.85
Nb/Nb*	1.31	1.25	1.34	1.83	1.36	1.13	1.09	1.42	0.98	1.69
P/P*	2.81	2.18	2.43	1.81	3.19	2.02	1.69	2.17	1.24	1.99
Zr/Zr*	2.77	3.60	2.15	2.03	4.82	1.81	1.43	1.84	1.23	3.22
Hf/Hf*	2.86	3.55	2.16	1.97	4.66	1.97	1.56	1.91	1.34	3.18
Ti/Ti*	1.60	1.33	1.35	1.23	1.69	1.18	1.12	1.34	0.99	1.87
Al_2O_3/TiO_2	22.5	23.4	24.1	24.3	23.6	21.4	23.1	19.9	22.7	18.2
CaO/Al_2O_3	0.45	0.71	0.64	0.70	0.35	0.62	0.63	0.52	0.87	0.41

Table 4-1. Continued

Group	C	D	D	D	D	D	D	D
Horizon	K	K	K	K	K	K	K	K
Zone	SVZ	SVZ	NVZ	NVZ	NVZ	NVZ	NVZ	NVZ
Sample	TMO-285-B2	HSO-091-G	TMO-227-C	TMO-227-D	TMO-229-A	TMO-229-C	TMO-229-F	TMO-229-H
Rock type	kom. ol. phy.	kom. ol. phy.	kom. ol. phy.	kom. ol. phy.	kom. ol. phy.	kom. ol. phy.	kom. ol. phy.	kom. ol. phy.
Flow type	spfx.	n. spfx.	spfx.	spfx.	n. spfx.	n. spfx.	n. spfx.	n. spfx.
Flow no.\thick	na	na	4(~10)	4(~10)	6(>100)	6(>100)	6(>100)	6(>100)
SiO_2	46.97	45.29	44.89	44.76	44.84	44.61	44.08	45.28
TiO_2	0.29	0.13	0.21	0.19	0.16	0.19	0.18	0.18
Al_2O_3	5.80	3.99	4.47	4.11	4.11	4.48	3.90	4.89
Fe_2O_3	11.36	9.84	10.64	10.77	9.43	9.52	9.82	10.16
MnO	0.17	0.13	0.17	0.16	0.10	0.10	0.11	0.10
MgO	30.44	39.95	37.01	37.84	39.97	38.72	39.14	37.12
CaO	4.09	0.03	1.97	1.48	0.79	1.78	2.19	1.62
Na_2O	0.26	0.02	0.03	0.09	0.03	0.05	0.03	0.04
K_2O	0.02	0.01	0.01	0.01	0.01	0.01	0.01	0.01
P_2O_5	0.03	0.01	0.02	0.01	0.02	0.02	0.02	0.02
Cr_2O_3	3823	3153	3339	3351	2663	2610	2750	3270
Ni	1766	2715	2475	2418	2697	2576	2473	2406
V	113	71	74	76	80	82	67	102
Co	99	103	98	102	100	94	92	91
LOI	8.55	11.4	11.7	11.88	11.92	12.58	13.09	11.11
Total	100.7	100.6	100.4	100.6	100.6	100.4	100.5	100.5
Co	105	101	101	99	98	100	84	90
Cr	2580	2040	2100	2090	1690	1650	1650	2010
Ni	1490	2190	1980	1960	2150	2040	1950	1970
Sc	21	12	15	14	12	13	12	12
V	121	74	77	73	85	83	66	99
Zn	82	49	63	62	53	53	54	60
Ga	6.3	4.4	4.5	4.3	4.1	5.2	4.4	6.2
Nb	0.38	0.18	0.24	0.34	0.28	0.36	0.27	0.34
Th	0.03	< 0.02	< 0.02	0.02	0.03	0.03	0.03	0.04
Y	5.7	2.1	3.4	2.6	3.6	3.9	3.9	3.2
Hf	0.48	0.22	0.34	0.39	0.35	0.39	0.45	0.26
Zr	16	7.5	11	15	13	14	18	9.3
La	0.6	0.1	0.3	0.2	0.3	0.3	0.4	0.3
Ce	1.5	0.3	0.7	0.5	0.6	0.7	1.0	0.7
Pr	0.23	0.05	0.12	0.08	0.11	0.12	0.16	0.11
Nd	1.2	0.3	0.6	0.4	0.6	0.6	0.8	0.6
Sm	0.43	0.11	0.21	0.16	0.22	0.23	0.26	0.2
Gd	0.72	0.24	0.35	0.25	0.32	0.40	0.42	0.31
Tb	0.14	0.05	0.07	0.05	0.07	0.09	0.09	0.07
Dy	0.95	0.33	0.49	0.37	0.5	0.57	0.51	0.46
Ho	0.21	0.07	0.11	0.09	0.12	0.13	0.13	0.11
Er	0.57	0.21	0.34	0.28	0.37	0.42	0.39	0.33
Tm	0.1	0.04	0.06	0.05	0.07	0.07	0.06	0.06
Yb	0.63	0.26	0.42	0.35	0.50	0.50	0.46	0.44
Lu	0.09	0.04	0.07	0.06	0.09	0.09	0.07	0.08
$(Th/Nb)_N$	0.65			0.49	0.89	0.69	0.92	0.97
$(Ce/Sm)_N$	0.85	0.66	0.81	0.76	0.66	0.74	0.93	0.85
$(Ce/Yb)_N$	0.63	0.30	0.44	0.38	0.32	0.37	0.57	0.42
$(Gd/Yb)_N$	0.93	0.75	0.68	0.58	0.52	0.65	0.74	0.57
Nb/Nb*	0.98			1.85	1.02	1.31	0.85	1.07
P/P*	1.41	3.25	2.18	2.24	2.04	1.74	1.40	2.26
Zr/Zr*	1.51	2.80	2.10	4.02	2.43	2.56	2.68	1.82
Hf/Hf*	1.68	3.05	2.41	3.88	2.43	2.64	2.48	1.89
Ti/Ti*	1.23	1.92	1.77	2.24	1.43	1.44	1.25	1.67
Al_2O_3/TiO_2	19.9	29.9	21.8	21.5	25.3	24.0	22.1	27.5
CaO/Al_2O_3	0.71	0.01	0.44	0.36	0.19	0.40	0.56	0.33

Table 4-2. Sm-Nd and LuHf isotopic compositions for PAg mafic and ultramafic volcanic rocks.

Sample	Rock type	MgO	$(Gd/Yb)_N$	Sm	Nd	^{147}Sm/^{144}Nd	^{143}Nd/^{144}Nd	εNd(T)	Lu	Hf	^{176}Lu/^{177}Hf	^{176}Hf/^{177}Hf	εHf(T)
Enriched basalt group-1 - EB-1													
T-3318-A	basalt	4.3	2.53						0.382	4.8	0.0109	0.281735 ± 5	4.5
T-3322-A	basalt	10.7	2.18	6.1	31.4	0.1167	0.511313 ± 6	2.3	0.289	2.1	0.0187	0.282148 ± 8	4.7
T-3322-B	basalt	7.2	3.24	8.0	36.8	0.1315	0.511587 ± 8	2.4	0.296	4.4	0.0093	0.281660 ± 11	4.9
Enriched basalt group-2 - EB-2													
T-3319-A	basalt	5.3	1.93	3.8	16.2	0.1411	0.511763 ± 8	2.5	0.237	2.6	0.0127	0.281835 ± 8	4.9
Enriched basalt group-3 - EB-3													
T-3324-A	basalt	4.4	1.26	5.8	19.0	0.1850	0.512532 ± 12	2.0	0.831	4.6	0.0251	0.282471 ± 8	4.3
T-3325-B	basalt	5.9	1.32	3.8	12.3	0.1875	0.512618 ± 8	2.9	0.495	2.6	0.0266	0.282557 ± 8	4.6
Depleted basalt - DB													
TM-7-D	basalt p. spfx.	12.2	1.07	2.0	5.4	0.2201	0.513162 ± 6	2.0	0.275	1.2	0.0307	0.282767 ± 14	4.4
TM0-239-E	basalt	7.8	1.16	1.9	4.7	0.2442	0.513580 ± 6	1.7	0.306	1.3	0.0319	0.282837 ± 11	4.7
TM0-239-E (dup.)									0.305	1.3	0.0317	0.282833 ± 8	4.9
Komatiite group-A													
TMO-011-F	plt. spfx.	24.9	1.25	1.03	2.6	0.2403	0.513553 ± 6	2.6	0.125	0.56	0.0310	0.282798 ± 18	5.1
TMO-011-F (dup.)									0.142	0.62	0.0320	0.282859 ± 13	5.3
TM0-011-H	plt. spfx.	24.6	1.32	0.96	2.4	0.2408	0.513563 ± 7	2.6					
TM0-239-12	plt. spfx.	24.9	1.18	0.86	2.1	0.2456	0.513629 ± 6	2.2	0.138	0.62	0.0311	0.282771 ± 15	3.9
TM0-239-12 (dup.)				0.88	2.2	0.2452	0.513634 ± 7	2.4					
TM0-011-A	cum.	29.8	1.25	0.78	2.1	0.2300	0.513339 ± 5	2.0					
Komatiite group-B													
HS0-091-SP3	plt. spfx.	27.0	1.05	0.58	1.4	0.2497	0.513814 ± 10	4.3					
TM-1-A	rdm. spfx.	27.5	1.13	0.67	1.6	0.2530	0.513779 ± 6	2.5	0.107	0.54	0.0275	0.282598 ± 9	4.4
TM-1-A (dup.)									0.114	0.60	0.0262	0.282534 ± 12	4.6
TM0-285-F8	plt. spfx.	26.2	0.96	1.08	2.6	0.2508	0.513732 ± 5	2.3					

Table 4-2. Continued

Sample	Rock type	MgO	$(Gd/Yb)_N$	Sm	Nd	$^{147}Sm/^{144}Nd$	$^{143}Nd/^{144}Nd$	εNd(T)	Lu	Hf	$^{176}Lu/^{177}Hf$	$^{176}Hf/^{177}Hf$	εHf(T)
Komatiite group-C													
HS0-091-SP2	plt. spfx.	29.2	0.80	0.50	1.0	0.2914	0.514515 ± 10	3.4	0.129	0.42	0.0432	0.283269 ± 21	-0.9
HS0-091-FCR	rdm. spfx.	29.3	0.94	0.41	0.84	0.2951	0.514778 ± 13	7.2					
TM0-226-B	plt. spfx.	29.1	0.84	0.59	1.3	0.2697	0.514149 ± 7	3.9	0.098	0.45	0.0307	0.282879 ± 8	8.5
TM0-227-B2	cum.	34.1	0.95	0.44	0.99	0.2699	0.514097 ± 9	2.8					
TM0-228-A	cum.	35.0	0.81	0.34	0.75	0.2781	0.514204 ± 8	2.0	0.075	0.27	0.0382	0.283156 ± 14	4.5
TM0-231-F	cum.	27.6	0.90	0.62	1.5	0.2510	0.513741 ± 6	2.5					
Komatiite group-D													
HS0-091-G	cum.	39.9	0.75	0.13	0.28	0.2847	0.514541 ± 21	6.2					
HS0-091-G (dup.)				0.16	0.34	0.2856	0.514570 ± 36	6.5					
TM0-227-D	cum.	37.8	0.58	0.15	0.37	0.2485	0.513679 ± 40	2.1					
TM0-229-A	cum.	40.0	0.52	0.21	0.52	0.2394	0.513561 ± 18	3.0					
TM0-229-H	cum.	37.1	0.57	0.21	0.52	0.2449	0.513661 ± 15	3.0					

Table 4-3. Partition coefficients used in this study.

P (GPa)	1.5		1-1.5		2.8		3.2-3.4				2.4-2.8		3.2-3.4			
T (°C)	1255		1055-1350		1525-1537		1580-1635				1500-1570		1590-1660			
	Plag.		Ol.		Cpx.		Cpx.		Pyx.-2		Opx.		Opx.		Pyx.-1	
Th			0.00003	(1,2)	0.005	(4)	0.016	(1)	0.010	(1,4)	0.001	(4)	0.0031	(1)	0.002	(1,4)
Nb			0.0002	(3)	0.007	(4)	0.025	(1)	0.016	(1,4)	0.001	(4)	0.0038	(1)	0.003	(1,4)
La	0.151	(5)	0.00006	(3)					0.024	(ext.)					0.003	(ext.)
Ce	0.119	(5,6)	0.00006	(3)	0.025	(4)	0.045	(1)	0.035	(1,4)	0.003	(4)	0.0065	(1)	0.005	(1,4)
Pr	*0.098*		*0.00009*						*0.044*			(4)				
P			*0.001*						*0.050*							
Nd	0.081	(5,6)	0.0002	(3)	0.048	(4)	0.065	(1)	0.057	(1,4)	0.015	(4)	0.012	(1)	0.013	(1,4)
Zr			0.005	(3)	0.038	(4)	0.046	(1)	0.042	(1,4)	0.022	(4)	0.017	(1)	0.019	(1,4)
Hf			0.004	(3)	0.060	(4)	0.090	(1)	0.075	(1,4)	0.044	(4)	0.0285	(1)	0.036	(1,4)
Sm	0.060	(5,6)	0.0007	(1,2,3)	0.079	(4)	0.087	(1)	0.083	(1,4)	0.024	(4)	0.0195	(1)	0.022	(1,4)
Ti			0.011	(2,3)					*0.100*							
Gd	0.054	(5,6)	0.002	(1,2,3)					*0.122*							
Tb	*0.054*		*0.003*						*0.147*							
Dy	0.055	(6)	*0.004*						*0.162*							
Y			0.005	(1,2,3)	0.182	(4)	0.175	(1)	0.179	(1,4)	0.094	(4)	0.059	(1)	0.076	(1,4)
Ho	*0.058*		*0.007*						*0.188*							
Er	*0.061*		*0.012*						*0.197*							
Tm	*0.064*		*0.020*						*0.207*							
Yb	0.067	(6)	0.032	(1,2,3)	0.187	(4)	0.249	(1)	0.218	(1,4)	0.133	(4)	0.1008	(1)	0.117	(1,4)
Lu	0.037	(5,6)	0.043	(1)	0.183	(4)	0.273	(1)	0.228	(1,4)	0.159	(4)	0.1163	(1)	0.138	(1,4)

Table 4-3. Continued

P (GPa)	2.4-2.8		3.2-3.4		~3		3		~4		4.7-9	
T (°C)	1490-1595		1600-1660				1530-1565				1750-1830	
	Per. Gt.		Per. Gt.		Gt.-2		Py. Gt. (84)		Gt.-1		Maj. Gt.	
Th	0.010	(4)	0.015	(1)	0.013	(1,4)	0.011	(7)	0.012	(1,4,7)		
Nb	0.017	(4)	0.030	(1)	0.024	(1,4)	0.03	(7)	0.026	(1,4,7)		
La							0.004	(7)	0.004	(9)		
Ce	0.020	(4)	0.021	(1)	0.021	(1,4)			0.021	(1,4)		
Pr							0.036	(7)				
P											0.263	(8)
Nd	0.094	(4)	0.070	(1)	0.082	(1,4)			0.082	(1,4)	0.057	(8)
Zr	0.565	(4)	0.445	(1)	0.505	(1,4)	0.4	(7)	0.505	(1,4)	0.415	(8)
Hf	0.597	(4)	0.428	(1)	0.512	(1,4)	0.68	(7)	0.512	(1,4)	0.472	(8)
Sm	0.331	(4)	0.221	(1)	0.276	(1,4)	0.28	(7)	0.276	(1,4)	0.182	(8)
Ti							0.2	(7)			0.270	(8)
Gd							0.55	(7)				
Tb											0.549	(8)
Dy												
Y	3.05	(4)	1.95	(1)	2.50	(1,4)	2.0	(7)	1.27	(1,4)*	1.04	(8)
Ho												
Er												
Tm												
Yb	5.73	(4)	3.95	(1)	4.84	(1,4)	3.3	(7)	2.57	(1,4)*	2.57	(8)
Lu	7.41	(4)	4.59	(1)	6.00	(1,4)	5.7	(7)	2.99	(1,4)*	3.03	(8)

Table 4-4. Major element compositions of garnet peridotite melts (KR-4003) and komatiite.

	Exp. melts			Komatiites	
	Avg. Run 45.03 and 45.02	Avg. Run 60.01 and 60.05	~5 GPa?	Group-A kom. liquid	Al-und. kom.
P (GPa)	4.5	6	5.0		~5.6
wt.% melt	25	26	25		
SiO_2	46.0	45.7	45.9	44.2	45.9
Al_2O_3	8.6	6.8	8.0	8.0	8.0
MgO	22.2	24.7	23.1	25.4	26.4
FeO	10.9	11.4	11.1	11.7	11.1
CaO	8.7	8.2	8.5	7.2	7.7

Table 4-5. Major element compositions of garnet peridotite (KR-4003) residues at ~4.5 GPa and various peridotitic mantle compositions.

	Mineral compositions and bulk residue KR-4003 lherzolite at ~4.5 GPa														
	(~12 wt.% melting)				(~37 wt.% melting)				Periodtitic mantle compositions						
	Ol.	Cpx.	Gt.	Res.	Ol.	Opx.	Gt.	Res.	Avg. Res. ~4.5 GPa and ~25 wt.%	DMM-1	DMMa	DMMb	PM	KLB-1	KR-4003
normative mode	0.59	0.29	0.12	1.00	0.70	0.28	0.02	1.00							
SiO_2	40.09	55.14	42.66	44.81	40.39	56.08	42.99	44.88	44.8	44.9	44.9	44.7	45.0	44.5	44.9
TiO_2		0.10	0.35	0.07		0.02	0.14	0.01	0.04	0.04	0.16	0.13	0.2	0.16	0.2
Cr_2O_3	0.15	0.43	1.01	0.33	0.21	0.46	1.82	0.31	0.32	0.39	0.50	0.57	0.38	0.31	0.4
Al_2O_3	0.20	3.51	22.47	3.76	0.24	3.55	22.24	1.53	2.6	2.4	4.3	4.0	4.5	3.6	4.3
FeO	9.05	4.97	5.46	7.13	7.57	4.71	4.64	6.71	7.1	8.3	8.1	8.2	8.1	8.1	8.0
MgO	49.71	26.80	22.38	39.80	50.96	32.93	24.41	45.43	42.6	41.6	38.2	38.7	37.8	39.2	37.3
CaO	0.30	7.53	4.27	2.89	0.26	2.20	3.47	0.86	1.87	2.14	3.5	3.2	3.6	3.4	3.5

Table 4-A-1. Duplicate trace element analyses of komatiite and basalt.

			Komatiite (group-A)			Komatiite (group-D)		
	d.l.	d.l. x10	TMO-011-H	TMO-011-H (dup.)	% diff.	TMO-229-E	TMO-229-E (dup.)	% diff.
ICP-AES								
Co	5	50	96	95	1	92	87	6
Cr	10	100	3010	3000		1560	1580	1
Ni	10	100	1070	1080	1	1780	1790	1
Sc	5	50	26	26	0	17	17	
V	5	50	156	157	1	101	104	3
Zn	0.1	1	77	78	1	47	50	6
ICP-MS								
Ga	0.5	5	7.8	7.7	1	5.2	5.4	4
Nb	0.05	0.5	0.75	0.73	3	0.40	0.42	5
Th	0.02	0.2	0.07	0.07		0.04	0.03	29
Y	0.02	0.2	9.6	9.5	1	5.6	5.7	2
Hf	0.05	0.5	0.82	0.74	10	0.41	0.36	13
Zr	0.5	5	27	26	4	14	13	7
La	0.1	1	0.7	0.7		0.4	0.4	
Ce	0.1	1	2.3	2.2	4	1.1	1.1	
Pr	0.02	0.2	0.44	0.43	2	0.19	0.17	11
Nd	0.1	1	2.5	2.4	4	1.1	1.0	10
Sm	0.02	0.2	0.95	0.95		0.40	0.42	5
Gd	0.02	0.2	1.50	1.40	7	0.63	0.70	11
Tb	0.02	0.2	0.26	0.26		0.13	0.13	
Dy	0.02	0.2	1.6	1.6		0.83	0.88	6
Ho	0.02	0.2	0.34	0.33	3	0.19	0.20	5
Er	0.02	0.2	0.90	0.89	1	0.55	0.57	4
Tm	0.02	0.2	0.14	0.15	7	0.09	0.09	
Yb	0.02	0.2	0.92	0.92		0.63	0.62	2
Lu	0.02	0.2	0.15	0.14	7	0.10	0.10	
$(Th/Nb)_N$			0.77	0.79		0.83	0.59	
$(Ce/Sm)_N$			0.59	0.56		0.67	0.63	
$(Ce/Yb)_N$			0.66	0.63		0.46	0.47	
$(Gd/Yb)_N$			1.32	1.23		0.81	0.92	
Nb/Nb*			1.17	1.14		1.09	1.32	
Zr/Zr*			1.19	1.17		1.43	1.36	
Hf/Hf*			1.34	1.23		1.56	1.40	

Table 4-A-1. Continued

			Basalt (DB)			Basalt (EB-1)		
	d.l.	d.l. x10	TM-7-D	TM-7-D (dup.)	% diff.	T-3322-B	T-3322-B (dup.)	% diff.
ICP-AES								
Co	5	50	58	58		45	46	2
Cr	10	100	858	867	1	152	153	1
Ni	10	100	186	190	2	64	64	
Sc	5	50	36	36		29	29	
V	5	50	225	225		270	271	
Zn	0.1	1	80	64	22	160	158	1
ICP-MS								
Ga	0.5	5	13	13		21	22	5
Nb	0.05	0.5	1.4	1.4		19	20	5
Th	0.02	0.2	0.09	0.10	11	0.90	0.92	2
Y	0.02	0.2	19	19		31	31	
Hf	0.05	0.5	1.2	1.2		3.6	3.9	8
Zr	0.5	5	41	41		140	155	10
La	0.1	1	1.4	1.5	7	21	22	5
Ce	0.1	1	4.7	4.9	4	63	64	2
Pr	0.02	0.2	0.82	0.85	4	9.4	9.6	2
Nd	0.1	1	4.4	4.6	4	43	44	2
Sm	0.02	0.2	1.7	1.7		9.5	9.7	2
Gd	0.02	0.2	2.5	2.5		8.4	8.3	1
Tb	0.02	0.2	0.45	0.46	2	1.2	1.2	
Dy	0.02	0.2	3.1	3.1		6.0	6.0	
Ho	0.02	0.2	0.67	0.66	2	1.1	1.1	
Er	0.02	0.2	1.8	1.9	5	2.5	2.6	4
Tm	0.02	0.2	0.29	0.29		0.35	0.36	3
Yb	0.02	0.2	1.9	1.9		2.1	2.1	
Lu	0.02	0.2	0.29	0.31	7	0.30	0.32	6
$(Th/Nb)_N$			0.53	0.59		0.39	0.38	
$(Ce/Sm)_N$			0.67	0.70		1.61	1.60	
$(Ce/Yb)_N$			0.65	0.68		7.90	8.02	
$(Gd/Yb)_N$			1.07	1.07		3.24	3.20	
Nb/Nb*			1.36	1.25		1.51	1.53	
Zr/Zr*			1.02	0.99		0.47	0.51	
Hf/Hf*			1.10	1.08		0.45	0.48	

Fig. 4-1. Distribution of Neoarchean, ca. 2735-2690 Ma supracrustal belts characterized by orthoquartzite-komatiite lithological associations within the central and northeastern Rae domain of Nunavut including, from southwest to northeast, the Woodburn Lake group (WLg), Prince Albert group (PAg), and Mary River group (MRg), respectively (see Fig. 2-10 in Chapter 2 and references therein). Also shown are the locations of Neo-to Mesoarchean aged, ca. 2775-2870 Ma basement components of the WLg and MRg (Jackson *et al.*, 1990; Wodicka *et al.*, 2002; Zaleski *et al.*, 2001; Bethune & Scammell, 2003), and undated granitoids that yielded predominantly "ancient" (Paleo-to Eoarchean) depleted mantle Nd model ages clustering between ca. 3.25-3.9 Ga (Thériault *et al.*, 1994). The undivided Archean aged crust (grey fill) within and external to the supracrustal belt corridor is dominated by Neoarchean, ca. 2620-2580 Ma intermediate-felsic plutonic rocks (see Fig. 2-11 in Chapter 2 and references therein). The extent of the regional bedrock mapping conducted southwest of Committee Bay between 2000 and 2002 is outlined (Fig. 4-2) along with the location of this study, within the southwestern portion of the PAg in the Laughland Lake area (LL area). Committee Bay (CB); Melville Peninsula (MP); Northwest Territories (NWT); Queen Maud Gulf (QMG).

Fig. 4-2. General geological map of the Committee Bay region delineating the supracrustal rocks of the PAg from granitoid rocks. Substantial occurrences of basalt, komatiite and orthoquartzite have been separated from undifferentiated PAg when possible. The locations of samples yielding U-Pb (zircon) ages for volcanism, syn-volcanic plutonism, and sedimentation (max. age) are shown and. Map simplified from that found in Skulski *et al.* (2003*c*).

Fig. 4-3. Schematic composite PAg stratigraphy illustrating the subdivision into lower (ca. 2730 Ma), middle (ca. 2710 Ma) and upper (≤ ca. 2690 Ma) chronostratigraphic sequences. References for U-Pb (zircon) ages are listed in Fig. 4-2.

Fig. 4-4. Detailed geological map of the Laughland Lake mafic-ultramafic volcanic succession within the northeast volcanic zone (NVZ). The locations of U-Pb (zircon) samples and geochemical and isotopic sampling for this study are indicated.

Fig. 4-5. Detailed geological map of the Laughland Lake mafic-ultramafic volcanic succession within the southwest volcanic zone (SVZ). The locations of U-Pb (zircon) samples and geochemical and isotopic sampling for this study are indicated.

Fig. 4-6. (a) Transmitted light image of random spinifex-textured komatiite. (b) Transmitted light image of plate spinifex-textured komatiite. (c) Transmitted light image of polyhedral olivine-phyric komatiite. (d) Air photograph of komatiite flow sequence containing spinifex-textured flows of variable thickness (~2 to >100 m) and the olivine-phyric flow unit interpreted as a remnant lava channel. (e) Acicular to stubby, compositionally zoned clinopyroxene and interstitial plagioclase in basalt.

Fig. 4-7. Plot of MgO (wt.%) versus $(Th/Nb)_N$ (primitive mantle normalized; McDonough & Sun (1995)) for peridotitic komatiite, basalt, and andesite-dacite of the PAg collected within the Laughland Lake mafic-ultramafic volcanic succession. Volcanic

rocks with $(Th/Nb)_N \geq 1$ (circles) possess a recognizable potential to have experienced crustal contamination (Chapter 3), the majority of samples discussed in this study (triangles) do not.

Fig. 4-8. Primitive mantle normalized (McDonough & Sun, 1995) extended element diagrams for the major basalt and komatiite groups. The heavy grey lines shown for group-A, -B, -C, and -D komatiite are group averages and include all samples.

Fig. 4-9. Plots of MgO (wt.%) versus selected trace/minor elements and ratios thereof for basalt and komatiite discussed in this study (symbols as in Fig. 4-8). Also included in the background are the high $(Th/Nb)_N$ crustally contaminated basalt and komatiite (x's) collected within the mafic-ultramafic volcanic succession (Chapter 3).

Fig. 4-10. Plots of MgO (wt.%) versus HFSE/HFSE* ratios for basalt and komatiite discussed in this study (symbols as in Fig. 4-8). These ratios were calculated by dividing the primitive mantle normalized value for the particular element by its interpolated value as calculated using the geometric mean of the bounding elements as they are ordered in the extended element plots shown in Fig. 4-8. Values ≤ 1 indicate negative HFSE anomalies whereas values > 1 indicate positive anomalies. As in Fig. 4-9, high $(Th/Nb)_N$ crustally contaminated basalt and komatiite within the mafic-ultramafic volcanic succession are also shown (Chapter 3).

Fig. 4-11. Plots of MgO (wt.%) versus selected major elements and Al_2O_3/TiO_2 (wt.% ratio) for basalt and komatiite discussed in this study. As in Fig. 4-9, high $(Th/Nb)_N$ crustally contaminated basalt and komatiite within the mafic-ultramafic volcanic succession are also shown (Chapter 3).

Fig. 4-12. Plots of $(Gd/Yb)_N$ versus major element oxides for group-A, -B and -C spinifex-textured and low-MgO olivine-phyric komatiite. These samples are interpreted to more closely approximate the compositions of erupted liquids for their respective groups. The regressions shown only include samples where the symbols have a superimposed cross (see text); group-A (n=4; TM0-011-F; TM0-011-G; TM0-011-H; TM0-239-12); group-B (n=4; HS0-091-SP3; TM-1; TM-1A; TM0-285-F8); group-C (n=6; HS0-091-SP1A; HS0-091-SP1B; HS0-091-SP2; HS0-091-FCR; TM0-228-C; TM0-231-F). In later discussions it is group averages of these samples that are used as proxies for erupted liquids.

Fig. 4-13. (a) Sm-Nd and (b) Lu-Hf isochron diagrams for basalt and komatiite analysed in this study. The Sm-Nd regression includes the 19 samples (circles) with εNd(T) values ≤ +3.0 (Table 4-2). External errors (smaller than symbols) for isochron plotting include 0.2 % for $^{147}Sm/^{144}Nd$ and ± 0.000015 for $^{143}Nd/^{144}Nd$. The Lu-Hf regression includes the 12 samples (circles) with εHf(T) values between +3.9 and +5.3 (Table 4-2). External errors (smaller than symbols) for isochron plotting include 0.5 % for $^{176}Lu/^{177}Hf$ and ± 0.000015 for $^{176}Hf/^{177}Hf$. A ^{176}Lu decay constant of 1.866 E-11 was used (Scherer *et al.*, 2001; Söderlund *et al.*, 2004). For both Sm-Nd and Lu-Hf isochrons averages were used for duplicates (Table 4-2) and age calculations were preformed using Isoplot software version 3.0 (Ludwig, 1992).

Fig. 4-14. (a) Plot of $^{147}Sm/^{144}Nd$ and (b) $(Gd/Yb)_N$ versus εNd(2730 Ma) for basalt and komatiite analysed in this study. Also shown are the high $(Th/Nb)_N$ crustally contaminated basalt, komatiite, and felsic volcanic rocks within the mafic-ultramafic volcanic succession (Chapter 3) and low $(Th/Nb)_N$ ca. 2690 Ma komatiite (crosses) collected within the upper PAg (MacHattie *et al.*, unpublished data). Most samples, irrespective of age or major/trace element composition possess initial Nd isotopic compositions between +1.5 and +3.0, however, several (n=5) display minimal to significant dispersion toward higher εNd(T) values.

Fig. 4-15. (a) $(Ce)_N$ versus $(Ce/Yb)_N$ plot for the four principal members in the basalt compositional continuum including the depleted basalt (n=4/4), minimally enriched basalt (n=1/5; (EB-3 sample HS0-091-I), moderately enriched basalt (n=2/3; EB-2 samples T-3318-B and TM0-285-D4), and highly enriched basalt (n=2/3; EB-1 samples T-3322-A and -B). The mixing curve shown (10 wt.% increments) involves the depleted and highly enriched basalt end-members. (b) $(Yb)_N$ versus $(Ce/Yb)_N$ plot for the four members in the basalt compositional continuum as in Fig. 4-15(a). (c) MgO (wt.%) versus $(Yb)_N$ for the four members in the basalt compositional continuum as in Fig. 4-15(a and b). The curve shown and labeled as a differentiation trend is a logarithmic fit to the nine individual samples (not shown) comprising the continuum.

Fig. 4-16 (a) MgO versus $(Gd/Yb)_N$ plot for the group-A and -C komatiite liquids (see Fig. 4-12) and group-D komatiite samples. The intersection of the regression of komatiite liquids (from Fig. 4-12) and a horizontal olivine differentiation trend fixed at the average $(Gd/Yb)_N$ of the group-D komatiite of ~0.63 occurs at ~31 wt.% MgO. This intersection defines the MgO content and associated $(Gd/Yb)_N$ for the group-D komatiite liquid. (b) Primitive mantle normalized extended element diagram displaying the group-A and -C komatiite liquids and the results of un-mixing 30 wt.% of the group-A liquid from that of group-C. The resultant composition has a $(Gd/Yb)_N$ ratio of ~0.63 (equivalent to the group-D komatiite) and is interpreted to be an appropriate representation of the incompatible element profile of the group-D komatiite liquid end-member (see also Appendix D).

Fig. 4-17. (a) MgO versus CaO plot displaying the group-A komatiite liquid, the DB, and a postulated crystal fractionation trend. Olivine and clinopyroxene compositions are averages from Munro Township peridotitic komatiite flows (Arndt *et al.*, 1977). (b) REE plot for the average low-MgO (~8 wt.%) DB (samples TM0-239-E and -F), the spinifex-textured group-A komatiite sample TM0-239-12, and a model basalt produced by ~50 wt.% crystal fractionation of an assemblage of 70 wt.% olivine and 30 wt.% clinopyroxene from the komatiite. The partition coefficients used are listed in Table 4-3.

Fig. 4-18. MgO versus Al_2O_3 plot for the group-A komatiite liquid and individual members of the four basalt groups defined in Fig. 4-15. Note that all basalt are co-liner with the group-A komatiite liquid suggesting that the enriched basalts may have been

generated by crystal differentiation of parental magmas less olivine-normative than the group-A komatiite liquid.

Fig. 4-19. (a) Melt (wt.%) versus Al_2O_3 (wt.%) for garnet-saturated melts of the KR-4003 peridotite between 4-7 GPa (Walter, 1998). (b) MgO (wt.%) versus Al_2O_3 (wt.%) plot displaying the individual members of the basalt compositional continuum, the group-A komatiite liquid, low degree garnet-saturated melts of the KR-4003 peridotite (Fig. 4-19(a)), various peridotitic mantle compositions (see Table 4-5), and the average olivine and clinopyroxene from Munro Township peridotitic komatiite (as in Fig. 4-17(a)). The heavy solid line is a regression involving the KR-4003 peridotite, group-A komatiite liquid, and the average of low degree garnet-saturated melts generated between 4 and 4.5 GPa (labeled as group-E komatiite liquid; see text). The fine dashed line is a regression involving a mineral assemblage consisting of 70 wt.% olivine and 30 wt.% clinopyroxene, the group-A komatiite liquid, and the DB. The coarse dashed line is a regression involving a involving a mineral assemblage consisting of 60 wt.% olivine and 40 wt.% clinopyroxene, the group-E komatiite liquid, and all basalt. The arrowed line indicates that ~50 wt.% crystal fractionation of a mineral assemblage consisting of ~60 wt.% olivine and ~40 wt.% clinopyroxene would have to be removed from the group-E komatiite liquid in order to generate enriched basalts possessing MgO contents between ~5-7 wt.%. (c) Melt (wt.%) versus CaO (wt.%) for the experimental runs plotted in Fig. 4-19(a). (d) MgO (wt.%) versus CaO (wt.%) plot involving the compositions and regression parameters as in Fig. 4-19(b).

Fig. 4-20. Solidus mineralogy of KR-4003 peridotite between 4-7 GPa (Walter, 1998).

Fig. 4-21. (a) Selected partition coefficients for various peridotitic garnets and illustrating the strong affinity for HFSE (Nb, P, Zr and Hf) relative to the REE (see Table 4-3). (b) The composite olivine, orthopyroxene (Pyx.-1), clinopyroxene (Pyx.-2), and garnet (Gt.-1) partition coefficients used to model mantle melting at ~4 GPa (see Table 4-3 and Fig. 4-22(a-d)).

Fig. 4-22. (a) $(Yb)_N$ versus $(Ce/Yb)_N$ plot for the group-E komatiite liquid (highly enriched basalt end-member corrected for ~50 wt.% crystal fractionation of a mineral assemblage consisting of 60 wt.% olivine and 40 wt.% clinopyroxene (olivine and Pyx.-2 partition coefficients in Table 4-3), the group-A komatiite liquid, and the results of modeling non-modal melting of garnet peridotite. With the exception of the 2 wt.% melt at 3 GPa which employs the 3 GPa mode of the KR-4003 peridotite (Fig. 4-20) and Walter's (1998) ~3 GPa melt reaction of 0.08 olivine + 0.81 clinopyroxene (Pyx.-2) + 0.30 garnet (Gt.-2) = 1.0 melt + 0.18 orthopyroxene (Pyx.-1), all other model melts employ the ~4 GPa mode of the KR-4003 peridotite of 53 wt.% olivine, 0.35 wt.% pyroxene, and 12 wt.% garnet (Fig. 4-20) and the melt reaction of 0.26 olivine + 0.50 pyroxene + 0.24 garnet = 1.0 melt (Walter, 1998). All the model melts which employ the ~4 GPa mode use the same olivine partition coefficients, and with the exception of the 2 wt.% melt of primitive mantle, employ the average depleted mantle MORB source of Salters & Strake (2004) and Workman & Hart (2005), as does the 2 wt.% melt at 3 GPa. As detailed in the figure, interchanging of the pyroxene (Pyx.-1 versus Pyx.-2) and garnet partition coefficients (between ~2.4 up to ~4 GPa) has an influence on the model melt compositions when the same percentage of melting, source composition, melt reaction, and modal mineralogy are employed (see text). (b and c) $(Ce)_N$ and Hf/Hf* versus $(Ce/Yb)_N$ plots of komatiite liquids and model melts as in Fig. 4-22(a)). (d) primitive mantle normalized extended trace element plot for the group-E komatiite liquid (Hf and Zr increased by 20 % (isotope dilution determinations for the derivative basalts); see Table 4-1 and 4-2 and Appendix B), the group-A komatiite liquid, the depleted MORB mantle, and the results of 2 and 25 wt.% melting of the depleted MORB mantle using the ~4 GPa melt reaction, mode, and Pyx.-1 and Gt.-1 partition coefficients (as in Fig. 4-22(a-c)).

Fig. 4-23. MgO (wt.%) versus CaO (wt.%) plot illustrating the co-liner relationship between the group-E, -A, and -D komatiite liquids, the KR-4003 peridotite, and the residue of ~25 wt.% melt extraction from the KR-4003 peridotite at ~4.5 GPa (Table 4-5). The depleted peridotite composition employed in the 1 GPa melting experiments of Wasylenki *et al.* (2003) is also shown (Table 4-5). Relative to the KR-4003 peridotite, ~60-65 wt.% melting appears to be necessary in order to generate a magma possessing the high-MgO (~31 wt.%) and low-CaO of the group-D komatiite liquid. Alternatively, ~30-35 wt.% re-melting of the refractory residue produced by ~25 wt.% melt extraction at 4.5 GPa is required. Both scenarios would yield residues that are very olivine-rich and transitional between harzbrurgite and dunite.

Fig. 4-24. (a) Primitive mantle normalized extended element plot displaying the average depleted MORB mantle composition of Salters & Strake (2004) and Workman & Hart (2005) and the model residues produced from this starting composition by 2 and 25 wt.% melt extraction between ~4-5 GPa (Fig. 4-22(d)). (b) Primitive mantle normalized extended element plot for the group-D komatiite liquid and a 30 wt.% non-modal melt of the refractory residue produced by ~25 wt.% melt extraction from the depleted MORB mantle between ~4-5 GPa (as in Fig. 4-24(a)) employing a harzburgite mineral assemblage. The partition coefficients used are listed in Table 4-3 and the orthopyroxene dominated melt reaction is from Walter (1998).

Fig. 4-25. Primitive mantle normalized extended trace element plot illustrating the relative difference between the group-D komatiite liquid and the 30 wt.% model melt of harzburgite depicted in Fig. 4-24(b). Note that the group-D komatiite liquid is systematically more enriched in the most incompatible trace elements relative to the model melt and possesses an excess enrichment which is inversely proportional to the bulk partition coefficients of the harzburgite and/or orthopyroxene, i.e. is proportional to the theoretical 0 wt.% melt in which the concentration of a trace element in a derivative liquid (Cl) relative to the original source (Co) equals 1/D. Note that the parameter Cl/Co in a model melt as low as 1 wt.% does not approach the degree of fractionation required.

Fig. 4-26. (a) $(Ce)_N$ versus $(Ce/Yb)_N$ plot for the group-A and group-E komatiite liquid end-members and a mixing curve between them. The reversed crystal fractionation pathway of the highly enriched basalt end-member is shown (~50 wt.% fractionation of a mineral assemblage consisting of 60 wt.% olivine and 30 wt.% clinopyroxene) along with those expected for the moderately and minimally enriched members in the basalt continuum. The latter employed the same mineral assemblage and partition coefficients and the crystal fractionation was reversed until the $(Lu)_N$ of the output moderately and minimally enriched komatiite magmas were ~2.3 (equal to the average for the group-A and -E komatiite liquids), and thus would intersect the mixing curve shown (~60-65 wt.% crystal fractionation). For the minimally enriched member, the average REE pattern of all 5 EB-3 was first calculated and this pattern was subsequently normalized to the $(Lu)_N$ of ~5.9 possessed by sample HS0-091-I prior to reversing the crustal fractionation model. This procedure (multiplying the average EB-3 (n=5) by 0.667) avoids biasing of the overall REE pattern of the minimally enriched basalt member by employing only one sample. (b) Primitive mantle normalized REE plot displaying the group-A and -E komatiite liquid end-members, the reconstituted moderately and minimally enriched komatiite members in the continuum (as in Fig. 4-26(a)), and the results of mixing 70 and 90 wt.% group-A liquid with 10 and 30 wt.% of the group-E liquid.

Fig. 4-27. Temperature (°C) versus pressure (GPa) diagram illustrating the presumed temperatures and depths of origin and P-T pathways taken by the residues and melts involved in the generation of the group-A, -D, and -E komatiite liquids. The solidus shown (heaviest black line) is the parameterization of Herzberg *et al.* (2000) for the fertile peridotite KLB-1 (see equation therein). The garnet-out and orthopyroxene-out curves labeled "Walter (1998)" are drawn relative to the KLB-1 solidus, however, are constrained from data in Walter's (1998) experiments using the KR-4003 peridotie. For

the garnet-out curve, a solidus intersection is placed at 2.6 GPa and is constrained at higher pressures by the plotting parameters at 3, 4.5, and 6 GPa of +17.5, +50, and +62.5 °C (temperatures above the solidus). Similarly, the orthopyroxene-out curve has the plotting parameters at 2, 3, 4, 5, and 6 GPa of +140, +130, +120, +100, and +90 °C, respectively. The refractory peridotite solidus shown at 1 GPa and ~1262 °C is that obtained in the meting experiments of Wasylenki *et al.* (2003). Based on the temperature versus melt % data from these experiments this peridotite composition should achieve ~30 wt.% melting at 1 GPa close to a temperature of ~1547 °C, near the orthopyroxene-out curve for this composition (see text). The extrapolation of this ~30 wt.% melt contour to higher pressure (> 1 GPa) is assumed to be sub-parallel to the orthopyroxene-out curve of Walter (1998). The group-E komatiite liquid is plotted at the solids at ~4.25 GPa whereas the group-A komatiite liquid is positioned 35 °C above the solidus at 5 GPa (see text). The initiation of melting for the group-A komatiite liquid may have been at a pressure as high as ~6.8 GPa assuming that to achieve temperatures ~35 °C above the solidus via continuous melting might require ~1.8 GPa of decompression (Kinzler & Grove 1992). A ~6.8 GPa initiation of melting for the group-A komatiite liquid would be close to ~210 km depth assuming an average density for the overlying material of ~3.12 g/cm^3. Sub-solids mantle adiabats (0.3 °C per km) shown for the solidus intersections at ~4.25 (labeled ambient Archean mantle adiabat?) and ~6.8 GPa (thermal anomaly adiabat?) indicate that a ΔT of ~150 °C may be necessary in the mantle source region (see text). With respect to the generation of the group-D komatiite liquid, a solid mantle adiabat extending from the group-A komatiite liquid segregation depth is shown to approximate the maximum depth at which the residue produced by the extraction of the group-A komatiite liquid might achieve ~30 wt.% melting based upon its compositional and mineralogical similarity with the refractory peridotite of Wasylenki *et al.* (2003). In this model, the ~30 wt.% melting of refractory peridotite would require a maximum depth of ~2 GPa and constrains the lithosphere to be ≤ 60 km thick. The eruption temperatures shown for the group-A and -D komatiite liquids were determined using the MgO contents shown and the equation found in Nisbet *et al.* (1993).

Fig. 4-28. Schematic cross-section of the lithospheric architecture (age and structure) present within the central and northeastern Rae domain during the formation of the lower PAg volcanic succession. The main components of the continental margin architecture involve an older, presumably thicker lithosphere to the west and a comparatively young, juvenile, and inherently/tectonically thin margin to the east. The formation of the lower PAg is envisioned to require three principal phases: (1) initial focusing and/or deflection of upwelling mantle toward the thin margin by the lithospheric architecture; (2) initial melting (stage 1) commencing within the garnet-stability field at ~4.25 and ~6.8 GPa (group-A and -E komatiite liquids) followed quickly by the arrival of these melts at shallow lithospheric depths where they pool, mix, and differentiate to form basalt; and (3) the highly refractory residues generated by advanced melting within the garnet stability field are re-melted (stage 2).

Fig. 4-29. (a) Plot of $(Gd/Yb)_N$ and (b) Hf/Hf* versus MgO (wt.%) for basalt and komatiite collected within the lower PAg (symbols as in Fig. 4-9; this study and Chapter 3) as well as those collected from supracrustal strands outside the Laughland Lake area

(NTS 56K) within the Arrowsmith River (NTS 56O-south), Walker Lake (NTS 56J-north), and Ellice Hills (NTS 56P) map sheets and which comprise, at least in part, volcanic sequences within the middle (ca. 2710 Ma) and upper (ca. 2690 Ma) PAg (e.g. see Fig. 4-2 and 4-3; MacHattie *et al.*, unpublished data). These basalt and komatiite (grey filled circles) include 48 samples possessing SiO_2 contents ≤ 55 wt.% (only filtering done), MgO between ~3-34 wt.%, and $(Th/Nb)_N$ between ~0.4-3.2 (n=47/48 ≤ 1.7). The basalt and komatiite collected from outside the confines of the lower PAg display a strikingly similar overall geochemical distribution in which low-MgO magmas (≤ 18 wt.%) are universally HREE-depleted ($(Gd/Yb)_N$ ~1.1-2) and possess minimal to pronounced negative HFSE anomalies (Hf/Hf* ~0.6-1.0), whereas high-MgO magmas (≥ 22 wt.%) are both HREE-depleted and -enriched ($(Gd/Yb)_N$ ~0.8-1.3) and posses minimal to pronounced positive HFSE anomalies (Hf/Hf* ~0.8-2.8; n=29/32 ~0.9-1.6).

Fig. 4-B-1. (a) Lu (ppm) as determined by quadrupole-ICP-MS versus Lu (ppm) as determined by ID-MC-ICP-MS for the 14 samples analysed for Hf isotopes. The two methods display excellent agreement in Lu concentration ($R^2 = 1$ and y-intercept = 0.01). (b) Hf (ppm) as determined by quadrupole-ICP-MS versus Hf (ppm) as determined by ID-MC-ICP-MS for the 14 samples analysed for Hf isotopes. Basalt with elevated Hf (~2-5 ppm) yielded significantly higher Hf concentrations (absolute difference of ~0.3-0.9 ppm) by fusion compared with quadrupole-ICP-MS. Most of the low Hf basalt and komatiite (≤ 2 ppm) yielded minimally higher and lower Hf by isotope dilution (avg. absolute difference of ~0.09 ppm). The major exception is the olivine-phyric komatiite sample TM0-228-A which yielded a significantly lower Hf concentration by ID-MC-ICP-MS.

Fig. 4-B-2. Plot of Hf/Hf* (quadrupole-ICP-MS) versus Hf/Hf* (ID-MC-ICP-MS). For both ratios, primitive mantle normalized Nd and Sm (used for interpolation) are from quadrupole-ICP-MS data. For komatiite Hf/Hf* a ±0.3 error is applied to the data (see text).

Fig. 4-B-3. (a) P/P* versus Ti/Ti* for basalt and komatiite analysed in this study. For most samples Ti and P/REE ratios are well-correlated. Minor Ti, P or REE mobility may be responsible for the dispersion apparent in some komatiite. The significant improvement of data regressions when these samples are omitted may support this inference. (b) P/P* versus Hf/Hf* (quadrupole-ICP-MS) for basalt and komatiite analysed in this study. For most samples Hf and P/REE ratios are also well-correlated and approximate a 1:1 array.

Fig. 4-C-1. (a) $(Th/Nb)_N$ versus Nb/Nb* for high and low $(Th/Nb)_N$ basalt and komatiite within the lower PAg (this study and Chapter 3; symbols as in Fig. 4-9). Also show are intermediate felsic volcanic rocks within the lower PAg (Chapter 3) and TTG-type crust (Condie, 2005). A power fit ($R^2 = 0.92$) is shown for all PAg magmas. (b) Expanded view of Fig. 4-C-1(a) displaying only low $(Th/Nb)_N$ basalt and komatiite. Three curves are shown: (1) power law fit as in Fig. 4-C-1(a); (2) effect of increasing Th concentration of the most depleted group-C komatiite sample TM0-228-C via 0.005 ppm increments on

$(Th/Nb)_N$ and Nb/Nb*; and (3) a mixing curve involving komatiite sample TM0-228-C and TTG-type crust (Condie, 2005), increments are wt.% TTG. Note that samples from all major basalt and komatiite groups have samples which possess $(Th/Nb)_N$ ratios of ~0.65 or lower (EB-3 only exception), and that the within-group variation within this ratio is significant for all groups. (c) Primitive mantle normalized extended element diagram illustrating the effects of mixing and un-mixing a TTG-type contaminant upon various basalt and komatiite samples and/or groups. Note that: (1) exceptionally minor amounts of contamination can greatly influence $(Th/Nb)_N$ (and Nb/Nb*); and (2) very little to no effect is detectable in the less incompatible trace elements. (d) Primitive mantle normalized extended element diagram illustrating the effects of un-mixing dacite T-3319-B (Chapter 3) from basalt samples T-3318-A and T-3319-A until they possess $(Th/Nb)_N$ ratios between ~0.5-0.6. Note that apart from Th, Nb and La, most other trace elements are significantly less affected by mixing/un-mixing of the dacite.

Fig.4-D-1. (a) MgO (wt.%) versus TiO_2 (wt.%) and (b) Al_2O_3 for the group-C and -D komatiite. The regressions shown include all samples except those from flow 3, and both intersect the x-axis between ~50-55 wt.% MgO. (c) Primitive mantle normalized MREE and HREE abundances for the group-C komatiite liquid and cumulates produced by adding 50 wt.% olivine to this composition. Olivine compositions were calculated as 1% instantaneous solids and the composite olivine partition coefficients listed in Table 4-3 for olivine-1 and those of Arndt & Lesher (1992) for olivine-2 (labeled Kambalda Kd's) were used. Also included is the Kambalda olivine composition analysed by Arndt &

Lesher (1992) and the Yb partition coefficients between olivine and komatiite liquid determined experimentally by Canil & Fedortchouk (2001).

Fig. 4-D-2. (a) Primitive mantle normalized extended element plot for the average group-D komatiite from flows #4 and 6 (no Zr and Hf from samples TM0-227-D and TM0-229-C and -F; Fig. 4-B-3(b)) and the postulated group-D liquid produced by un-mixing 30 wt.% of the group-A liquid from that of group-C. (b) Mixtures between the group-D komatiite liquid and 1 wt.% TTG (Condie, 2005) and 1.5 wt.% of the average EB-1 and -2 (n=6).

Fig. 4-E-1. (a) Al_2O_3 versus CaO plot for the DB, EB-3, and group-A komatiite liquid and postulated crystal fractionation pathways (dashed lines). Minerals plotted include: olivine and clinopyroxene from Munro Township peridotitic komatiite flows (Arndt *et al.*, 1977); augite and pigeonite from pyroxene spinifex-textured komatiitic basalt flows from Dundonald Township (Arndt & Fleet, 1979); and experimentally crystallized plagioclase from a komatiitic basalt composition (Kinzler & Grove, 1985). (b) Primitive mantle normalized REE plot for the low (HS0-091-I) and high (avg. TM0-3324-A, -B) ΣREE EB-3 end-members and results of crystal fractionation modeling of the REE. Partition coefficients used are listed in Table 4-3.

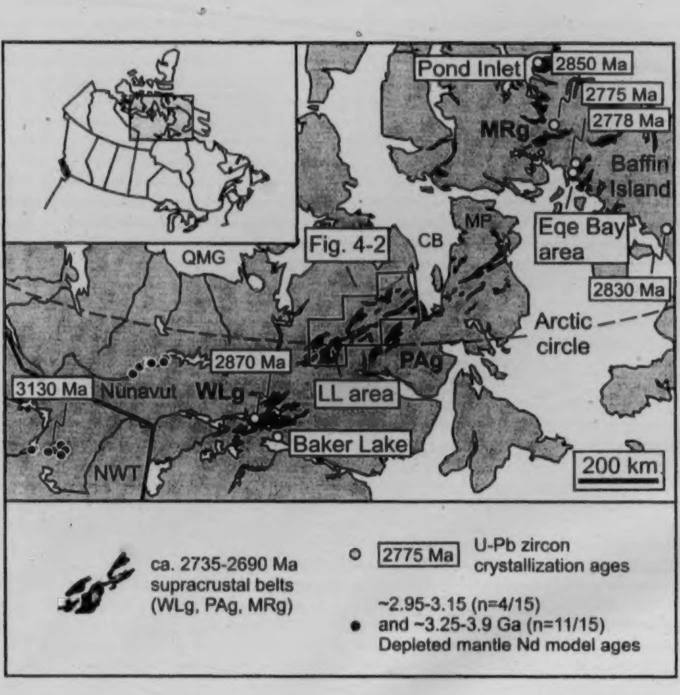
Pond Inlet
2850 Ma
2775 Ma
2778 Ma
MRg
Baffin Island
Eqe Bay area
MP
CB
Fig. 4-2
QMG
2830 Ma
Arctic circle
PAg
2870 Ma
3130 Ma
Nunavut
WLg
LL area
Baker Lake
NWT
200 km
ca. 2735-2690 Ma supracrustal belts (WLg, PAg, MRg)
2775 Ma U-Pb zircon crystallization ages
~2.95-3.15 (n=4/15) and ~3.25-3.9 Ga (n=11/15) Depleted mantle Nd model ages

Figure 4-1

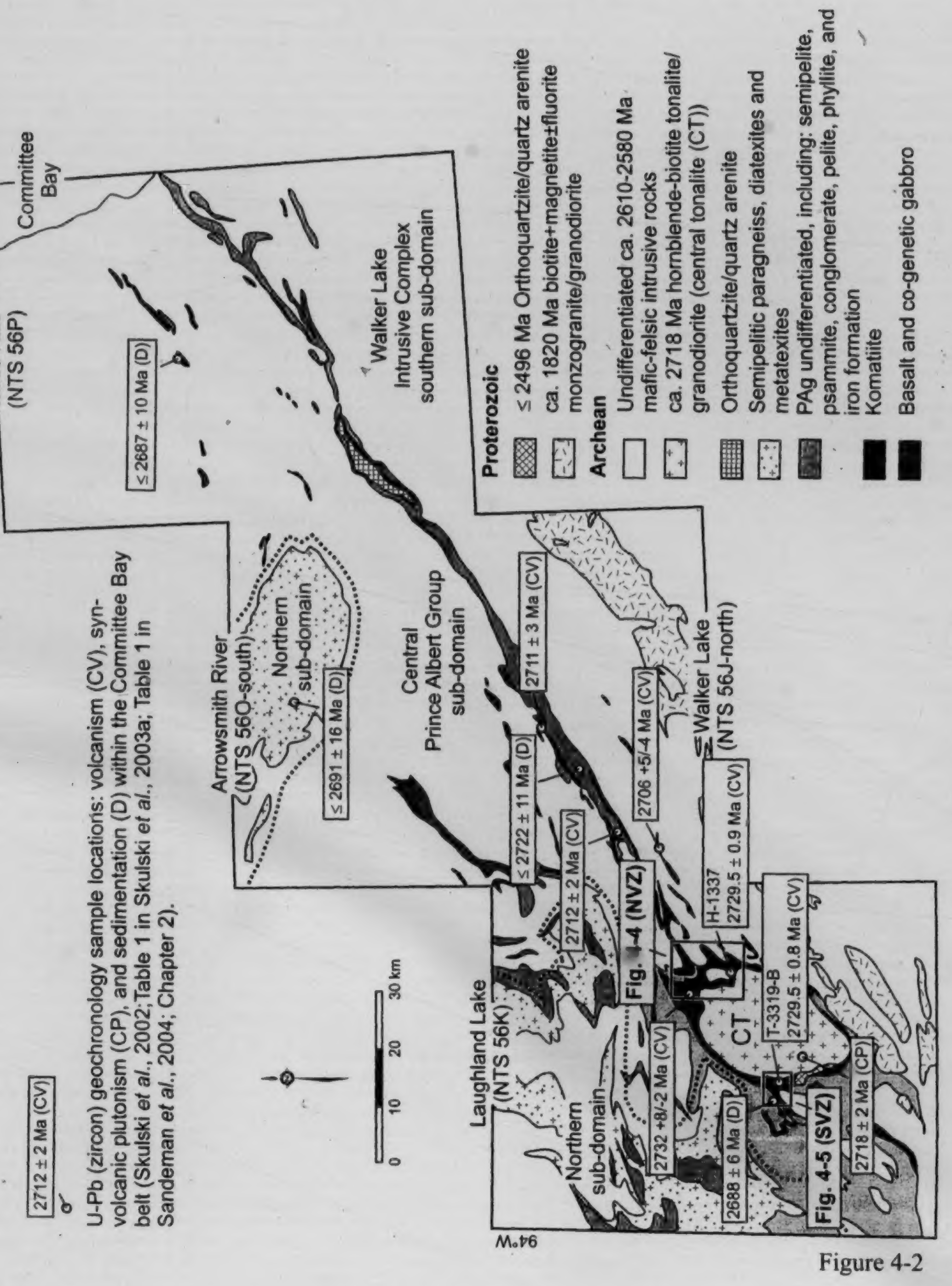
2712 ± 2 Ma (CV)
0
10
20
30 km
68°N
94°W
Ellice Hills
(NTS 56P)
Committee
Bay
≤ 2687 ± 10 Ma (D)
Walker Lake
Intrusive Complex
southern sub-domain
Arrowsmith River
(NTS 56O-south)
Northern
sub-domain
≤ 2691 ± 16 Ma (D)
Central
Prince Albert Group
sub-domain
2711 ± 3 Ma (CV)
≤ 2722 ± 11 Ma (D)
2712 ± 2 Ma (CV)
2706 +5/-4 Ma (CV)
Walker Lake
(NTS 56J-north)
H-1337
2729.5 ± 0.9 Ma (CV)
Fig. -4 (NVZ)
Laughland Lake
(NTS 56K)
Northern
sub-domain
2732 +8/-2 Ma (CV)
CT
T-3319-B
2729.5 ± 0.8 Ma (CV)
2688 ± 6 Ma (D)
Fig. 4-5 (SVZ)
2718 ± 2 Ma (CP)
Proterozoic
≤ 2496 Ma Orthoquartzite/quartz arenite
ca. 1820 Ma biotite+magnetite±fluorite monzogranite/granodiorite
Archean
Undifferentiated ca. 2610-2580 Ma mafic-felsic intrusive rocks
ca. 2718 Ma hornblende-biotite tonalite/ granodiorite (central tonalite (CT))
Orthoquartzite/quartz arenite
Semipelitic paragneiss, diatexites and metatexites
PAg undifferentiated, including: semipelite, psammite, conglomerate, pelite, phyllite, and iron formation
Komatiite
Basalt and co-genetic gabbro

U-Pb (zircon) geochronology sample locations: volcanism (CV), syn-volcanic plutonism (CP), and sedimentation (D) within the Committee Bay belt (Skulski *et al.*, 2002; Table 1 in Skulski *et al.*, 2003a; Table 1 in Sandeman *et al.*, 2004; Chapter 2).

Figure 4-2

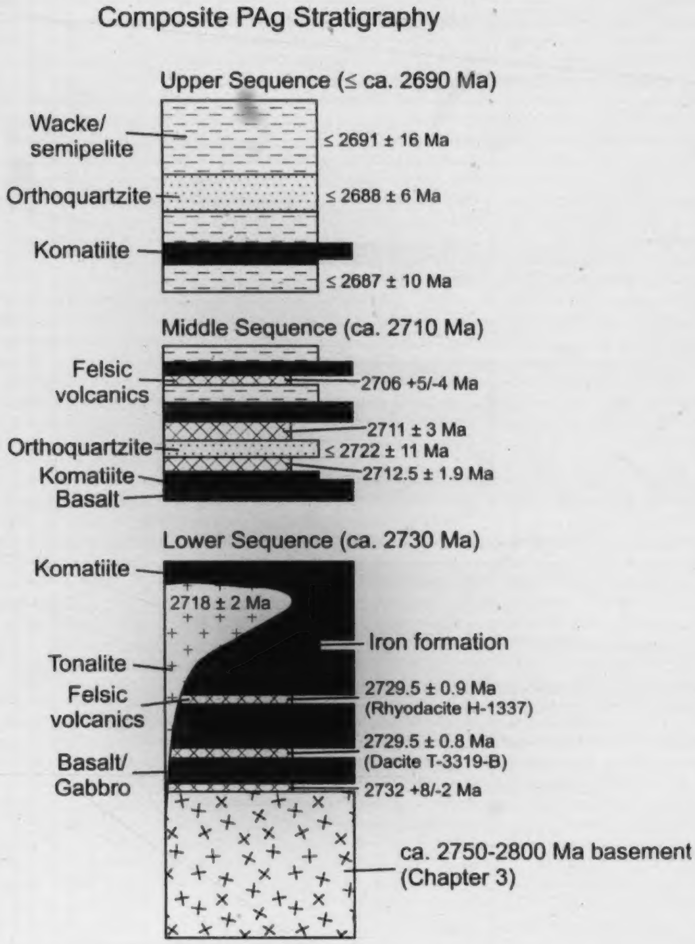
Composite PAg Stratigraphy
Upper Sequence (≤ ca. 2690 Ma)
Wacke/ semipelite
≤ 2691 ± 16 Ma
Orthoquartzite
≤ 2688 ± 6 Ma
Komatiite
≤ 2687 ± 10 Ma
Middle Sequence (ca. 2710 Ma)
Felsic volcanics
2706 +5/-4 Ma
2711 ± 3 Ma
Orthoquartzite
≤ 2722 ± 11 Ma
Komatiite
2712.5 ± 1.9 Ma
Basalt
Lower Sequence (ca. 2730 Ma)
Komatiite
2718 ± 2 Ma
Iron formation
Tonalite
Felsic volcanics
2729.5 ± 0.9 Ma (Rhyodacite H-1337)
2729.5 ± 0.8 Ma (Dacite T-3319-B)
Basalt/ Gabbro
2732 +8/-2 Ma
ca. 2750-2800 Ma basement (Chapter 3)

Figure 4-3

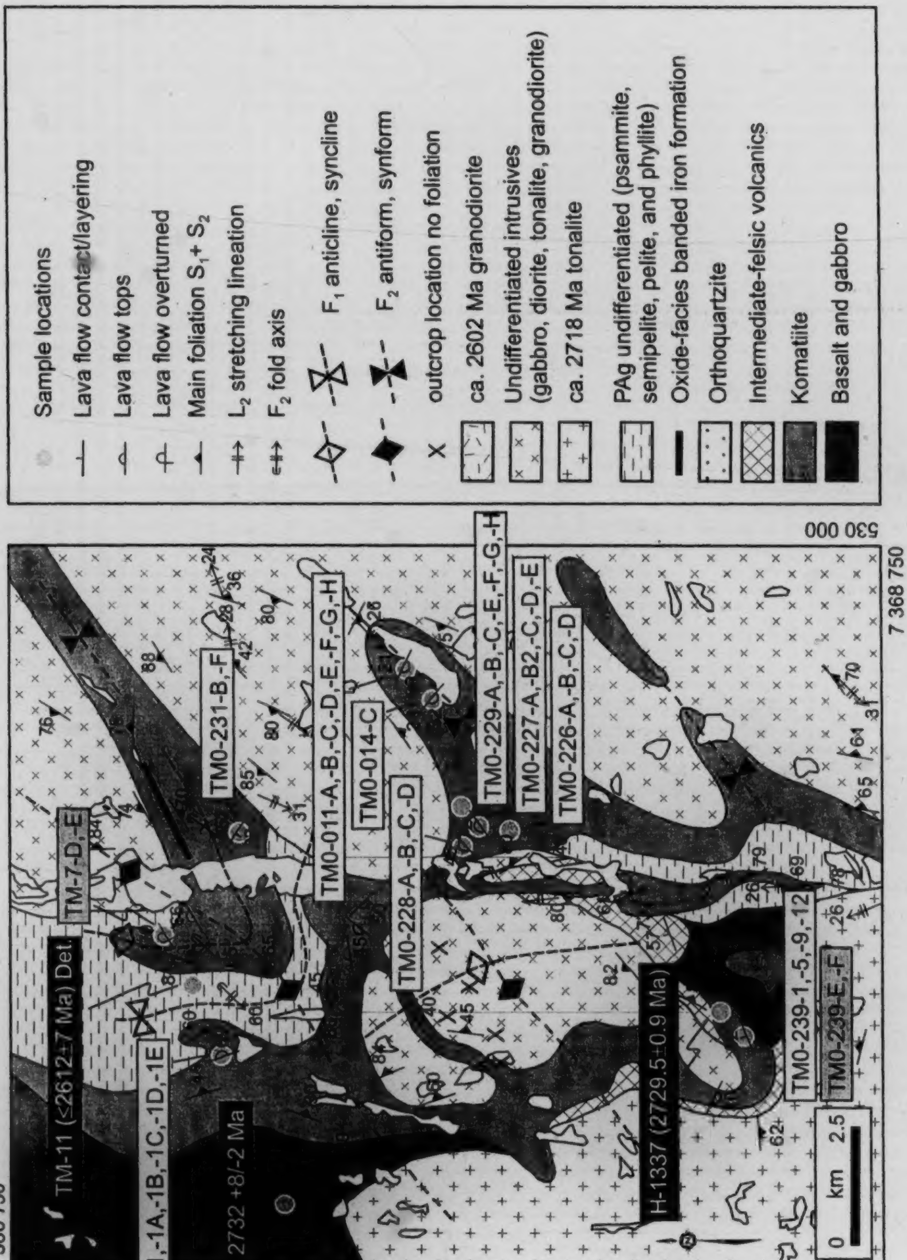
7 386 750
515 000
530 000
7 368 750
TM-11 (≤2612±7 Ma) Det
2732 +8/-2 Ma
TM-1,-1A,-1B,-1C,-1D,-1E
TM-7-D,-E
TM0-231-B,-F
TM0-011-A,-B,-C,-D,-E,-F,-G,-H
TM0-014-C
TM0-228-A,-B,-C,-D
TM0-229-A,-B,-C,-E,-F,-G,-H
TM0-227-A,-B2,-C,-D,-E
TM0-226-A,-B,-C,-D
H-1337 (2729.5±0.9 Ma)
TM0-239-1,-5,-9,-12
TM0-239-E,-F
0 km 2.5
Sample locations
Lava flow contact/layering
Lava flow tops
Lava flow overturned
Main foliation $S_1 + S_2$
L_2 stretching lineation
F_2 fold axis
F_1 anticline, syncline
F_2 antiform, synform
outcrop location no foliation
ca. 2602 Ma granodiorite
Undifferentiated intrusives (gabbro, diorite, tonalite, granodiorite)
ca. 2718 Ma tonalite
PAg undifferentiated (psammite, semipelite, pelite, and phyllite)
Oxide-facies banded iron formation
Orthoquartzite
Intermediate-felsic volcanics
Komatiite
Basalt and gabbro

Figure 4-4

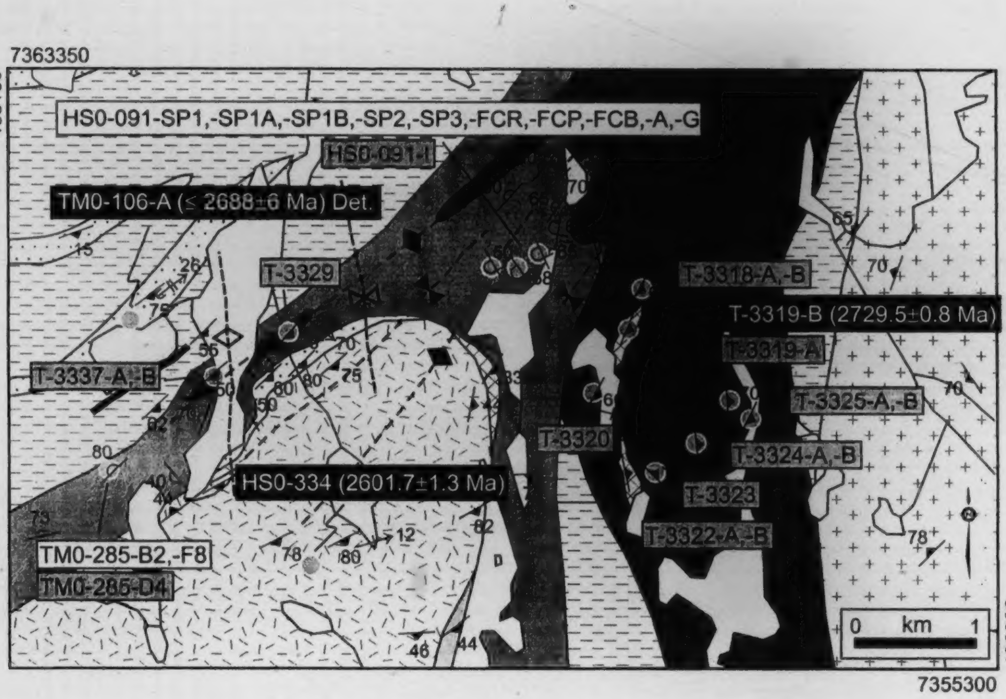
7363350
485150
HS0-091-SP1,-SP1A,-SP1B,-SP2,-SP3,-FCR,-FCP,-FCB,-A,-G
HS0-091-I
TM0-106-A (≤ 2688±6 Ma) Det.
T-3329
T-3318-A,-B
T-3319-B (2729.5±0.8 Ma)
T-3319-A
T-3337-A,-B
T-3325-A,-B
T-3320
T-3324-A,-B
HS0-334 (2601.7±1.3 Ma)
T-3323
T-3322-A,-B
TM0-285-B2,-F8
TM0-285-D4
0 km 1
496900
7355300

Figure 4-5

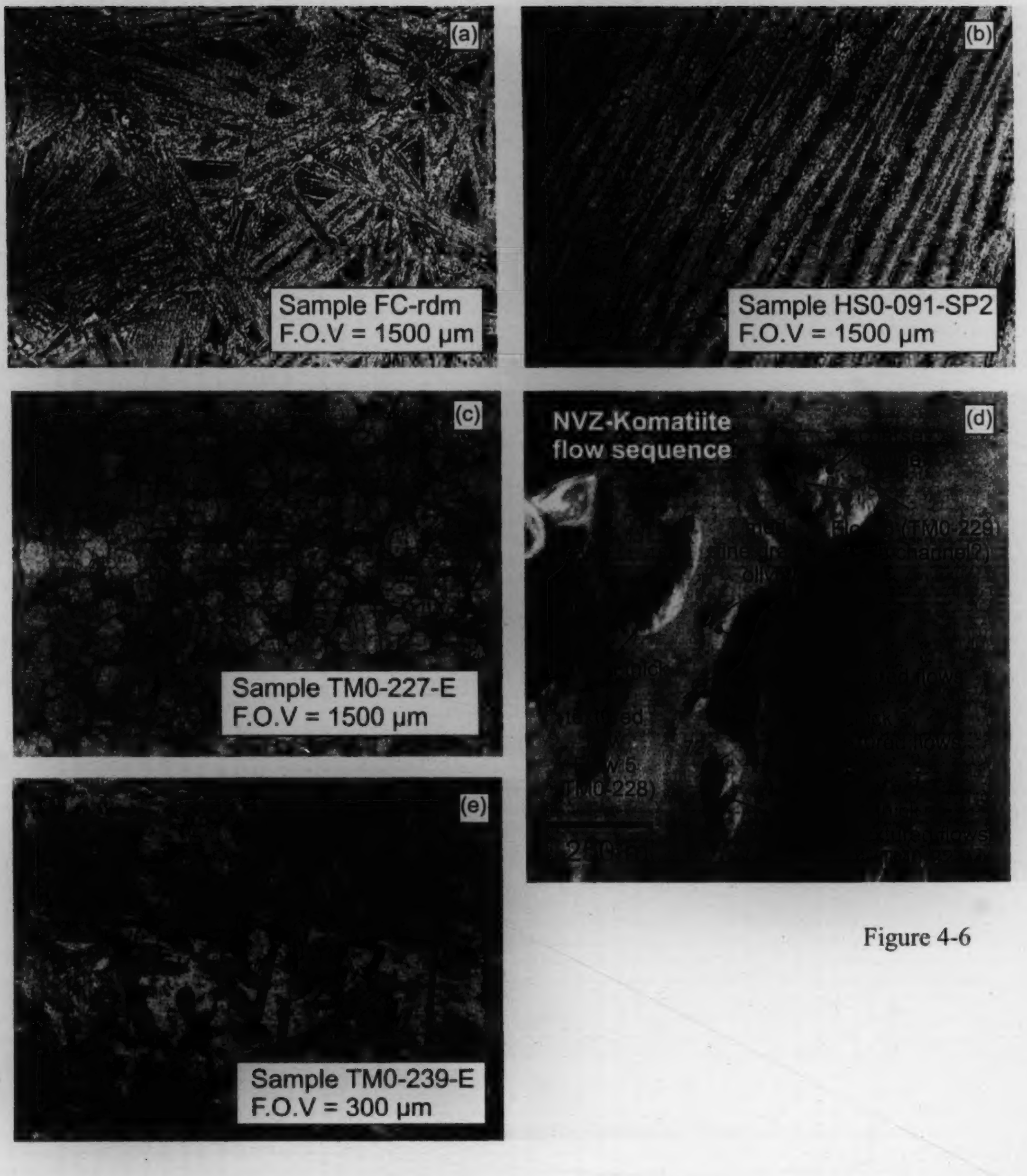
(a)
Sample FC-rdm
F.O.V = 1500 µm
(b)
Sample HS0-091-SP2
F.O.V = 1500 µm
(c)
Sample TM0-227-E
F.O.V = 1500 µm
NVZ-Komatiite
flow sequence
(d)
(TM0-229)
channel?)
(TM0-228)
(e)
Sample TM0-239-E
F.O.V = 300 µm

Figure 4-6

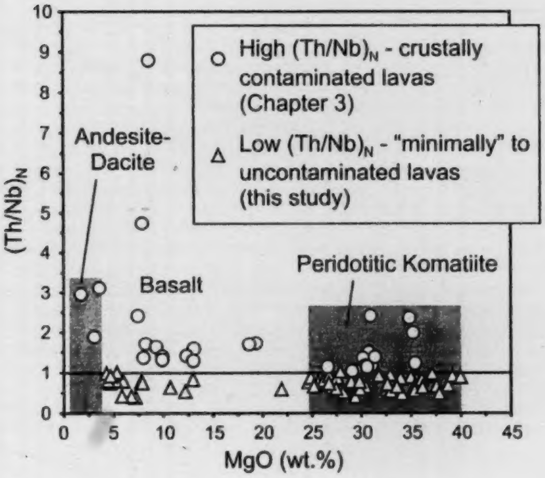
10
9
8
7
6
5
4
3
2
1
0
(Th/Nb)$_N$
0
5
10
15
20
25
30
35
40
45
MgO (wt.%)
Andesite-Dacite
Basalt
Peridotitic Komatiite
○ High (Th/Nb)$_N$ - crustally contaminated lavas (Chapter 3)
△ Low (Th/Nb)$_N$ - "minimally" to uncontaminated lavas (this study)

Figure 4-7

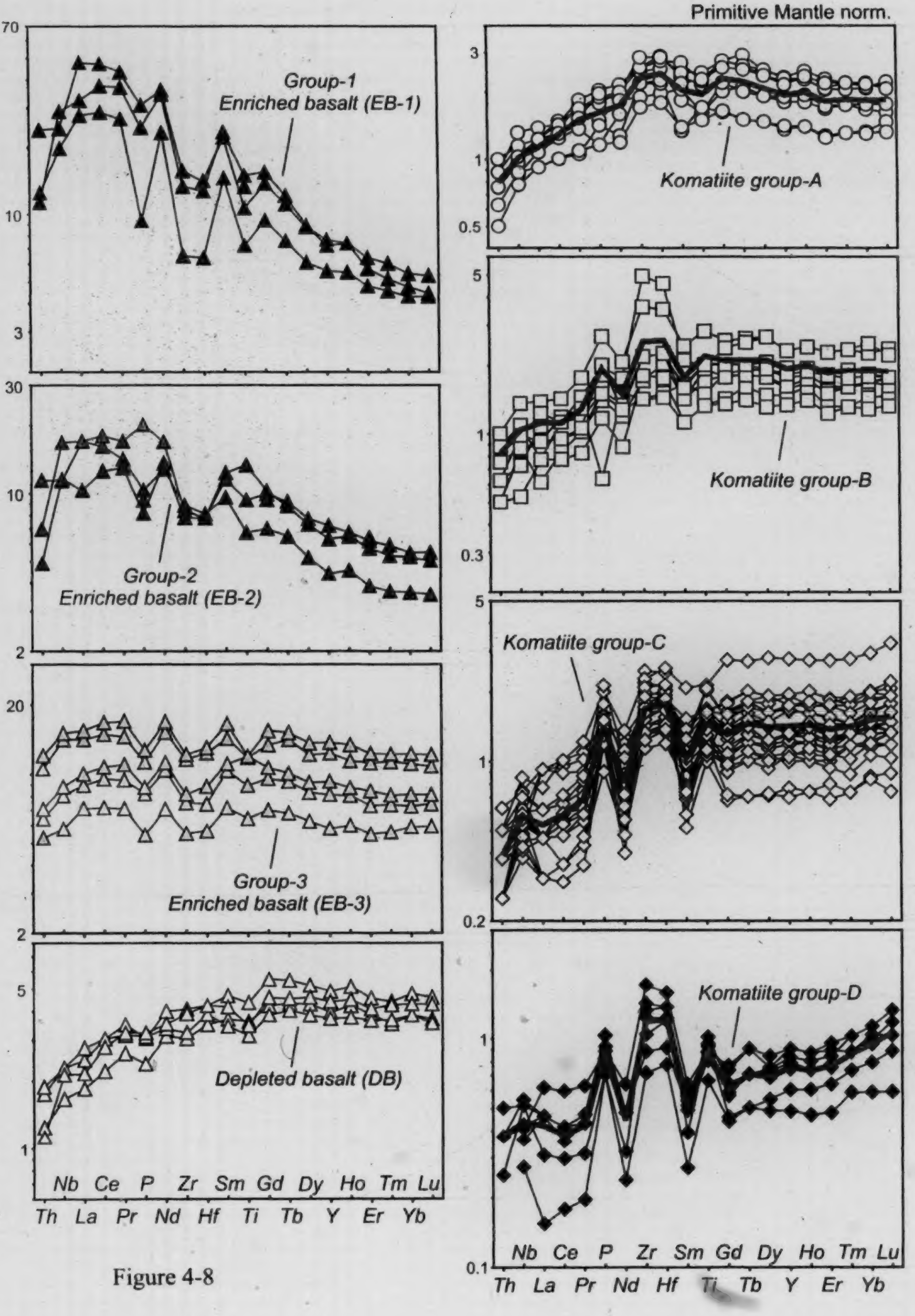
Primitive Mantle norm.
70
10
3
Group-1
Enriched basalt (EB-1)
30
10
2
Group-2
Enriched basalt (EB-2)
20
2
Group-3
Enriched basalt (EB-3)
5
1
Depleted basalt (DB)
Nb Ce P Zr Sm Gd Dy Ho Tm Lu
Th La Pr Nd Hf Ti Tb Y Er Yb
3
1
0.5
Komatiite group-A
5
1
0.3
Komatiite group-B
5
1
0.2
Komatiite group-C
1
0.1
Komatiite group-D
Nb Ce P Zr Sm Gd Dy Ho Tm Lu
Th La Pr Nd Hf Ti Tb Y Er Yb

Figure 4-8

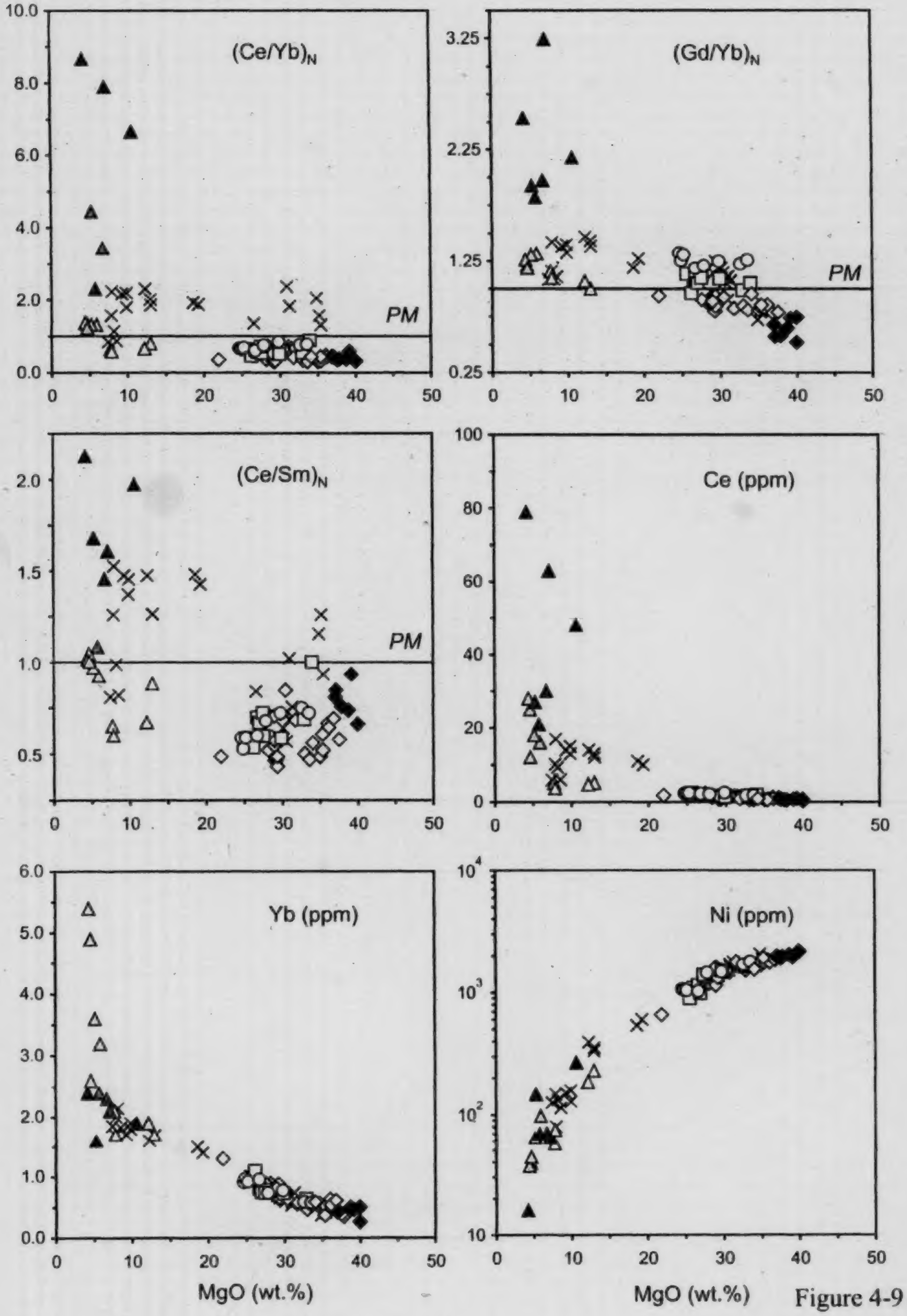
(Ce/Yb)N
PM
10.0
8.0
6.0
4.0
2.0
0.0
(Gd/Yb)N
PM
3.25
2.25
1.25
0.25
(Ce/Sm)N
PM
2.0
1.5
1.0
0.5
Ce (ppm)
100
80
60
40
20
0
Yb (ppm)
6.0
5.0
4.0
3.0
2.0
1.0
0.0
Ni (ppm)
10⁴
10³
10²
10
0
10
20
30
40
50
MgO (wt.%)
MgO (wt.%)

Figure 4-9

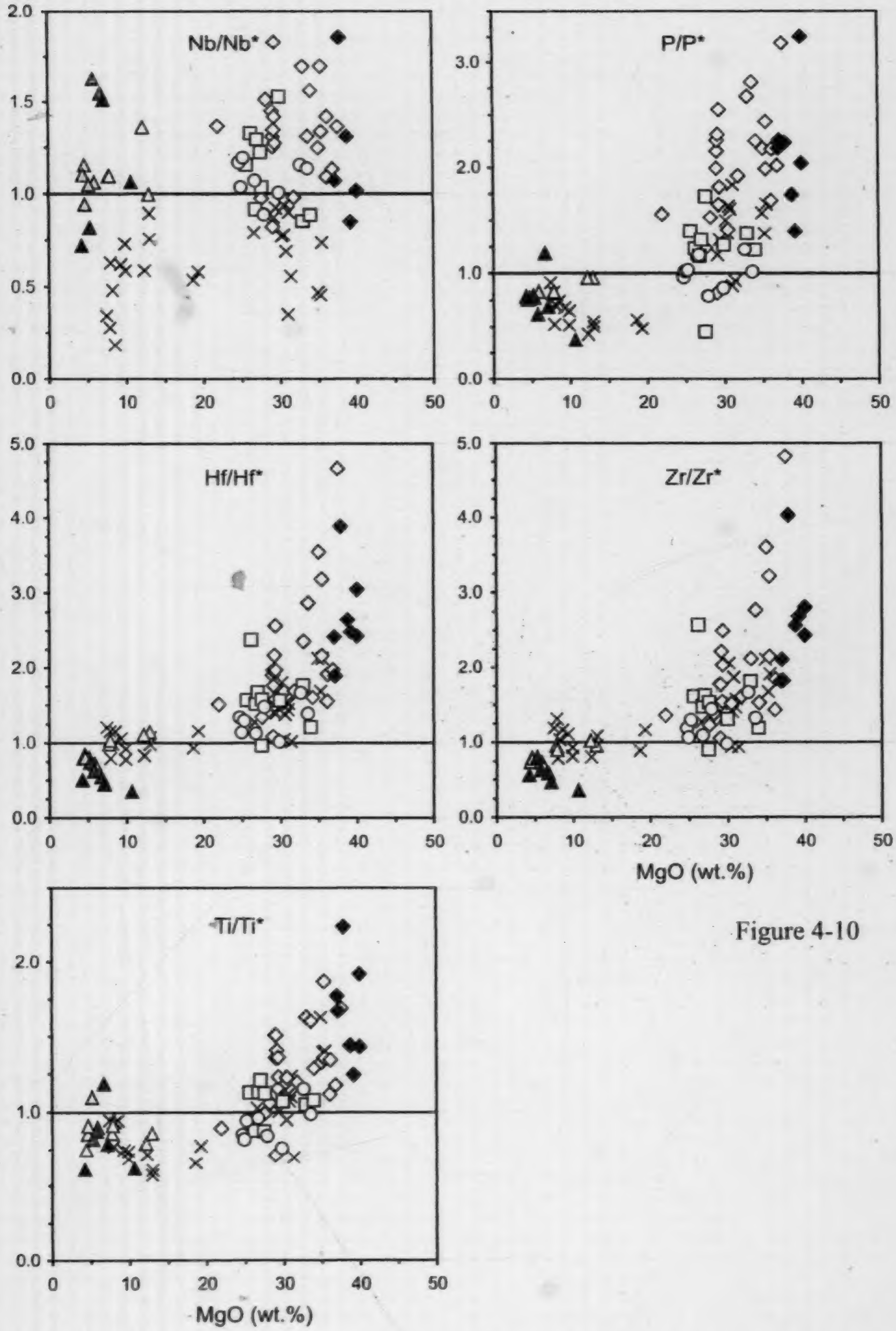
Nb/Nb*
P/P*
Hf/Hf*
Zr/Zr*
Ti/Ti*
0.0
0.5
1.0
1.5
2.0
3.0
4.0
5.0
0
10
20
30
40
50
MgO (wt.%)

Figure 4-10

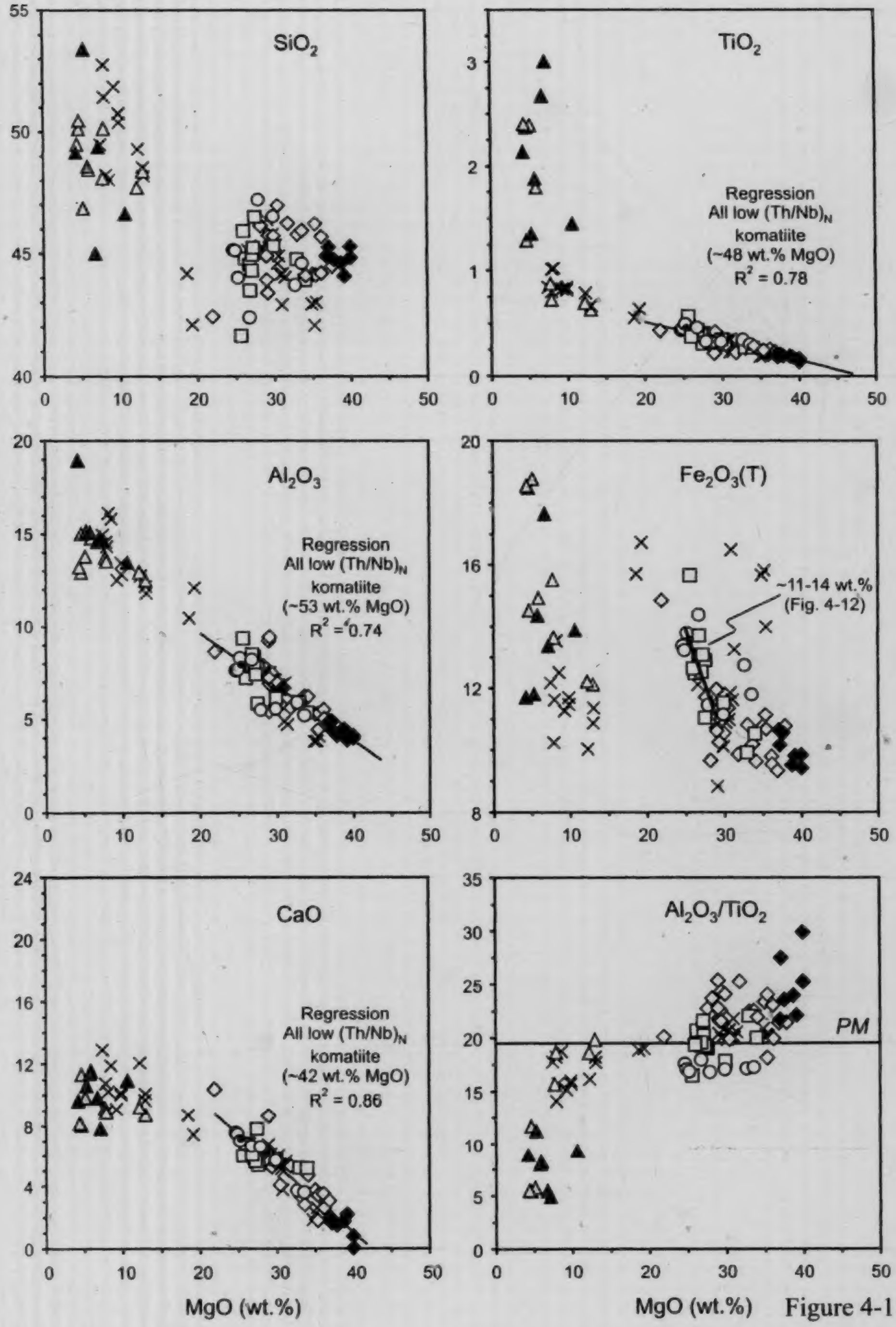

SiO$_2$
55
50
45
40
TiO$_2$
3
2
1
0
Regression
All low (Th/Nb)$_N$
komatiite
(~48 wt.% MgO)
R^2 = 0.78
Al$_2$O$_3$
20
15
10
5
0
Regression
All low (Th/Nb)$_N$
komatiite
(~53 wt.% MgO)
R^2 = 0.74
Fe$_2$O$_3$(T)
20
16
12
8
~11-14 wt.%
(Fig. 4-12)
CaO
24
20
16
12
8
4
0
Regression
All low (Th/Nb)$_N$
komatiite
(~42 wt.% MgO)
R^2 = 0.86
Al$_2$O$_3$/TiO$_2$
35
30
25
20
15
10
5
0
PM
0
10
20
30
40
50
MgO (wt.%)
MgO (wt.%)

Figure 4-11

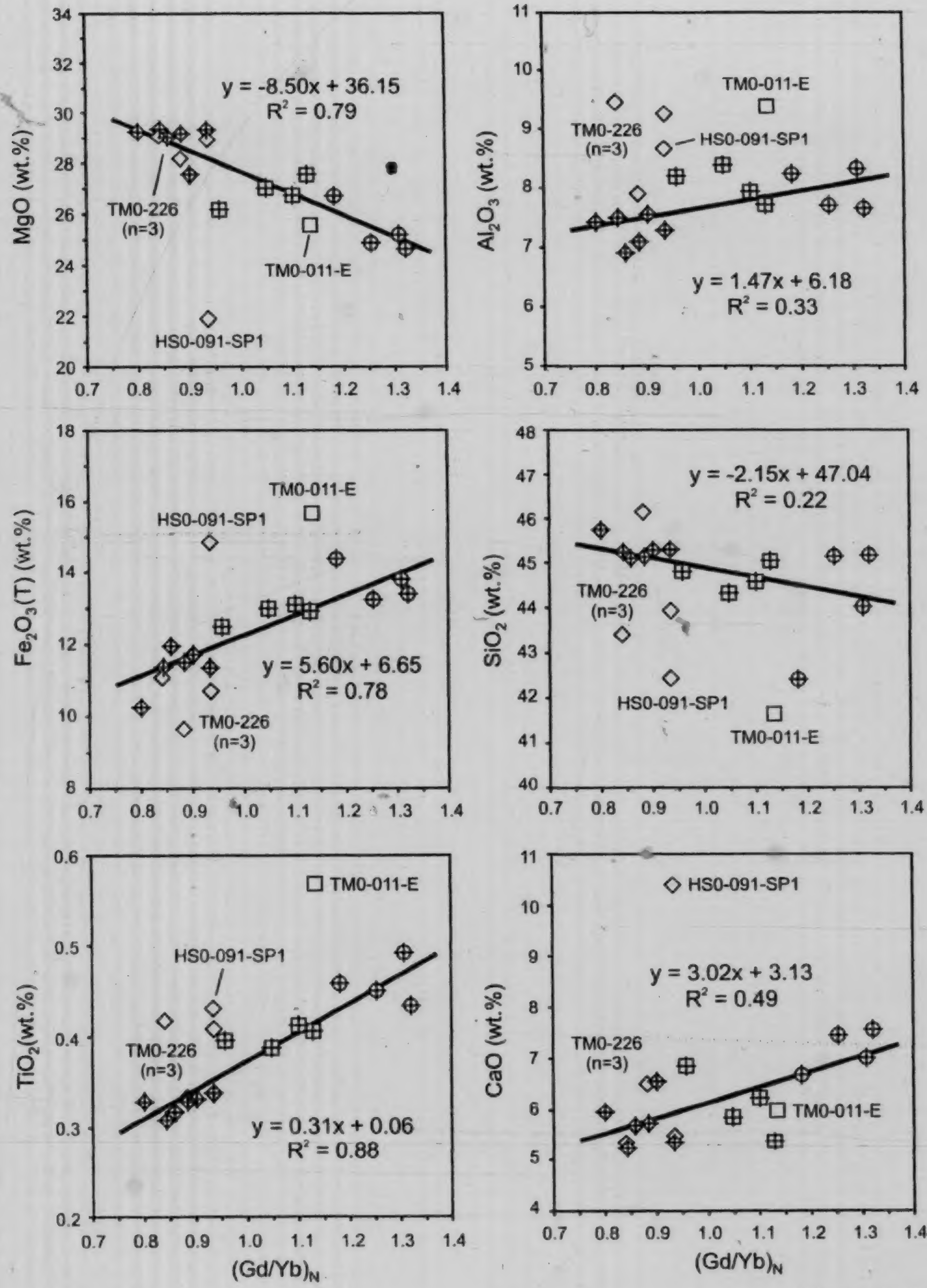
MgO (wt.%)
y = -8.50x + 36.15
R² = 0.79
TM0-226
(n=3)
TM0-011-E
HS0-091-SP1
Al2O3 (wt.%)
TM0-011-E
TM0-226
(n=3)
HS0-091-SP1
y = 1.47x + 6.18
R² = 0.33
Fe2O3(T) (wt.%)
TM0-011-E
HS0-091-SP1
y = 5.60x + 6.65
R² = 0.78
TM0-226
(n=3)
SiO2 (wt.%)
y = -2.15x + 47.04
R² = 0.22
TM0-226
(n=3)
HS0-091-SP1
TM0-011-E
TiO2(wt.%)
TM0-011-E
HS0-091-SP1
TM0-226
(n=3)
y = 0.31x + 0.06
R² = 0.88
CaO (wt.%)
HS0-091-SP1
y = 3.02x + 3.13
R² = 0.49
TM0-226
(n=3)
TM0-011-E
(Gd/Yb)N
(Gd/Yb)N
0.7
0.8
0.9
1.0
1.1
1.2
1.3
1.4

Figure 4-12

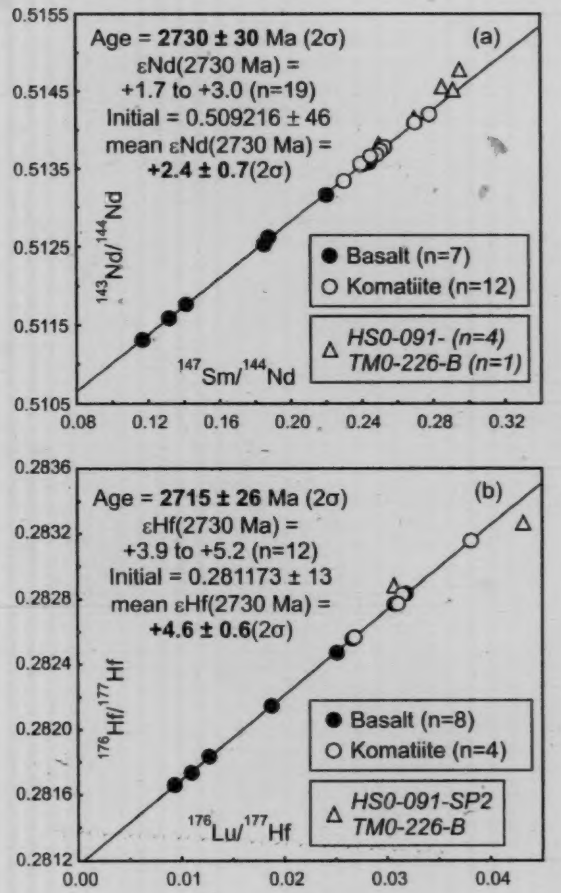
(a)
Age = **2730 ± 30** Ma (2σ)
εNd(2730 Ma) =
+1.7 to +3.0 (n=19)
Initial = 0.509216 ± 46
mean εNd(2730 Ma) =
+2.4 ± 0.7(2σ)
● Basalt (n=7)
○ Komatiite (n=12)
△ *HS0-091- (n=4)*
TM0-226-B (n=1)
$^{143}Nd/^{144}Nd$
$^{147}Sm/^{144}Nd$
0.5155
0.5145
0.5135
0.5125
0.5115
0.5105
0.08
0.12
0.16
0.20
0.24
0.28
0.32
(b)
Age = **2715 ± 26** Ma (2σ)
εHf(2730 Ma) =
+3.9 to +5.2 (n=12)
Initial = 0.281173 ± 13
mean εHf(2730 Ma) =
+4.6 ± 0.6(2σ)
● Basalt (n=8)
○ Komatiite (n=4)
△ *HS0-091-SP2*
TM0-226-B
$^{176}Hf/^{177}Hf$
$^{176}Lu/^{177}Hf$
0.2836
0.2832
0.2828
0.2824
0.2820
0.2816
0.2812
0.00
0.01
0.02
0.03
0.04

Figure 4-13

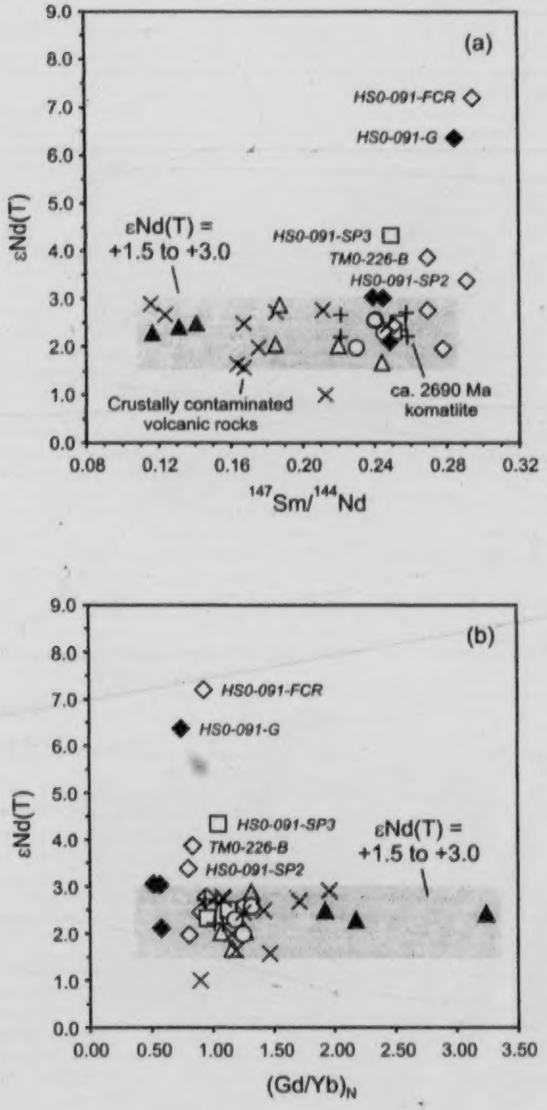

(a)
εNd(T)
^{147}Sm/^{144}Nd
9.0
8.0
7.0
6.0
5.0
4.0
3.0
2.0
1.0
0.0
0.08
0.12
0.16
0.20
0.24
0.28
0.32
HS0-091-FCR
HS0-091-G
HS0-091-SP3
TM0-226-B
HS0-091-SP2
εNd(T) = +1.5 to +3.0
Crustally contaminated volcanic rocks
ca. 2690 Ma komatiite
(b)
εNd(T)
(Gd/Yb)$_N$
0.00
0.50
1.00
1.50
2.00
2.50
3.00
3.50
HS0-091-FCR
HS0-091-G
HS0-091-SP3
TM0-226-B
HS0-091-SP2
εNd(T) = +1.5 to +3.0

Figure 4-14

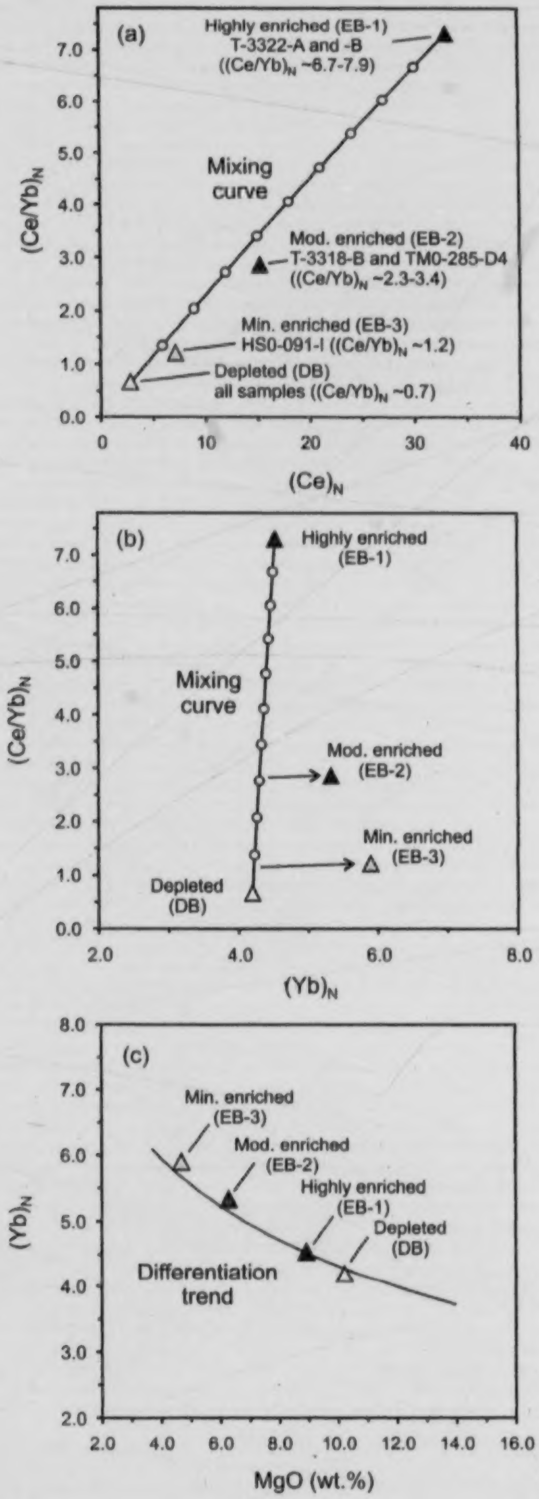
(a)
Highly enriched (EB-1)
T-3322-A and -B
($(Ce/Yb)_N$ ~6.7-7.9)
Mixing curve
Mod. enriched (EB-2)
T-3318-B and TM0-285-D4
($(Ce/Yb)_N$ ~2.3-3.4)
Min. enriched (EB-3)
HS0-091-I ($(Ce/Yb)_N$ ~1.2)
Depleted (DB)
all samples ($(Ce/Yb)_N$ ~0.7)
$(Ce/Yb)_N$
0.0
1.0
2.0
3.0
4.0
5.0
6.0
7.0
0
10
20
30
40
$(Ce)_N$
(b)
Highly enriched (EB-1)
Mixing curve
Mod. enriched (EB-2)
Min. enriched (EB-3)
Depleted (DB)
$(Ce/Yb)_N$
0.0
1.0
2.0
3.0
4.0
5.0
6.0
7.0
2.0
4.0
6.0
8.0
$(Yb)_N$
(c)
Min. enriched (EB-3)
Mod. enriched (EB-2)
Highly enriched (EB-1)
Depleted (DB)
Differentiation trend
$(Yb)_N$
2.0
3.0
4.0
5.0
6.0
7.0
8.0
2.0
4.0
6.0
8.0
10.0
12.0
14.0
16.0
MgO (wt.%)

Figure 4-15

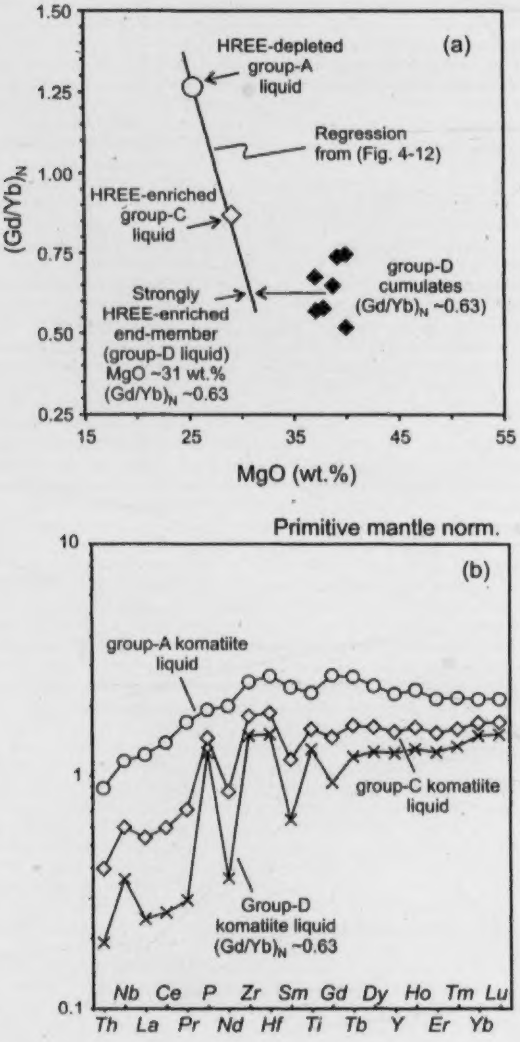
1.50
1.25
1.00
0.75
0.50
0.25
(Gd/Yb)$_N$
HREE-depleted group-A liquid
(a)
Regression from (Fig. 4-12)
HREE-enriched group-C liquid
group-D cumulates (Gd/Yb)$_N$ ~0.63)
Strongly HREE-enriched end-member (group-D liquid) MgO ~31 wt.% (Gd/Yb)$_N$ ~0.63
15
25
35
45
55
MgO (wt.%)
Primitive mantle norm.
10
1
0.1
(b)
group-A komatiite liquid
group-C komatiite liquid
Group-D komatiite liquid (Gd/Yb)$_N$ ~0.63
Nb Ce P Zr Sm Gd Dy Ho Tm Lu
Th La Pr Nd Hf Ti Tb Y Er Yb

Figure 4-16

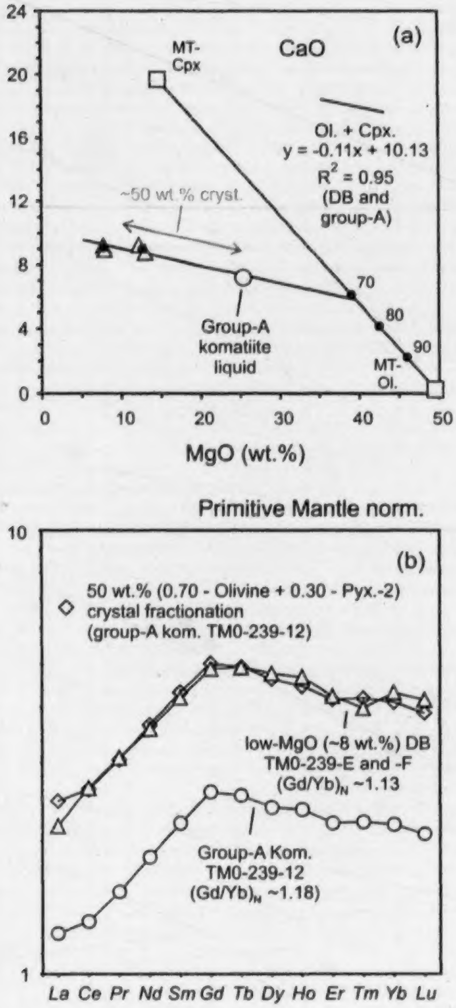
(a)
CaO
MT-Cpx
Ol. + Cpx.
y = -0.11x + 10.13
R² = 0.95
(DB and group-A)
~50 wt.% cryst.
70
80
90
MT-Ol.
Group-A komatiite liquid
MgO (wt.%)
0
10
20
30
40
50
0
4
8
12
16
20
24
Primitive Mantle norm.
(b)
50 wt.% (0.70 - Olivine + 0.30 - Pyx.-2) crystal fractionation (group-A kom. TM0-239-12)
low-MgO (~8 wt.%) DB TM0-239-E and -F (Gd/Yb)N ~1.13
Group-A Kom. TM0-239-12 (Gd/Yb)N ~1.18)
10
1
La Ce Pr Nd Sm Gd Tb Dy Ho Er Tm Yb Lu

Figure 4-17

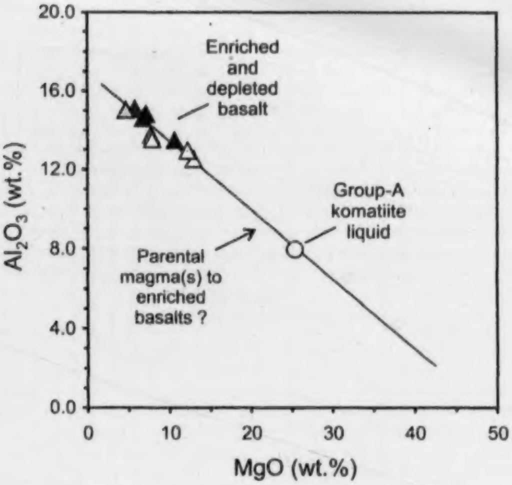
20.0
16.0
12.0
8.0
4.0
0.0
Al_2O_3 (wt.%)
0
10
20
30
40
50
MgO (wt.%)
Enriched and depleted basalt
Group-A komatiite liquid
Parental magma(s) to enriched basalts ?

Figure 4-18

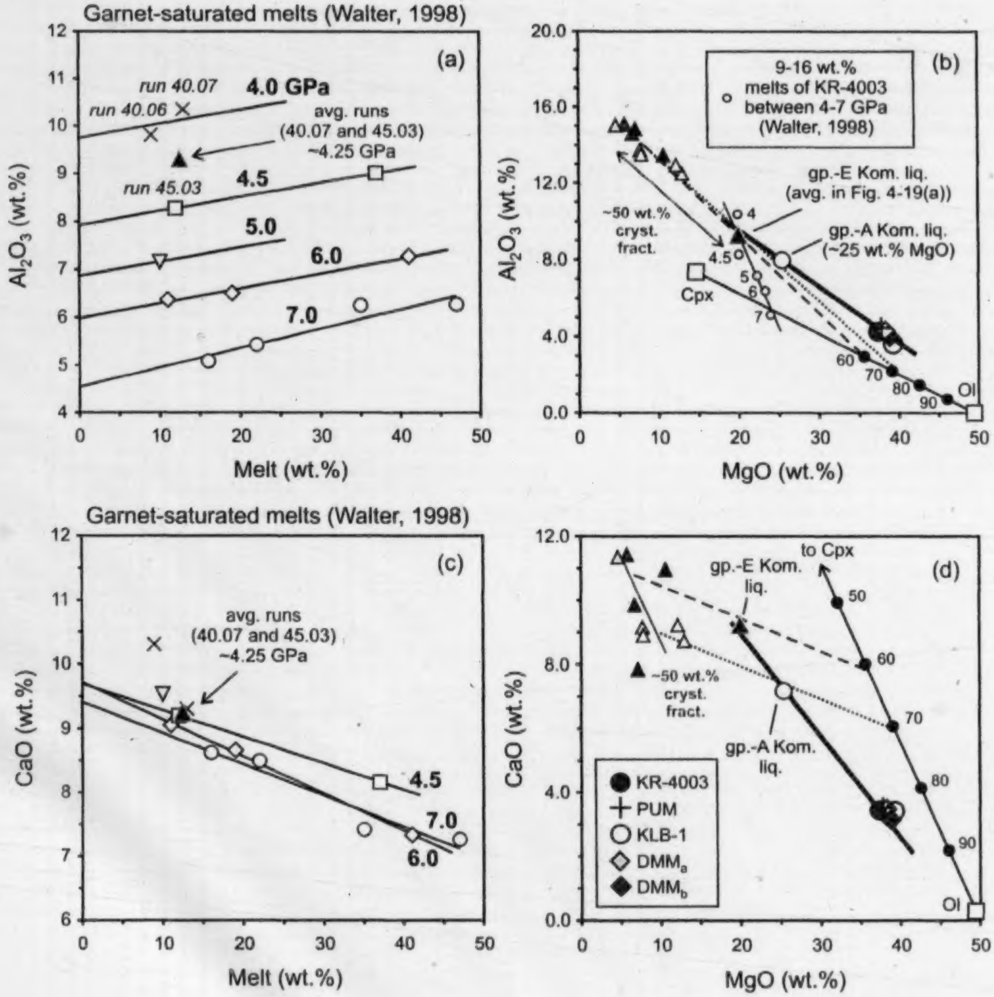
Garnet-saturated melts (Walter, 1998)
(a)
run 40.07
run 40.06
4.0 GPa
avg. runs
(40.07 and 45.03)
~4.25 GPa
run 45.03
4.5
5.0
6.0
7.0
Al_2O_3 (wt.%)
Melt (wt.%)
(b)
9-16 wt.%
melts of KR-4003
between 4-7 GPa
(Walter, 1998)
gp.-E Kom. liq.
(avg. in Fig. 4-19(a))
gp.-A Kom. liq.
(~25 wt.% MgO)
~50 wt.%
cryst.
fract.
4
4.5
5
6
7
Cpx
60
70
80
90
Ol
Al_2O_3 (wt.%)
MgO (wt.%)
Garnet-saturated melts (Walter, 1998)
(c)
avg. runs
(40.07 and 45.03)
~4.25 GPa
4.5
7.0
6.0
CaO (wt.%)
Melt (wt.%)
(d)
to Cpx
gp.-E Kom.
liq.
50
60
70
80
90
~50 wt.%
cryst.
fract.
gp.-A Kom.
liq.
KR-4003
PUM
KLB-1
DMM_a
DMM_b
Ol
CaO (wt.%)
MgO (wt.%)

Figure 4-19

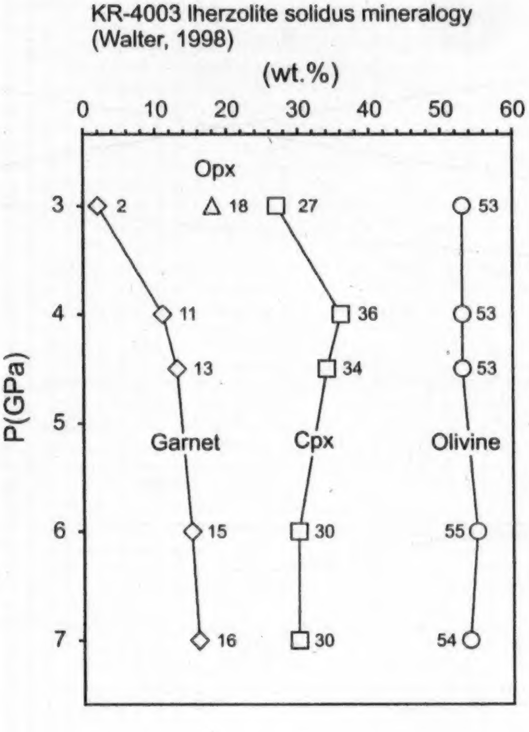
KR-4003 lherzolite solidus mineralogy
(Walter, 1998)
(wt.%)
0
10
20
30
40
50
60
P(GPa)
3
4
5
6
7
Opx
2
18
27
53
11
36
53
13
34
53
Garnet
Cpx
Olivine
15
30
55
16
30
54

Figure 4-20

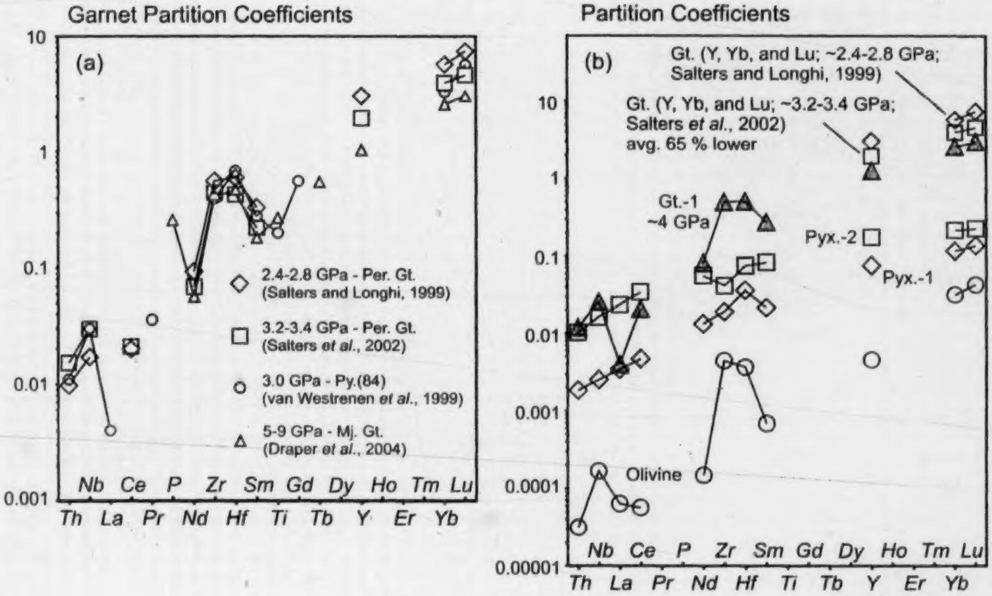
Garnet Partition Coefficients
(a)
10
1
0.1
0.01
0.001
2.4-2.8 GPa - Per. Gt.
(Salters and Longhi, 1999)
3.2-3.4 GPa - Per. Gt.
(Salters et al., 2002)
3.0 GPa - Py.(84)
(van Westrenen et al., 1999)
5-9 GPa - Mj. Gt.
(Draper et al., 2004)
Nb Ce P Zr Sm Gd Dy Ho Tm Lu
Th La Pr Nd Hf Ti Tb Y Er Yb
Partition Coefficients
(b)
Gt. (Y, Yb, and Lu; ~2.4-2.8 GPa;
Salters and Longhi, 1999)
Gt. (Y, Yb, and Lu; ~3.2-3.4 GPa;
Salters et al., 2002)
avg. 65 % lower
Gt.-1
~4 GPa
Pyx.-2
Pyx.-1
Olivine
10
1
0.1
0.01
0.001
0.0001
0.00001
Nb Ce P Zr Sm Gd Dy Ho Tm Lu
Th La Pr Nd Hf Ti Tb Y Er Yb

Figure 4-21

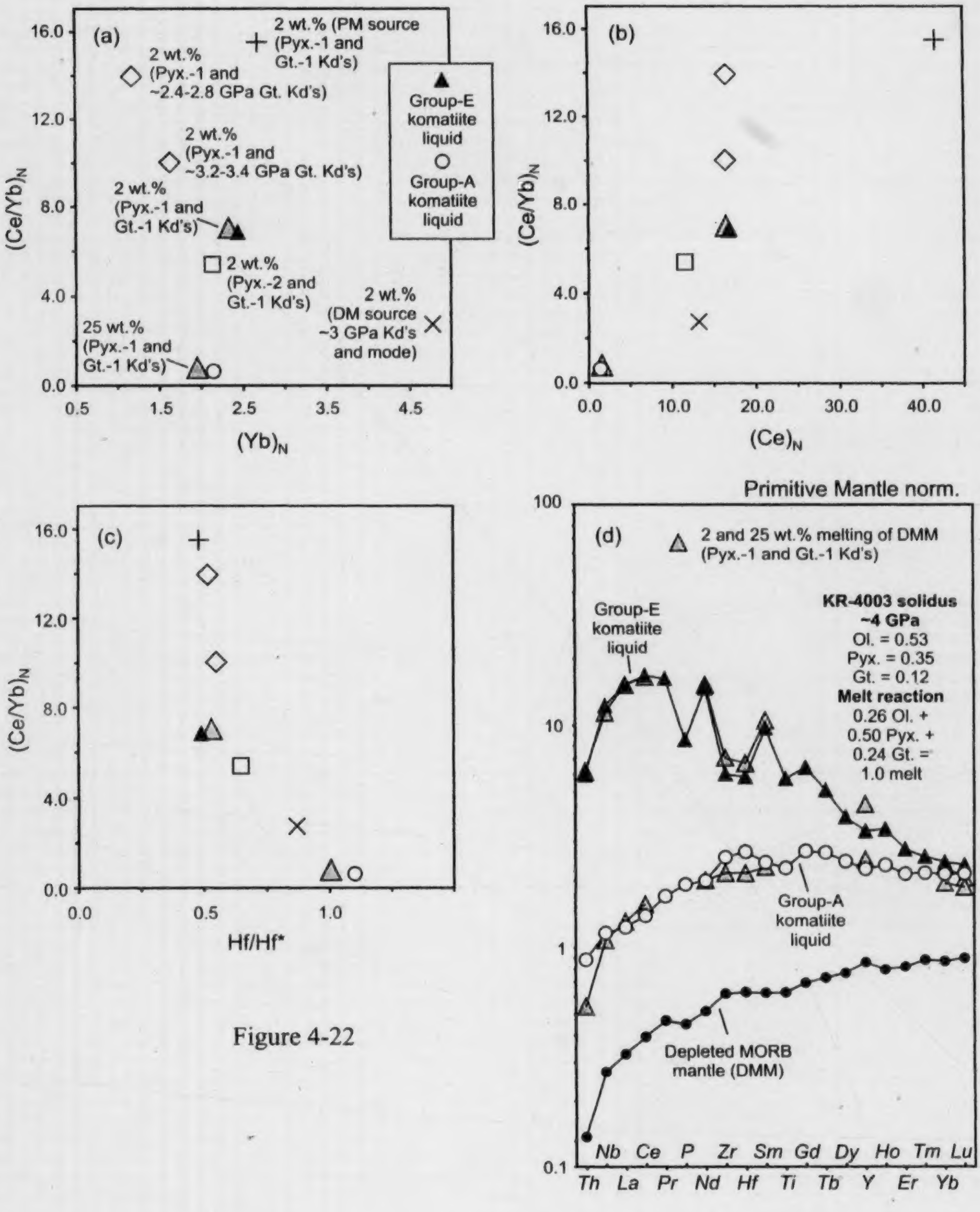
(a)
16.0
12.0
8.0
4.0
0.0
0.5
1.5
2.5
3.5
4.5
(Ce/Yb)$_N$
(Yb)$_N$
2 wt.% (PM source (Pyx.-1 and Gt.-1 Kd's)
2 wt.% (Pyx.-1 and ~2.4-2.8 GPa Gt. Kd's)
2 wt.% (Pyx.-1 and ~3.2-3.4 GPa Gt. Kd's)
2 wt.% (Pyx.-1 and Gt.-1 Kd's)
2 wt.% (Pyx.-2 and Gt.-1 Kd's)
2 wt.% (DM source ~3 GPa Kd's and mode)
25 wt.% (Pyx.-1 and Gt.-1 Kd's)
Group-E komatiite liquid
Group-A komatiite liquid
(b)
16.0
12.0
8.0
4.0
0.0
0.0
10.0
20.0
30.0
40.0
(Ce/Yb)$_N$
(Ce)$_N$
(c)
16.0
12.0
8.0
4.0
0.0
0.0
0.5
1.0
(Ce/Yb)$_N$
Hf/Hf*
Primitive Mantle norm.
(d)
2 and 25 wt.% melting of DMM (Pyx.-1 and Gt.-1 Kd's)
100
10
1
0.1
Group-E komatiite liquid
KR-4003 solidus ~4 GPa
Ol. = 0.53
Pyx. = 0.35
Gt. = 0.12
Melt reaction
0.26 Ol. + 0.50 Pyx. + 0.24 Gt. = 1.0 melt
Group-A komatiite liquid
Depleted MORB mantle (DMM)
Nb Ce P Zr Sm Gd Dy Ho Tm Lu
Th La Pr Nd Hf Ti Tb Y Er Yb

Figure 4-22

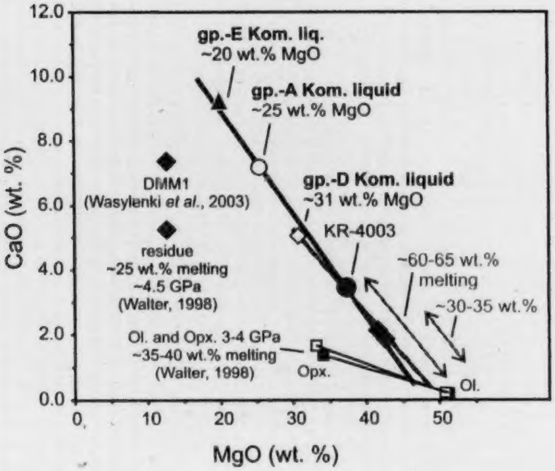
gp.-E Kom. liq.
~20 wt.% MgO
gp.-A Kom. liquid
~25 wt.% MgO
gp.-D Kom. liquid
~31 wt.% MgO
KR-4003
DMM1
(Wasylenki et al., 2003)
residue
~25 wt.% melting
~4.5 GPa
(Walter, 1998)
~60-65 wt.%
melting
~30-35 wt.%
Ol. and Opx. 3-4 GPa
~35-40 wt.% melting
(Walter, 1998)
Opx.
Ol.
CaO (wt. %)
MgO (wt. %)
12.0
10.0
8.0
6.0
4.0
2.0
0.0
0
10
20
30
40
50

Figure 4-23

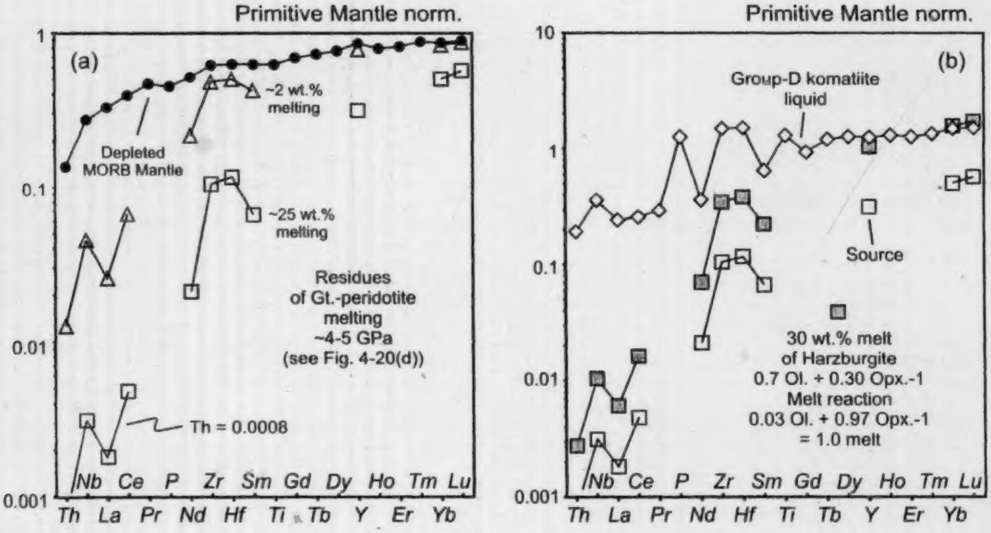
Primitive Mantle norm.
(a)
1
0.1
0.01
0.001
Depleted MORB Mantle
~2 wt.% melting
~25 wt.% melting
Residues of Gt.-peridotite melting ~4-5 GPa (see Fig. 4-20(d))
Th = 0.0008
Th La Pr Nd Hf Ti Tb Y Er Yb
Nb Ce P Zr Sm Gd Dy Ho Tm Lu
Primitive Mantle norm.
(b)
10
1
0.1
0.01
0.001
Group-D komatiite liquid
Source
30 wt.% melt of Harzburgite 0.7 Ol. + 0.30 Opx.-1 Melt reaction 0.03 Ol. + 0.97 Opx.-1 = 1.0 melt
Th La Pr Nd Hf Ti Tb Y Er Yb
Nb Ce P Zr Sm Gd Dy Ho Tm Lu

Figure 4-24

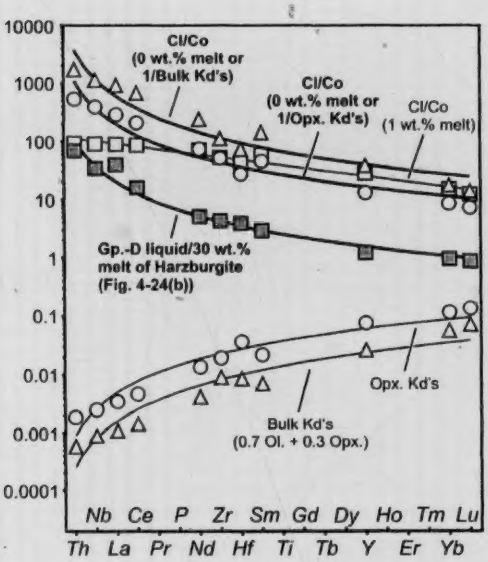
10000
1000
100
10
1
0.1
0.01
0.001
0.0001
Cl/Co
(0 wt.% melt or
1/Bulk Kd's)
Cl/Co
(0 wt.% melt or
1/Opx. Kd's)
Cl/Co
(1 wt.% melt)
Gp.-D liquid/30 wt.%
melt of Harzburgite
(Fig. 4-24(b))
Opx. Kd's
Bulk Kd's
(0.7 Ol. + 0.3 Opx.)
Nb Ce P Zr Sm Gd Dy Ho Tm Lu
Th La Pr Nd Hf Ti Tb Y Er Yb

Figure 4-25

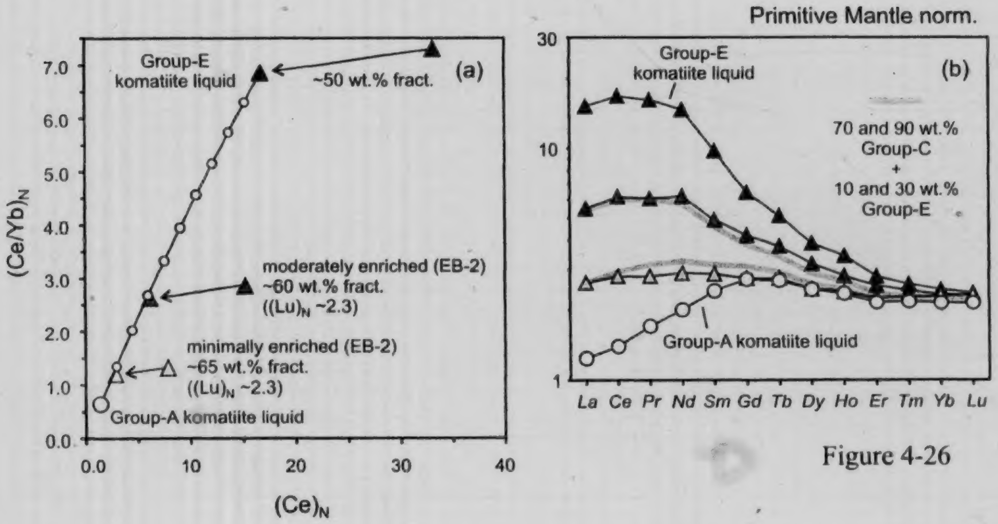
(a)
(Ce/Yb)N
(Ce)N
0.0
1.0
2.0
3.0
4.0
5.0
6.0
7.0
0.0
10
20
30
40
Group-E komatiite liquid
~50 wt.% fract.
moderately enriched (EB-2) ~60 wt.% fract. ((Lu)N ~2.3)
minimally enriched (EB-2) ~65 wt.% fract. ((Lu)N ~2.3)
Group-A komatiite liquid
(b)
Primitive Mantle norm.
1
10
30
Group-E komatiite liquid
70 and 90 wt.% Group-C + 10 and 30 wt.% Group-E
Group-A komatiite liquid
La Ce Pr Nd Sm Gd Tb Dy Ho Er Tm Yb Lu

Figure 4-26

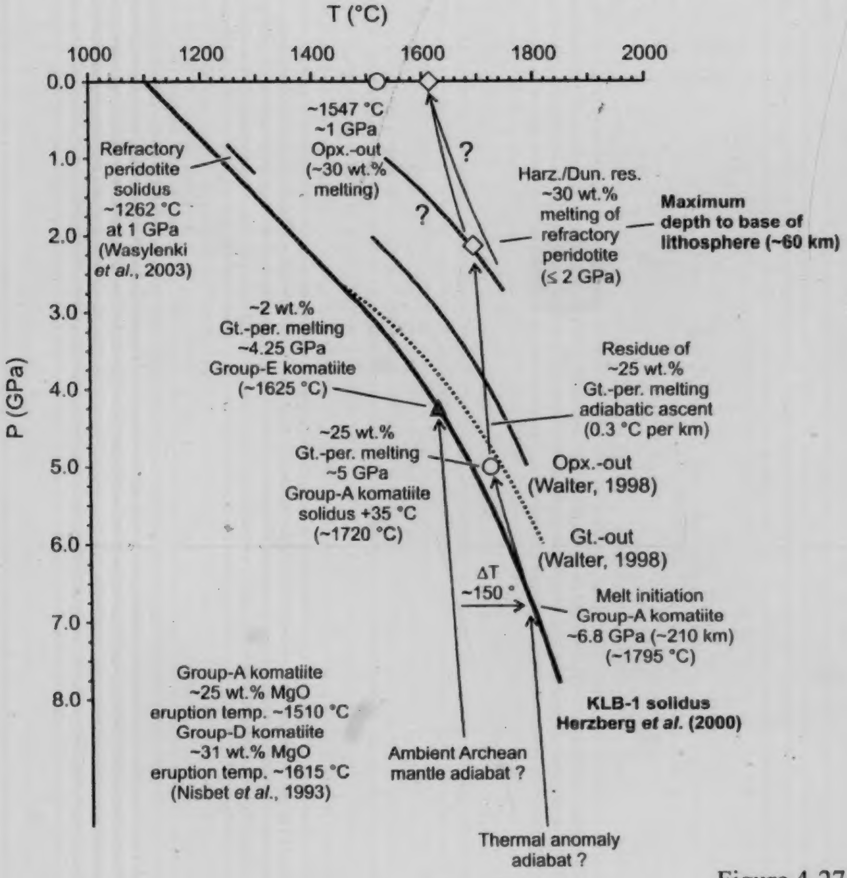
T (°C)
1000
1200
1400
1600
1800
2000
P (GPa)
0.0
1.0
2.0
3.0
4.0
5.0
6.0
7.0
8.0
Refractory peridotite solidus ~1262 °C at 1 GPa (Wasylenki et al., 2003)
~1547 °C ~1 GPa Opx.-out (~30 wt.% melting)
?
?
Harz./Dun. res. ~30 wt.% melting of refractory peridotite (≤ 2 GPa)
Maximum depth to base of lithosphere (~60 km)
~2 wt.% Gt.-per. melting ~4.25 GPa Group-E komatiite (~1625 °C)
Residue of ~25 wt.% Gt.-per. melting adiabatic ascent (0.3 °C per km)
~25 wt.% Gt.-per. melting ~5 GPa Group-A komatiite solidus +35 °C (~1720 °C)
Opx.-out (Walter, 1998)
Gt.-out (Walter, 1998)
ΔT ~150 °
Melt initiation Group-A komatiite ~6.8 GPa (~210 km) (~1795 °C)
KLB-1 solidus Herzberg et al. (2000)
Group-A komatiite ~25 wt.% MgO eruption temp. ~1510 °C Group-D komatiite ~31 wt.% MgO eruption temp. ~1615 °C (Nisbet et al., 1993)
Ambient Archean mantle adiabat ?
Thermal anomaly adiabat ?

Figure 4-27

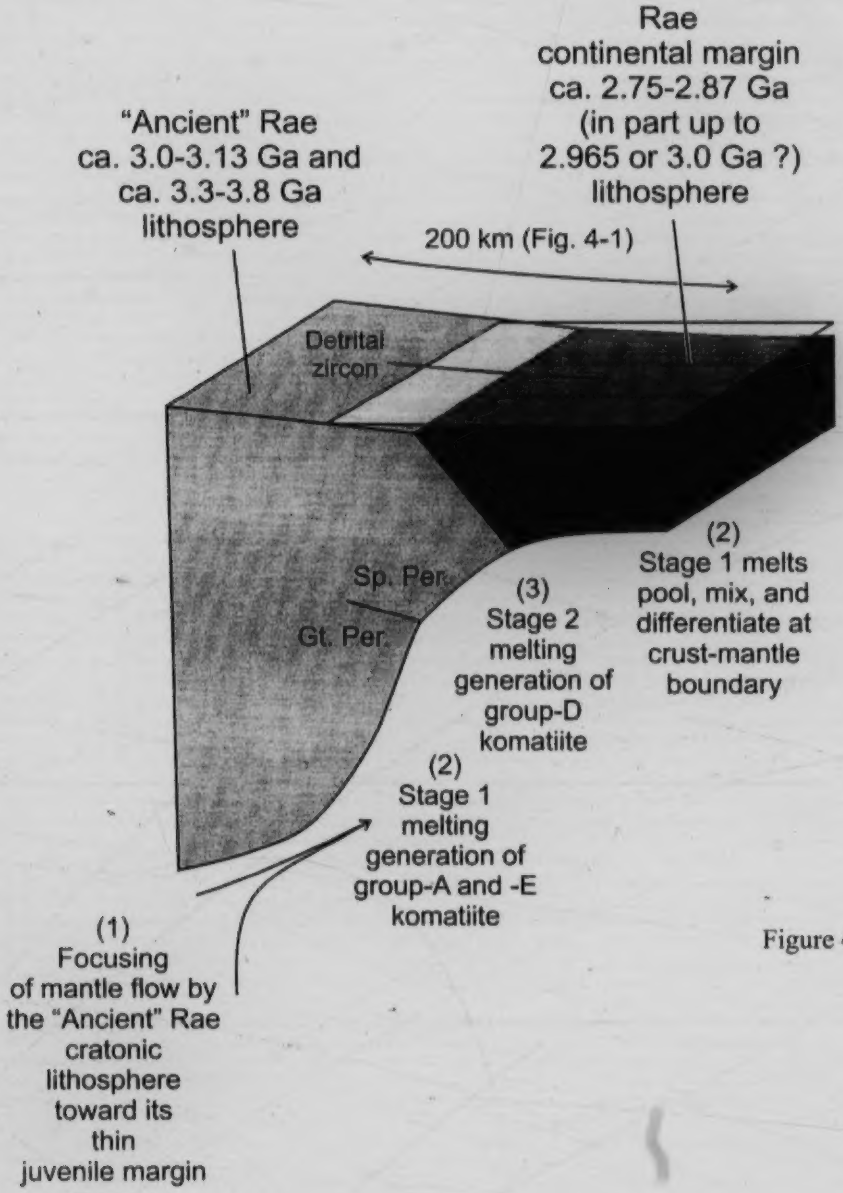
"Ancient" Rae
ca. 3.0-3.13 Ga and
ca. 3.3-3.8 Ga
lithosphere
Rae
continental margin
ca. 2.75-2.87 Ga
(in part up to
2.965 or 3.0 Ga ?)
lithosphere
200 km (Fig. 4-1)
Detrital
zircon
Sp. Per.
Gt. Per.
(2)
Stage 1 melts
pool, mix, and
differentiate at
crust-mantle
boundary
(3)
Stage 2
melting
generation of
group-D
komatiite
(2)
Stage 1
melting
generation of
group-A and -E
komatiite
(1)
Focusing
of mantle flow by
the "Ancient" Rae
cratonic
lithosphere
toward its
thin
juvenile margin

Figure 4-28

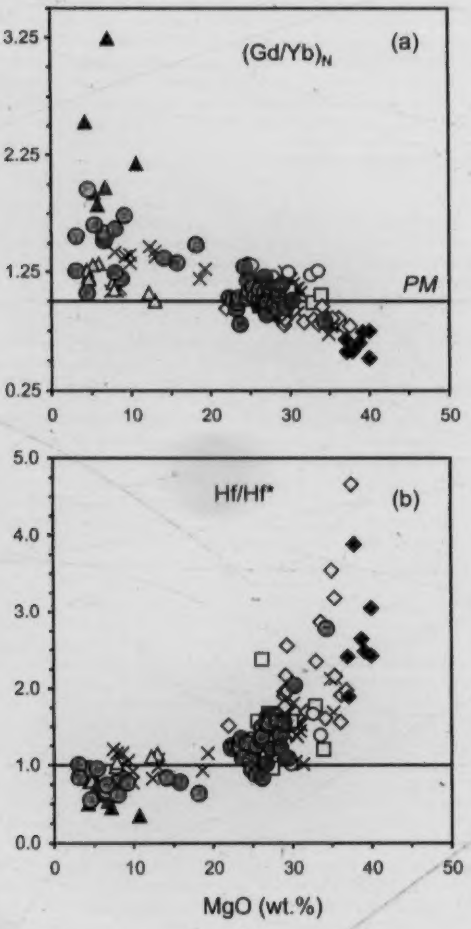
(Gd/Yb)$_N$
(a)
PM
3.25
2.25
1.25
0.25
0
10
20
30
40
50
Hf/Hf*
(b)
5.0
4.0
3.0
2.0
1.0
0.0
MgO (wt.%)

Figure 4-29

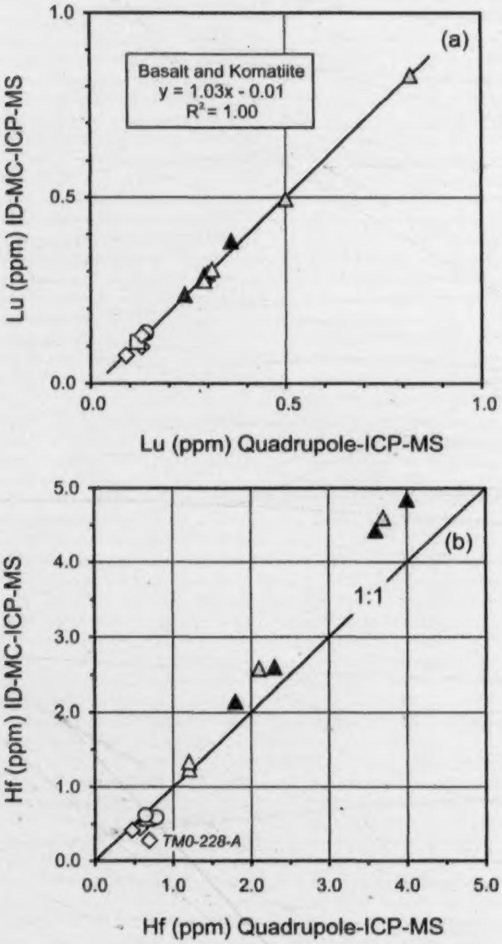
1.0
0.5
0.0
Lu (ppm) ID-MC-ICP-MS
(a)
Basalt and Komatiite
y = 1.03x - 0.01
R² = 1.00
0.0
0.5
1.0
Lu (ppm) Quadrupole-ICP-MS
5.0
4.0
3.0
2.0
1.0
0.0
Hf (ppm) ID-MC-ICP-MS
(b)
1:1
TM0-228-A
0.0
1.0
2.0
3.0
4.0
5.0
Hf (ppm) Quadrupole-ICP-MS

Figure 4-B-1

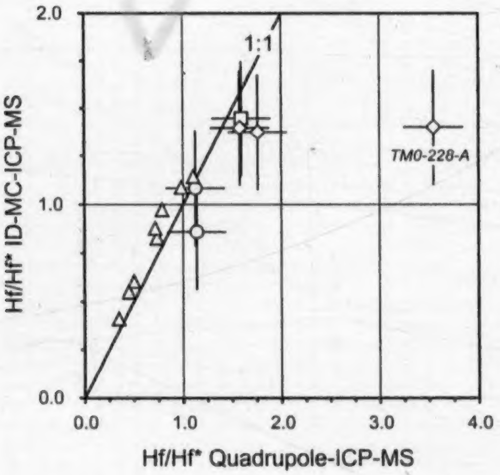
2.0
1.0
0.0
1:1
TM0-228-A
0.0
1.0
2.0
3.0
4.0
Hf/Hf* ID-MC-ICP-MS
Hf/Hf* Quadrupole-ICP-MS

Figure 4-B-2

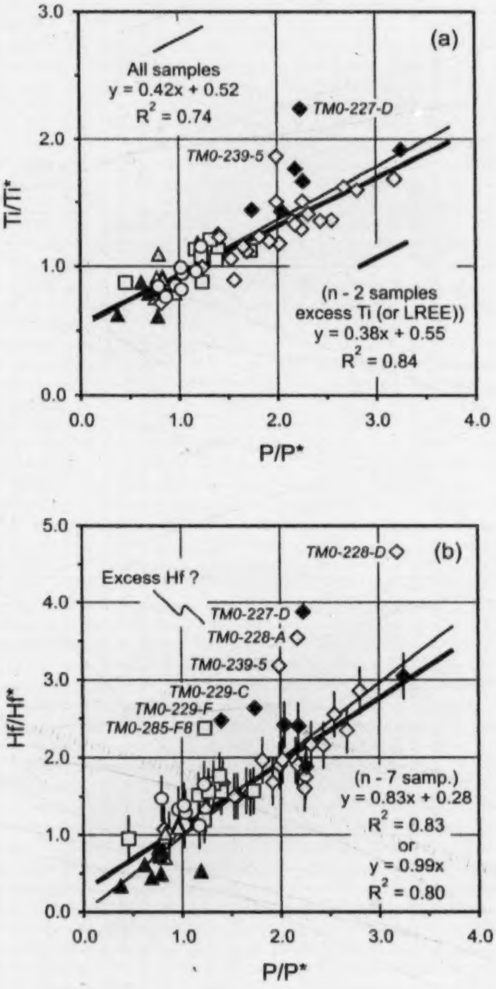

3.0
2.0
1.0
0.0
Ti/Ti*
(a)
All samples
y = 0.42x + 0.52
R^2 = 0.74
TM0-227-D
TM0-239-5
(n - 2 samples
excess Ti (or LREE))
y = 0.38x + 0.55
R^2 = 0.84
0.0
1.0
2.0
3.0
4.0
P/P*
5.0
4.0
3.0
2.0
1.0
0.0
Hf/Hf*
(b)
TM0-228-D
Excess Hf ?
TM0-227-D
TM0-228-A
TM0-239-5
TM0-229-C
TM0-229-F
TM0-285-F8
(n - 7 samp.)
y = 0.83x + 0.28
R^2 = 0.83
or
y = 0.99x
R^2 = 0.80
0.0
1.0
2.0
3.0
4.0
P/P*

Figure 4-B-3

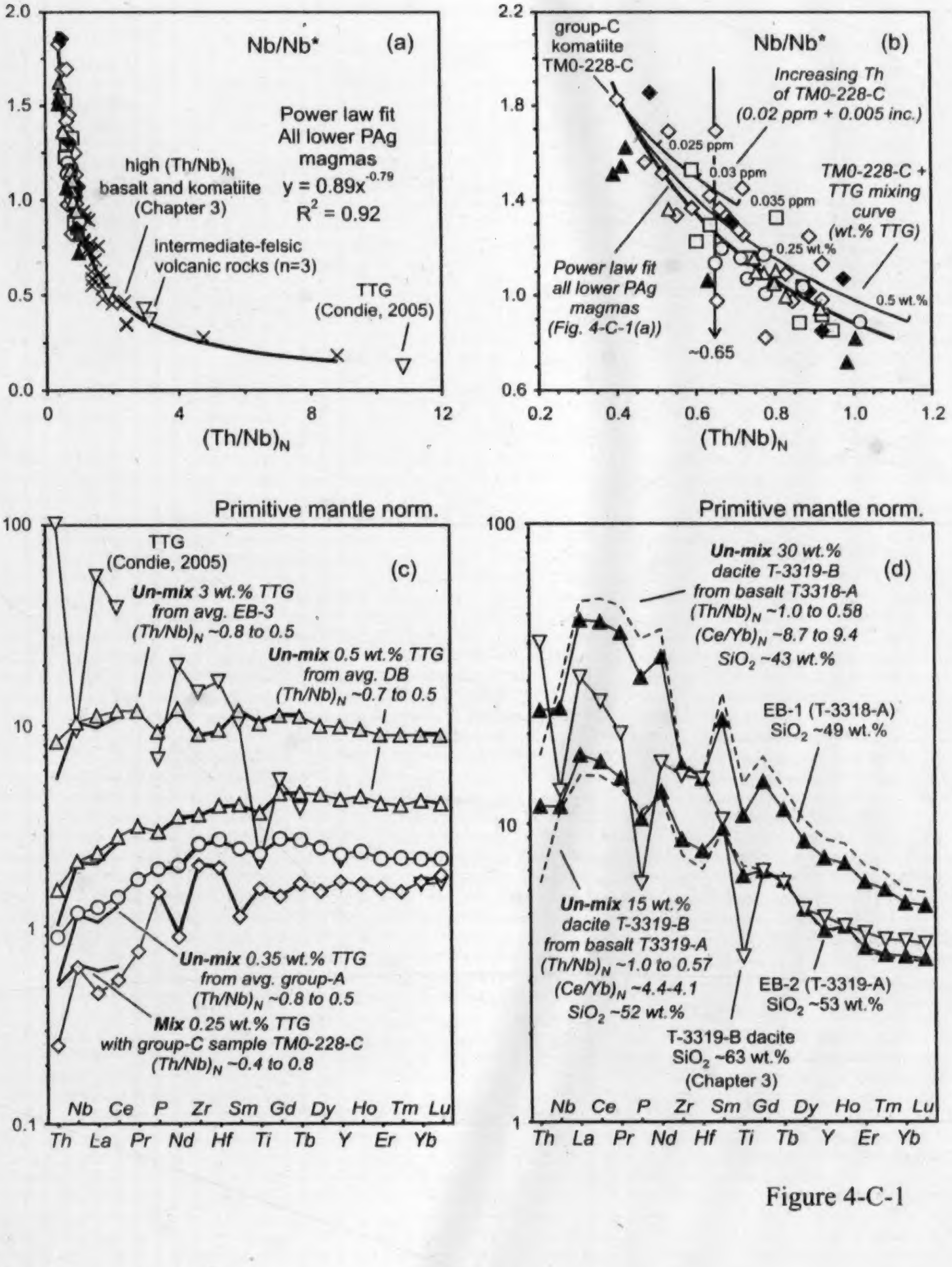

2.0
1.5
1.0
0.5
0.0
0
4
8
12
(Th/Nb)N
Nb/Nb*
(a)
Power law fit
All lower PAg
magmas
y = 0.89x-0.79
R2 = 0.92
high (Th/Nb)N
basalt and komatiite
(Chapter 3)
intermediate-felsic
volcanic rocks (n=3)
TTG
(Condie, 2005)
2.2
1.8
1.4
1.0
0.6
0.2
0.4
0.6
0.8
1.0
1.2
(Th/Nb)N
group-C
komatiite
TM0-228-C
Nb/Nb*
(b)
Increasing Th
of TM0-228-C
(0.02 ppm + 0.005 inc.)
0.025 ppm
0.03 ppm
0.035 ppm
TM0-228-C +
TTG mixing
curve
(wt.% TTG)
0.25 wt.%
0.5 wt.%
Power law fit
all lower PAg
magmas
(Fig. 4-C-1(a))
~0.65
Primitive mantle norm.
100
10
1
0.1
(c)
TTG
(Condie, 2005)
Un-mix 3 wt.% TTG
from avg. EB-3
(Th/Nb)N ~0.8 to 0.5
Un-mix 0.5 wt.% TTG
from avg. DB
(Th/Nb)N ~0.7 to 0.5
Un-mix 0.35 wt.% TTG
from avg. group-A
(Th/Nb)N ~0.8 to 0.5
Mix 0.25 wt.% TTG
with group-C sample TM0-228-C
(Th/Nb)N ~0.4 to 0.8
Nb Ce P Zr Sm Gd Dy Ho Tm Lu
Th La Pr Nd Hf Ti Tb Y Er Yb
Primitive mantle norm.
100
10
1
(d)
Un-mix 30 wt.%
dacite T-3319-B
from basalt T3318-A
(Th/Nb)N ~1.0 to 0.58
(Ce/Yb)N ~8.7 to 9.4
SiO2 ~43 wt.%
EB-1 (T-3318-A)
SiO2 ~49 wt.%
Un-mix 15 wt.%
dacite T-3319-B
from basalt T3319-A
(Th/Nb)N ~1.0 to 0.57
(Ce/Yb)N ~4.4-4.1
SiO2 ~52 wt.%
EB-2 (T-3319-A)
SiO2 ~53 wt.%
T-3319-B dacite
SiO2 ~63 wt.%
(Chapter 3)
Nb Ce P Zr Sm Gd Dy Ho Tm Lu
Th La Pr Nd Hf Ti Tb Y Er Yb

Figure 4-C-1

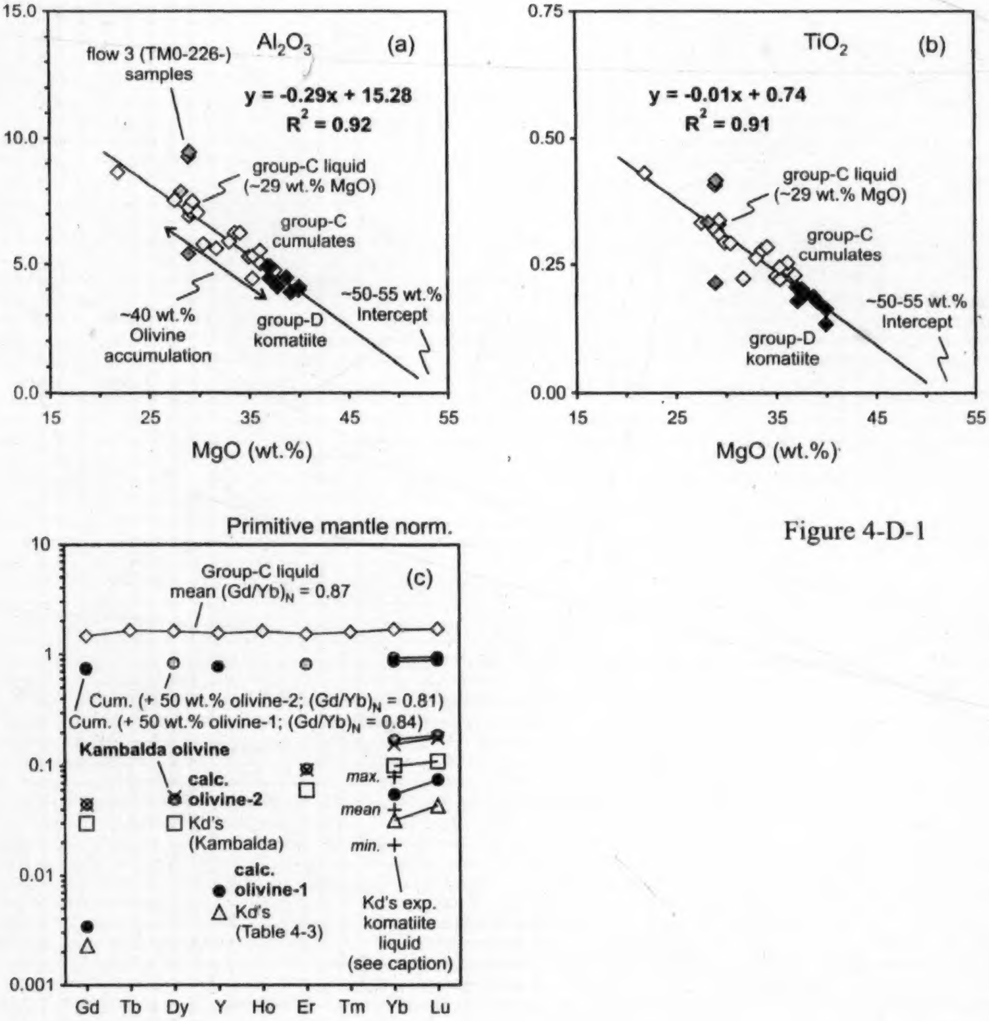
Al2O3
(a)
flow 3 (TM0-226-) samples
y = -0.29x + 15.28
R² = 0.92
group-C liquid (~29 wt.% MgO)
group-C cumulates
~40 wt.% Olivine accumulation
group-D komatiite
~50-55 wt.% Intercept
15.0
10.0
5.0
0.0
15
25
35
45
55
MgO (wt.%)
TiO2
(b)
y = -0.01x + 0.74
R² = 0.91
group-C liquid (~29 wt.% MgO)
group-C cumulates
~50-55 wt.% Intercept
group-D komatiite
0.75
0.50
0.25
0.00
15
25
35
45
55
MgO (wt.%)
Primitive mantle norm.
(c)
Group-C liquid mean (Gd/Yb)N = 0.87
Cum. (+ 50 wt.% olivine-2; (Gd/Yb)N = 0.81)
Cum. (+ 50 wt.% olivine-1; (Gd/Yb)N = 0.84)
Kambalda olivine
calc. olivine-2
Kd's (Kambalda)
calc. olivine-1
Kd's (Table 4-3)
max.
mean
min.
Kd's exp. komatiite liquid (see caption)
10
1
0.1
0.01
0.001
Gd
Tb
Dy
Y
Ho
Er
Tm
Yb
Lu

Figure 4-D-1

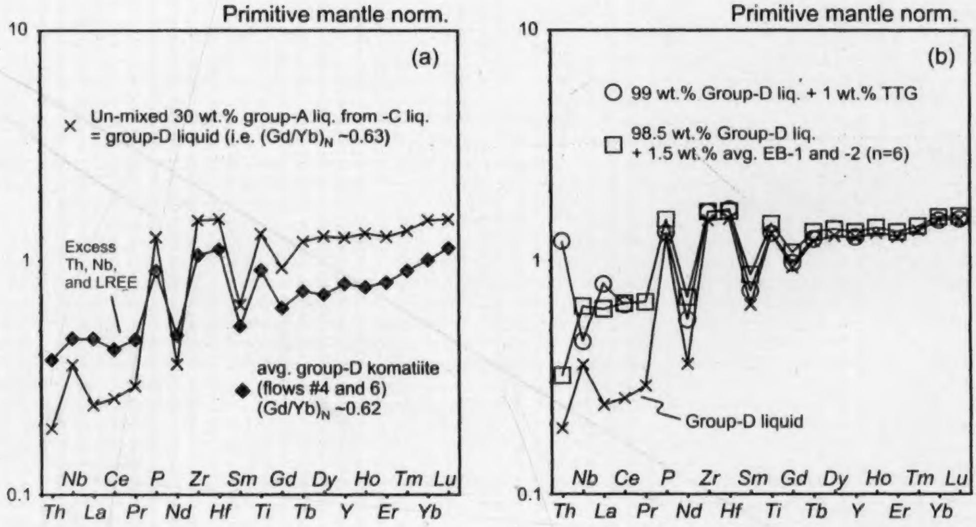
Primitive mantle norm.
(a)
10
1
0.1
× Un-mixed 30 wt.% group-A liq. from -C liq. = group-D liquid (i.e. $(Gd/Yb)_N$ ~0.63)
Excess Th, Nb, and LREE
◆ avg. group-D komatiite (flows #4 and 6) $(Gd/Yb)_N$ ~0.62
Th Nb La Ce Pr P Nd Zr Hf Sm Ti Gd Tb Dy Y Ho Er Tm Yb Lu
Primitive mantle norm.
(b)
10
1
0.1
○ 99 wt.% Group-D liq. + 1 wt.% TTG
□ 98.5 wt.% Group-D liq. + 1.5 wt.% avg. EB-1 and -2 (n=6)
Group-D liquid
Th Nb La Ce Pr P Nd Zr Hf Sm Ti Gd Tb Dy Y Ho Er Tm Yb Lu

Figure 4-D-2

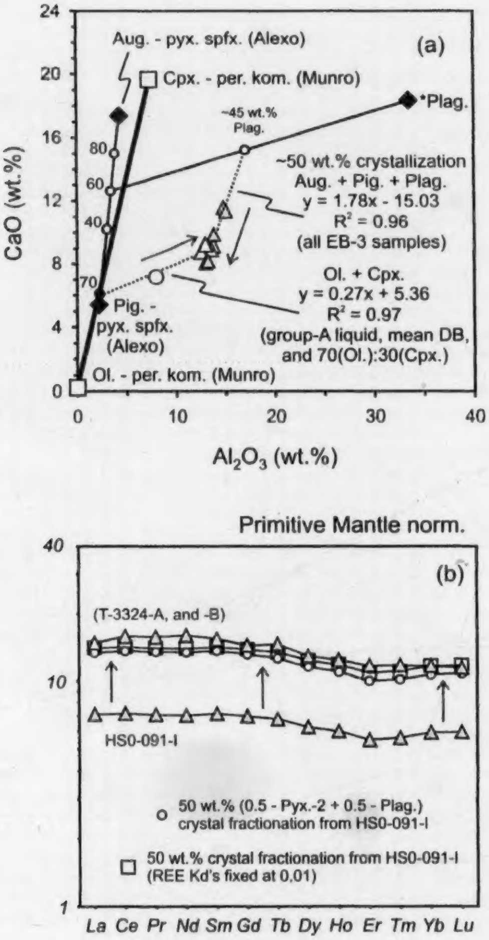
(a)
Aug. - pyx. spfx. (Alexo)
Cpx. - per. kom. (Munro)
~45 wt.% Plag.
*Plag.
~50 wt.% crystallization
Aug. + Pig. + Plag.
y = 1.78x - 15.03
R² = 0.96
(all EB-3 samples)
Ol. + Cpx.
y = 0.27x + 5.36
R² = 0.97
(group-A liquid, mean DB, and 70(Ol.):30(Cpx.)
80
60
40
70
Pig. - pyx. spfx. (Alexo)
Ol. - per. kom. (Munro)
CaO (wt.%)
Al2O3 (wt.%)
0
4
8
12
16
20
24
0
10
20
30
40
Primitive Mantle norm.
(b)
(T-3324-A, and -B)
HS0-091-I
50 wt.% (0.5 - Pyx.-2 + 0.5 - Plag.) crystal fractionation from HS0-091-I
50 wt.% crystal fractionation from HS0-091-I (REE Kd's fixed at 0.01)
40
10
1
La
Ce
Pr
Nd
Sm
Gd
Tb
Dy
Ho
Er
Tm
Yb
Lu

Figure 4-E-1

REFERENCES

Anderson, D. L. (1982). Hotspots, polar wander Mesozoic convection and the geoid. *Nature* **297**, 391-393.

Anderson, D. L. (1994). Superplumes or supercontinents? *Geology* **22**, 39-42.

Anderson, D. L. (1998). The scales of mantle convection. *Tectonophysics* **284**, 1-17.

Arndt, N. T. (1994). Archean Komatiites. In: Condie, K.C. (ed.) *Archean Crustal Evolution*. Amsterdam: Elsevier, pp. 11-44.

Arndt, N. T. (1999). Why was flood volcanism on submerged continental platforms so common in the Precambrian? *Precambrian Research* **97**, 155-164.

Arndt, N. T., Albarède, F. & Nisbet, E. G. (1997). Mafic and Ultramafic Magmatism. In: de Wit, M. J. & Ashwal, L. D. (eds) *Greenstone Belts*. Oxford: Oxford University Press, pp. 233-254.

Arndt, N. T. & Fleet, M. (1979). Stable and metastable pyroxene crystallization in layered komatiite lava flows. *American Mineralogist* **64**, 856-864.

Arndt, N. T. & Lesher, C. M. (1992). Fractionation of REEs by olivine and the origin of Kambalda komatiites, Western Australia. *Geochimica et Cosmochimica Acta* **56**, 4191-4204.

Arndt, N. T., Naldrett, A. J. & Pyke, D. R. (1977). Komatiitic and Iron-rich Tholeiitic Lavas of Munro Township, Northeast Ontario. *Journal of Petrology* **18**, 319-369.

Arth, J. G. (1976). Behavior of trace-elements during magmatic processes - summary of theoretical models and their applications. *Journal of Research of the US Geological Survey* **4**, 41-47.

Asimow, P. D., Hirschmann, M. M. & Stolper, E. M. (2001). Calculation of peridotite partial melting from thermodynamic models of minerals and melts, IV. Adiabatic decompression and the composition and mean properties of mid-ocean ridge basalts. *Journal of Petrology* **42**, 963-998.

Ayer, J., Amelin, Y., Corfu, F., Kamo, S., Ketchum, J., Kwok, K., Trowell, N. (2002). Evolution of the southern Abitibi greenstone belt based on U-Pb geochronology: autochthonous volcanic construction followed by plutonism, regional deformation and sedimentation. *Precambrian Research* **115**, 63-95.

Berman, R. G., Sanborn-Barrie, M., Stern, R. A. & Carson, C. J. (2005). Tectonometamorphism at *ca.* 2.35 and 1.85 Ga in the Rae Domain, western Churchill

Province, Nunavut, Canada: insights from structural, metamorphic and *in situ* geochronological analysis of the southwestern Committee Bay Belt. *Canadian Mineralogist* **43**, 409-442.

Bethune, K. M. & Scammell, R. J. (2003). Geology, geochronology, and geochemistry of Archean rocks in the Eqe Bay area, north-central Baffin Island, Canada: constraints on the depositional and tectonic history of the Mary River Group of northeastern Rae Province. *Canadian Journal of Earth Sciences* **40**, 1137-1167.

Bizzarro, M. Baker, J. A. & Ulfbeck, D. (2003). A new digestion and chemical separation technique for rapid and highly reproducible determination of Lu/Hf and Hf isotope ratios in geological materials by MC-ICP-MS. *Geostandards Newsletter* **27**, 133-145.

Blake, T. S. (1993). Late Archaean crustal extension, sedimentary basin formation, flood basalt volcanism and continental rifting: the Nullagine and Mount Jope Supersequences Western Australia. *Precambrian Research* **60**, 185-241.

Blenkinsop, T. G., Fedo, C. M., Bickle, M. J., Eriksson, K. A., Martin, A., Nisbet, E. G. & Wilson, J. F. (1993). Ensialic origin for the Ngezi Group, Belingwe greenstone belt, Zimbabwe. *Geology* **21**, 1135-1138.

Blichert-Toft, J. & Albarède, F. (1997). The Lu-Hf isotope geochemistry of chondrites and the evolution of the mantle-crust system. *Earth and Planetary Science Letters* **148**, 243-258.

Blichert-Toft, J. & Arndt, N. T. (1999). Hf isotopic compositions of komatiites. *Earth and Planetary Science Letters* **171**, 439-451.

Blichert-Toft, J., Arndt, N. T. & Gruau, G. (2004). Hf isotopic measurements on Barberton komatiites: effects of incomplete sample dissolution and importance for primary and secondary magmatic signatures. *Chemical Geology* **207**, 261-275.

Blundy, J. D., Robinson, J. A. C. & Wood, B. J. (1998). Heavy REE are compatible in clinopyroxene on the spinel lherzolite solidus. *Earth and Planetary Science Letters* **160**, 493-504.

Bolhar, R., Woodhead, J. D. & Hergt, J. M. (2003). Continental setting inferred for emplacement of the 2.9-2.7 Ga Belingwe Greenstone Belt, Zimbabwe. *Geology* **31**, 295-298.

Campbell, I. H. & Griffiths, R. W. (1993). The evolution of the mantle's chemical structure. *Lithos* **30**, 389-399.

Campbell, I. H., Griffiths, R. W. & Hill, R. I. (1989). Melting in an Archaean mantle plume: heads it's basalts, tails it's komatiites. *Nature* **339**, 697-699.

Canil, D. & Fedortchouk, Y. (2001). Olivine-liquid partitioning of vanadium and other trace elements, with applications to modern and ancient picrites. *The Canadian Mineralogist* **39**, 319-330.

Carson, C. J., Berman, R. G., Stern, R. A., Sanborn-Barrie, M., Skulski, T. & Sandeman, H. A. I. (2004). Age constraints on the Paleoproterozoic tectonometamorphic history of the Committee bay region, western Churchill Province, Canada: evidence from zircon and in situ monazite SHRIMP geochronology. *Canadian Journal of Earth Sciences* **41**, 1049-1076.

Compston, W., Williams, I. S., Campbell, I. H. & Gresham, J. J. (1986). Zircon xenocrysts from the Kambalda volcanics, age constraints and direct evidence for older continental crust below the Kambalda-Norseman greenstones. *Earth and Planetary Science Letters* **76**, 299-311.

Condie, K. C. (2001). *Mantle plumes and Their Record in Earth History*. Oxford, UK: Cabridge Univ. Press., 306 pp.

Condie, K. C. (2005). TTGs and adakites: are they both slab melts? *Lithos* **80**, 33-44.

Corfu, F. & Noble, S. R. (1992). Genesis of the southern Abitibi greenstone belt, Superior Province, Canada; evidence from zircon Hf isotope analyses using a single filament technique. *Geochimica et Cosmochimica Acta* **56**, 2081-2097.

Corfu, F. & Stott, G. M. (1993). Age and petrogenesis of two late Archean magmatic suites, northwestern Superior Province, Canada; zircon U-Pb and Lu-Hf isotopic relations. *Journal of Petrology* **34**, 817-838.

Corfu, F. & Stott, G. M. (1996). Hf isotopic composition and age constraints on the evolution of the Archean central Uchi Subprovince, Ontario, Canada. *Precambrian Research* **78**, 53-63.

Cousens, B. L. (2000). Geochemistry of the Archean Kam Group, Yellowknife Greenstone Belt, Slave Province, Canada. *Journal of Geology* **108**, 181-197.

Creaser, R. A., Erdmer, P., Stevens, R. A. & Grant, S. L. (1997). Tectonic affinity of Nisutlin and Anvil assemblage strata from Teslin tectonic zone, northern Canadian Cordillera: Constraints from neodymium isotope and geochemical evidence. *Tectonics* **16**, 107-121.

Draper, D. S., Xirouchakis, D. & Agee, C. B. (2003). Trace element partitioning between garnet and chondritic melt from 5 to 9 GPa: implications for the onset of the majorite transition in the martian mantle. *Physics of the Earth and Planetary Interiors* **139**, 149-169.

Dupré, B., Chauvel, C. & Arndt, N. T. (1984). Pb and Nd isotopic study of two Archean komatiitic flows from Alexo, Ontario. *Geochimica et Cosmochimica Acta* **48**, 1965-1972.

Gurnis, M. (1988). Large-scale mantle convection and the aggregation and dispersal of supercontinents. *Nature* **322**, 695-699.

Henderson, J. B. & Thériault, R. J. (1994). U-Pb zircon evidence for circa 3.1 Ga crust south of the McDonald Fault, northwestern Canadian Shield, Northwest Territories. In: Radiogenic age and isotopic studies: Report 8. Geological Survey of Canada, Current Research 1994-F, pp. 43-47.

Herzberg, C. (1995). Generation of plume magmas through time: an experimental perspective. *Chemical Geology* **126**, 1-16.

Herzberg, C., Raterron, P. & Zhang, J. (2000). New experimental observations on the anhydrous solidus for peridotite KLB-1. *Geochemistry Geophysics Geosystems* **1**, 2000GC000089.

Herzberg, C. & Zhang, J. (1996). Melting experiments on anhydrous peridotite KLB-1: Compositions of magmas in the upper mantle and transition zone. *Journal of Geophysical Research* **101**, 8271-8295.

Hll, R. E. T, Barnes, S. J., Gole, M. J. & Dowling, S. E. (1995). The volcanology of komatiites as deduced from field relationships in the Norseman-Wiluna greenstone belt, Western Australia. *Lithos* **34**, 159-188.

Hunter, M. A., Bickle, M. J., Nisbet, E. G., Martin, A. & Chapman, H. J. (1998). Continental extensional setting for the Archean Belingwe Greenstone Belt, Zimbabwe. *Geology* **26**, 883-886.

Jackson, G. D., Hunt, P. A., Loveridge, W. D. & Parrish, R. R. (1990). Reconnaissance geochronology of Baffin Island, N.W.T. In: Radiogenic age and isotopic studies: Report 3. Geological Survey of Canada, Paper 89-2, pp. 123-148.

Jackson, G. D. & Taylor, F. C. (1972). Correlation of major Aphebian rock units in the Canadian Shield. *Canadian Journal of Earth Sciences* **9**, 1650-1699.

Kerr, A. C., White, R. V. & Saunders, A. D. (2000). LIP Reading: Recognizing Oceanic Plateaux in the Geological Record. *Journal of Petrology* **41**, 1041-1056.

Kinzler, R. J. & Grove, T. L. (1985). Crystallization and differentiation of Archean komatiite lavas from northeast Ontario: phase equilibrium and kinetic studies. *American Mineralogist* **70**, 40-51.

Kinzler, R. J. & Grove, T. L. (1992). Primary Magmas of Mid-Ocean Ridge Basalts 2. Applications. *Journal of Geophysical Research* **97**, 6907-6926.

Lesher, C. M. & Arndt, N. T. (1995). REE and Nd isotope geochemistry, petrogenesis and volcanic evolution of contaminated komatiites at Kambalda, Western Australia. *Lithos* **34**, 127-157.

Ludwig, K. R. (1992). ISOPLOT – a plotting and regression program for radiogenic isotope data, version 2.57. U.S. Geological Survey Open File report 91, p. 445.

Machado, N., Brooks, C. & Hart, S. R. (1986). Determination of initial $^{87}Sr/^{86}Sr$ and 143Nd/144Nd in primary minerals from mafic and ultramafic rocks: Experimental procedure and implications for the isotopic characteristics of the Archean mantle under the Abitibi greenstone belt, Canada. *Geochimica et Cosmochimica Acta* **50**, 2335-2348.

McDade, P., Blundy, J. D. & Wood, B. J. (2003). Trace element partitioning on the Tinaquillo Lherzolite solidus at 1.5 GPa. *Physics of the Earth and Planetary Interiors* **139**, 129-147.

McDonough, W. F. & Sun, S.-s. (1995). The Composition of the Earth. *Chemical Geology* **120**, 223-253.

McKenzie, D. & Bickle, M. J. (1988). The volume and composition of melt generated by extension of the lithosphere. *Journal of Petrology* **29**, 625-679.

Navon, O. & Stolper, E. (1987). Geochemical consequences of melt percolation: The upper mantle as a chromatographic column. *The Journal of Geology* **95**, 285-307.

Nelson, D. R., Trendall, A. F., de Laeter, J. R., Grobler, N. J. & Fletcher, I. R. (1992). A comparative study of the geochemical and isotopic systematics of late Archaean flood basalts from the Pilbara and Kaapvaal Cratons. *Precambrian Research* **54**, 231-256.

Nesbitt, R. W., Sun, S-s. & Purvis, A. C. (1979). Komatiites: Geochemistry and genesis. *Canadian Mineralogist* **17**, 165-186.

Nisbet, E. G., Cheadle, M. J., Arndt, N. T. & Bickle, M. J. (1993). Constraining the potentential temperature of the Archean mantle: A review of the evidence from komatiites. *Lithos* **30**, 291-307.

Perring, C. S., Barnes, S. J. & Hill, R. E. T. (1995). The physical volcanology of Archaean komatiite sequences from Forrestania, Southern Cross Province, Western Australia. *Lithos*. **34**, 189-207.

Polat, A. & Münker, C. (2004). Hf-Nd isotope evidence for contemporaneous subduction processes in the source of late Archean arc lavas from the Superior Province. *Chemical Geology* **213**, 403-429.

Pollack, H. N. (1997). Thermal Characteristics of the Archaean. In: de Wit, M. J. & Ashwal, L. D. (eds) *Greenstone Belts*. Oxford: Oxford University Press, pp. 223-232.

Presnall, D. C., Gudfinnsson, G. H. & Walter, M. J. (2002). Generation of mid-ocean ridge basalts at pressures from 1 to 7 GPa. *Geochimica et Cosmochimica Acta* **66**, 2073-2090.

Puchtel, I. S., Hofmann, A. W., Mezger, K., Jochum, K. P., Shchipansky, A. A. & Samsonov, A. V. (1998). Oceanic plateau model for continental crustal growth in the Archaean: A case study from the Komstomuksha greenstone belt, NW Baltic Shield. *Earth and Planetary Science Letters* **155**, 57-74.

Salters, V. J. M. & Longhi, J. (1999). Trace element partitioning during the initial stages of melting beneath mid-ocean ridges. *Earth and Planetary Science Letters* **166**, 15-30.

Salters, V. J. M. & Stracke, A. (2004). Composition of the depleted mantle. *Geochemistry Geophysics Geosystems* **5**, 2003GC000597.

Salters, V. J. M., Longhi, J. E. & Bizimis, M. (2002). Near mantle solidus trace element partitioning at pressures up to 3.4 GPa. *Geochemistry Geophysics Geosystems* **3**, 2001GC000148.

Sanborn-Barrie, M., Sandeman, H., Skulski, T., Brown, J., Young, M., MacHattie, T., Deyell, C., Carson, C., Panagapko, D. & Byrne, D. (2003). Structural geology of the northeastern Committee Bay belt, Ellce Hills area, central Nunavut. In: Current Research. Geological Survey of Canada, Paper 2003-C23.

Sanborn-Barrie, M., Skulski, T., Sandeman, H., Berman, R., Johnstone, S., MacHattie, T. & Hyde, D. (2002). Structural and metamorphic geology of the Walker Lake-Arrowsmith River area, Committee Bay belt, Nunavut. In: Current Research. Geological Survey of Canada, Paper 2002-C12.

Sandeman, H. A., Brown, J., Studnicki-Gizbert, C., MacHattie, T., Hyde, D., Johnstone, S., Greiner, E. & Plaza, D. (2001). Bedrock mapping in the Committee Bay Belt, Laughland Lake area, central mainland, Nunavut. In: Current Research. Geological Survey of Canada, Paper 2001-C12.

Sandeman, H. A., Skulski, T. & Sanborn-Barrie, M. (2004). Geology, Ellice Hills, Nunavut. Geological Survey of Canada, Open File Map1794, scale 1:100 000.

Scherer, E., Münker, C. & Mezger, K. (2001). Calibration of the Lutetium-Hafnium Clock. *Science* **293**, 683-687.

Schmidberger, S. S., Simonetti, A., Francis, D. & Gariepy, C. (2002). Probing Archean lithosphere using the Lu-Hf isotope systematics of peridotite xenoliths from Somerset Island kimberlites, Canada. *Earth and Planetary Science Letters* **197**, 245-259.

Shimizu, K., Nakamura, E., Kobayashi, K. & Maruyama, S. (2004). Discovery of Archean continental and mantle fragments inferred from xenocrysts in komatiites, the Belingwe greenstone belt, Zimbabwe. *Geology* **32**, 285-288.

Shimizu, K., Nakamura, E. & Maruyama, S. (2005). The Geochemistry of Ultramafic and Mafic Volcanics from the Belingwe Greenstone Belt, Zimbabwe: Magmatism in an Archean Continental Large Igneous Province. *Journal of Petrology* **46**, 2367-2394.

Skulski, T., Sanborn-Barrie, M. & Sandeman, H. (2003*a*). Geology, Walker Lake and Arrowsmith River Area, Nunavut. Geological Survey of Canada, Open File Map 3777, scale 1:100 000.

Skulski, T., Sandeman, H., MacHattie, T., Sanborn-Barrie, M., Rayner, N., & Byrne, D. (2003*b*). Tectonic setting of 2.73-2.7 Ga Prince Albert Group, Churchill Province, Nunavut. In: Program with Abstracts, Geological Association of Canada-Mineralogical Association of Canada annual meeting, Vancouver, B.C.

Skulski, T., Sandeman, H., Sanborn-Barrie, M., MacHattie, T., Hyde, D., Johnstone, S., Panagapko, D. & Byrne, D. (2002). Contrasting crustal domains in the Committee Bay belt, Walker Lake-Arrowsmith River area, central Nunavut. In: Current Research. Geological Survey of Canada, Paper 2002-C11.

Skulski, T., Sandeman, H., Sanborn-Barrie, M., MacHattie, T., Young, M., Carson, C., Berman, R., Brown, J., Rayner, N., Panagapko, D., Byrne, D. & Deyell, C. (2003*c*). Bedrock geology of the Ellice Hills map area and new constraints on the regional geology of the Committee Bay area, Nunavut. In: Current Research. Geological Survey of Canada, Paper 2003-C22.

Söderlund, U., Patchett, P. J., Vervoort, J. D. & Isachsen, C. E. (2004). The ^{176}Lu decay constant determined by Lu-Hf and U-Pb isotope systematics of Precambrian mafic intrusions. *Earth and Planetary Science Letters* **219**, 311-324.

Sproule, R. A., Lesher, C. M., Ayer, J. A., Thurston, P. C., Herzberg, C. T. (2002). Spatial and temporal variations in the geochemistry of komatiites and komatiitic basalts in the Abitibi greenstone belt. *Precambrian Research* **115**, 153-186.

Storey, M., Mahoney, J. J., Kroenke, L. W. & Saunders, A. D. (1991). Are oceanic plateaus sites of komatiite formation? *Geology* **19**, 376-379.

Takahashi, E. (1986). Melting of a Dry Peridotite KLB-1 up to 14 GPa: Implications on the Origin of Peridotitic Upper Mantle. *Journal of Geophysical Research* **91**, 9367-9382.

Takahashi, E. & Scarfe, C. M. (1985). Melting of Peridotite to 14 GPa and the genesis of komatiite. *Nature* **315**, 566-568.

Thériault, R. J., Henderson, J. B. & Roscoe, S. M. (1994). Nd isotopic evidence for early to mid-Archean crust from high grade gneisses in the Queen Maud Block and south of the McDonald Fault, western Churchill Province, Northwest Territories. In: Radiogenic age and isotopic studies: Report 8. Geological Survey of Canada, Current Research 1994-F, pp. 37-42.

Tomlinson, K. Y., Hughes, D. J., Thurston, P. C. & Hall, R. P. (1999). Plume magmatism and crustal growth at 2.9 to 3.0 Ga in the Steep Rock and Lumby Lake area, Western Superior Province. *Lithos* **46**, 103-136.

van Westrenen, W., Blundy, J. & Wood, B. (1999). Crystal-chemical controls on trace element partitioning between garnet and anhydrous silicate melt. *American Mineralogist* **84**, 838-847.

Vervoort, J. D. & Blichert-Toft, J. (1999). Evolution of the depleted mantle: Hf isotope evidence from juvenile rocks through time. *Geochimica et Cosmochimica Acta* **63**, 533-556.

Walter, M. J. (1998). Melting of Garnet Peridotite and the Origin of Komatiite and Depleted Lithosphere. *Journal of Petrology* **39**, 29-60.

Wasylenki, L. E., Baker, M. B., Kent, A. J. R. & Stolper, E.M. (2003). Near-solidus Melting of the Shallow Upper Mantle: Partial Melting Experiments on Depleted Peridotite. *Journal of Petrology* **44**, 1163-1191.

Wei, K., Trønnes, R. G. & Scarfe, C. M. (1990). Phase relations of Aluminum-Undepleted and Aluminum-Depleted Komatiites at Pressures of 4-12 GPa. *Journal of Geophysical Research* **95**, 15817-15827.

Wodicka, N., St-Onge, M. R., Scott, D. J. & Corrigan, D. (2002). Preliminary report on the U-Pb geochronology on the northern margin of the Trans-Hudson Orogen, central Baffin Island, Nunavut. In: Radiogenic age and isotopic studies: Report 15. Geological Survey of Canada, Current Research 2002-F7.

Workman, R. K. & Hart, S. R. (2005). Major and trace element composition of the depleted MORB mantle (DMM). *Earth and Planetary Science Letters* **231**, 53-72.

Yamashita, K. & Creaser, R. A. (1999). Geochemical and Nd isotopic constraints for the origin of Late Archean turbidites from the Yellowknife area, Northwest Territories, Canada. *Geochimica et Cosmochimica Acta.* **63**, 2579-2598.

Zaleski, E., Davis, W. J. & Sandeman, H. A. (2001). Continental extension, mantle magmas and basement-cover relationships. In: Extended Abstracts, Proceedings of the 4th International Archean Symposium, Perth, Australia, pp. 374-376.

Zanetti, A., Tiepolo, M., Oberti, R. & Vannucci, R. (2004). Trace-element partitioning in olivine: modeling of a complete data set from a synthetic hydrous basanite melt. *Lithos* **75**, 39-54.

Chapter 5. Summary of major conclusions and avenues for future research

INTRODUCTION

Within the preceding chapters of this thesis new field mapping, U-Pb zircon age dating, and geochemistry were presented from supracrustal rocks collected within the ca. 2.7 Ga Prince Albert group (PAg). The PAg is a ~600 km long, clastic-dominated supracrustal belt located within the central and northeastern Rae domain of Nunavut that is characterized by a unique orthoquartzite-komatiite association and significant amounts of komatiite. Prior to the initiation of this study, the age, stratigraphy, setting, and origin of the mafic-ultramafic magmas was completely unknown, and the regional relationship of the PAg with contiguous supracrustal belts within the region was entirely speculative. Combining the new data presented in this thesis with available regional-scale field observations and U-Pb zircon and Nd isotopic age constraints, significant advances have been made toward understanding the nature and origin of the supracrustal belts within the central and northeastern Rae domain, the petrogenesis of the mafic and ultramafic magmas, and insights into the pre-greenstone crustal history of the region. In addition, the exceptional preservation of mafic and ultramafic magmas within the lower PAg has provided a rare and important glimpse into an Archean melting regime. These insights have importance for broader issues concerning the nature and origin of Archean mafic-ultramafic magmas, the chemical and thermal structure of the Archean mantle, and the mantle melting processes.

The main conclusions of the thesis are briefly outlined below, beginning with those that are specific to the regional setting of the PAg and contiguous supracrustal belts, followed by those that pertain directly to the detailed magmatic development of the lower PAg, the nature and origin of the mantle upwelling(s) imaged within the PAg, and finally, the conclusions which, in my opinion, can be extrapolated to broader issues of Archean komatiite and basalt petrogenesis. As with the completion of any thesis, perhaps more questions have been raised than answered, however, the questions posed at the end of the thesis should be significantly more targeted and provide avenues and prospects for potential future research, either to refine the proposed petrogenetic model(s) and/or to provide first order tests of the theory and assumptions that go into such models. Following a summary of the main conclusions, I propose some immediate as well as long-term suggestions for future research projects which have the potential to significantly improve the ideas and conclusions put forth in this thesis.

EXTENT, DURATION, AND REGIONAL SETTING OF SUPRACRUSTAL BELTS WITHIN THE CENTRAL AND NORTHEASTERN RAE DOMAIN

The co-linear distribution of the supracrustal belts within the central and northeastern Rae domain, their similar orthoquartzite-komatiite lithological associations, and U-Pb zircon age constraints indicate that the WLg, PAg, and MRg are, as previously suggested, components of a much larger composite, co-genetic network of clastic-dominated supracrustal belts that is ~1400 km long and up to ~400 km wide. The predominant mafic-ultramafic and associated felsic volcanism within these belts began between ca. 2735-2730 Ma and persisted until at least ca. 2690 Ma.

Based on directly dated plutonic rocks, the basement within the supracrustal corridor ranges in age between ca. 2775-2870 Ma, however, a ca. 2750-2800 Ma component appears to predominate based on the direct documentation of ca. 2775 Ma crust within the Eque Bay area on Baffin Island and the prevalence of a ca. 2750-2800 Ma xenocrystic zircon population within ca. 2730-2700 Ma intermediate-felsic volcanic rocks within both the Eque Bay area and the lower PAg. Accompanying geochemical and Nd isotopic data for ca. 2730 Ma intermediate-felsic volcanic rocks within the lower PAg containing this prominent xenocrystic zircon population have confirmed its young and juvenile character. In contrast, ancient ca. 3.1 and 3.3-3.8 Ga detrital zircon identified within PAg and younger siliciclastic sedimentary rocks appear to have sampled a more enigmatic ancient crust located ~200 km to the west of the supracrustal belts where ca. 3.1 Ga granitoids have been dated and undated granitoids yield predominantly ancient ca. 3.3-3.9 Ga Nd model ages. Importantly, the occurrence of ancient detrital zircons within middle and upper PAg siliciclastic supracrustal rocks indicates that during the eruption of mafic-ultramafic magmas, detritus from westerly positioned ancient crust was being shed into the supracrustal corridor. The juvenile character of the ca. 2750-2800 Ma basement underlying the PAg and its chemical affinities with supra-subduction zone generated magmas, coupled with its position adjacent to ancient crustal components suggests that the supracrustal belts formed, at least in part, upon the most outboard and juvenile components of a pre-existing continental margin.

The linear nature of the supracrustal network, its orientation perpendicular to a prominent pre-existing crustal age structure, and the fact that volcanism and sedimentation within these belts was focused for ~45 m.y. upon the most outboard and juvenile crustal components of the Rae continental margin suggests that the pre-existing lithospheric architecture and associated linear structure(s) inherent to the Rae continental margin controlled the large-scale distribution of magmatism and sedimentation. The abrupt initiation of volcanism along the entire ~1400 km strike length of the supracrustal network between ca. 2735-2730 Ma suggests that active extension along pre-exiting structures must have preceded and facilitated the initiation of volcanism.

DETAILED MAGMATIC EVOLUTION OF THE LOWER PAG

The mafic-ultramafic volcanic succession of the lower PAg was discovered exposed upon the southwest and northeastern margins of the central tonalite intrusion within the Laughland Lake area. Together the so-called southwest and northeast volcanic zones expose ~300 km^2 of the lower PAg volcanic stratigraphy, which is dominated by komatiite, lesser volumes of basalt, rare intercalations of intermediate-felsic volcanic rocks and iron formation.

Field mapping and major element analyses of the volcanic rocks indicate that the lower PAg is distinctly bimodal and consists predominantly of low-MgO basalt (~4-13 wt.% MgO) or high-MgO komatiite (~25-40 wt.%). The unequal distribution of mafic and ultramafic magmas within the volcanic succession provided the basis for a subdivision into a lower ~1 km thick volcanic horizon comprised exclusively of basalt and an upper ~2 km thick volcanic horizon dominated by peridotitic komatiite and lesser amounts of basalt.

Identical high-precision U-Pb zircon crystallization ages for dacite intercalated with basalt within the southwest volcanic zone and with komatiite within the northeast volcanic zone of 2729.5 ± 0.8 and 2729.5 ± 0.9 Ma indicate that the transition from basalt- to komatiite-dominated volcanism occurred rapidly.

The intermediate-felsic volcanic rocks are interpreted be have been generated by high-degree partial melting of juvenile ca. 2750-2800 Ma lower crust. This is based on the recognition of a prominent population of ca. 2750-2800 Ma zircon xenocrysts, similar bulk rock geochemical compositions with estimates for the lower continental crust, a lack of evidence for formation by crystal differentiation from any known PAg basalt or komatiite, and initial Nd isotopic compositions equivalent to the ca. 2730 Ma depleted mantle.

Integrated geochemical modeling of basalt and komatiite within the lower PAg indicates that three principal processes were involved: (1) partial melting of a uniform, time integrated incompatible trace element depleted mantle possessing a mean εNd(2730 Ma) of +2.4 and εHf(2730 Ma) of +4.6; (2) pooling, mixing, and crystal differentiation of some mantle-derived magmas at shallow lithospheric depths; and (3) contamination of some mantle-derived magmas at the base of the crust via the addition of primitive lower crustal melts and rarely by minor additions of a more enriched crustal component as magmas passed through the crust and/or erupted at the surface. Magma mixing (+/- crystal differentiation/contamination) involving three primary ultramafic magmas generated in two successive stages of mantle melting are required to generate the complete spectra of basalt and komatiite recognized within the lower PAg.

The initial stage of melting (stage 1) produced two primary ultramafic magmas from a relatively fertile garnet peridotite source that possessed a degree of incompatible trace element depletion equivalent to the modern depleted MORB mantle. These end-member stage 1 melts include an enriched, near-solidus ultramafic melt (~18-20 wt.% MgO) generated by ~2 wt.% melting at ~4.25 GPa and a depleted, high-degree ultramafic melt (~25 wt.% MgO) generated by ~25 wt.% melting at ~5 GPa and which initially intersected the solidus at ~6.8 GPa.

The second stage of melting (stage 2) produced a single primary ultramafic magma by re-melting of the refractory residue produced by the extraction of the high-degree stage 1 melt at ~5 GPa. This stage 2 end-member ultramafic melt (~31 wt.% MgO) is strongly depleted and can be satisfactorily modeled by ~30 wt.% melting of the refractory peridotite residue at a pressure of ≤ 2 GPa and appears to coincide with orthopyroxene exhaustion and the formation of a dunite residue.

Modeling crystal fractionation and crustal contamination indicates that all basalt within the lower PAg were ultimately generated as a result of olivine and high-CaO clinopyroxene fractionation from the stage 1 melt end-members and/or mixtures thereof as they pooled, mixed, and differentiated at the crust-mantle boundary simultaneously.

The magmatic development of the lower PAg can be explained by a two stage model controlled by the relative arrival time and density contrast of the stage 1 and stage 2 melts at shallow lithospheric depths. The initial stage of volcanic construction, the formation of the basalt horizon, involved only direct (enriched and depleted and contaminated and uncontaminated basalt) and indirect (intermediate-felsic volcanic rocks) derivatives produced as the stage 1 melts pooled at the base of the crust. Their high density prohibited their eruption prior to significant crystal differentiation. The formation of the komatiite horizon began with the arrival of the stage 2 melt at the lithosphere where, because of its low density, it traversed the latter rapidly and relatively unimpeded, however, initially encountered significant volumes of the primary, high-degree stage 1 ultramafic melts and began to mix. The remaining stage 1 melt derivatives in sufficient volume at the crust-mantle boundary as the stage 2 melt arrived included the some derivative depleted and contaminated basalt, and minor intermediate-felsic volcanic magmas which erupted simultaneously with the primary stage 1 and stage 2 ultramafic magmas.

THE THERMAL AND PHYSICAL STRUCTURE, TEMPORAL LIFESPAN, AND ORIGIN OF THE MANTLE UPWELLING(S) WITHIN THE PAG

The precise thermal structure of the mantle upwelling imaged by the mafic and ultramafic magmas within the lower PAg is still uncertain, however, it must have been dominated by the high-temperature mantle component as this mantle achieved ~25 wt.% melting within the garnet stability field at ~5 GPa and a further ~30 wt.% melting at ≤ 2 GPa. In contrast, the low-temperature mantle component is only required to contribute ~2 wt.% melt at ~4 GPa. Such a negligible contribution to the melting suggests two possibilities: (1) either the low-temperature mantle was not physically part of the upwelling and may represent incipient melting of ambient mantle near its solidus at ~4 GPa in response to thermal energy input from the high-degree stage 1 melt as it migrated within a channelized melt conduit; or (2) the low-temperature mantle was a relatively thin veneer of ambient mantle entrained along the periphery of the high-temperature upwelling. In either case the predominance of a high-temperature mantle component suggest that the mantle upwelling can be described as a thermal anomaly.

Regardless of the detailed thermal aspects of the structure of the thermal anomaly, it is clear that no new garnet-saturated melts were entering the melt column from below during the production of the highly depleted stage 2 melt at ≤ 2 GPa. This finding provides direct and unequivocal evidence that the thermal anomaly imaged by the lower PAg magmas was a circumscribed parcel of mantle. The height of the anomaly is constrained to be < to << 90 km, the difference in the segregation depths for the high-degree stage 1 and stage 2 melts. The length and width of the thermal anomaly are unconstrained and require further study.

The lifespan of the thermal anomaly imaged within the lower PAg is only constrained to the time required for the parcel of high-temperature mantle to traverse the ~150 km interval between its intersection with the peridotite solidus at ~6.8 GPa and the termination of melting at ≤ 2 GPa. The high-precision U-Pb zircon age constraints indicate that a minimal time span, perhaps << 1 m.y., may define the transition from basalt- to komatiite-dominated magmatism within the lower PAg and, as such, effectively dates the volcanic succession to ca. 2730 Ma. A tighter constraint for the lifespan of the anomaly comes from the fact that the stage 1 melts were still differentiating during the arrival of the stage 2 melt and that they mixed and erupted together to form the komatiite horizon. This observation indicates that the lifespan of the thermal anomaly is only constrained to the time required for a komatiite melt to undergo the ~50 wt.% crystal differentiation required to produce basalt. The overall lifespan of thermal anomalies within the PAg, however, is ~40-45 m.y. based on the U-Pb zircon age constraints for ultramafic magmatism and the recognition that < 2730 Ma basalt and komatiite display the same geochemical patterns as those within the lower PAg. These data indicate several, discrete thermal anomalies were involved in ca. 2735-2690 Ma mafic-ultramafic magmatism, particularly if the duration of a single anomaly is indeed on the order of ~1-2 m.y.

The requirement that the low- and high-temperature mantle components imaged by the stage 1 melt products be compositionally indistinguishable indicates that a mechanism is required to heat-up the upper mantle by ~150 °C at a depth ≥ 200 km in order to generate a thermally anomalous high-temperature mantle. Heat transferred into the base of the upper mantle from below, perhaps by conduction from lower mantle upwellings initiated at the core-mantle boundary is currently the preferred source of heat.

IMPLICATIONS FOR THE CHEMICAL AND THERMAL STRUCTURE OF THE ARCHEAN MANTLE

Trace element and isotopic constraints indicate that the mantle source involved in the stage 1 melting, including both the low- and high-temperature components, was a relatively fertile peridotite uniformly depleted in highly incompatible trace elements. This mantle is indistinguishable in terms of its depleted Nd and Hf isotopic composition from juvenile ca. 2.7 Ga igneous rocks of upper mantle origin within the southern Superior Province. In terms of its major and trace element composition, it is indistinguishable from the modern depleted upper mantle MORB source. These data indicate that the average composition of the upper mantle has remained relatively constant since the late Archean.

The low-temperature mantle component imaged during the stage 1 melting has a potential temperature of ~1580 °C, intersects the fertile peridotite solidus near ~4 GPa, and generates a relatively low-MgO ultramafic magma (~18-20 wt.%). These features suggest that this mantle component may be the ambient Archean upper mantle. The fact that this mantle is ~200 °C hotter than the mean potential temperature of the upper mantle derived from studies of MORB magmas of ~1350 °C is in excellent agreement with secular cooling models which suggest that the average temperature of the mantle has decreased by ~200 °C since ca. 2.7 Ga.

The physical and thermal structure of thermal anomalies within the ca. 2.7 Ga mantle is not analogous to the standard mantle plume morphology employed almost universally in studies of Archean mafic-ultramafic magmatism. This study has shown that thermally anomalous ca. 2.7 Ga mantle upwellings are discrete parcels of relatively fertile upper mantle peridotite.

AVENUES FOR FUTURE RESEARCH: CENTRAL AND NORTHEASTERN RAE DOMAIN

The significant ~1 b.y. pre-greenstone detrital zircon record preserved within the three siliciclastic supracrustal rocks sampled from the Laughland Lake area have successfully imaged the major crust formation events currently recognized and/or inferred within the central and northeastern Rae domain. Simply considering the size of the region, significantly more direct (U-Pb zircon crystallization) and indirect (xenocrystic zircon and Nd isotopes) sampling of the Archean crust within the central and northeastern Rae domain is required to more quantitatively define potential pre-greenstone crustal age boundaries (e.g. ca. 2750-2800 Ma versus ca. 3.3-3.8 Ga). A regional Nd isotopic survey of archived igneous rocks coupled with U-Pb zircon age dating of the same samples might yield more detailed insights into the pre-greenstone crustal age structure than are currently possible. Transects on the order of several hundred kilometers in length perpendicular to the structural grain and preliminary age structure recognized within the region (northeast to southwest) would be most informative.

Initiation of a U-Pb zircon age dating study of the undated granitoid rocks which yielded predominantly ancient ca. 3.3-3.9 Ga depleted mantle Nd model ages located ~200 km west of the southern PAg and WLg should be conducted to determine if these granitoids are within this age range or if they are younger and recycled ancient crustal components. Documenting the existence of in-situ ancient crust either through the study of xenocrystic zircon populations or directly dating basement exposures would be an important starting point to understanding the pre-greenstone crustal development of the central and northeastern Rae domain.

The suggestion that the ca. 2750-2800 Ma basement underlying the lower PAg formed within a juvenile supra-subduction zone setting, either within a juvenile continental margin setting or an oceanic volcanic arc exotic to the pre-existing Rae crust needs to be further substantiated. Geochemical and Nd isotopic data for the directly dated ca. 2775 Ma basement component of the MRg located on Baffin Island ~800 km to the northeast might provide important insights into the nature and origin of this crust on Baffin Island.

Geochemical and Nd isotopic data need to be acquired from well-preserved volcanic successions within the WLg and MRg of known age so that attempts can be made to reconstruct/refine the physical and thermal structure of the mantle upwelling(s) described in this study. Documenting the distribution of high-MgO (~30-31 wt.%) komatiite possessing group-D like geochemical characteristics (e.g. positive HFSE anomalies and HREE-enrichment) may provide insights into the number of thermal anomalies and lithospheric thickness and architecture.

AVENUES FOR FUTURE RESEARCH: AL-UNDEPLETED KOMATIITE AND ASSOCIATED BASALT PETROGENESIS

If thermal anomalies originating at the core-mantle boundary imparting energy into the base of the upper mantle are responsible for generating the thermally anomalous mantle upwellings recognized within the ca. 2735-2690 Ma PAg komatiite-bearing volcanic successions, and these anomalies are in fact part of a globally-distributed Al-undepleted komatiite magmatic event, then compiling high-precision U-Pb ages of intercalated intermediate-felsic volcanic rocks within globally distributed ca. 2.7 Ga Al-undepleted komatiite-bearing volcanic successions should yield ages within this ~45 m.y. time interval.

Similarly, if the two stage melting model described here as well as the low- and high-temperature mantle components imaged by the stage 1 melts within the lower PAg are applicable to globally distributed ca. 2.7 Ga Al-undepleted komatiite-bearing volcanic successions, then similar geochemical patterns to those documented within the lower PAg and younger basalt and komatiite within the group might be recognizable within a global compilation of Al-undepleted komatiite and basalt geochemistry. For example, low-MgO magmas (e.g. ≤ 20 wt.% MgO) might be expected to possess minimal to pronounced HREE-depletion and minimal to pronounced negative HFSE anomalies (i.e. result from differentiation of enriched to depleted stage 1 komatiite magmas originally possessing ~18-25 wt.% MgO and mixtures thereof). In contrast, high-MgO magmas (e.g. ~25-31 wt.%) might be expected to possess variable HREE-enrichment to -depletion and minimal to pronounced positive HFSE anomalies (i.e. represent primary stage 1 and stage 2 melts and mixtures thereof).